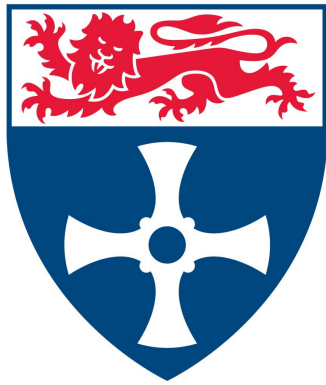


**“Nanopore Characterisation and Gas Sorption Potential of
European Gas Shales”**



Newcastle
University

Wolfson Northern Carbon Reduction Laboratories

School of Civil Engineering and Geoscience

Newcastle University

Thomas Rexer

A Thesis Submitted for the Degree of

Doctor of Philosophy

May 2014

Abstract

An inter-laboratory study of high-pressure gas sorption measurements on two carbonaceous shales has been conducted to assess the reproducibility of sorption isotherms on shale and identify possible sources of error. The measurements were carried out by 7 different international research laboratories on either in-house or commercial sorption equipment using manometric as well as gravimetric methods. Excess sorption isotherms for methane, carbon dioxide and ethane were measured at 65°C and at pressures up to 25 MPa on two organic-rich shales at dry conditions. The inter-laboratory reproducibility of the methane excess sorption isotherms was better for the high-maturity shale (within 0.02 – 0.03 mmol g⁻¹) than for the low-maturity sample (up to 0.1 mmol g⁻¹), which is in agreement with results of earlier studies on coals. The procedures for sample conditioning prior to the measurement, the measurement procedures and the data reduction approach must be optimized to achieve higher accuracy. Unknown systematic errors in the measured quantities must be minimized first by applying standard calibration methods.

Furthermore, the adsorption of methane on a dry, organic-rich, high-maturity Alum shale sample was studied at a wide temperature range (300 – 473 K) and pressures up to 14 MPa. These conditions are relevant to gas storage under geological conditions. Maximum methane excess uptake is 0.176 – 0.042 mmol g⁻¹ (125 - 30 scf t⁻¹) at 300 - 473 K. Supercritical adsorption was parameterized using the modified Dubinin-Radushkevich and the Langmuir equations.

Gas in shales is stored in three different states: adsorbed, compressed (free) and dissolved; quantifying each underpins calculations of gas storage capacity and also the mechanisms by which gas must be transported from pore (surfaces), to fracture, to the well. While compressed gas dominates in meso- and macropores, it is often assumed that (a) sorbed gas occurs mainly in micropores (< 2nm) and (b) micropores are mainly associated with organic matter. In the third part of this thesis, those ideas are tested by characterising the porous structure of six shales and isolated kerogens from the Posidonia Formation in combination with high pressure methane sorption isotherms at 45, 65 and 85°C. Together, these data help us to understand the extent to which (a) small pores control CH₄ sorption and (b) whether “sorption” pores are associated with the organic and inorganic phases within shales.

Samples were selected with vitrinite reflectance of 0.6, 0.9 and 1.45%. Pore volumes – named sorption pore volumes here - were determined on dry shales and isolated kerogens by CO₂ isotherms measured at -78°C and up to 0.1 MPa. These volumes include micropores (pore

width < 2nm) and narrow mesopores; according to the Gurvitch Rule this is the volume available for sorption of most gases. Sorption pore volumes of Posidoniashales range from 0.008 to 0.016 cm³ g⁻¹, accounting for 21 - 66% of total porosity. Whilst sorption pore volumes of isolated kerogen are much higher, between 0.095 – 0.147 cm³ g⁻¹, normalization by TOC shows that only half the sorption pore volume of the shales is located within the kerogen.

Excess uptakes on dry Posidonia shales at 65°C and 11.5MPa range from 0.056–0.110 mmol g⁻¹ (40–78 scf t⁻¹) on dry shale, and from 0.36–0.70 mmol g⁻¹ (253–499 scf t⁻¹) on dry kerogen. Enthalpies of adsorption show no variation with TOC and maturity, respectively. The correlation between maximum CH₄ sorption and CO₂ sorption pore volume at 195 K is very strong and goes through the origin, suggesting that the vast majority of sorbed CH₄ occurs in pores smaller than 6 nm. Approximately half the sorption pore volume and thus CH₄ sorption potential of these dry shales is in organic matter, with the rest likely to be associated with clay minerals. Sorption mass balances using isotherms for kerogen and clay minerals do not always account for the total measured sorbed CH₄ on dry shales, suggesting that some sorption may occur at interfaces between minerals and organic matter.

Acknowledgement

First of all, I would like to thank my supervisors, Professor K. Mark Thomas and Professor Andrew C. Aplin for providing me with the opportunity to undertake my studies in the Wolfson Northern Carbon Reduction Laboratories. I would like to convey to them my sincere gratitude for the guidance and support they have provided throughout my time at the Newcastle University. Mark's scientific approach and reasoning have shaped my research experience. Andy's assurance, positive attitude and knowledge have provided an invaluable support throughout my time as a PhD student.

Furthermore, I would like to acknowledge the GASH consortium for providing funding and sample material for this study.

I would like to express special thanks to Eliza J. Mathia. She has supported me profoundly with her expertise in petroleum geochemistry and enabled an excellent scientific interexchange of findings and interpretations in the course of the GASH project. I also want to express my gratitude to the colleagues at RWTH Aachen, especially to Dr Matus Gasparik for the fruitful collaboration and interesting scientific discussions. Thanks must also be extended to Dr Mike Benham, HidenIsochema Ltd., for his generous support with the adsorption equipment. Moreover, I would like to acknowledge Dr Jon G. Bell. His support in the lab, advice and many interesting discussions were equally valuable. Special thanks go to Dr Nykky Allen who introduced me to the experimental and theoretical aspects of the adsorption equipment in the first months of my PhD studies.

Here, I would also like to mention Seyedhamid Karimi, Ciprian B. Spatar, Majid Goodarzi, Jayne Armstrong and Chinedu Nwali for their support and advice.

Collaborations

Chapter 3 and the emanated publication are based on the collaborative work of 7 international research institutes. The study was led by Dr Matus Gasparik, RWTH Aachen University, and myself. My contributions to the study are detailed at the beginning of the chapter.

The high-pressure methane isotherms in Chapter 4 were measured at HidenIsochema Ltd. in Warrington, U.K.

Table of Contents

Abstract	I
Acknowledgement	III
Collaborations	IV
Table of Contents	V
Table of Figures	VII
Table of Tables	XI
List of Nomenclature	XIV
1. Introduction	1
2. Experimental	9
2.1 Mercury Injection Porosimetry	9
2.2 Petrophysical Methods	9
2.2.1 Grain Density Measurement	9
2.2.2 Total Organic Carbon Measurements	10
2.2.3 X-ray Diffraction	10
2.2.4 Rock Eval Pyrolysis	10
2.3 Adsorption and Pore Characterization	11
2.3.1 Adsorption Theories	11
2.3.2 Gravimetric Analyser	13
2.3.3 Manometric Analyzer	14
3. International inter-laboratory comparison of high-pressure CH₄, CO₂ and C₂H₆ sorption isotherms on carbonaceous shales	20
3.1 Introduction	21
3.1.1 Motivation for Inter-Laboratory Study of High-Pressure Sorption on Shales	21
3.1.2 Inter-Laboratory Studies of CO ₂ Sorption on Coal	23
3.1.3 Experimental Methods of High-Pressure Sorption Measurements	24
3.1.4 Goals of this Study	27
3.2 Materials and Methods	27
3.2.1 Sample Preparation and Sample Characterization	27
3.2.2 Pore Characterization	28
3.2.3 Sample Preparation	28
3.2.4 Gravimetric and Manometric Sorption Measurements	29
3.2.5 Equation of State (EoS)	33
3.3 Results	33
3.3.1 Pore Characterization (WNCRL Newcastle)	33
3.3.2 Sample Density (He-Density)	35
3.3.3 Excess Sorption Isotherms for CH ₄ , CO ₂ and C ₂ H ₆ at 65°C	36
3.4 Discussion	41
3.4.1 Repeatability versus Reproducibility	41
3.4.2 Void Volume / Sample Volume Measurements	42
3.4.3 Thermodynamic Equilibrium	44
3.4.4 Blank Tests (RWTH Aachen)	47
3.4.5 Equation of State (EoS)	48
3.4.6 Gas Impurities (Moisture)	49

3.4.7	Other Sources of Uncertainty	50
3.5	Recommendations for Optimizing High-Pressure Sorption Measurements on Shales	51
3.6	Conclusions	55
4	Methane adsorption on shale under simulated geological temperature and pressure conditions	59
4.1	Introduction	60
4.2	Experimental	62
4.2.1	Materials	62
4.2.2	High-Pressure Adsorption	63
4.2.3	Low Pressure Adsorption	63
4.2.4	Absolute Isotherms and Surface Excess	63
4.2.5	Isotherm Models	64
4.3	Results	66
4.3.1	Shale Characterization	66
4.3.2	Pore Characterization by Low Pressure Adsorption	66
4.3.3	Methane Isotherms	70
4.3.4	Modelling of Isotherms	73
4.3.5	Isosteric Enthalpy of Adsorption	78
4.4	Discussion	79
4.5	Conclusions	82
5	High-pressure Methane Adsorption and Characterization of Pores in Posidonia Shales and Isolated Kerogens	87
5.1	Introduction	88
5.1.1	Posidonia Shales	90
5.2	Experimental	90
5.2.1	Materials	90
5.2.2	Rock Eval Pyrolysis	90
5.2.3	Mercury Injection Porosimetry	90
5.2.4	Kerogen Isolation	91
5.2.5	Pore Characterization by Low Pressure Sorption	91
5.2.6	High Pressure Methane Sorption	92
5.3	Results	92
5.3.1	Total Organic Carbon Content and Grain Densities	92
5.3.2	Rock Eval Pyrolysis	93
5.3.3	Mineralogy	94
5.3.4	Pore Characterization	95
5.3.5	Methane Sorption	102
5.4	Discussion	116
5.5	Conclusions	119
6	Conclusions	125
	Appendix A	131
	Appendix B	136
	Appendix C	171
	Remarks on Unit Conversions	214

List of Figures

Figure 2.1:	Simplified schematic diagram of the manometric sorption equipment (Hiden IMI)	15
Figure 2.2:	Volume partitioning in the Hiden IMI manometric sorption apparatus	16
Figure 3.1:	Comparison of typical sorption capacities for methane on activated carbon, high-rank coals and shales measured at RWTH Aachen	22
Figure 3.2:	Micropore size distribution of the Namurian shale sample	34
Figure 3.3:	Same as Figure 3.2 for the Posidonia shale sample	35
Figure 3.4:	Comparison of the helium densities determined by individual laboratories	36
Figure 3.5:	Comparison of the CH ₄ , CO ₂ and C ₂ H ₆ excess sorption isotherms at 65°C for the over-mature Namurian shale	38
Figure 3.6:	Comparison of CH ₄ , CO ₂ and C ₂ H ₆ excess sorption isotherms at 65°C for the immature Posidonia shale	41
Figure 3.7:	Example of proposed void volume determination in a manometric device	44
Figure 3.8:	Examples of the uptake curves of the CH ₄ and CO ₂ during the manometric sorption experiment on the Posidonia shale sample from RWTH	46
Figure 3.9:	Example of uptake curve of the CH ₄ during the manometric sorption experiment	46
Figure 3.10:	CH ₄ and CO ₂ excess sorption isotherms for the Posidonia sample measured at RWTH	48
Figure 3.11:	Comparison of the raw CH ₄ and CO ₂ excess sorption isotherms for the Posidonia shale calculated using different equations of state	49
Figure 3.12:	CO ₂ sorption isotherms at 273 K on shale measured with a modified gravimetric setup with and without gas pre-drying	50
Figure 4.1:	Subcritical Isotherms for Alum Shale #1: N ₂ (78 K), CO ₂ (195 K) and CH ₄ (112 K) absolute isotherms on a relative pressure basis	68
Figure 4.2:	Subcritical Isotherms for Alum Shale #1: Surface excess CH ₄ (112 K), CH ₄ (173 K) and CO ₂ (273 K)	68
Figure 4.3:	Micropore size distribution of Alum Shale #1	70
Figure 4.4:	Methane surface excess adsorption for Alum Shale #1: Isotherms for temperature range (300 – 473 K)	71

Figure 4.5:	Methane surface excess adsorption for Alum Shale #1: The variation of maximum surface excess with 1/Temperature (K^{-1})	72
Figure 4.6:	Methane surface excess adsorption for Alum Shale #1: The variation of surface excess with 1/Temperature (K^{-1}) for isobars at 5, 7, 9, 11 and 13 MPa	72
Figure 4.7:	Optimal Supercritical Dubinin-Radushkevich (SDR) (Variant 1) fit	76
Figure 4.8:	Optimal Langmuir fit (Variant 8)	77
Figure 4.9:	Adsorbed phase densities calculated from the SDR model and equation 7	78
Figure 4.10:	Adsorption isosteres for methane adsorption on Alum Shale #1	79
Figure 4.11:	Methane excess isotherm and absolute isotherms based on different models at a) 318 K and b) 448	81
Figure 4.12:	Predicted amounts of excess and absolute adsorbed methane based on Alum Shale sorption data presented in this paper	82
Figure 5.1:	CO ₂ adsorption isotherms for shales at -78°C	97
Figure 5.2:	CO ₂ isotherms for kerogens at -78°C	97
Figure 5.3:	Correlation of Total Pore Volume with CO ₂ Sorption Pore Volume (-78°C) plus MICP Pore Volume	98
Figure 5.4:	N ₂ adsorption isotherms at -196°C for Posidoni ashales	99
Figure 5.5:	N ₂ adsorption isotherms at -196°C for Posidonia kerogens	99
Figure 5.6:	Methane surface excess adsorption isotherms at 45°C on Posidonia shales	102
Figure 5.7:	Methane surface excess adsorption isotherms at 65°C and 85°C on Posidonia shales	103
Figure 5.8:	Methane surface excess isotherms for Posidonia kerogens at 45°C	104
Figure 5.9:	Methane surface excess adsorption isotherms for Posidonia kerogens at 65°C	104
Figure 5.10:	Plot of Maximum methane surface excess uptake at 45°C versus TOC	105
Figure 5.11:	Graph of CH ₄ maximum excess uptake at 45°C and 10 MPa on shale (squares) and kerogen (triangles) versus CO ₂ sorption pore volume (-78°C)	106
Figure 5.12:	Graph of CH ₄ excess uptake at 65°C and 11.5 MPa on shale (squares) and kerogen (triangles) versus CO ₂ sorption pore volume (-78°C)	106
Figure 5.13:	Absolute methane isotherms on shale at 65°C	111

Figure 5.14:	Absolute methane isotherms on kerogen at 65°C	111
Figure 5.15:	Mass balances of methane surface excess sorption on shale at 65°C	113
Figure 6.1:	Corrleation of methane excess uptake at 65°C and 11.5 MPa with the CO ₂ sorption pore volume	128
Figure S B1:	Nitrogen adsorption isotherms on Alum Shale #1 at 77 K	136
Figure S B2:	Fit of the SDR model (Variant 2) to the experimental data	151
Figure S B3:	Fit of the SDR model (Variant 3) to the experimental data	153
Figure S B4:	Fit of the Langmuir model (Variant 4) to the experimental data	155
Figure S B5:	Parameter calculated by the Langmuir model (Variant 4)	155
Figure S B6:	Fit of the Langmuir model (Variant 5) to the experimental data	157
Figure S B7:	Parameter calculated by the Langmuir model (Variant 5)	157
Figure S B8:	Fit of the Langmuir model (Variant 6) to the experimental data	159
Figure S B9:	Parameter calculated by the Langmuir model (Variant 6)	159
Figure S B10:	Fit of the Langmuir model (Variant 7) to the experimental data	161
Figure S B11:	Parameter calculated by the Langmuir model (Variant 7)	161
Figure S B12:	Fit of the Langmuir model (Variant 9) to the experimental data	163
Figure S B13:	Parameter calculated by the Langmuir model (Variant 9)	163
Figure S B14:	Methane excess and absolute isotherms based on different models over a range of temperature	168
Figure S C1:	Characterization data for kerogens and shale	175
Figure S C2:	Carbon dioxide (-78°C) and nitrogen (-196°C) isotherms for pyrite	178
Figure S C3:	Absolute methane isotherms on shale at 45°C	197
Figure S C4:	Absolute methane isotherms on shale at 85°C	197
Figure S C5:	Absolute methane isotherms on kerogen at 45°C (points)	198
Figure S C6:	Micropore Size Distributions on shale calculated	201
Figure S C7:	Micropore Size Distributions on kerogen calculated	204
Figure S C8:	Comparison of methane surface excess at specific pressures with CO ₂ sorption pore volume	206

Figure S C9:	Comparison of supercritical methane isotherms normalized to TOC for shales and kerogens	209
Figure S C10:	Comparison of porosity characteristics determined from subcritical low pressure adsorption	212

List of Tables

Table 2.1:	Acceptable variations for TOC measurements	10
Table 2.2:	IUPCA pore classification	11
Table 2.3:	Manometric Apparatus specification	16
Table 3.1:	Basic geochemical data of the studied samples	28
Table 3.2:	Information on experimental parameters reported by individual laboratories	31
Table 3.3:	Results of the pore size characterization by means of low-pressure CO ₂ (195 K and 273 K) and N ₂ (77 K) sorption	34
Table 4.1:	Mineralogical Composition (%) of Alum Shale #1 measured by X-ray powder diffraction	66
Table 4.2:	Ultrapore-, micropore- and pore volumes determined by low pressure adsorption	69
Table 4.3:	Variants of the SDR and Langmuir isotherm models tested	74
Table 4.4:	Fitting parameters for the optimal DR (Variant I) and the optimal Langmuir fit (Variant 8)	74
Table 5.1:	Well depth, TOC, grain and helium densities, mercury injection pore volumes and total porosities for Posidonia shales and kerogens	93
Table 5.2:	Rock-Eval pyrolysis results for Posidonia shales	94
Table 5.3:	Mineral composition of Posidonia shales in wt%	94
Table 5.4:	Shale and kerogen pore volumes measured by different techniques	101
Table 5.5:	Parameters calculated by fitting the Langmuir equation to the shale methane sorption data	110
Table 5.6:	Isosteric Enthalpies of Adsorption of CH ₄ on shales and kerogens at zero surface coverage ($Q_{st,n=0}$)	116
Table S A1:	CO ₂ isotherms at 273 K	131
Table S A2:	CO ₂ isotherm at 194.5 K	131
Table S A3:	N ₂ isotherms at 77 K in tabular form	132
Table S A4:	Namurian Shale CH ₄ isotherms	133
Table S A5:	Posidonia Outcrop CH ₄ isotherms	134
Table S A6:	Posidonia Outcrop CO ₂ isotherms	135

Table S B1:	CO ₂ Isotherms at 194.5 K in tabular form	136
Table S B2:	N ₂ Isotherms at 77 K in tabular form	137
Table S B3:	CO ₂ Isotherms at 273 K	138
Table S B4:	CH ₄ excess isotherm data 300 K	139
Table S B5:	CH ₄ excess isotherm data 303 K	140
Table S B6:	CH ₄ excess isotherm data 308 K	141
Table S B7:	CH ₄ excess isotherm data 318 K	142
Table S B8:	CH ₄ excess isotherm data 338 K	143
Table S B9:	CH ₄ excess isotherm data 358 K	144
Table S B10:	CH ₄ excess isotherm data 373 K	145
Table S B11:	CH ₄ excess isotherm data 398 K	146
Table S B12:	CH ₄ excess isotherm data 423 K	147
Table S B13:	CH ₄ excess isotherm data 448 K	148
Table S B14:	CH ₄ excess isotherm data 473 K	149
Table S B15:	All parameters calculated by fitting the SDR model (Variant 2) to the experimental data	150
Table S B16:	All parameters calculated by fitting the SDR model (Variant 3) to the experimental data	152
Table S B17:	All parameters calculated by fitting the Langmuir model (Variant 4) to the experimental data	154
Table S B18:	All parameters calculated by fitting the Langmuir model (Variant 5) to the experimental data	156
Table S B19:	All parameters calculated by fitting the Langmuir model (Variant 6) to the experimental data	158
Table S B20:	All parameters calculated by fitting the Langmuir model (Variant 7) to the experimental data	160
Table S B21:	All parameters calculated by fitting the Langmuir model (Variant 8) to the experimental data	162
Table S C1:	Isolated Posidonia kerogen characterization data	177

Table S C2:	Low pressure isotherms for CO ₂ adsorption on shales and kerogens at 273K	179
Table S C3:	Low pressure isotherms for CO ₂ adsorption on shales and kerogens at 195 K	182
Table S C4:	Low pressure isotherms for N ₂ adsorption on shales and kerogens at 77 K	184
Table S C5:	High Pressure CH ₄ Isotherms for shales and Kerogens	187

List of Nomenclature

Symbol	Physical quantity*
$^{\circ}\text{C}$	Degree Celsius
β	D-R equation: adsorbate characteristic parameters
γ	Fluid surface tension
ϑ	Contact angle of liquid on a plane surface
ΔH	Enthalpy of adsorption
Δp	Pressure difference between liquid and gas pressure ($p_{\text{liquid}} - p_{\text{gas}} < 0$)
A_0	Virial Equation: adsorbate – adsorbent interaction
A_1	Virial Equation: adsorbate – adsorbate interaction
ρ_{ad}	Adsorbed phase density
ρ_s	Particle density of the shale
ρ_w	Grain density measurement: Density of water at the measured water bath temperature
c	BET equation: constant related to adsorption energy
CoK_{α}	Cobalt K-alpha emission
D	D-R equation: interaction constant which, equal to $-1/(\beta E_0)^2$
E_0	Adsorbate characteristic parameters
f	Manometric apparatus: Fraction of the sample cell at temperature T_s (temp. dependent)
HI	Rock Eval Pyrolysis: Hydrogen Index
K_H	Henry's Law constant
L	Litre (1 dm^3)
M	Molar Mass
m_1	Grain density measurement: mass of the pycnometer
m_2	Grain density measurement: mass of the pycnometer plus dry sample
m_3	Grain density measurement: mass of the pycnometer plus dry sample plus water
m_4	Grain density measurement: mass of the pycnometer plus water
n_0	Maximum absolute amount adsorbed
n_{ad}	Amount adsorbed
n_{ab}	Absolute amount adsorbed
n_{ex}	Excess amount adsorbed
n_m	Monolayer coverage
n_{max}	Maximum amount adsorbed
OI	Rock Eval Pyrolysis: Oxygen Index

p	Pressure
p_0	Saturated vapour pressure
p^0	Pressure at perfect gas reference state
p_1	Manometric apparatus: Pressure in the reference cell before dosing
p_2	Manometric apparatus: Pressure in the reference and sample cell after dosing and kinetic
PI	Rock Eval Pyrolysis: Production Index
R	Ideal gas constant (8.314 J mol ⁻¹ K ⁻¹)
r	Pore radius
$S1$	Rock Eval Pyrolysis: Amount of evaporated molecules at the first stage (typically molecules with less than 40 carbon atoms)
$S2$	Rock Eval Pyrolysis: Amount of evaporated molecules at the second stage (typically products of cracking reactions)
scf	Standard cubic foot (see 'Remarks on Unit Conversion')
T	Temperature
t	Short ton (U.S. measurement system; equivalent to 907.18474 kg)
T_{max}	Rock Eval Pyrolysis: Temperature of maximum amount of evaporation
T_{R1}	Manometric apparatus: Temperature in the reference cell before dosing
T_{R2}	Manometric apparatus: Temperature in the reference cell after dosing
T_{SI}	Manometric apparatus: Temperature in the volume V_{SI} after dosing
T_S	Manometric apparatus: Temperature in the volume $V_S \cdot f$ after dosing
TOC	Total organic carbon
V_D	Manometric apparatus: Diaphragm valve volume
V_p	Pore volume
V_R	Manometric apparatus: Volume of the reference cell
VR	Vitrinite Reflectance [%R _O] - percentage of reflected light from a sample immersed in oil
V_S	Manometric apparatus: Volume of the sample cell minus the skeletal volume of the adsorbent
V_{SC}	Manometric apparatus: Volume of the sample cell at reference cell temperature
Z_{R1}	Compressibility factor for conditions in the reference volume prior to dosing
Z_{R2}	Compressibility factor for conditions in the reference volume after dosing
Z_{SI}	Compressibility factor for conditions in V_{SC} after dosing
Z_S	Compressibility factor for conditions in $V_S \cdot f$ after dosing

*Only units which are not part of the International System of Units (SI) are stated here.

Chapter 1

General Introduction and Objectives

Approaching peak oil production, record oil prices and growing oil demand by emerging markets has intensified the search for new energy sources in recent years.¹⁻⁵ Among all new resources none has seen such a rapid increase as shale gas. Gas is generated both biologically as a result of methanogenesis and by thermal cracking of organic matter (metagenesis).⁶ Most of the generated gas is expelled from the source rock and the retained gas has become what is considered an “unconventional” gas resource. The composition of the gas occurring in shales varies from formation to formation, but is largely composed of methane, ethane, butane, propane, nitrogen and carbon dioxide.⁷⁻¹⁰ In comparison to conventional gas reservoirs, shale has insufficient matrix permeability for significant fluid flow to boreholes.¹¹ Thus, exploitation of shale gas requires horizontally drilling into the formation and fracturing the rock by water-chemical mixture at high pressures. Advances in these two technologies and an increasing price for natural gas have made shale gas economically viable. Production in the US has risen by more than 600% up to 7,994 billion cubic feet from 2007 to 2011 and this has helped the economic recovery of US industry.^{2,3,12} While some expect that shale gas will make the US a gas exporting country and shift political weight worldwide, others have claimed that the forecasts are based on overinflated industry claims and that the shale gas “bubble” is soon to burst.^{2,13} In 2012 the US Energy Information Administration (EIA) had to downgrade their shale gas estimates in the US by more than 40% from 2011 to 2012.³ Considerable uncertainty exists as little is known about the percentage of recoverable gas until the well is finally abandoned. A crucial step for improving estimates is to better understand and constrain the ways in which gas is stored in shales.

Gas is stored in three different phases within shales: as a) compressed gas in intergranular porosity and natural fractures, b) adsorbed gas on pores in organic matter and clays and c) dissolved in kerogen and bitumen.^{11,14} The amount of compressed gas depends on the porosity and reservoir temperature and pressure. Especially, pores in the range of 1 – 500 nm are assumed to influence or control gas capacity and permeability of shales.¹⁴⁻¹⁷ Pores in this size range are abundant in pyrobitumen of many shale systems. Pyrobitumen-like phases originate most likely from the exsolution of gaseous hydrocarbons during secondary thermal cracking of retained oil in the organic phase.^{15,17-20} However, in geological system some of the pores are filled by water.¹⁴

The adsorbed gas in shale is physisorbed on the surfaces of minerals and organic matter. Physisorption is the adherence of molecules to the pore surface of materials by weak

van der Waals interactions.^{21,22} For shales it has been shown that sorption capacity largely depends on the total organic carbon (TOC) content.²³⁻²⁵ Clay content has also been linked to methane uptake.^{26,27} Similar to coal, maturation (coalification) of shales alters the pore system and increasing sorption capacities as well as increasing micropore volumes with maturation have been reported.^{15,23,25} However, the extent of micropore generation and the link to sorption capacity remains poorly constrained and is, thus, the main motivation for this thesis.

Objectives

This thesis is subdivided into three results chapters and each chapter deals with a specific issue or set of issues. The content and findings of chapters 4 and 5 have been published in *Energy&Fuels*. Chapter 3 is based on collaboration with 6 international institutes and has been submitted for publication.

Aims and objectives of the thesis are outlined below. A more detailed description of objectives and the background are given at the beginning of each results chapter.

Optimisation of sorption measurements on shale (Chapter 3)

a. Modification of high-pressure, high-temperature manometric equipment to accurately determine gas uptake on shales and kerogens

Gas uptake on shales is two magnitudes lower than on commercial activated carbon material and about 10 times lower than on coal.²⁸ Main error sources on manometric equipment are leakage, inaccuracies in volume calibration, presence of moisture and insufficient equilibration times.²⁹ Gas uptake measured on manometric adsorption equipment is determined accumulatively and thus systematic errors can strongly affect results.³⁰ Consequently, extrapolation of sorption capacity of shales from laboratory measurements to shale reservoirs can lead to imprecise gas-in-place estimates.

b. Validation of sorption results and suggestion of standards for gas sorption measurements on shale

Determination of sorption isotherms has attracted a lot of research interest and various institutes and research groups have published high-pressure isotherms on

shale.^{23,25,31-34} Inter-laboratory comparisons of gas uptake on coal samples have shown discrepancies.^{28,35,36} Due to the difficulty of the adsorption measurements on shale, it was the aim of this study to collect isotherms on shale, identify the causes of discrepancies and suggest procedures to minimize these differences.²⁸

Effect of high temperature on methane sorption on shale and modelling of high-pressure high-temperature methane sorption (Chapter 4)

A case study on an Alum Shale sample of gas window maturity was conducted for better understanding temperature impact on the reduction of the gas sorption capacity on shales as well as testing different models to describe methane sorption over a wide range of pressure and temperature. The Alum Shale sample was obtained from the Skelbro-2 well in Bornholm, Denmark at a depth of 9.4 m.³⁷

a. Quantification of the effect of temperature on gas storage capacity on shales

Physisorption is an exothermic process. Thus, with increasing temperature, adsorption capacity decreases.²¹ The effect of temperature is quantified by the isosteric enthalpy of adsorption. The enthalpy of adsorption can vary with pressure depending on the specific sorption mechanism, e.g. energetically homogeneous/heterogeneous surface and attraction/repulsion between sorbed gas particles.^{21,22} Determining isosteric enthalpies on shales and relating it to maturity, TOC and kerogen type can eventually facilitate better prediction of the amount of sorbed gas at various temperatures.

b. Quantification of absolute amounts and modelling of gas sorption on shale

Various models are available to describe gas sorption on porous materials.³⁸⁻⁴⁰ These models are typically suitable for subcritical gas sorption. Here these models are tested and modified to apply them to high pressure methane sorption on shale. Constraining models will help to parameterize sorption on shale and, ideally, provide estimates of adsorbed phase volumes and densities so that these parameters can be related to petrophysical properties.

Pore Characterization and gas adsorption on shales (Chapter 5)

To improve the understanding of sorption in shales, a case study on shales from the Posidonia formation was conducted. This black shale formation is a reference source rock of Type II kerogen and is regarded as one of the most widespread and economically important petroleum source rocks of Western Europe.⁴¹⁻⁴³ Shale samples from three different boreholes progressively increasing in maturity from early oil window to gas window maturity were obtained.⁴⁴ Kerogens were isolated from the shales by chemical degradation of minerals.^{43,45,46} The aims were as follows:

a. Investigation of the micropore evolution with maturity in shales and kerogens

Ross and Bustin's pioneering work has shown that part of the adsorbed gas is stored within micropores in shales.²³ Furthermore, it has been shown that the microporosity in organic matter and coal increases with vitrinite content.^{47,48} Among the minerals, clays are the only minerals to exhibit a significant micropore volume.^{23,26} However, the effect of maturation on micropore volume evolution has not yet been investigated. The volume of pores below about 6 nm can be quantified by low pressure sorption methods. In the present study multiple gases over a range of temperatures and pressures are sorbed on shale and isolated kerogen. Various models are applied to quantify the pore volumes.

b. Identification of links between pore space and high-pressure sorption

In the present study, pore volumes and surface areas measured by sorption techniques on shales and kerogen are compared against high-pressure methane capacities. This will help to better understand gas sorption capacities of shales. Furthermore, establishing links between porosity and high-pressure methane sorption capacities will serve as a basis to gain insight into reduction of gas sorption capacities by water vapour as well as competitive gas sorption on shales. This will eventually improve 'gas-in-place' estimates as most shale reservoirs consist of a mixture of different gases and water.

c. Assessment of the role of the organic matrix in sorption on shale

All pore characterization and sorption capacity measurements conducted on shale were, in addition, conducted on kerogen isolated from the shales. Pore volumes and methane capacities on kerogen were investigated to reveal the role of organics in sorption of shales as

well as the interdependency between pore volume, pore size distribution and methane capacities on kerogen. Furthermore, comparing sorption capacities of kerogens and TOC-normalized capacities of shale will help to differentiate between sorbed gas within and sorbed gas associated (gas sorbed at the organic-inorganic interface) with organic matter and sorbed gas in the inorganic shale phase, respectively.

References

- (1) Thusi, B.; Svarich, B.; Melon, F.; Vargas, F.; Amini, F.; Rabinovich, G.; Schmidt, G.; Iancu, I.; Moncombie, J.-E.; Tagle, J. A.; Hammes, K.; Re, L. L.; Florette, M.; Bohm, M.; Howard, M. W.; Paveh, M. T.; Monti, P.; Cheliak, P.; Luebke, R.; Sculari, S.; Hercberg, S.; Koljonen, T.; Maassen, U.; Breisig, V.; Chodzicki, W. World Energy Resources 2013 Survey: Summary. *World Energy Resources* [Online Early Access]. Published Online: 2013.
- (2) *Annual Energy Outlook 2013*, U.S. Department of Energy, 2013.
- (3) *International Energy Outlook 2013*, U.S. Department of Energy, 2013.
- (4) *Technically Recoverable Shale Oil and Shale Gas Resources: An Assessment of 137 Shale Formations in 41 Countries Outside the United States*, U.S. Department of Energy, 2013.
- (5) US: http://www.eia.gov/dnav/ng/ng_prod_shalegas_s1_a.htm, 2013; Vol. 2013.
- (6) Tissot, B. P.; Welte, D. H. *Petroleum formation and occurrence: a new approach to oil and gas exploration*, 1978.
- (7) Berner, U.; Faber, E. *Org. Geochem.* **1996**, *24*, 947.
- (8) Hill, R. J.; Jarvie, D. M.; Zumberge, J.; Henry, M.; Pollastro, R. M. *AAPG Bull.* **2007**, *91*, 445.
- (9) Martini, A. M.; Walter, L. M.; Ku, T. C. W.; Budai, J. M.; McIntosh, J. C.; Schoell, M. *AAPG Bull.* **2003**, *87*, 1355.
- (10) Martini, A. M.; Walter, L. M.; McIntosh, J. C. *AAPG Bull.* **2008**, *92*, 327.
- (11) Curtis, J. B. *AAPG Bull.* **2002**, *86*, 1921.
- (12) *Review of Emerging Resources: U.S. Shale Gas and Shale Oil Plays*, U.S. Department of Energy, 2011.
- (13) Engdahl, F. W. *Global Research* **2013**, *13*.
- (14) Passey, Q.; Bohacs, K.; Esch, W.; Klimentidis, R.; Sinha, S. In *International Oil and Gas Conference and Exhibition in China 2010*.
- (15) Bernard, S.; Wirth, R.; Schreiber, A.; Schulz, H.-M.; Horsfield, B. *Int. J. Coal Geol.* **2012**, *103*, 3.
- (16) Curtis, M. E.; Ambrose, R. J.; Sondergeld, C. H.; Society of Petroleum Engineers.
- (17) Curtis, M. E.; Sondergeld, C. H.; Ambrose, R. J.; Rai, C. S. *AAPG Bull.* **2012**, *96*, 665.
- (18) Loucks, R. G.; Reed, R. M.; Ruppel, S. C.; Jarvie, D. M. *Journal of Sedimentary Research* **2009**, *79*, 848.
- (19) Loucks, R. G.; Reed, R. M.; Ruppel, S. C.; Hammes, U. *AAPG Bull.* **2012**, *96*, 1071.
- (20) Curiale, J. A. *Org. Geochem.* **1986**, *10*, 559.
- (21) Gregg, S. J.; Sing, K. S. W.; Academic Press Inc: London, 1982; Vol. 2.
- (22) Do, D. D. *Adsorption Analysis: Equilibria and Kinetics*; Imperial College Press, 1998.
- (23) Ross, D. J. K.; Bustin, R. M. *Mar. Pet. Geol.* **2009**, *26*, 916.

- (24) Zhang, T. W.; Ellis, G. S.; Ruppel, S. C.; Milliken, K.; Yang, R. S. *Org. Geochem.* **2012**, *47*, 120.
- (25) Gasparik, M.; Bertier, P.; Gensterblum, Y.; Ghanizadeh, A.; Krooss, B. M.; Littke, R. *Int. J. Coal Geol.*
- (26) Ji, L.; Zhang, T.; Milliken, K. L.; Qu, J.; Zhang, X. *Applied Geochemistry* **2012**, *27*, 2533.
- (27) Liu, D.; Yuan, P.; Liu, H.; Li, T.; Tan, D.; Yuan, W.; He, H. *Applied Clay Science* **2013**, *85*, 25.
- (28) Gensterblum, Y.; van Hemert, P.; Billemont, P.; Battistutta, E.; Busch, A.; Krooss, B. M.; De Weireld, G.; Wolf, K. *Int. J. Coal Geol.* **2010**, *84*, 115.
- (29) van Hemert, P.; Bruining, H.; Rudolph, E. S. J.; Wolf, K.-H. A. A.; Maas, J. G. *Review of Scientific Instruments* **2009**, *80*.
- (30) Rouquerol, J.; Rouquerol, F.; Sing, K. S. W. *Adsorption by Powders and Porous Solids*; Academic Press: San Diego, 1999.
- (31) Lu, X. C.; Li, F. C.; Watson, A. T. *Fuel* **1995**, *74*, 599.
- (32) Chalmers, G. R. L.; Bustin, R. M. *Bull. Can. Pet. Geol.* **2008**, *56*, 22.
- (33) Gasparik, M.; Ghanizadeh, A.; Bertier, P.; Gensterblum, Y.; Bouw, S.; Krooss, B. M. *Energy Fuels* **2012**, *26*, 4995.
- (34) Weniger, P.; Kalkreuth, W.; Busch, A.; Krooss, B. M. *Int. J. Coal Geol.* **2010**, *84*, 190.
- (35) Goodman, A. L.; Busch, A.; Duffy, G. J.; Fitzgerald, J. E.; Gasem, K. A. M.; Gensterblum, Y.; Krooss, B. M.; Levy, J.; Ozdemir, E.; Pan, Z.; Robinson, R. L.; Schroeder, K.; Sudibandriyo, M.; White, C. M. *Energy Fuels* **2004**, *18*, 1175.
- (36) Goodman, A. L.; Busch, A.; Bustin, R. M.; Chikatamarla, L.; Day, S.; Duffy, G. J.; Fitzgerald, J. E.; Gasern, K. A. M.; Gensterblum, Y.; Hartman, C.; Jing, C.; Krooss, B. M.; Mohammed, S.; Pratt, T.; Robinson, R. L.; Romanov, V.; Sakurovs, R.; Schroeder, K.; White, C. M. *Int. J. Coal Geol.* **2007**, *72*, 153.
- (37) Schovsbo, N. H. *Gff* **2002**, *124*, 107.
- (38) Langmuir, I. *Journal of the American Chemical Society* **1918**, *40*, 1361.
- (39) Brunauer, S.; Emmett, P. H.; Teller, E. *Journal of the American Chemical Society* **1938**, *60*, 309.
- (40) Dubinin, M. M.; Zaverina, E. D.; Serpinsky, V. V. *Journal of the Chemical Society (Resumed)* **1955**, 1760.
- (41) Littke, R.; Baker, D. R.; Leythaeuser, D. *Org. Geochem.* **1988**, *13*, 549.
- (42) Vandenbroucke, M.; Behar, F.; Santorcuato, A.; Rullkotter, J. *Org. Geochem.* **1993**, *20*, 961.
- (43) Vandenbroucke, M.; Largeau, C. *Org. Geochem.* **2007**, *38*, 719.

- (44) Bernard, S.; Horsfield, B.; Schulz, H.-M.; Wirth, R.; Schreiber, A.; Sherwood, N. *Mar. Pet. Geol.* **2012**, *31*, 70.
- (45) Durand, B.; Nicaise, G. *Kerogen, Insoluble Organic Matter from Sedimentary Rocks* **1980**, 35.
- (46) Saxby, J. D. *Chemical Geology* **1970**, *6*, 173.
- (47) Cai, Y. D.; Liu, D. M.; Pan, Z. J.; Yao, Y. B.; Li, J. Q.; Qiu, Y. K. *Fuel* **2013**, *103*, 258.
- (48) Clarkson, C. R.; Bustin, R. M. *Fuel* **1996**, *75*, 1483.

Chapter 2

Experimental

The principles of experimental methods and techniques used throughout this thesis are introduced in this chapter. More detailed information about calculations based on the experimental data, e.g. pore volume from mercury injection, is given in the following chapters.

2.1 Mercury Injection Porosimetry

Pore size distributions can be calculated from Mercury Injection Porosimetry by means of the Young-Laplace equation for cylindrical pores (Equation 3.1) which relates the expansion of non-wetting fluids and the mechanical equilibrium of liquid drops on surfaces.¹

$$\Delta p = -2 \gamma \frac{\cos(\theta)}{r}$$

Equation 3.1 – Young-Laplace Equation for cylindrical pores

where

Δp pressure difference between liquid and gas pressure ($p_{\text{liquid}} - p_{\text{gas}} < 0$)

γ fluid surface tension

θ contact angle of the intrusion liquid

r pore radius

Mercury-air interfacial tension at 20°C is 485 mN m⁻¹.² A contact angle of 141° for the mercury surface was assumed.

2.2 Petrophysical Methods

2.2.1 Grain Density Measurement

Typically ~ 3 mg of shale was pre-dried overnight at 105°C in air. The crushed sample (particle size < 0.5 mm) was weighed in a pre-weighed pycnometer (50 mL). 10 mL of Teepol® soap solution (concentration: 5%) were added and the pycnometer was filled up with degassed water. The weight of the pycnometer plus sample plus water was measured at 25°C. The weight of the pycnometer when filled with de-aired water only was measured at 25°C to determine the volume of the pycnometer. The particle density was calculated as follows:

$$p_s = \frac{p_w (m_2 - m_1)}{(m_4 - m_1) - (m_3 - m_2)}$$

Equation 3.2 – Buoyancy Grain Density Measurement

where

- ρ_s particle density of the shale
 ρ_w density of water at the measured water bath temperature (0.997 g ml⁻¹)
 m_1 is the mass of the pycnometer
 m_2 mass of the pycnometer plus dry sample
 m_3 mass of the pycnometer plus dry sample plus water
 m_4 mass of the pycnometer plus water

2.2.2 Total Organic Carbon Measurements

Samples were crushed to pass through a 0.5 mm sieve. 0.1 g of powder, in a porous crucible, was treated with sufficient hydrochloric acid, 4 mol L⁻¹, to remove carbonates. After the acid had drained from the crucible, the crucible and sample were dried overnight at 65°C. The total organic carbon content was then measured using a Leco CS244 Carbon/Sulphur Analyser.

Table 2.1: Acceptable variations for TOC measurements.

Carbon concentration [%]	Acceptable variation [%]
0 – 0.25	0.025 absolute
0.25 – 7.50	10.0 relative
> 7.5	0.75 absolute

2.2.3 X-ray Diffraction

The XRD data were obtained using a Siemens D5000 diffractometer, using CoK_α radiation, at the James Hutton Institute in Aberdeen. The samples were scanned from 2-75° 2θ, with a step time of 2 seconds per 0.02 degree step. The minerals were quantified by Hillier's method.^{3,4}

2.2.4 Rock Eval Pyrolysis

100 mg of shale or 10 mg of kerogen are loaded on a Delsi Rock Eval OSA pyrolysis instrument (Rock Eval Type II). The sample chamber is heated in a helium stream and the emitted gases are measured by means of a Flame Ionization Detector. At 300°C the temperature is kept constant for 3 min. Molecules with, typically, less than 40 carbon atoms evaporate and are quantified (S1 peak). The temperature is increased (25°C/min) to 550°C. Along the heating process cracking reactions occur and the products are evaporated (S2 peak). The temperature with the maximum generation rate of cracking products (T_{max}) is recorded.

Based on the results kerogen characteristics are calculated and used to determine the origin and the evolution level of the organic material. The characteristics calculated are as the hydrogen index ($HI = 100 \times S2 / TOC$) and the production index ($PI = S1 / (S1+S2)$).⁵

Experimental error for samples is +/-5% standard deviation. Duplicate samples were analysed again, when they gave values outside this range. However, samples exhibiting very low values for S1 and S2, respectively, are allowed to exceed the stated deviation range.

The instrument is calibrated using Norwegian Geochemical Standards (NGS) SR-1 and JR-1 available through Norwegian Petroleum Directorate.⁶ The standard (usually JR-1) is analysed as a control sample at the beginning, middle and end of a batch of samples and analyses are rejected and repeated if the values do not fall within the specified deviation range.

2.3 Adsorption and Pore Characterization

2.3.1 Adsorption Theories

The models used to calculate micropore volumes, sorption pore volumes and BET surface areas are described in this section. More information can also be found elsewhere.^{7,8} It should be noted that the calculation of (micro-) pore volumes and the surface area are all based on the interpretation of adsorption isotherms by models. These models represent simplified concepts of the adsorption mechanism and the data, i.e. pore volumes and surface areas, thus represent only 'equivalent' or 'apparent' pore volumes and surface areas.^{9,10} For this reason a combination of different models and isotherms - as recommended by Marsh et al. - to characterize pores in shales were used in this thesis.⁹

Pore classification

Pores are classified in accordance with the IUPAC classification scheme.^{11,12}

Table 2.2: IUPAC pore classification.

Pore Width [nm]	Subclassification	Classification
< 0.7	Ultramicropores	Micropores
0.7 – 1.4	Micropores	
1.4 – 2.0	Supramicropores	
2 – 50		Mesopores
> 50		Macropores

Gurvitch Rule - Sorption Pore Volume

Sorption pore volumes are calculated by converting maximum uptake (at $p/p_0 \approx 1$) into volume (see Equation 3.3). According to the Gurvitch Rule adsorption uptake (at $p/p_0 \approx 1$) when expressed as a volume of liquid – using the liquid density at the same temperature and equilibrium vapour pressure - should be the same for all adsorptives on a given adsorbent.^{9,13,14} Deviations from the rule are mostly due to kinetic effects, e.g. when either molecules are physically excluded from certain pores because of their large size or when molecules do not possess sufficient kinetic energy to overcome the free energy barrier to pore entry.^{14,15}

$$V_p = n_{max} M \rho_{ad}^{-1}$$

Equation 3.3 – Gurvitsch Rule

where

V_p pore volume

n_{max} sorption uptake at $p/p^0 \sim 1$

M molar mass of the gas

ρ_{ad} adsorbed phase density

An adsorbed phase density of 1.177 g cm^{-3} for CO_2 at adsorption at 195 K was assumed. This is the liquid density at the triple point.¹⁶ An adsorbed phase density of 0.808 g cm^{-3} for N_2 sorption at 78 K was assumed^{7,17,18}. Molar masses are 44.01 g mol^{-1} (CO_2) and 28.01 (N_2).

Dubinin-Radushkevich Model – Micropore Volumes

The Dubinin-Radushkevich (DR) Model describes the filling of pores (rather than layer by layer adsorption as the BET model).¹⁹ The process of pore filling is dominant in micropores. Accordingly, the micropore volume can be calculated from the DR equation at low and medium relative pressure. Research on activated carbon suggests that the DR model accounts for ultramicropores when applied to subatmospheric CO_2 isotherms at 273 K.^{7,8,20}

In this study the DR model (see Equation 3.4) was used to calculate ultramicropore volumes from CO_2 isotherms at 273.1 K (pressure range 0.00030 – 0.01 kPa). An adsorbed phase density of 1.032 g cm^{-3} was assumed.

$$n_{ab} = n_0 \exp \left[-D \left(\ln \left(\frac{p_0}{p} \right) R T \right)^2 \right]$$

Equation 3.4 – Dubinin Radushkevich Equation

where

n_{ab} absolute amount adsorbed

n_0 maximum absolute amount adsorbed

p_0 saturation pressure

p pressure

R gas constant

T temperature [K]

D interaction constant which is equal to $-1/(\beta E_0)^2$ where β and E_0 are adsorbate characteristic parameters

Brunauer, Emmett, Teller (BET) model - Surface Area

The BET equation is based on multilayer adsorption on an energetically homogeneous surface.²¹ The BET model is extensively used to calculate equivalent surface areas of porous materials.⁷⁻⁹ In this study the BET equation (see Equation 3.5) was applied to determine the BET surface area of shales and kerogen from the linear region ($0.05 \leq p/p^0 \leq 0.35$) of N_2 isotherms at 77 K /78 K.

$$\frac{p}{p(p_0 - p)} = \frac{1}{n_m c} + \frac{(c - 1)}{n_m c} \cdot \frac{p}{p_0}$$

Equation 3.5 – BET Model

where

c BET constant which is related to the net heat of adsorption [-]

n_m monolayer coverage

p_0 saturated vapour pressure

2.3.2 Gravimetric Analyzer

Adsorption characteristics of methane, nitrogen and carbon dioxide on the shale were investigated using an Intelligent Gravimetric Analyzer (IGA), supplied by Hiden Isochema Ltd., Warrington, UK. The system is an ultra-high vacuum (UHV) system comprising of a computer controlled microbalance with pressure and temperature regulation systems. The mass was recorded using a microbalance which had a stability of $\pm 1 \mu\text{g}$ and a weighing resolution of $0.2 \mu\text{g}$. For temperature control liquid nitrogen and solid carbon dioxide/acetone cryogenic baths were used. Computer-controlled thermostats containing an ethylene glycol/water mixture were used to maintain temperatures at 273 K. Pressure transducers have ranges of 0 - 0.01, 0 - 0.1 and 0 - 2 MPa. The set pressure point was controlled by computer (set-point accuracy:

0.02 % within the range employed). Sample temperatures were recorded using a platinum resistance temperature detector located 5 mm from the sample.

Moisture content of pure gases can affect sorption experiments on shales at temperatures above 273 K in sorption apparatuses with a large void volume. This is due to a large ratio of moisture to sample mass in the system. A modified gravimetric apparatus was used for measurements of CO₂ isotherms at 273 K. A zeolite cylinder bed (~ 5 x 20 cm) filled with sodium aluminium silicate (1 nm molecular sieve, 2 mm beads) from Merck KGaA was used for gas pre-drying. Additionally, a reactor filled the same zeolites was attached to the sample reactor. Before running isotherms the zeolite beds were dried (> 400°C) and outgassed (see also Chapter 4).

2.3.3 Manometric Analyzer

The equipment used was an “Intelligent Manometric Instrument” (IMI) from Hiden Isochema Ltd. The system can operate up to a pressure of 20 MPa and 500°C. A schematic diagram of the apparatus is shown in Figure 2.1. The reference cell is effectively the pipe volume between the valves PCV1 to PCV5. The sample cell is the volume between valve PCV4 and PCV6. Samples are loaded into the reactor which is a 10 cm³ VCR manifold. The gas is supplied from gas cylinders. The IMI provides 3 ports for gas supply, which are isolated by valve PCV1 to PCV3. Mass flow controllers regulate the gas flow in the CO₂, CH₄ and He lines.

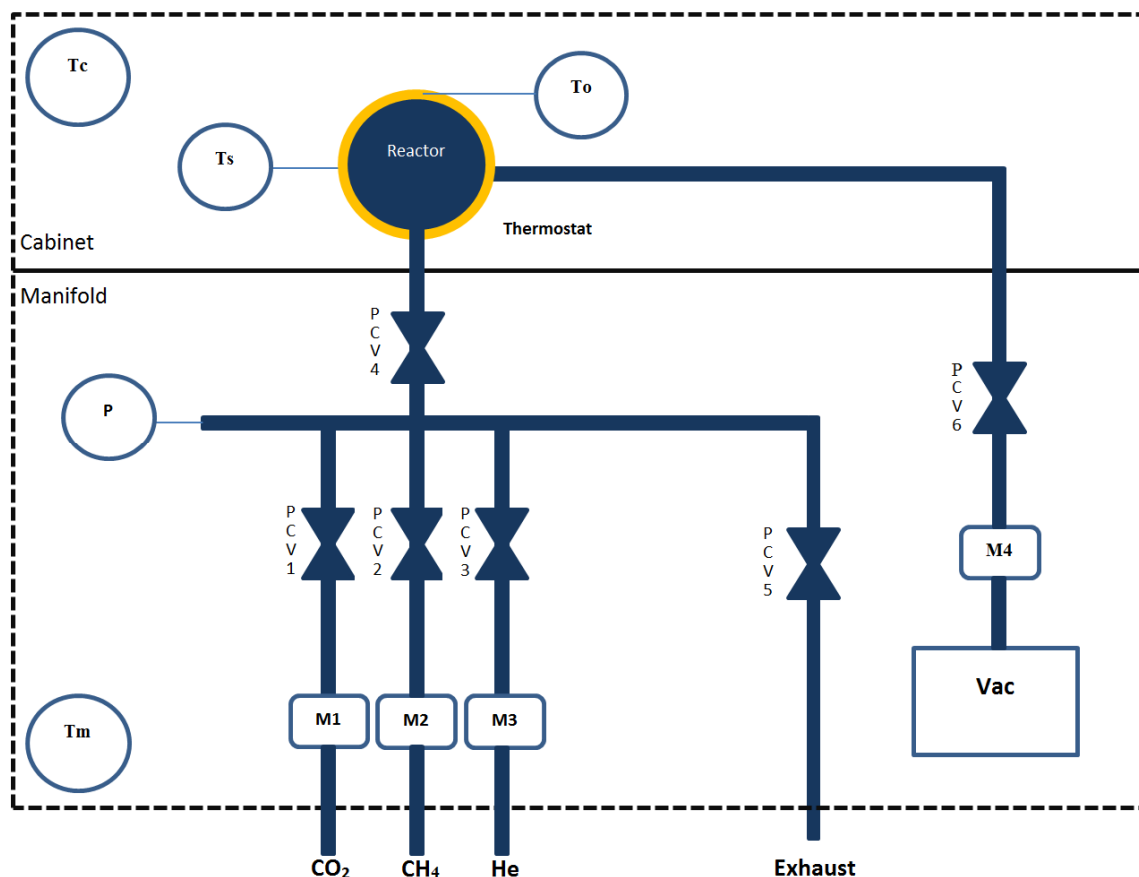


Figure 2.1: Simplified schematic diagram of the manometric sorption equipment (Hiden IMI).

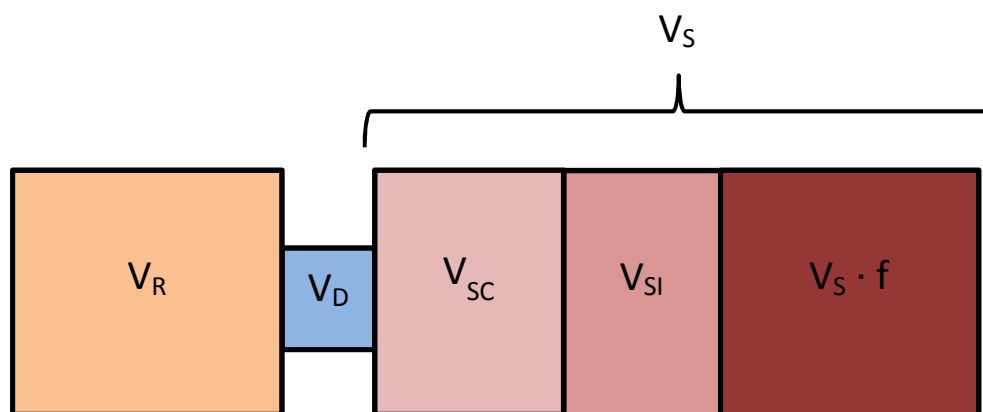
The system is outgassed by a combination of two pumps – a turbo-molecular drag pump and a diaphragm pump. With this setup vacuums below 5×10^{-7} MPa are obtained. The valves (PCV1 to PCV6) are diaphragm SWAGELOK® valves which are pneumatically operated by nitrogen at 0.6 MPa.

The pressure in the system is measured by a thin film strain gauge (“P” in Figure 2.1). Temperatures are measured by platinum resistance thermometers (PRT) or type K thermocouples. The sample temperature is determined by a type K thermocouple (T_s) in the reactor coupling at the top of the reactor. Two PRTs are used to determine the manifold (T_m) and the cabinet (T_c) temperature. Another PRT (T_0) is used to measure the thermostat temperature. The thermostat is an integral band heater which is attached to the reactor to heat the sample cell. A Hiden Cryofurnace cooled by nitrogen gas generated from liquid nitrogen was used to measure isotherms at or below 273 K. The IMI is operated by software provided by Hiden Isochema Ltd. Specification parameters of the IMI are shown in Table 2.3.

Table 2.3: Manometric Apparatus specification.

Manometric Instrument IMI	
Max. Pressure possible	20 MPa
Pressure accuracy	+/- 0.05 % of range
Vacuum pressure	$< 5 \cdot 10^{-7}$ MPa
Volume of the reference cell	$6.4030 \pm 0.0014 \text{ cm}^3$
Volume of the sample cell	$16.3297 \pm 0.0032 \text{ cm}^3$
Diaphragm Volume	$0.05045 \pm 0.0004 \text{ cm}^3$
Heating system	Integral band heater
Temp. measurement accuracy: reference cell ($\pm^\circ\text{C}$ or K)	0.02
Temp. measurement accuracy: sample cell ($\pm^\circ\text{C}$ or K)	0.27

The uptake calculation is based on mass balance before and after dosing gas into the sample cell. The gas compressibility, the temperature difference between reference and sample cell as well as the dead volume of the diaphragm valve (PCV4) need to be taken into account. It is practical to divide the sample cell volume into three partitions. This is necessary as the temperature throughout the sample cell (V_S) is not constant. V_{SC} is the volume of the sample cell at the manifold temperature, V_{SI} is the volume at the cabinet temperature and $V_S \cdot f$ is the volume at the temperature measured by the thermocouple in the reactor (Figure 2.2). The fraction f varies with different reactor temperatures and must be determined by running blank helium isotherms.

**Figure 2.2:** Volume partitioning in the Hidden IMI manometric sorption apparatus.

V_R is the reference volume and V_D is the dead volume of the diaphragm valve. The uptake is calculated by setting up the mass balances before and after dosing (see Equation 3.6). The isotherm results on the accumulative measurement of n_{ad} at a range of increasing pressure.

$$n_{ad} = p_2 \frac{V_R + V_D + V_{SC}}{Z_{R2} R T_{R2}} + \frac{p_2 V_{SI}}{Z_{SI} R T_{SI}} + \frac{p_2 V_S f}{Z_S R T_S} - \frac{p_1 V_R}{Z_{R1} R T_{R1}}$$

Equation 3.6 – IMI Mass Balance

where

n_{ad}	Excess amount of gas adsorbed [mol]
R	Ideal gas constant [$\text{J mol}^{-1} \text{K}^{-1}$]
p_1	Pressure in the reference cell before dosing [Pa]
p_2	Pressure in the reference and sample cell after dosing and kinetic equilibration [Pa]
V_R	Volume of the reference cell [m^3]
V_{SC}	Volume of the sample cell at reference cell temperature [m^3]
V_S	Volume of the sample cell minus the skeletal volume of the adsorbent [m^3]
V_D	Diaphragm valve volume [m^3]
f	Fraction of the sample cell at temperature T_S (temp. dependent)
T_{R1}	Temperature in the reference cell before dosing [K]
T_{R2}	Temperature in the reference cell after dosing [K]
T_{SI}	Temperature in the volume V_{SI} after dosing [K]
T_S	Temperature in the volume $V_S \cdot f$ after dosing [K]
Z_{R1}	compressibility factor for conditions in the reference volume prior to dosing
Z_{R2}	compressibility factor for conditions in the reference volume after dosing
Z_{SI}	compressibility factor for conditions in V_{SC} after dosing
Z_S	compressibility factor for conditions in $V_S \cdot f$ after dosing

Saturated vapor pressures and gas densities were calculated from the NIST Standard Reference database 23 by using the REFPROP Version 9.0 software.²² The following equations of state (EOS) were used: CO_2 (Span and Wagner)²³, N_2 (Span *et al*)²⁴, CH_4 (Setzmann and Wagner)²⁵ and He (Lemmon *et al*)²².

References

- (1) Leon, C. *Advances in Colloid and Interface Science* **1998**, *76*, 341.
- (2) Neikov, O. D.; Naboychenko, S. S.; Murashova, I. V.; Gopienko, V. G.; Frishberg, I. V.; Lotsko, D. V.; Elsevier.
- (3) Hillier, S. *Clay Min.* **1999**, *34*, 127.
- (4) Hillier, S. In *Clay Mineral Cements in Sandstones*; Worden, R. H. a. M. S., Ed.; Blackwell: 2009, p 213.
- (5) Espitalie, J.; Madec, M.; Tissot, B.; Mennig, J. J.; Leplat, P.; Offshore Technology Conference.
- (6) Weiss, H. M.; Wilhelms, A.; Mills, N.; Scotchmer, J.; Hall, P. B.; Lind, K.; Brekke, T. *Norsk Hydro, Statoil, Geolab Nor, SINTEF Petroleum Research and the Norwegian Petroleum Directorate* **2000**.
- (7) Gregg, S. J.; Sing, K. S. W.; Academic Press Inc: London, 1982; Vol. 2.
- (8) Do, D. D. *Adsorption Analysis: Equilibria and Kinetics*; Imperial College Press, 1998.
- (9) Marsh, H. *Carbon* **1987**, *25*, 49.
- (10) Sing, K. *Colloids and Surfaces A: Physicochemical and Engineering Aspects* **2001**, *187–188*, 3.
- (11) Sing, K. S. W.; Sing, K. S. W.; Everett, D. H.; Haul, R.; Moscou, L.; Pierotti, R. A.; Rouquerol, J.; Siemieniowska, T. *Pure Appl. Chem* **1982**, *54*, 2201.
- (12) Rouquerol, J.; Avnir, D.; Fairbridge, C. W.; Everett, D. H.; Haynes, J. M.; Pernicone, N.; Ramsay, J. D. F.; Sing, K. S. W.; Unger, K. K. *Pure and Applied Chemistry* **1994**, *66*, 1739.
- (13) Gurvitch, L. J. *Phys. Chem. Soc. Russ.* **1915**, *47*, 805.
- (14) Fletcher, A. J.; Thomas, K. M.; Rosseinsky, M. J. *Journal of Solid State Chemistry* **2005**, *178*, 2491.
- (15) Dollimore, D.; Shingles, T. *Journal of Applied Chemistry* **1969**, *19*, 218.
- (16) Lemmon, E. W.; Huber, M. L.; McLinden, M. O. *NIST Reference Fluid Thermodynamic and Transport Properties - REFPROP*, U.S. Department of Commerce, 2010.
- (17) Hong, M.; Li, S.; Funke, H. F.; Falconer, J. L.; Noble, R. D. *Microporous Mesoporous Mat.* **2007**, *106*, 140.
- (18) Bhatia, S. K.; Shethna, H. K. *Langmuir* **1994**, *10*, 3230.
- (19) Dubinin, M. M.; Zaverina, E. D.; Serpinsky, V. V. *Journal of the Chemical Society (Resumed)* **1955**, 1760.
- (20) Dubinin, M. M. *Carbon* **1989**, *27*, 457.
- (21) Brunauer, S.; Emmett, P. H.; Teller, E. *Journal of the American Chemical Society* **1938**, *60*, 309.

- (22) Lemmon, E. W.; Huber M.L.; McLinden, M. G. *NIST Standard Reference Database 23. NIST Reference Fluid Thermodynamic and Transport Properties—REFPROP Version 8 US* Department of Commerce, 2010.
- (23) Span, R.; Wagner, W. *Journal of Physical and Chemical Reference Data* **1996**, 25, 1509.
- (24) Span, R.; Lemmon, E. W.; Jacobsen, R. T.; Wagner, W.; Yokozeki, A. *Journal of Physical and Chemical Reference Data* **2000**, 29, 1361.
- (25) Setzmann, U.; Wagner, W. *Journal of Physical and Chemical Reference Data* **1991**, 20, 1061.

Chapter 3

International inter-laboratory comparison of high-pressure CH₄, CO₂ and C₂H₆ sorption isotherms on carbonaceous shales

This chapter has been submitted for publication to the International Journal of Coal Geology (with all results made anonymous). The study represented in this chapter was conducted in close cooperation with Dr. Matus Gasparik and his coworkers at the Energy and Mineral Resources Group at the RWTH Aachen University. My contribution to this work is in particular high-pressure methane and carbon dioxide isotherms (as shown in Figure 3.5 and 3.6), the low-pressure pore characterization (Table 3.3) and pore size distribution by NLDFT (Figure 3.2 and 3.3), helium densities (Figure 3.4), additional shale characterization by petrophysical measurements (Table 3.1, not all data shown), isotherms before and after pre-drying of gas (Figure 3.12), help with obtaining the data in Table 3.2 as well writing up of and theoretical assistance with, respectively, chapter 3.1, 3.2.2, 3.3.1, 3.3.3, 3.4.6, 3.5 and 3.6.

Abstract

An inter-laboratory study of high-pressure gas sorption measurements on two carbonaceous shales has been conducted in order to assess the reproducibility of the sorption isotherms and identify possible sources of error. The measurements were carried out by seven international research laboratories on either in-house or commercial sorption equipment using manometric as well as gravimetric methods. Excess sorption isotherms for methane, carbon dioxide and ethane were measured at 65°C and at pressures up to 25 MPa on two organic-rich shales in the dry state. The samples had a total organic carbon (TOC) content of 15.1% and 4.4% and vitrinite reflectance (VR) values of 0.5%R₀ (immature) and 2.0 %R₀ (over-mature), respectively. The specific surface areas and the micropore volumes determined by low-pressure N₂ (77 K) and CO₂ (273 K) sorption were 6.6 m² g⁻¹ and 6.9 mm³ g⁻¹ for the immature and 9.5 m² g⁻¹ and 9.4 mm³ g⁻¹ for the over-mature sample, respectively. The inter-laboratory reproducibility of the methane excess sorption isotherms was better for the high-maturity shale (within 0.02 – 0.03 mmol g⁻¹) than for the low-maturity sample (up to 0.1 mmol g⁻¹), similar to observations in earlier inter-laboratory studies on coals. The reproducibility for CO₂ and C₂H₆ sorption isotherms was satisfactory at pressures below 5 MPa but at higher pressures the results deviate considerably. Artefacts in the shape of the excess sorption isotherms and negative excess sorption values for CO₂ and C₂H₆ observed by some laboratories are considered to be

due to measurement uncertainties, gas impurities (cross contaminations) and the uncertainty in equation of state (EoS).

The low sorption capacity of carbonaceous shales (as compared to coals and activated carbons) requires very high accuracy of pressure and temperature measurement and precise temperature control. The procedures for sample conditioning prior to the measurement, the measurement procedures and the data reduction approach must be optimized to meet the required accuracy. Unknown systematic errors in the measured quantities must be minimized first by applying standard calibration methods. Blank sorption measurements with a non-sorbing sample (e.g. steel cylinders) can be used to identify and quantitatively account for measuring artefacts resulting from unknown residual systematic errors or from the limited accuracy of the EoS. The possible sources of error causing the observed discrepancies are discussed.

3.1 Introduction

3.1.1 *Motivation for Inter-Laboratory Study of High-Pressure Sorption on Shales*

Shale Gas is gaining importance as energy resource; it is increasing its contribution to the industrial production of natural gas and lowering its cost. There is considerable research interest in sorption properties of shales, stimulated not only by their economic potential for natural gas, but also by efforts to develop approaches to mitigate climate change through capture and storage of CO₂ in geologic formations. The physical sorption of hydrocarbon gas (mostly methane) in shales provides gas storage capacity in addition to the “free gas” capacity of the pore system. While methane sorption is considered to take place predominantly in microporous organic matter (kerogen), inorganic (clay minerals) constituents may contribute a significant portion of sorption capacity in shales with low organic matter contents. Quantification of the total storage capacity, including sorbed gas and free gas is a prerequisite for estimations of resource potential and technically recoverable amounts of gas at given reservoir conditions. Due to the high variability and complex nature of the chemical composition and pore structure of these rocks, industry has to rely on experimental high-pressure/high-temperature sorption data, and these have to be reproducible among different laboratories.

Accurate measurement of high-pressure sorption isotherms on shales is challenging due to the fact that (i) the typical sorption capacity of shales is only about one tenth of that of coal and 1% of that of activated carbon (Figure 3.1) and (ii) sorption isotherms have to be

measured up to high pressures (> 20 MPa) and temperatures (> 100°C) in order to be representative of the in-situ reservoir conditions typical for shales.

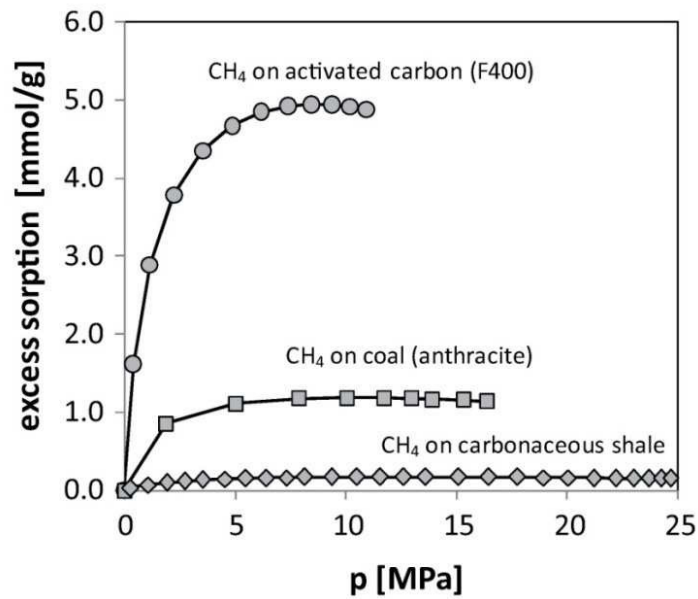


Figure 3.1: Comparison of typical sorption capacities for methane on activated carbon, high-rank coals and shales measured at RWTH Aachen.

The quality of gas sorption isotherms on coals has been assessed in various earlier inter-laboratory studies.¹⁻⁴ Such comparisons have not yet been conducted or reported for gas shales. This makes it difficult to assess the reproducibility of sorption isotherms obtained from different laboratories. Questions arise concerning the extent to which differences in results can be attributed to heterogeneities, sample preparation or the measurement technique. Therefore, strict control must be exerted on experimental methodology and variables in order to obtain reproducible results. The need for inter-laboratory accuracy is well recognized by regulatory agencies and industry and is a driver for the development of standard methods. Further, the research community recognizes that several factors including the operator, the equipment, the calibration of the equipment, and the laboratory environment including temperature and humidity can influence the variability of a test result. Laboratories use different instrumentation and procedures for measuring gas sorption isotherms because no standard method exists.

Here, the results from the first inter-laboratory reproducibility study of high-pressure gas sorption isotherms on gas shales are reported. Excess sorption isotherms for CH₄, CO₂ and C₂H₆ were measured at 65°C and at pressures up to 25 MPa on two organic-rich shales with different Total Organic Carbon (TOC) contents and thermal maturity. Seven international research laboratories participated in this Round Robin study. These include RWTH Aachen

University in Germany (RWTH), Newcastle University in the United Kingdom (WNCRL), the University of Mons in Belgium (UMONS), CSIRO Energy Technology in Australia (CSIRO), the Chinese Academy of Sciences at Guizhou in China (GIGCAS), the University of Texas at Austin in the United States (BEG) and the Research Institute of Petroleum Exploration and Development (RIPED) in China. This study attempted to find out if and to what extent differences in laboratory procedures influence the results of sorption measurements and if the qualities of published isotherms are comparable. This work will provide guidance for estimating the reproducibility that might be expected when comparing adsorption isotherms from different laboratories. The project was performed as an “open” round-robin with regular updates and exchange of results and experience among the participants. The common objective is the improvement of data quality and reliability and the refinement of experimental techniques.

3.1.2 Inter-Laboratory Studies of CO₂ Sorption on Coal

Two inter-laboratory comparisons on high-pressure CO₂ sorption on coal initiated by the U.S. Department of Energy, National Energy Technology Laboratory and RWTH Aachen, respectively, have been carried out previously.¹⁻⁴ In the first round of the inter-laboratory study by Goodman et al. (2004), CO₂ sorption isotherms at 22°C and 55°C up to 7 MPa were measured on five Argonne Premium Coal samples (pre-dried at 80°C) by four independent research groups.¹ Good agreement was found for the isotherms on high rank coals, while isotherms on mid- and low-rank coals deviated by more than 100%. The deviations were attributed to residual-moisture content caused by different procedures for removing moisture among the research institutes. In the second round of the inter-laboratory study CO₂ isotherms at 55°C and pressures up to 15 MPa were measured on three moisture-equilibrated coals by six independent research groups.² A good agreement was found up to 8 MPa with the exception of those instances where the moisture content of the coal was significantly different from the as-received moisture. Above 8 MPa the reported isotherms diverged significantly.

The second inter-laboratory study initiated by RWTH Aachen University was conducted among three European research laboratories on coals. In the first round of the study the comparison of CO₂ sorption isotherms at 45°C and up to 16 MPa on activated carbon (FiltrisorbF400) showed an excellent agreement (deviation in sorption capacity less than 5% or 0.4 mmol g⁻¹).³ In the second round of this study three coal samples of varying rank were studied under the same experimental conditions.⁴ Differences due to sample drying were

minimized by increasing the drying temperature to 105°C (as compared to 80°C in Goodman et al. (2004)). Good agreement (deviations in the range of 0.02 – 0.07 mmol g⁻¹) was observed at low pressures (< 6-8 MPa) except for the lowest-rank (lignite) coal sample. However, at high pressures (> 10 MPa) the isotherms from individual laboratories diverged significantly (> 0.3 mmol g⁻¹). The authors discuss possible sources of error due to coal swelling, residual moisture, particle size and gas impurities.

In their conclusions, Gensterblum et al. (2010) emphasize the need to improve the reproducibility of high-pressure sorption measurements.⁴ This requires a thorough optimization of the instrumentation and the measuring procedures, and well-defined sample preparation procedures. This is even more crucial for sorption studies on shales, where reservoir conditions are typically in both, high-pressure (> 20 MPa) and high-temperature (> 100°C) ranges.

3.1.3 Experimental Methods of High-Pressure Sorption Measurements

Among the different methods used to study gas sorption (manometric, volumetric, gravimetric, chromatographic, temperature-programmed desorption, etc.), the two most commonly used to study gas sorption equilibria at high pressures are the manometric and the gravimetric method. The experimentally determined quantity (irrespective of the method used) is the “excess sorption” or “Gibbs surface excess”.⁵ The uptake of gas by the sorbent sample is determined at constant temperature as a function of gas pressure (or density) giving the excess sorption isotherm. The experimental techniques make use of different physical principles to measure sorption. The manometric and the gravimetric techniques have been used extensively in sorption studies on carbonaceous materials (e.g. activated carbons, coals) with hydrocarbon (e.g. CH₄, C₂H₆) and non-hydrocarbon (CO₂, N₂, etc.) gases. Comparative studies between the gravimetric and manometric methods performed with N₂ and CO₂ on activated carbons showed a very good agreement.^{3,4,6,7}

Gravimetric Method

The gravimetric method makes use of direct measurement of mass change of a sample being exposed to sorptive gas at constant pressure and temperature. The modern gravimetric devices utilize a high-precision magnetic suspension balance for mass measurements down to µg resolution. Most published data utilizing the gravimetric technique were obtained on commercial devices (e.g. Rubotherm). Some laboratories use in-house modifications of these devices in order to adapt them for specific experimental conditions – e.g. high temperatures, in-situ moisture equilibration.^{6,8} Several studies use an in-house built gravimetric sorption

apparatus.⁹⁻¹¹ The recent availability of accurate equations of state for pure gases on-line has obviated the need for a reference cell in gravimetric systems studying single gas sorption, but this then requires more accurate temperature and pressure measurements in these systems than was hitherto necessary.

Due to the buoyancy force acting on the sample and the sample holder during the gravimetric sorption measurement, the measured apparent mass has to be corrected for the buoyancy term in order to obtain the excess sorbed mass (m_{excess}). The “reduced mass” (Ω) is obtained by considering the buoyancy acting on the sample holder determined in a calibration test. The buoyancy correction term is the product of sample volume determined by helium expansion ($V_s^{He,0}$) and the density of the sorptive gas ($\rho_g(p, T)$) (hence, the buoyancy correction in the gravimetric method is analogous to the void volume correction, the “non-sorption” case, in the manometric method):

$$m_{excess}(p, T) = \Omega(p, T) + \rho_g(p, T)V_s^{He,0}$$

Equation 3.1 – Gravimetric mass balance

In this equation (and in Eq. 3.1) the superscript 0 in the sample volume $V_s^{He,0}$ is used to stress the fact that no corrections to the sample volume (as determined initially by the He expansion) need to be applied in order to obtain pure excess sorption. Some authors have applied such corrections in order to obtain the “absolute” sorption, taking into account the non-negligible volume effect of the adsorbed molecules, or to account for sorption of helium or swelling effects of adsorbent sample.¹²

The advantage of the gravimetric method over the manometric is that it does not suffer from cumulative errors as is the case for the latter. Also, the leakage does not affect the measurement accuracy as long as the pressure in the sample cell can be kept constant. On the other hand, the accuracy of the gravimetric technique is compromised at high-pressures (>10 MPa) due to a large buoyancy term, especially on materials with relatively low sorption capacity (such as shales).

The manometric method

In the manometric method, the uptake of gas is measured by monitoring the drop in pressure in a fixed known volume containing the adsorbent sample. This technique is sometimes referred to as Sievert’s method. The measuring device consists of reference (RC) and sample (SC) cells with calibrated volumes equipped with high-precision pressure sensor

kept at constant temperature conditions. The experiment can be designed as constant-volume (manometric) or constant-pressure (volumetric) measurement.¹³

The measurement is done by successively transferring the sorptive gas through the reference cell into the sample cell containing the adsorbent sample. The excess sorption is then calculated as a difference between the total amount of gas transferred (m_{total}) into the SC and the non-adsorbed gas occupying the void volume of sample cell:

$$m_{excess}(p, T) = m_{total}(p, T) - \rho_g(p, T)V_{void}^{He,0}$$

Equation 3.2 – Manometric mass balance

The void volume ($V_{void}^{He,0}$) is commonly determined by helium assuming its sorption can be neglected. Multiplied by the density of the sorptive gas $\rho_g(p, T)$, the “non-sorption” reference state is calculated. The gas density is determined by appropriate equation of state (EoS) at the experimental p, T conditions. Since m_{total} is a cumulative sum of the volume of the reference cell (V_{rc}) multiplied by the gas density difference in the reference cell before (ρ_{rc}^i) and after (ρ_{rc}^f) the expansion into the sample cell:

$$m_{total} = \sum_{j=1}^n V_{rc}(\rho_{rc}^i - \rho_{rc}^f)$$

Equation 3.3 – Manometric Isotherm Calculation

The measurement uncertainties in the manometric method accumulate during the isotherm determination. The uncertainty accumulation can be reduced experimentally. Mohammad et al. (2009) argue that the measurement accuracy can be significantly improved if the setup is designed as constant-pressure (volumetric) rather than constant-volume (manometric). There are number of other ways for reducing the accumulation of uncertainty in the manometric setup, one being optimizing the relative ratio of the void volume and the reference cell volume (i.e. the ratio of the sample cell to reference cell volume). While some authors provide their own estimates for the optimal volume ratio for CO₂, thorough optimization methods should be applied to determine the best strategy for dosing the sorptive gas into the sample cell.^{4,13}

Sources of uncertainty

A comprehensive review of the sources of uncertainty in measured sorption data for coals is provided in Busch and Gensterblum (2011).¹⁴ Additional sources of uncertainty relevant for sorption studies on shales concern the high-temperature manometric devices in which the reference and the sample cells are kept at different temperatures. If a thermal

gradient exists over a part of the sample cell volume (e.g. the tubing connecting it to the rest of the apparatus) this has to be accounted for in the calculation of the excess sorption. Moreover, due to the thermal expansion of the sample cell experiencing high temperatures a careful temperature calibration needs to be performed in addition to the volume calibration.

3.1.4 Goals of this Study

Currently there are no accepted standards for high-pressure (high-temperature) sorption measurements. Research laboratories and equipment manufacturers specializing on sorption use their own (commercial or in-house) equipment and apply their own set of “standard” and quality assurance procedures. The published sorption data on shales are used by various academic and industrial groups in the field of shale gas exploration and underground CO₂ storage. It is therefore crucial to assess the inter-laboratory reproducibility among different laboratories and to review the means of quantifying and reducing the uncertainty in experimental sorption data. This work follows the previous Round Robin studies on activated carbon and coals and intends to test the capabilities of gravimetric and manometric sorption techniques for studying the sorption behaviour of shales with relatively low sorption capacity.^{3,4} The aims of this study were 1) to show to what extent are the sorption data reported by different laboratories reproducible; 2) to identify the main sources of uncertainty that result in observed deviations between individual labs and 3) to suggest the necessary measures to improve the accuracy of measured sorption data on shales.

3.2 Materials and Methods

3.2.1 Sample Preparation and Sample Characterization

Two shale samples were collected for this study. These samples include the Upper Chokier ("Namurian") shale from Belgium and the lower Toarcian ("Posidonia") shale from Holzmaden in South Germany. It was desirable to obtain samples with significant differences in Total Organic Carbon (TOC) content and thermal maturity in sufficient quantities. The basic geochemical data of the selected samples are listed in Table 3.1. The TOC contents of the Namurian and the Posidonia sample are 4.4 wt.% and 15.1 wt.%, respectively. The thermal maturity in terms of vitrinite reflectance is 2.0%R₀ for the Namurian, and 0.5%R₀ for the Posidonia sample.

Table 3.1: Basic geochemical data of the studied samples.

	Sample	Namurian	Posidonia
TOC & VR	TOC ¹ (wt %)	4.4	15.1
	TOC ² (wt %)	3.8	12.3
	VR(%R ₀)	2.0	0.5
Rock-Eval	S1 (mg/g)	n.d.	7.0
	S2 (mg/g)	n.d.	84.2
	S3 (mg/g)	n.d.	1.8
	T _{max} (°C)	n.d.	429
	HI (mg HC/g TOC)	n.d.	561
	OI (mg CO ₂ /g TOC)	n.d.	12
XRD	Qtz + Fsp (wt %)	44.2	10.6
	Carbonates (wt %)	5.4	20.3
	Total clays (wt %)	40.3	20.3

¹Results by RWTH²Results by WNCRL

3.2.2 Pore Characterization

To characterize the micropore and mesopore systems of the shale samples CO₂ isotherms (at 273 K and 195 K up to 0.1 MPa) and N₂ isotherms (77 K, up to 0.096 MPa) were measured on a gravimetric sorption apparatus at the Wolfson Northern Carbon Reduction Laboratories (WNCRL) at the University of Newcastle. Details of the apparatus can be found in Rexer et al.¹⁵

The equivalent surface area was determined from the N₂ isotherms using the Brunauer-Emmett-Teller (BET) equation.¹⁶ The ultra-micropore volumes (pore width <0.7 nm) were obtained from the CO₂ by the Dubinin-Radushkevich model.¹⁷ The micropore size distribution was determined from the CO₂ isotherms by a non-local density functional theory (NLDFT) equilibrium model assuming slit pores.¹⁸ The Sorption Pore Volume was calculated from 195 K isotherms according to the Gurvitsch rule.¹⁹⁻²¹

3.2.3 Sample Preparation

Larger chunks of rock material (> 3 kg) were crushed and milled to a powder (average particle size < 100 µm) using a laboratory disc mill (Siebtechnik GmbH) at RWTH Aachen. In order to ensure the homogeneity of the sample material distributed to different laboratories,

the original parent powder sample was passed two times through the sample divider (Retsch GmbH). Individual sample aliquots were filled into glass vials in the sample divider and shipped to all laboratories.

Sample Drying

In this first phase of the Round Robin study the sorption isotherms were measured on dry shale samples to ensure that the same experimental conditions are reproduced in each lab. A drying procedure was suggested to which all the labs were asked to adhere. This two-step drying process consisted of pre-drying the sample at 110°C under vacuum for 18 hours followed by additional “in-situ” drying after the transfer of the sample into the sample cell (110°C, vacuum, 2-8 hours). It should be noted, however, that not all the labs were able to perform this second drying step under the vacuum conditions (the experimental setup of one of the participating laboratory was not equipped with a vacuum system) or at the desired temperature (the in-situ drying temperature in one of the labs was only 80°C).

3.2.4. Gravimetric and Manometric Sorption Measurements

Seven international research groups have participated in this round robin study. The sorption equipment used by individual groups was either commercial or in-house manometric (RWTH, WCNRL, BEG, RIPED, GIGCAS) and gravimetric (CSIRO, UMONS). The details of the technical parameters of the measuring devices used by each group including the references to the original setup description are given in Table 3.2.

The manometric devices used by RWTH, WCNRL, BEG, RIPED, GIGCAS have the same basic components such as reference volume, sample cell, valves, high-precision pressure and temperature sensors and temperature control units, but differ in size. At RWTH Aachen, in addition to the manometric setup with a single temperature control unit for both, the reference and the sample cell (described in Krooss et al 2002), a special setup was constructed that operates at two different temperatures of the reference and the sample cell.²² This arrangement enables measurement at high temperatures (> 150°C) of the sample cell, which is thermally isolated from the temperature sensitive parts of the setup. Two-temperature systems are also used by the WCNRL and the GIGCAS laboratory. It should be noted here that this arrangement leads to a temperature gradient along a part of the sample cell volume that spans the two temperature zones. This needs to be accounted for in the calculation of the excess sorption. At RWTH Aachen this was solved by a temperature calibration of the setup in combination with blank expansion tests with stainless-steel cylinder placed in the sample cell for a range of temperatures. These blank sorption isotherms were then subtracted from the

measured sorption isotherms to obtain the final result. Comparison tests between the single- and two-temperature setup showed a good agreement.²³

Two laboratories (UMONS and CSIRO) use gravimetric methods. The gravimetric setup at UMONS is a modified Rubotherm device with magnetic suspension balance adapted for measurements at high pressures and is described in de Weireld et al. and also Gensterblum et al. (2009).^{3,6} The gravimetric setup at CSIRO is an in-house built device in which a larger sample cell and reference cell are suspended mechanically. The description of the setup is provided in Day et al.¹⁰

Table 3.2: Information on experimental parameters reported by individual laboratories.

parameter [Ⓐ]	method [Ⓐ]	RWTH ^{a)}	WNCRL ^{b)}	BEG ^{c)}	CSIRO ^{d)}	UMONS ^{e)}	RIPED ^{f)}	GIGCAS ^{g)}
		manometric	manometric	manometric	gravimetric	gravimetric	manometric	manometric
p_{\max} [MPa]		30	15		22	16	35	20
p accuracy		$\pm 0.01\%$ FS ¹	$\pm 0.05\%$ FS	n.a.	$\pm 0.04\%$ FS	$\pm 0.1\%$ FS	$\pm 0.1\%$ FS	$\pm 1\%$ of reading
magn. susp. balance accuracy (gravimetric)		n.a.	n.a.	n.a.	5 mg	0.01 mg	n.a.	n.a.
$V_{\text{ref. cell}}$ [cm ³]		1.765 / 7.318	6.403 \pm 0.001	2.38	310.23 \pm 0.09		85.8 \pm 0.2	4.56
$V_{\text{sample cell}}$ [cm ³]		11.666 / 51.554	16.330 \pm 0.003	7.15		6.2	190.04 \pm 0.07	15
m_{sample} [g]		$\sim 13 / 55$	~ 10	~ 6	230 - 250	~ 3.5	~ 140	~ 8
typical $V_{\text{void}}/V_{\text{ref. cell}}$		3 - 4		~ 2	~ 0.7	n.a.	~ 1.23	2-3
Temperature control								
Heating system		air-bath	band heater	air-bath	air-bath	air-bath	oil-bath	band heater
No. of heating zones		1 / 2	2	1	4	1	1	2
T accuracy [°C]		0.1	n.a.	n.a.	n.a.	0.1	0.1	0.1
T stability [°C]		0.2 / 0.1	0.02 / 0.27	n.a.	0.02	0.3	0.02	0.02 / 0.1
Gas purity								
	He	99.999%	99.9995%	n.a.	n.a.	n.a.	99.999%	99.999%
	CH ₄	99.995%	99.995%	99.995%	99.995%	99.995%	99.995%	99.995%
	CO ₂	99.995%	99.995%	n.a.	99.995%	99.996%	99.999%	n.a.
	C ₂ H ₆	99.60%	n.a.	n.a.	n.a.	99.99%	n.a.	n.a.
sample treatment								
pre-drying		yes (110°C)	yes (110°C)	n.a.	yes (80°C)	no	yes (110°C)	yes (110°C)
in-situ drying		yes	yes	yes	yes	yes	yes	yes
$T_{\text{in-situ drying}}$ [°C]		110	110	110	80	110	110	110
vacuum		yes	yes	yes	yes	yes	no	yes
\sim duration [h]		> 8	~ 12	n.a.	48 - 96	24	2	2
Void / sample volume measurement								
gas		He	He	He	He	He	He	He
p range [MPa]		1 - 15	0.6	n.a.	n.a.	1 - 10	1.85 - 2	1-5
$T_{\text{sample cell}}$ [°C]		65	65	n.a.	n.a.	65	65	65

Equation of state (EOS)

He	Kunz et al. (2007)	McCarty & Arp (1990)	n.a.	n.a.	McCarty & Arp (1990)	Peng- Robinson	McCarty & Arp (1990)
CH ₄	Kunz et al. (2007)	Setzmann & Wagner (1991) ²	n.a.	Setzmann & Wagner (1991) ²	Setzmann & Wagner (1991)	Peng- Robinson	Setzmann & Wagner (1991)
CO ₂	Kunz et al. (2007)	Span & Wagner (1996) ²	n.a.	Span & Wagner (1996) ²	Span & Wagner (1996)	Peng- Robinson	n.a.
C ₂ H ₆	Kunz et al. (2007)	n.a.	n.a.	Friend et al. (1991) ²	Friend et al. (1991) ²	n.a	n.a.

¹⁾ = precision relative to calibration standard with 0.025% uncertainty

²⁾ REFPROP (NIST) database

Setup description (references):

a) In-house, Krooss et al. (2002)

b) Commercial, Rexer et al. (2013)

c) In-house, Zhang et al. (2012)

d) In-house, Day et al. (2005)

e) Commercial-modified, De Weireld et al.(1999)

f) Commercial - Model 300 by TerraTek Systems, USA

g) Commercial - Model PCTPro by Hy-Energy Scientific Instruments, USA (now Seratam Instrumentation)

3.2.5 Equation of State (EoS)

In mass balance calculations of the sorption measurement an equation of state (EoS) is required to calculate the density of the gas (CO₂, CH₄) at a certain pressure and temperature. In specially designed gravimetric setups it is possible to directly measure the gas density with a high degree of accuracy. However, in this study each laboratory used an EoS to calculate the gas densities from the p,T data. The most commonly used and currently the most accurate EoS for CO₂ and CH₄ are those by Span and Wagner (1996) and Setzmann and Wagner (1991), respectively.^{24,25} These have been incorporated in the recent multi-component EoS by Kunz et al. (2007, 2012).^{26,27} Other, more widely used EoS, are those by Peng–Robinson (PR) and Soave–Redlich–Kwong (SRK). The two latter ones can be applied to a large suite of gas species by introducing different interaction parameters but they are not sufficiently accurate. As pointed out by Mavor et al, the differences in EoS can lead to variations of up to 20% in the calculated sorption capacities (see also van Hemert et al. and Busch and Gensterblum (2011)).^{14,28}

3.3 Results

The results of this study are presented anonymously, except from WNCRL Newcastle and RWTH Aachen, and in the following the other laboratories will be referred to as “Lab 1”, “Lab 2”, etc.

3.3.1 Pore Characterization (WNCRL Newcastle)

Low-pressure pore characterization reveals a Dubinin-Radushkevich (DR) ultra-micropore volume (pore width < 0.7 nm) of 9.4 mm³ g⁻¹ and a CO₂ sorption pore volume (SPV) of 7.8 mm³ g⁻¹ for the Namurian sample. The almost identical pore volumes indicate that this sample is highly microporous. A fraction of the micropores is probably generated by kerogen cracking in the oil and gas window.

The Posidonia shale sample exhibits a lower DR micropore volume (6.9 mm³ g⁻¹) which constitutes less than a half of the total sorption pore volume. Thus, it can be argued that a significant fraction of sorption sites is provided by pores larger than 2 nm. BET surface areas are 9.5 m² g⁻¹ and 6.6 m² g⁻¹ for the Namurian and for the Posidonia sample, respectively.

Table 3.3: Results of the pore size characterization by means of low-pressure CO₂ (195 K and 273 K) and N₂ (77 K) sorption.

	DR-micropore volume [mm ³ g ⁻¹]	Sorption pore volume [mm ³ g ⁻¹]	BET [m ² g ⁻¹]
Namurian	9.4	7.8	9.5
Posidonia	6.9	15.8	6.6

Micropore size distributions of the Namurian and the Posidonia sample are shown in Figure 3.2 and Figure 3.3, respectively. In accordance with DR and SPV pore volume measurements the Namurian Shale shows an abundance of ultra-micropores (< 0.7 nm pore diameter) and little porosity above pore diameter > 0.7 nm. The portion of pore volumes in the ultra-micropore range is lower for the Posidonia shale outcrop sample.

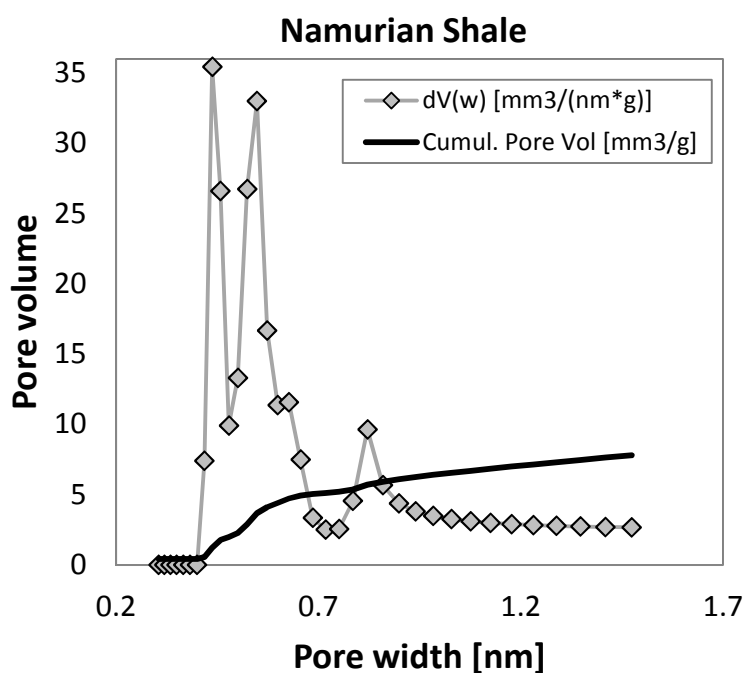


Figure 3.2: Micropore size distribution of the Namurian shale sample showing the cumulative (V) and differential (dV(w)) pore volume. The pore size distribution was determined by fitting the CO₂ isotherm at 273 K to a slit pore nonlocal density functional theory (NLDFT) model.

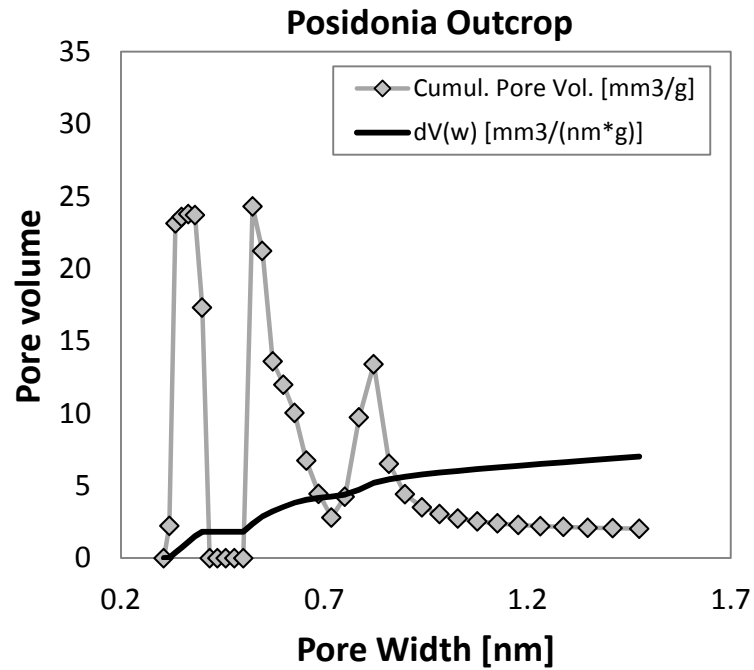


Figure 3.3: Micropore size distribution of the the Posidonia shale sample.

3.3.2 Sample Density (He-Density)

The variation of the sample density determined from the void volume (manometric method) or sample volume (gravimetric method) measurements reported by individual laboratories are shown in Figure 3.4 for both samples. For the high-maturity Namurian sample the results from different laboratories are consistent with the exception of the Lab 1. The standard deviation (excluding the result by Lab 1) is only 0.7%. On the other hand, the results for the immature Posidonia sample show a much larger variation (3.4%) with two laboratories providing significantly different density values from repeated measurements on different sorption setups with different sample aliquots. These discrepancies might be indicative of sample heterogeneity (insufficient homogenization or transport-related) and the measurement errors in sample volume determination.

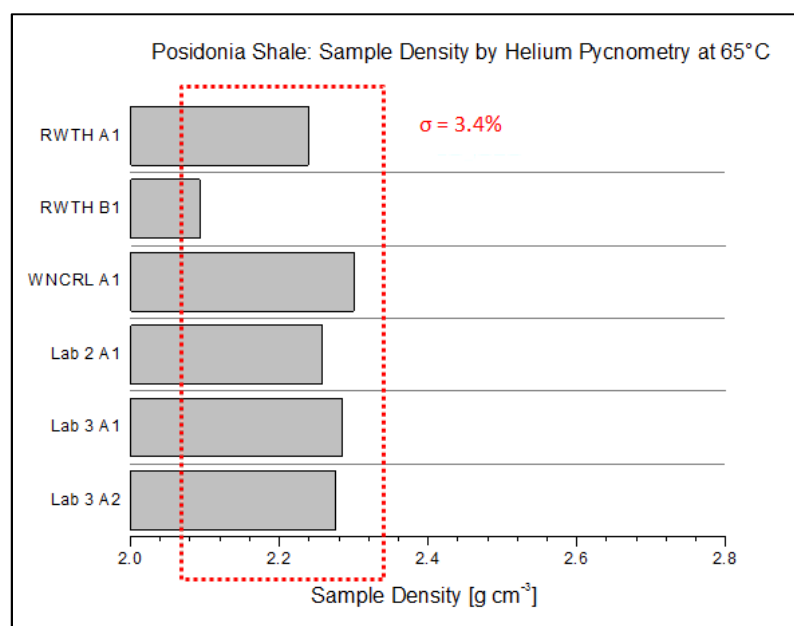
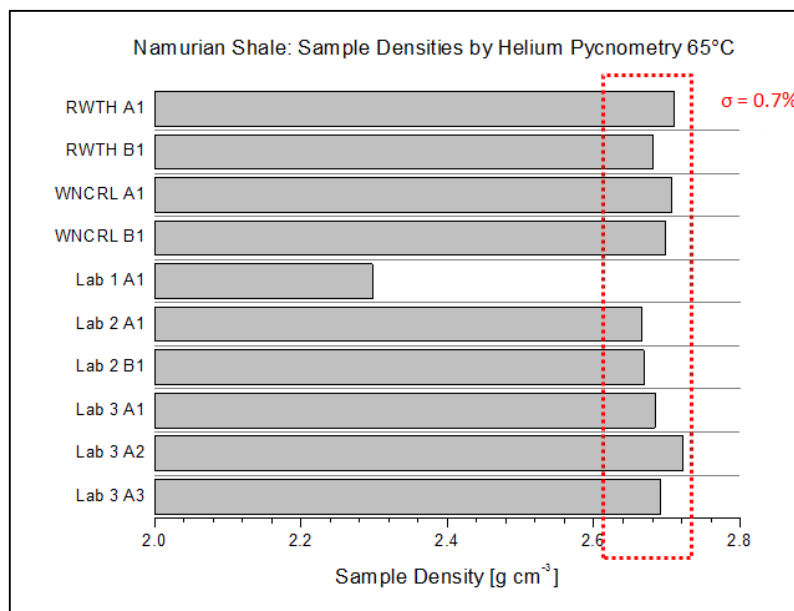


Figure 3.4: Comparison of the helium densities determined by individual laboratories.

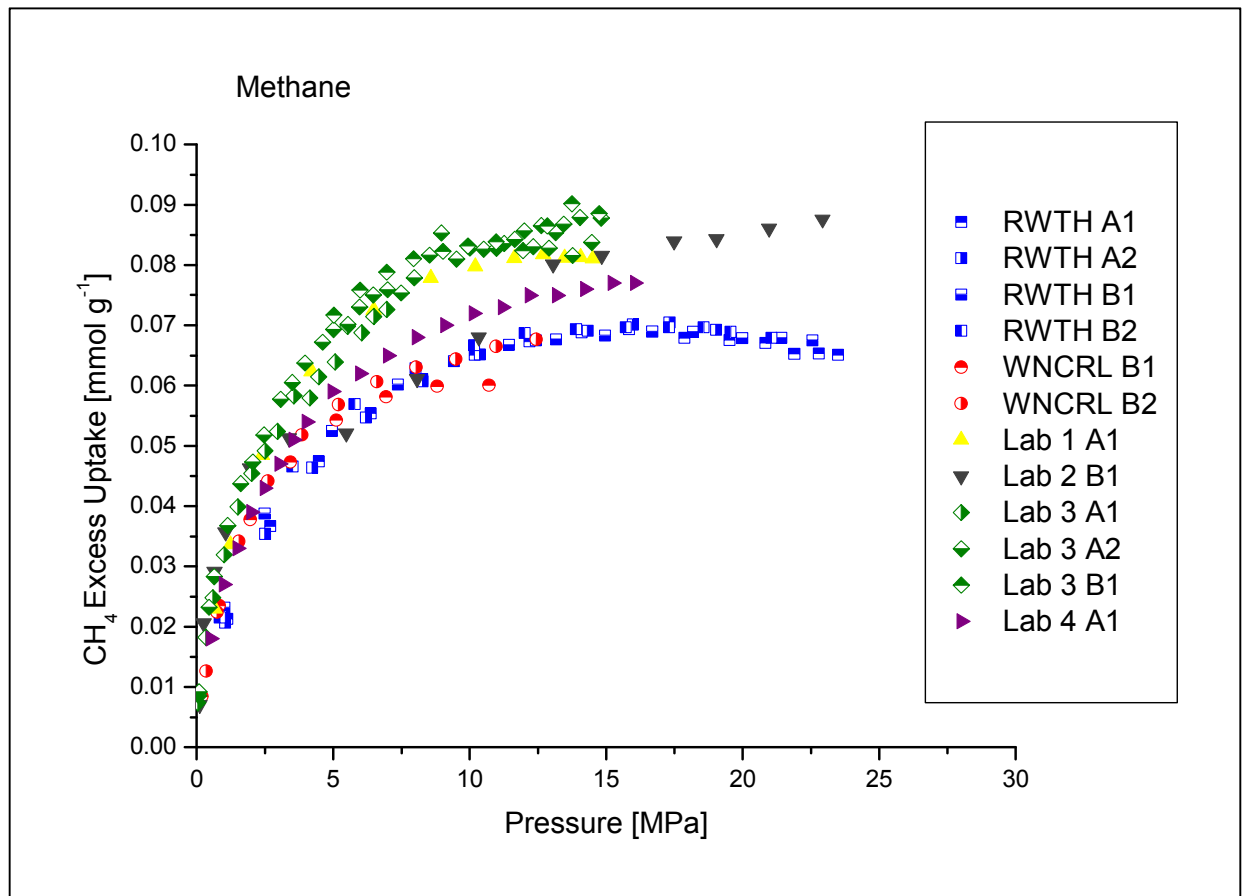
3.3.3 Excess Sorption Isotherms for CH₄, CO₂ and C₂H₆ at 65°C

The measured excess sorption isotherms are presented in Figure 3.5 and Figure 3.6. The repeated measurements (if reported) for a single laboratory are indicated, respectively, by different numbers (1, 2, ...) when performed as consecutive tests on the same setup and by different letters (A, B, ...) when performed on a modified or different setup.

Namurian Shale

The CH₄ excess sorption isotherms for the highly mature (VR = 2.0 %R₀) Namurian shale are presented in Figure 3.5. Discrepancies in the high-pressure range of 0.02 to 0.03 mmol g⁻¹ are observed between individual laboratories. The shapes of the isotherms do not vary significantly, except for the results from Lab 2 where a step increase in sorption capacity is observed at ~ 10 MPa. The sorption capacities measured by RWTH Aachen and WNCRL

Newcastle laboratories show a very good agreement and are lower than those of all other laboratories. Isotherms measured by Lab 1 and Lab 3 show very good agreement but are higher than those of all other labs. The results from Lab 4 are intermediate between these two groups. Interestingly, the sorption isotherm measured by Lab 2 seems to follow the first group at $p < 10$ MPa and the second group at $p > 10$ MPa. It should be noted, however, that such a step change in CH_4 excess sorption is rather unusual and physically not explainable. Hence, we consider it to be an experimental artefact.



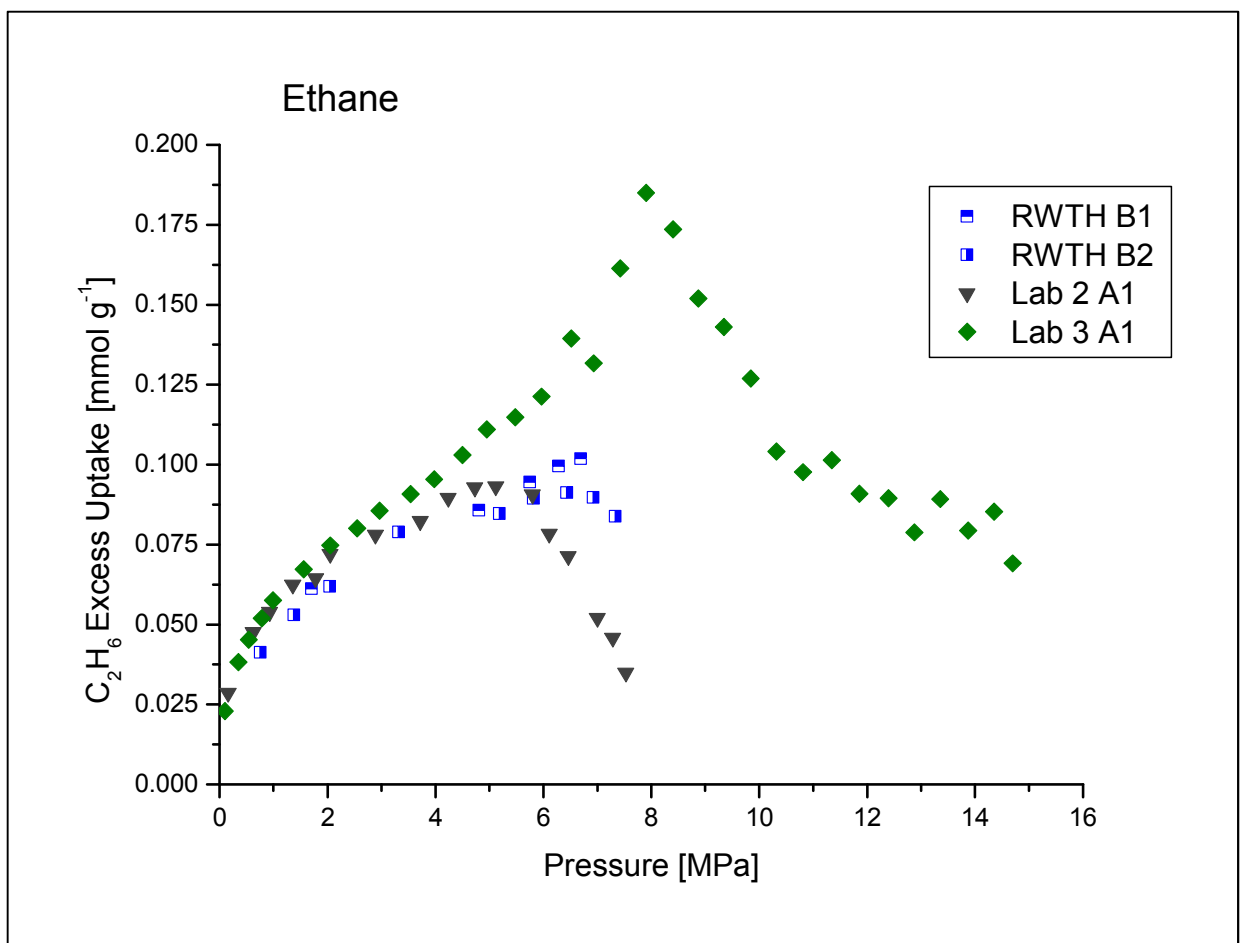
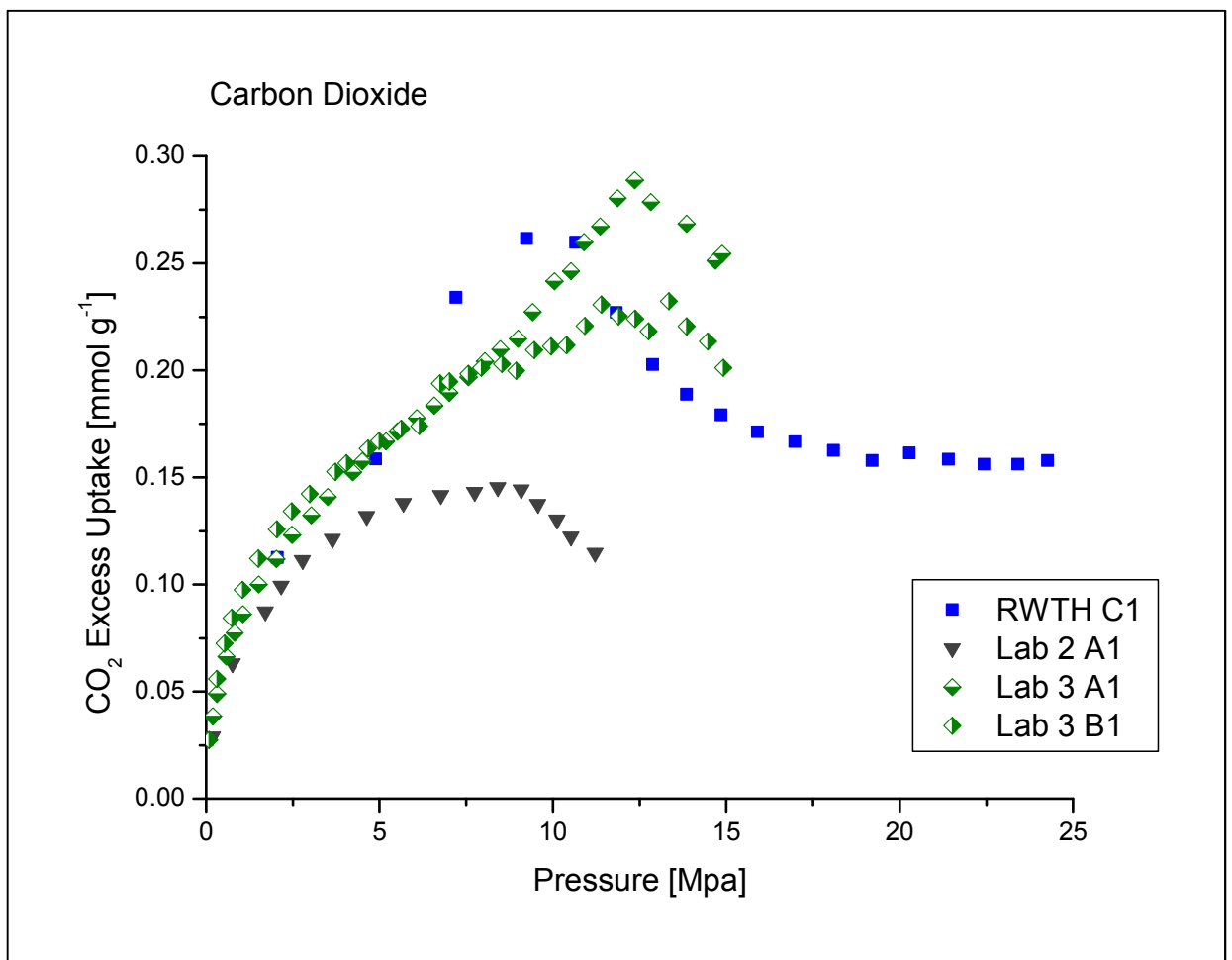


Figure 3.5: Comparison of the CH₄, CO₂ and C₂H₆ excess sorption isotherms at 65°C for the over-mature Namurian shale.

The CO₂ sorption isotherms for the Namurian shale were only provided by three laboratories. The results show a relatively good reproducibility (within 0.05 mmol g⁻¹) up to a pressure of ~ 8 MPa, corresponding roughly to the critical pressure of CO₂ (7.374 MPa), above which the isotherms diverge significantly. The CO₂ isotherms of Lab 2 are lower than those of RWTH and Lab 3. At high pressures the isotherms measured at RWTH and Lab 3 are close to each other. However, they differ in the position of the maxima of the excess sorption.

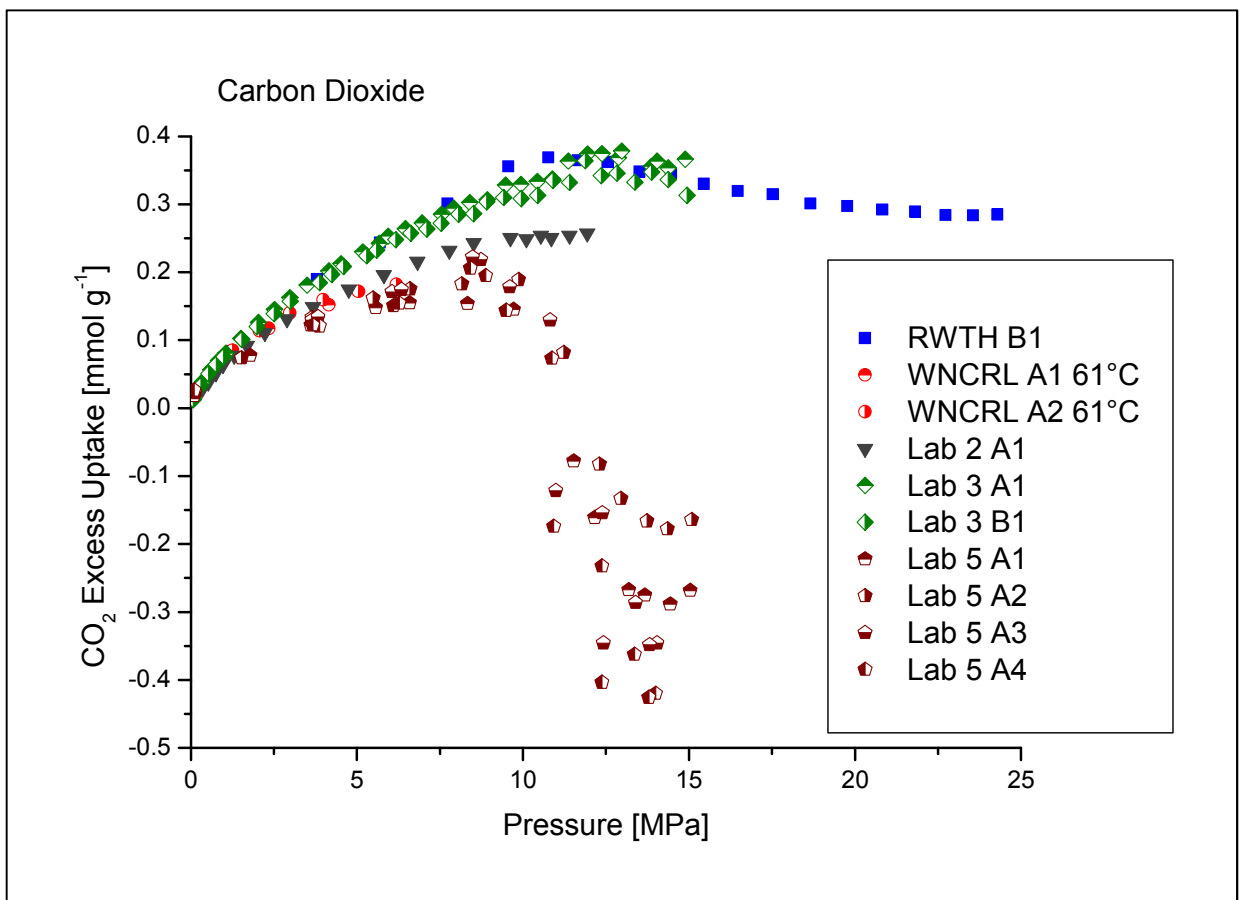
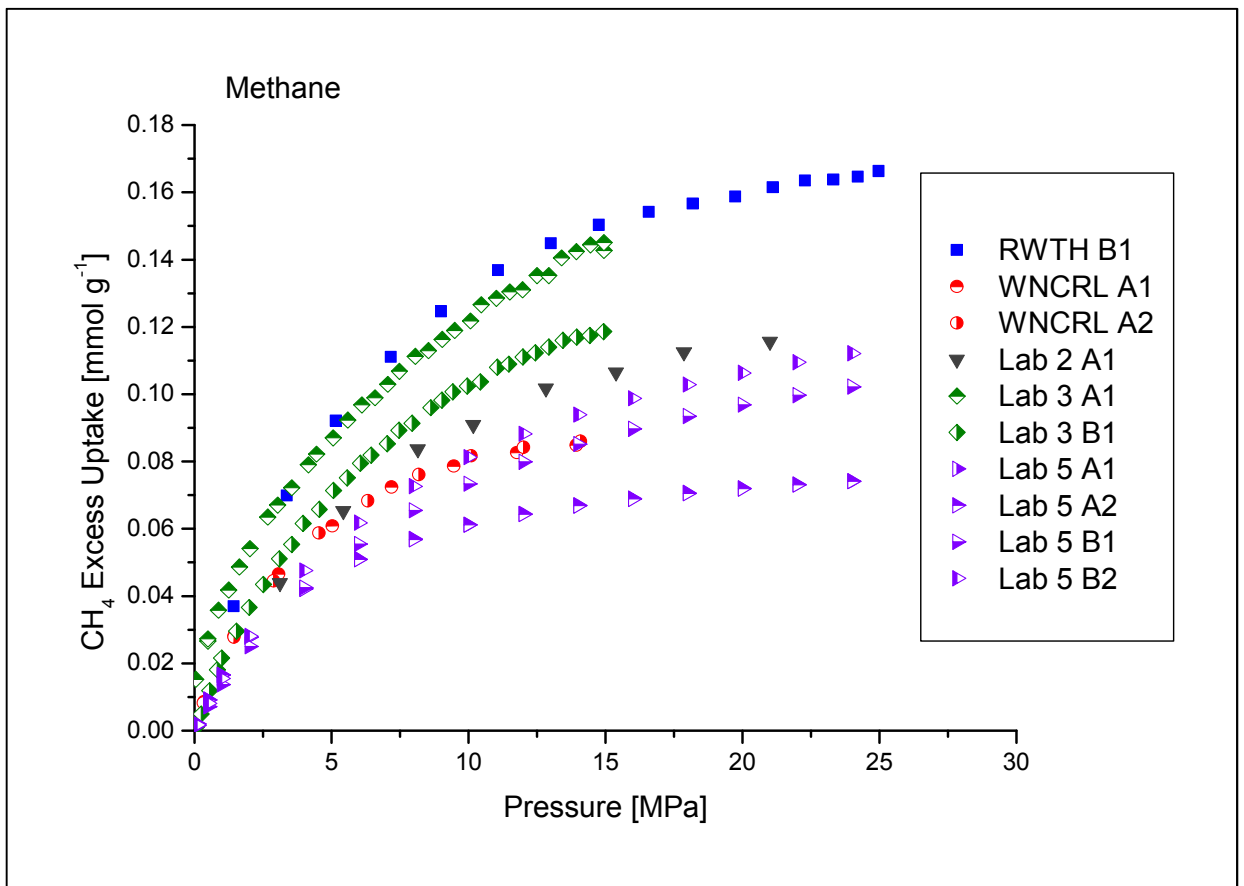
The C₂H₆ excess sorption isotherms for the Namurian shale show a very good agreement up to 5 MPa, corresponding to the critical pressure of C₂H₆ (4.872 MPa) and deviate significantly thereafter. The Lab 3 results show the highest sorption capacity, while the results from Lab 2 show a strong decreasing trend in excess sorption above 5 MPa. The results from Lab 3 show additionally a sharp spike in the excess sorption at ~8 MPa. The results for both, CO₂ and C₂H₆, show that the rapid increase in gas density above the critical pressure significantly amplifies the differences in measured sorption among different labs.

Posidonia Shale

The CH₄ sorption isotherms for the immature Posidonia shale are shown in Figure 3.6. It is observed that the scatter in the results from individual labs is higher than for the high-maturity Namurian shale. The results of the repeatability measurements reported by Lab 3 and Lab 5 are not satisfactory. The highest sorption capacities were measured by RWTH and Lab 3.

The CO₂ isotherms for the Posidonia sample show a good agreement between RWTH and Lab 3, while results for other labs deviate increasingly with increasing pressure and the measured excess sorption is systematically lower than for RWTH and Lab 3. The isotherms measured by Lab 5 become negative for pressures above ~ 11 MPa. This is considered to be an measurement artefact due to a choice of EoS (Peng-Robinson) as well as due to possible cross-contamination of the CO₂ with He (the setup in Lab 5 had no vacuum system).

The results for the C₂H₆ sorption were only reported by two labs. The isotherms determined by Lab 2 and Lab 3 show an excellent agreement up to a pressure of 5 MPa after which they diverge somewhat. Moreover, the excess sorption isotherms by Lab 3 show a sharp spike-like maximum at ~ 8 MPa and a steep decrease in excess sorption with pressure thereafter.



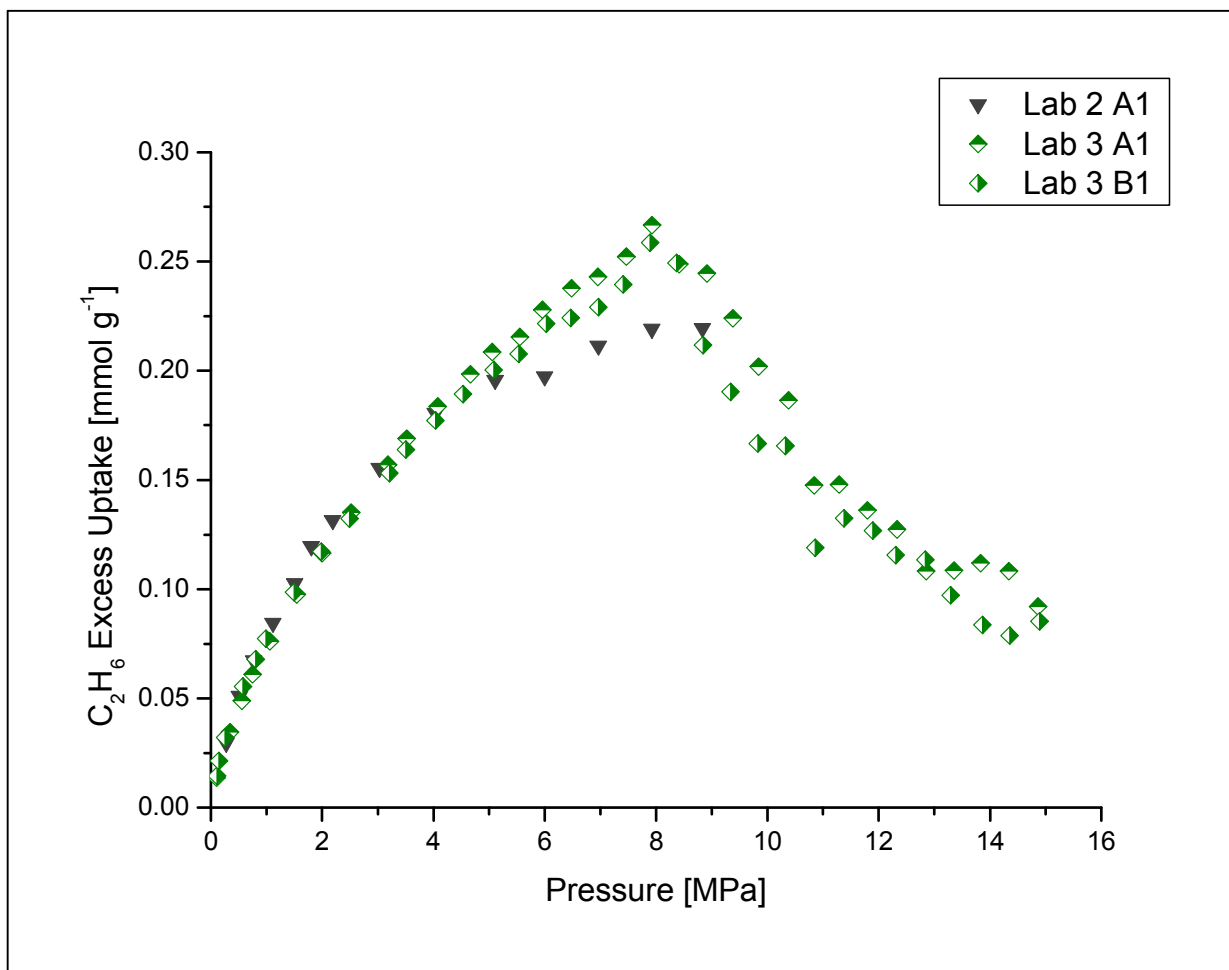


Figure 3.6: Comparison of CH₄, CO₂ and C₂H₆ excess sorption isotherms at 65°C for the immature Posidonia shale.

3.4. Discussion

3.4.1 Repeatability versus Reproducibility

The results of this study show that an excellent intra-laboratory repeatability of excess sorption isotherms of hydrocarbon gases and CO₂ on shales is achievable in spite of low sorption capacities (although this was not generally the case for all labs in this study). In this context, repeatability denotes the consistency of repeated measurements performed by a single laboratory, for a given sample, on the same setup and at the same conditions. Thus, the random and quantifiable errors due to temperature fluctuations and measurement uncertainty (pressure, temperature, mass) do not pose a major problem for high-pressure sorption measurements with today's instrumentation. The observed discrepancies in “inter-laboratory reproducibility” hence result from the unknown systematic measurement errors and/or from differences in sample conditioning prior to the experiment. The systematic errors cannot be identified and quantified with certainty. However they can be reduced to some acceptable level experimentally and in the data reduction procedure. Strict control must be exerted on the experimental conditions and the sample treatment. In the simpler case of

measurements on dry samples (this study) this means that care should be taken when drying and de-gassing the sample. While all laboratories were asked to follow a specific sample drying and degassing procedure there were some technical limitations in some of the labs. Moreover, the highly variable instrument design between individual laboratories requires that each experimentalist adapts the procedure to approach as close as possible for the desired experimental conditions based on the knowledge of the instrument behaviour. In particular, the variable sizes of the sample cells, the connecting tubing system, the valves as well as highly varying heat transfer efficiencies of different temperature control systems and limits on the maximum achievable vacuum can easily lead to different levels of sample “dryness” or “activation” (de-gassing) even at the same prescribed conditions. Especially at low pressures (vacuum) and for large sample cells, the actual temperature of the sample in the sample cell will be influenced by heat transfer effects including heat capacity of the medium used (air- vs. liquid-baths vs. electrical resistivity heaters directly on the sample cell). One advantage of the gravimetric methods in this respect is that it allows direct observation of sample degassing. For optimal design of the manometric devices the temperature sensor should be directly in contact with the sample. Such a design is moreover desired for improved monitoring of the establishment of the thermodynamic equilibrium as well as for studies on uptake kinetics.

3.4.2 Void Volume / Sample Volume Measurements

Both the manometric and the gravimetric techniques rely on accurate measurement of volume for the determination of the excess sorption. In the manometric method, the void volume is measured to define the quantity of non-adsorbed gas whereas in the gravimetric method the sample volume, as well as the volume of the sample holder and the hangdown, are required for the buoyancy correction. The measurements are performed with helium as a "reference gas" (although the issues of helium sorption and possible differences in pore-volume accessibility compared to other gases are often mentioned in the literature, they are not essential for the discussion of the inter-laboratory reproducibility).

Sakurovs et al. (2009) pointed out that inaccuracies in the void volume or the sample volume measurements are the major sources or errors in excess sorption isotherms and are mainly responsible for the observed inter-laboratory inconsistencies.¹¹ The low sorption capacity of shales, as well as the high pressures (> 20 MPa) that are of interest for shale gas exploration, demand high accuracies in the volume measurement and the helium density. For errors in excess sorption to be within 10%, the uncertainty in the void/sample volume should be well within 0.1%.

The buoyancy correction represents the most significant source of error in the gravimetric method and is analogous to the void volume correction in the manometric method. The buoyancy correction requires an accurate determination of the volumes of the sample, the balance pan and the hangdown as well as the gas density. For low-sorbing material such as shales the magnitude of the buoyancy term becomes very large relative to the mass increase by the uptake of gas, especially for low sample amounts (< 1 g) that are typically used in commercial instruments.

For the evaluation of the void volume measurement with helium in the manometric method in a range of pressures, the most straightforward and unambiguous procedure is to construct the total-mass-of-transferred-helium (m_{trans}^{He}) versus the equilibrium density of helium in the sample cell (ρ_{sc}^{He}) isotherms. Equations 3.4a and 3.4b give the m_{trans}^{He} for a single-temperature and a two-temperature (temperature gradient within the sample cell volume) manometric setup, respectively.

$$m_{trans}^{He} = V_{rc} \sum (\rho_{rc}^{He,i} - \rho_{rc}^{He,f}) \quad (a)$$

$$m_{trans}^{He} = V_{rc} \sum (\rho_{rc}^{He,i} - \rho_{rc}^{He,f}) - V_{sc}^* \rho_{rc}^{He,f} \quad (b)$$

Equation 3.4 – Total Mass of Transferred Helium

In Eq. 3.4b, V_{sc}^* denotes the portion of the sample cell volume (tubing) which is kept at the temperature of the reference cell. An example of void volume determination using this procedure is shown in Figure 3.7. This procedure is preferable as (1) it does not require any subjective data point elimination or selection (i.e. outliers, data scatter as the equilibrium pressure approaches the maximum pressure value); (2) the slope is independent of the initial pressure value and (3) it mimics the evaluation of the excess isotherm in which the total amount of sorptive gas transferred into the sample cell is measured. It is, moreover, analogous to the measurement of the “helium isotherm” in the gravimetric method to obtain the sample volume for the buoyancy correction.

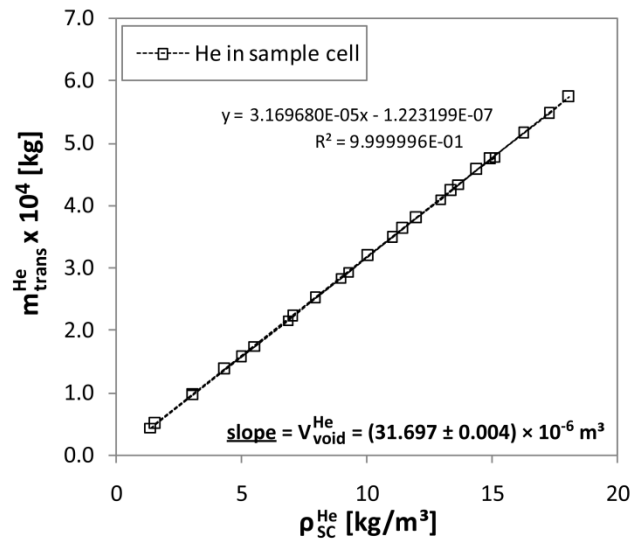


Figure 3.7: Example of proposed void volume determination in a manometric device. The total amount of helium transferred successively into the sample cell is plotted against helium density. The slope of this “helium isotherm” is equal to the void volume. The data represent two repeated measurement on the Namurian sample on a two-temperature manometric sorption device and Eq. 3.4b was used to calculate m_{trans}^{He} .

3.4.3. Thermodynamic Equilibrium

The transient processes which take place during the equilibration step include 1) temperature changes and 2) diffusion-controlled transport of the sorptive gas onto the sorption sites (or into the micropores). The temperature changes result mainly from the Joule-Thompson effect of a gas being expanded through an orifice (e.g. valve, in-line filter) into the sample cell and from the evolved heat of sorption. These temperature effects usually happen in relatively short time interval compared to the time it takes to reach equilibrium through the slow diffusion process. However, they are very dependent on the instrument design (size of the cells, gas-dosing system, etc.), the heat transfer efficiency of the heating system and are also sample and gas-specific (Joule-Thompson coefficient, thermal conductivity, etc.). The establishment of equilibrium is inferred by monitoring the changes in pressure (manometric method) or weight (gravimetric method). There are no general criteria or recommendations with respect to the equilibration times. Insufficient equilibration times will lead to an underestimation of the sorption capacity and possibly some effect on the isotherm shape. For samples with a significant proportion of pores in the nano-scale range the equilibration process can be very lengthy and a true equilibrium may never be reached in an experiment due to kinetic restrictions. It is important, however, to define at least a “technical equilibrium” meaning that the measured pressure (or mass) changes should be on the same order of magnitude as the changes due to temperature fluctuations (resolution limit) over a sufficiently long time interval. On the other hand, substantially long equilibration times

require a very good leak-tightness of the setup and/or explicit consideration of leakage in the mass balance (e.g. van Hemert et al., 2009a). Figure 3.8 shows an example of the pressure equilibration (uptake) curves of CH₄ and CO₂ during a manometric sorption experiments on the Posidonia sample performed by RWTH. The uptake curves are plotted with a logarithmic time axis as this offers a much better visual analysis of the slow late-time uptake (van Hemert, 2009b). It is observed that for CO₂ during the first three equilibration steps the equilibrium has not been fully attained within the duration of the expansion step. It is also observed that at lower pressures (more precisely at low occupancy of the sorption sites) the equilibration process is considerably longer than at high pressures (high occupancy of the sorption sites). Accordingly, the equilibration times should be sufficiently long initially in order to approach as closely as possible the thermodynamic equilibrium while they can be reduced with the progression of the experiments (depending on the uptake kinetics) in order to minimize the effect of leakage.

In Figure 3.9 an example of CH₄ uptake curve is shown for which thermal effects, mainly due to Joule-Thompson effect, can be observed in the initial phase of the pressure equilibration. Such observations are typically encountered for CH₄, CO₂ and C₂H₆ in manometric setups with large sample cell volumes. Depending on the setup characteristics these effects are only observed within the first 30 – 60 seconds following the gas expansion into the sample cell.

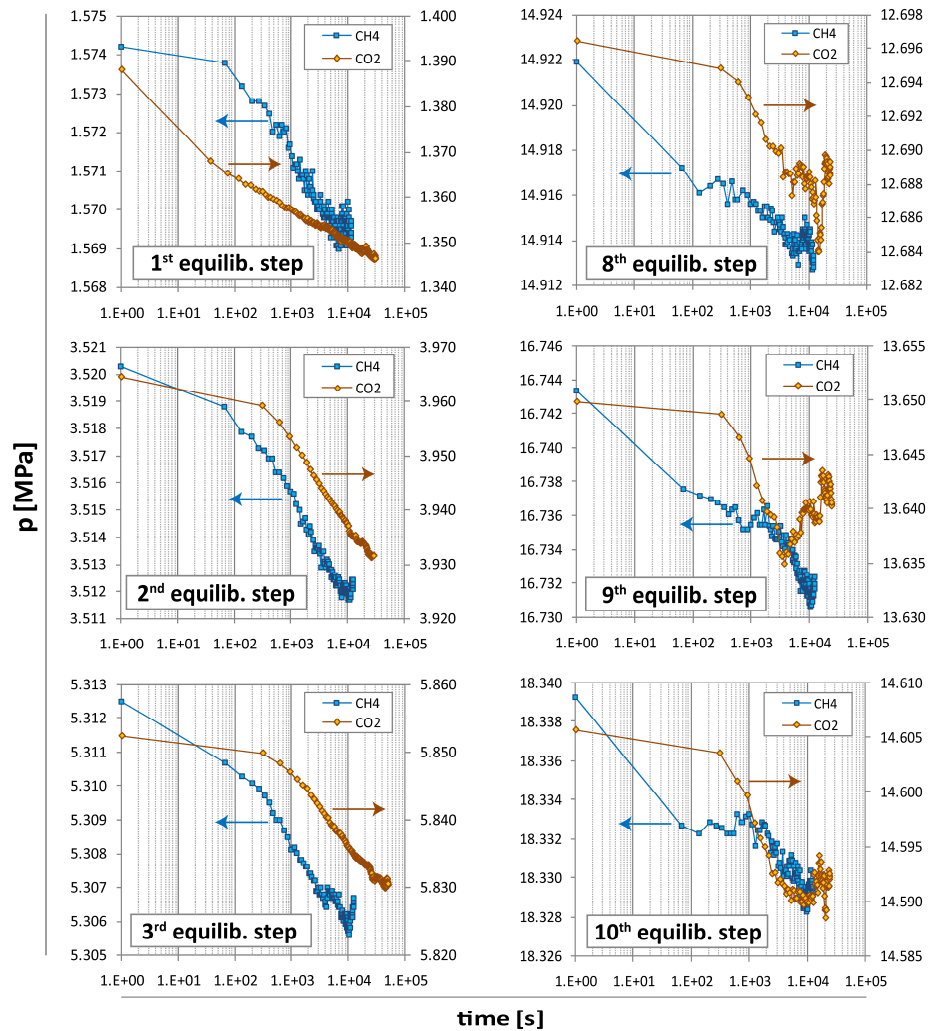


Figure 3.8: Examples of the uptake curves of the CH₄ and CO₂ during the manometric sorption experiment on the Posidonia shale sample from RWTH. The time axis is in logarithmic form. The uptake curves for CO₂ for the first three equilibration steps indicate that the equilibrium has not been fully attained within duration of the expansion step. For the later equilibration steps for CO₂ (8.– 10.) and for all equilibration steps for CH₄ the pressure data at the end of the equilibration step show only fluctuations due to temperature variations.

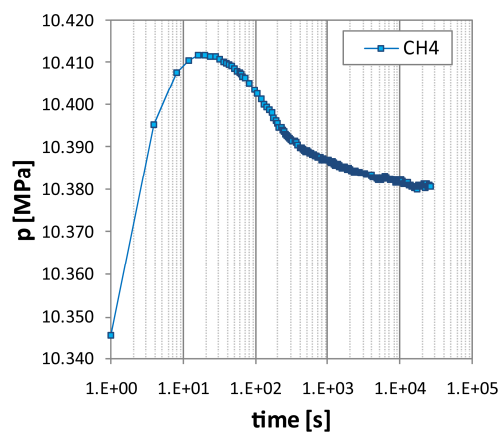


Figure 3.9: Example of uptake curve of the CH₄ during the manometric sorption experiment showing initially (first 30 seconds) thermal effects (Joule-Thompson effect). Such a situation is typically observed for large sample cells (the sample cell volume in this example was $\sim 55 \text{ cm}^3$).

3.4.4. Blank Tests (RWTH Aachen)

For sorption measurements on materials with a low sorption capacity, and especially for gases at a proximity to the critical conditions it is important to isolate the actual sorption behaviour of the sample from experimental artefacts. Blank sorption measurements using a non-sorbing sample (ideally of the same material as the sample cell, e.g. stainless steel) can be performed as a sort of device-specific diagnostic test to identify and quantitatively account for such artefacts. These can result from unknown systematic errors in pressure and temperature that propagate into the gas density calculated by the EoS; (2) the actual EoS; (3) gas impurities and/or (4) due to fundamentally different interaction of different gases (He vs. CH₄ vs. CO₂, etc.) with the inner walls of the instrument components with which they are in direct contact. These blank measurements can be performed during the setup calibration with gases and at temperatures of interest.

Blank sorption measurements have been performed systematically for the manometric setup from RWTH. Stainless steel cylinders of different sizes were used to create a range of void volumes typically encountered in sorption tests with shale/coal samples. From the “raw” excess sorption isotherm measured on a shale sample, the “blank” excess sorption isotherm at an equivalent void volume is subtracted to obtain the final corrected excess sorption isotherm. An example of the measured (“raw”) excess sorption isotherms and the blank isotherms of CH₄ and CO₂ is shown in Figure 3.10 for the Posidonia sample. For CH₄, the downward bending of the excess sorption isotherm following a maximum is reduced or eliminated (for immature samples such as Posidonia). For CO₂, the “concave-upward” isotherm part preceding, and the strong downward trend, following the maximum in excess sorption are eliminated or reduced after the blank correction.

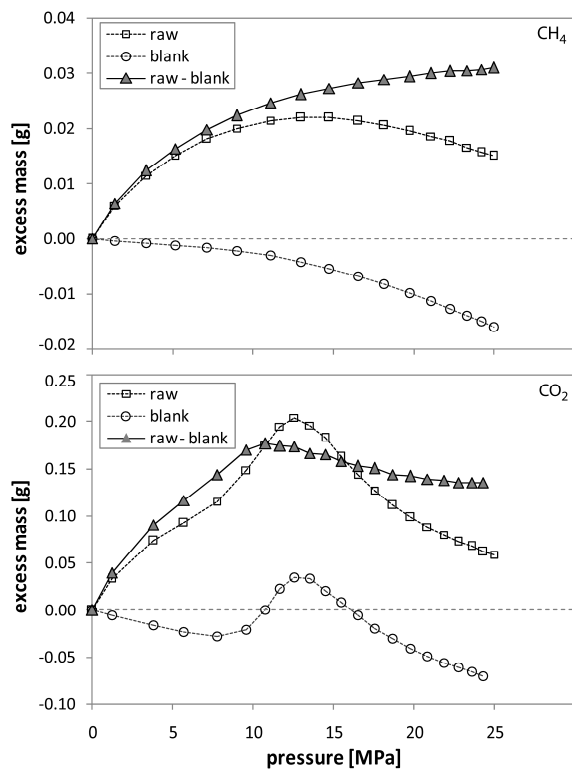


Figure 3.10: CH₄ and CO₂ excess sorption isotherms for the Posidonia sample measured at RWTH. The excess mass (in grams) is plotted along with the “blank” sorption isotherm obtained from a measurement with a stainless steel cylinder placed in the sample cell. The void volumes in the sorption and in the blank experiment were roughly equal.

3.4.5. Equation of State (EoS)

For high-pressure sorption isotherm measurements the choice of the equation of state will have a significant influence on the calculated sorption quantity. While some modern gravimetric instruments enable direct measurements of gas density, all laboratories involved in this study relied on the EoS to calculate the gas density (or compressibility factors) from measured pressure and temperature data. Commonly used EoS include, for example, the cubic equations of Peng-Robinson (P-R) or Soave-Redlich-Kwong (SRK), which are based on critical point data and acentric factors, or the virial-type equation of Benedict-Webb-Rubin. Currently, the most accurate EoS for CH₄ and CO₂, are however, the multi-parameter wide-range EoS by Setzmann and Wagner (1991) (Se-W) and Span and Wagner (1996) (Sp-W), respectively. These EoS are based on the dimensionless Helmholtz energy and provide excellent accuracy even at the critical region. They are used for instance in the National Institute of Standards and Technology (NIST) Chemistry WebBook and in the NIST REFPROP software package. Recently, the same group introduced the GERG 2004 (Kunz et al., 2007) and the new GERG 2008 (Kunz and Wagner, 2012) EoS for multi-component mixtures for up to 21 natural gas components which will be used as an ISO standard (ISO 20765-2/3) for natural gases.

In this study, one laboratory (Lab 5) reported using the P-R EoS for the calculations of the CH₄ and CO₂ density, while other laboratories used the Se-W and Sp-W EoS, respectively. Figure 3.11 demonstrates the difference in the calculated excess sorption for CH₄ and CO₂ using the P-R and the Se-W / Sp-W EoS. Clearly, the isotherm based on the P-R EoS deviates significantly from that based on the more accurate Se-W and Sp-W EoS and, moreover, produces artefacts that cannot be explained by thermodynamic considerations (note the shape of the CO₂ sorption isotherm).

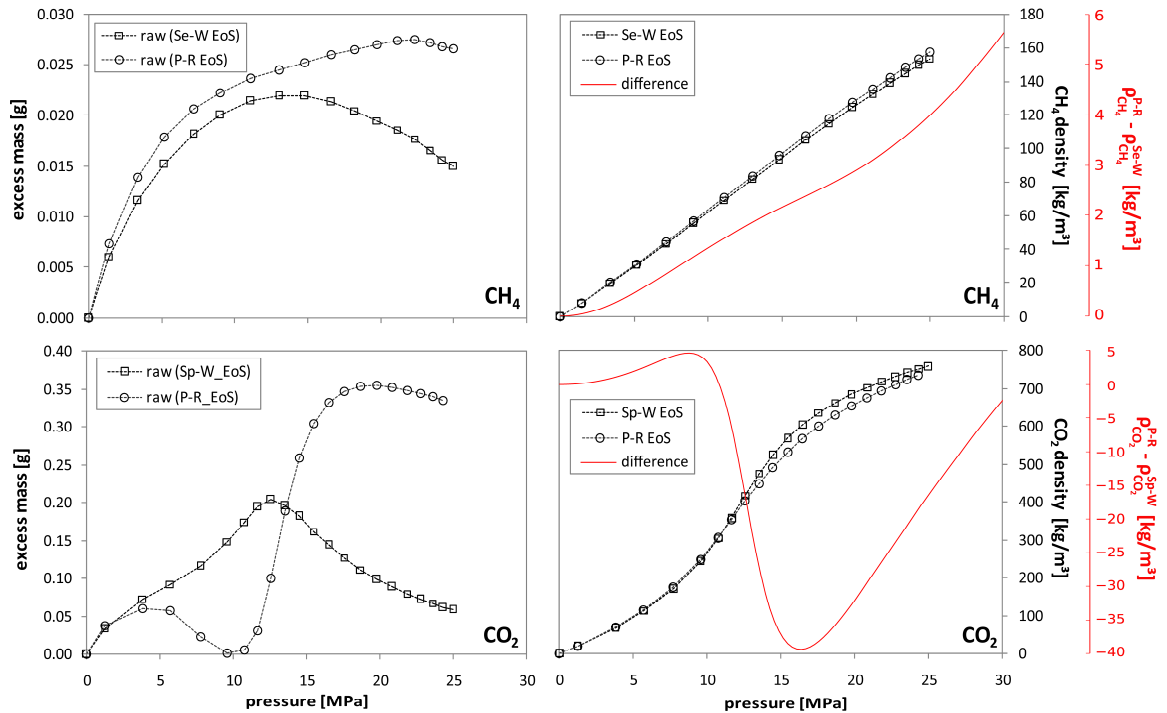


Figure 3.11: Comparison of the raw CH₄ and CO₂ excess sorption isotherms for the Posidonia shale calculated using the equations of state (EoS) of Setzmann and Wagner (Se-W) and Span and Wagner (Sp-W) for CH₄ and CO₂, respectively, with those based on the Peng-Robinson (P-R) EoS.

3.4.6. Gas Impurities (Moisture)

Small amounts of adsorbed water can significantly influence the sorption capacities of gases. The trace amounts of water (usually in ppm range) in high-purity gases can affect the sorption experiments on shales in sorption instruments with a large void volume relative to the sample size. This is because of relatively high absolute moisture content compared to sample mass. A set of test measurements to study this effect was performed by WNCLR on a modified gravimetric setup for measurements of CO₂ isotherms at 273 K with and without a zeolite gas drier. The stream was passed through a zeolite cylinder bed (~ 5 x 20 cm) filled with sodium aluminium silicate (1 nm molecular sieve, 2 mm beads) from Merck KGaA. Additionally, a reactor filled with the same zeolites was attached to the sample reactor. Before running isotherms the zeolite beds were dried (> 400°C) and outgassed. The results are

shown in Figure 3.12. The higher uptake (mass increase) observed for the experiment without the gas pre-drying indicates additional sorption of water. Although similar tests have not been performed for high-pressure sorption, the same issues apply.

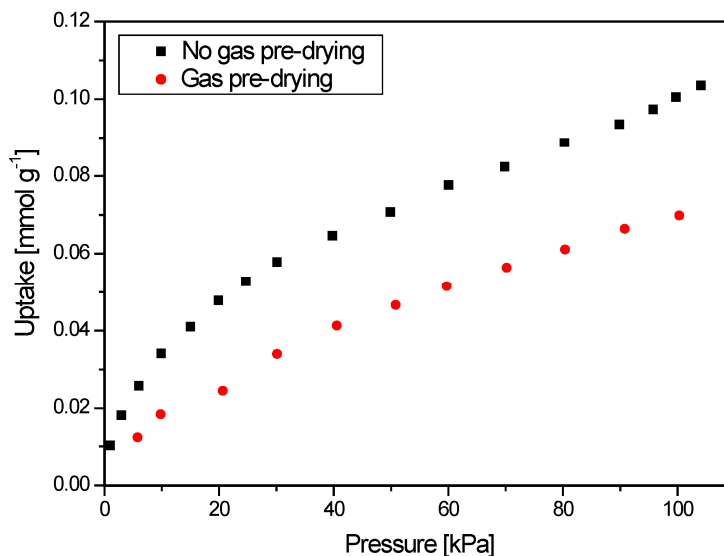


Figure 3.12: CO₂ sorption isotherms at 273 K on shale measured with a modified gravimetric setup with and without gas pre-drying. Trace moisture contents present in high-purity gases can affect sorption measurements on devices with large void volumes relative to sample mass.

3.4.7. Other Sources of Uncertainty

Other sources of uncertainty in high-pressure sorption measurements not discussed here in detail can be found in the literature on sorption in coals.^{3,4,11,14,22} These comprise of errors due to leakage, sample compression and swelling, gas impurities or due to solvent properties of the supercritical CO₂. Of these, leakage is the most significant as high leakage rates during the sorption experiment may overestimate the sorption capacity, or even give unrealistic results. Each experimentalist should take all necessary measures to minimize the leakage and to ensure that its effect on the sorption measurements (and for specific applications) is acceptable. A detailed analysis considering the influence of leakage on the mass balance of the sorption experiments was provided by van Hemert et al.²⁸ Gas impurities (e.g. residual helium in sample cell / gas supply tubing) can result from insufficient evacuation of the sample cell or insufficient purging of the gas supply tubes and will compromise the mass balance. Gensterblum et al. (2010) discuss the effects of gas impurities for CO₂ sorption measurements on coals.⁴ For sorption studies on shales, if the sorption device is equipped with a vacuum system (10⁻² Pa and lower) with proper purging and sample cell evacuation these effects will be insignificant.

3.5 Recommendations for Optimizing High-Pressure Sorption Measurements on Shales

The discrepancies in high-pressure sorption measurements on shales reported in this study indicate that the current quality standards in measurement procedures need to be improved. The identification of the different types of errors (procedural, calibration, errors due to poor equipment design) is not possible from the reported results and equipment specifications alone. Therefore, tentative recommendations are proposed here for the optimization of sorption measurement and for data reporting. These recommendations were adapted from Zlotea et al.²⁹

a) Methodology

In general, both methods, manometric and gravimetric provide consistent results and from the data reported here no systematic discrepancies between the two methods (beyond those for a single method) are observed. Both methods have advantages and disadvantages. The drawback of the manometric method is the accumulation of errors for multi-point sorption isotherm. A thorough optimization of the procedure of successive gas transfer into the sample cell is anything but trivial. The estimates for an optimal ratio of reference cell volume to void volume vary in the literature from 2 to 10 and optimal dosing might require variable volume of the reference cell for controlled ratios of the initial and equilibrium density (depending on the proximity to the critical point). On the other hand, the magnitude of the buoyancy term and temperature fluctuations relative to the mass increase due to gas uptake, decreases significantly the sensitivity in the gravimetric method for low-sorbing shales. The very small sample amounts (< 1g) typically used in commercial gravimetric instruments should also be considered.

b) Volume Calibration

The volume calibration of the reference and sample cells (manometric) and the buoyancy correction of the empty sample pan (gravimetric) require very accurate volume measurements ($\ll 0.1\%$ standard error). Certified volume standards (e.g. precision balls and electro-polished steel cylinders) should be used and thermal expansion coefficients have to be known and considered in the volume calibration. For the manometric instrument, at least a three-point calibration (empty sample cell + two measurements with calibration standards of different volumes) should be performed. The calibration should be repeated in regular intervals and always after modifications on the device.

c) Calibration of Pressure and Temperature Sensors and of Magnetic Balance

The calibration of the individual components is necessary to reduce the unknown systematic errors, which may affect the gas densities calculated for the EoS and the mass readings in the gravimetric setups. The entire measuring loop (sensor + data acquisition system) should be calibrated at the experimental conditions of interest (the temperature compensation limits for many high-accuracy pressure transducers are limited to 40 – 50°C).

d) Pressure Measurements

Pressure measurements should be performed using the highest available standards in terms of accuracy. For optimal measurements over an extended range of pressures two (or more) pressure transducers with different full-scale range can be used. In the manometric method, the pressure data are sometimes obtained by separate pressure transducers attached to the reference and the sample cell. In this, as well as in the previous case, it is important that the different pressure transducers are carefully cross-calibrated so as to not introduce additional errors into the mass balance.

e) Temperature control and Measurements

The temperature of the thermostated parts should be stable within <0.1 K. In manometric setups the temperature stability can be further increased e.g. by aluminium or steel blocks with high thermal mass around the reference and the sample cell. Temperature measurements should be performed with high-accuracy platinum resistivity thermometers (Pt-100) and these should be calibrated by standard procedures (commercial calibration equipment provides accuracy level of 0.01 K). Temperature probes should be placed directly inside the reference cell and the sample cell (in contact with sample) if possible. Otherwise, the spatial and temporal variations in temperature should be considered in the error analysis. The equipment should be placed within the thermostated volume experiencing the lowest thermal gradients.

f) Temperature Gradient

For manometric sorption instruments with separate heating zones for the reference and the sample cell (allowing high temperatures in the reference cell), the thermal gradient existing in part of the sample cell volume (usually tubing connecting it to the reference cell) has to be quantified and accounted for in the mass balance calculation. A temperature calibration with an empty sample cell and/or with non-sorbing (steel) material with known thermal expansion properties can be performed to quantify the thermal boundary and determine the thermal expansion of the sample cell (this is necessary for measurements at

high temperatures). Care should be taken when performing measurements on moist samples on instruments with thermal gradients, as the moisture can condense in the cold spots and introduce errors in the calibration volume and the gas density.

g) Blank Tests

These tests are carried out with non-sorbing material (ideally the same material as that of the sample cell) in the pressure and temperature ranges of interest to verify the measurements and identify experimental artefacts. The blank tests can be performed as part of the volume calibration and should be carried out with at least two non-sorbing sample calibration standards so as to cover the typical range of void volumes occurring in the measurement.

h) Leakage Rate

The leakage rate should be determined prior to each experiment, ideally using helium at a representative pressure. Within the experimental possibilities the leakage should be reduced so that no corrections in mass balance are necessary (e.g. by reducing the amount of tube connections). The cumulative leaked amount of gas (considering the equilibration times) should be kept below the acceptable error margin with respect to the total excess sorbed amount. Corrections for the leakage in mass balance can be performed, however it is preferable to reduce the leakage by improved setup design.³⁰ The leakage is not critical for the gravimetric method as long as the pressure can be kept constant.

i) Void Volume / Sample Volume Measurement

The void volume and sample volume measurements with helium should ideally be performed for a range of pressures to check the consistency of void volume with pressure. For manometric setup a recommended data evaluation technique for multiple-point void volume measurement was presented in part 4.2.

j) Gas Purity

The trace impurities in high-purity / research grade gases do not pose any detectable influence on the measurement accuracy. However, it is very important to avoid any cross-contamination of the measurement gas due to insufficient purging and/or evacuation. Moreover, when measuring isotherms on dry samples, removal of moisture from the gas supply should be considered especially if the sample cell volume is very large relative to the sample amount.

k) Sample Outgassing

Sample out-gassing can be performed at different conditions depending on the application (dry versus moist samples, temperature sensitive materials, etc.). It is important, however, to consider the specific instrument design, especially the size of the sample cell, the heat transfer characteristics (gas versus liquid circulation versus electrical mantle heating) in order to adjust the out-gassing time. Temperature sensors in direct contact with the sample will enable verification that the sample has reached the desired temperature at high vacuum conditions.

For reporting the data the following relevant information should be included:

a) Sample Information:

All available geologic and geochemical sample information (e.g. TOC, RockEval, vitrinite reflectance, XRD, etc.). These analyses should be performed on an aliquot of the same sample as that used for sorption measurements.

b) Sample Treatment:

Crushing and sieving (particle/mesh size), sample homogenization, pre-drying (temperature, pressure), moisture adsorption procedure and moisture content.

c) Experimental Details:

Pressure range and temperature of the measurement; type of instrument (manometric, gravimetric, other); accuracy specifications and information on the calibration of pressure and temperature sensors, and magnetic balance; volume calibration of the reference/sample cells, buoyancy correction; temperature gradient corrections; experimental parameters (equilibration time or criteria), equations of state. We also recommend to report the sample mass, the ratio of void volume/dead space volume to sample mass, as well as the values and standard deviations for volumes of the sample and reference cell (as these data will be helpful for statistical evaluation of the measuring performance).

d) Analysis Gas:

Report purity, filtration (pre-drying) for each gas used in the experiment.

e) Repeatability of Sorption Measurement:

Were measurements repeated for the same/different sample aliquots and conditions and on the same/different instrument?

f) Evaluation of Data:

Data reduction equations for calculating void volume and excess sorption, mathematical treatment of the temperature gradient, special consideration in the mass balance, etc.

3.6. Conclusions

An inter-laboratory study was performed to assess the reproducibility of high-pressure sorption isotherms on shales. These are of interest for shale gas exploration and exploitation and for the assessment of the viability of CO₂ storage and enhanced methane production from shale. Seven international laboratories specialized on high-pressure gas sorption experiments have joined this “open round robin” in the first phase. Excess sorption isotherms of CH₄, CO₂ and C₂H₆ on two shales with high and low thermal maturity were determined at 65°C and at specified drying conditions.

The inter-laboratory reproducibility of the excess sorption isotherms for CH₄, was better for the high-maturity sample (within 0.02 – 0.03 mmol g⁻¹) than for the low-maturity sample (up to 0.1 mmol g⁻¹), similar to comparable round robin studies on coals. The reproducibility for CO₂ and C₂H₆ sorption isotherms was satisfactory at pressures below 5 MPa but at high pressures the individual results deviate considerably. Given that for the applications in shale gas exploration, the knowledge of sorption behaviour of shales at high pressures (and high temperatures) is of prime interest, the currently observed discrepancies between the individual laboratories call for further quality improvement and standardized methods. Since intra-laboratory consistency tests (though, not all) show that a high degree of repeatability is achievable, more attention should be paid to identifying and eliminating the unknown systematic errors through the usage of the highest-quality measuring instrumentation, calibration standards and optimization of operator-defined experimental parameters. A suitable benchmark test material (in sufficient quantity and representative of shales) may prove useful for future studies.

Associated Content

Appendix A

Acknowledgements

Shell Global Solutions is acknowledged for providing the financial support for this study. Furthermore, Pieter Bertier from Clay and Interface Mineralogy (RWTH Aachen) is thanked for carrying out and interpreting the XRD measurements and Alexej Merkel is thanked for technical assistance and assistance with the measurements.

References

- (1) Goodman, A. L.; Busch, A.; Duffy, G. J.; Fitzgerald, J. E.; Gasem, K. A. M.; Gensterblum, Y.; Krooss, B. M.; Levy, J.; Ozdemir, E.; Pan, Z.; Robinson, R. L.; Schroeder, K.; Sudibandriyo, M.; White, C. M. *Energy Fuels* **2004**, *18*, 1175.
- (2) Goodman, A. L.; Busch, A.; Bustin, R. M.; Chikatamarla, L.; Day, S.; Duffy, G. J.; Fitzgerald, J. E.; Gasern, K. A. M.; Gensterblum, Y.; Hartman, C.; Jing, C.; Krooss, B. M.; Mohammed, S.; Pratt, T.; Robinson, R. L.; Romanov, V.; Sakurovs, R.; Schroeder, K.; White, C. M. *Int. J. Coal Geol.* **2007**, *72*, 153.
- (3) Gensterblum, Y.; van Hemert, P.; Billemont, P.; Busch, A.; Charriere, D.; Li, D.; Krooss, B. M.; de Weireld, G.; Prinz, D.; Wolf, K. *Carbon* **2009**, *47*, 2958.
- (4) Gensterblum, Y.; van Hemert, P.; Billemont, P.; Battistutta, E.; Busch, A.; Krooss, B. M.; De Weireld, G.; Wolf, K. *Int. J. Coal Geol.* **2010**, *84*, 115.
- (5) Sircar, S. *Ind. Eng. Chem. Res.* **1999**, *38*, 3670.
- (6) Weireld, G. D.; Frre, M.; Jadot, R. *Measurement Science and Technology* **1999**, *10*, 117.
- (7) Belmabkhout, Y.; Frère, M.; De Weireld, G. *Measurement Science and Technology* **2004**, *15*, 848.
- (8) Billemont, P.; Coasne, B.; De Weireld, G. *Langmuir* **2011**, *27*, 1015.
- (9) Day, S.; Fry, R.; Sakurovs, R. *Int. J. Coal Geol.* **2008**, *74*, 41.
- (10) Day, S.; Sakurovs, R.; Weir, S. *Int. J. Coal Geol.* **2008**, *74*, 203.
- (11) Sakurovs, R.; Day, S.; Weir, S. *Int. J. Coal Geol.* **2009**, *77*, 16.
- (12) Dreisbach, F.; Lösch, H. W.; Harting, P. *Adsorption* **2002**, *8*, 95.
- (13) Mohammad, S.; Fitzgerald, J.; Robinson, R. L.; Gasem, K. A. M. *Energy Fuels* **2009**, *23*, 2810.
- (14) Busch, A.; Gensterblum, Y. *Int. J. Coal Geol.* **2011**, *87*, 49.
- (15) Rexer, T. F. T.; Benham, M. J.; Aplin, A. C.; Thomas, K. M. *Energy Fuels* **2013**, *27*, 3099.
- (16) Brunauer, S.; Emmett, P. H.; Teller, E. *Journal of the American Chemical Society* **1938**, *60*, 309.
- (17) Dubinin, M. M. *Quarterly Reviews, Chemical Society* **1955**, *9*, 101.
- (18) Ravikovitch, P. I.; Haller, G. L.; Neimark, A. V. *Advances in Colloid and Interface Science* **1998**, *76–77*, 203.
- (19) Gurvitch, L. J. *Phys. Chem. Soc. Russ.* **1915**, *47*, 805.
- (20) Marsh, H. *Carbon* **1987**, *25*, 49.
- (21) Fletcher, A. J.; Thomas, K. M.; Rosseinsky, M. J. *Journal of Solid State Chemistry* **2005**, *178*, 2491.
- (22) Krooss, B. M.; van Bergen, F.; Gensterblum, Y.; Siemons, N.; Pagnier, H. J. M.; David, P. *Int. J. Coal Geol.* **2002**, *51*, 69.

- (23) Gasparik, M.; Bertier, P.; Gensterblum, Y.; Ghanizadeh, A.; Krooss, B. M.; Littke, R. *Int. J. Coal Geol.*
- (24) Span, R.; Wagner, W. *Journal of Physical and Chemical Reference Data* **1996**, *25*, 1509.
- (25) Setzmann, U.; Wagner, W. *Journal of Physical and Chemical Reference Data* **1991**, *20*, 1061.
- (26) Kunz, O.; de Recherches Gazières, G. E. *The GERG-2004 wide-range equation of state for natural gases and other mixtures*; VDI Verlag, 2007.
- (27) Kunz, O.; Wagner, W. *Journal of Chemical & Engineering Data* **2012**, *57*, 3032.
- (28) van Hemert, P. Dissertation, University of Delft, 2009.
- (29) Zlotea, C.; Moretto, P.; Steriotis, T. *International Journal of Hydrogen Energy* **2009**, *34*, 3044.
- (30) van Hemert, P.; Bruining, H.; Rudolph, E. S. J.; Wolf, K.-H. A. A.; Maas, J. G. *Review of Scientific Instruments* **2009**, *80*.

Chapter 4

Methane adsorption on shale under simulated geological temperature and pressure conditions

Rexer, T. F. T.; Benham, M. J.; Aplin, A. C.; Thomas, K. M. *Energy Fuels* **2013**, 27, 3099.

Abstract

Shale gas is becoming an increasingly important energy resource. In this study the adsorption of methane on a dry, organic-rich Alum Shale sample was studied at pressures up to ~14 MPa and temperatures in the range 300 – 473 K, which are relevant to gas storage under geological conditions. Maximum methane excess uptake was 0.176 – 0.042 mmol g⁻¹ (125 - 30 scf t⁻¹) at 300 - 473 K. The decrease in maximum methane surface excess with increasing temperature can be described by a linear model. An isosteric enthalpy of adsorption 19.2 ± 0.1 kJ mol⁻¹ was determined at 0.025 mmol g⁻¹ using the van't Hoff equation. Supercritical adsorption was modelled using the modified Dubinin-Radushkevich and the Langmuir equations. The results are compared with absolute isotherms calculated from surface excess and the pore volumes obtained from subcritical gas adsorption (nitrogen (78 K), carbon dioxide (273 K and 195 K), and CH₄ (112 K)). The subcritical adsorption and the surface excess results allow an upper limit to be put on the amount of gas that can be retained by adsorption during gas generation from petroleum source rocks.

4.1 Introduction

The exploitation of gas associated with organic-rich shales is now economically viable as a result of recent advances in hydraulic fracturing and horizontal drilling technologies.¹ Shale gas currently comprises 34 % of gas production in the USA and an assessment of shale gas resources in 32 countries has found that shale gas could increase the world's technically recoverable gas resources by over 40%.²

Gas is stored in shales as adsorbed gas and possibly dissolved gas in oil and water, which are in equilibrium with homogeneous free gas phase in an interconnected pore structure. Quantifying each is important for understanding not only the potential of shales to store gas but also the rates and mechanisms by which gas is delivered from shale source rock to production well. The amount of homogeneous free bulk gas is relatively easy to understand (although not necessarily easy to predict) in terms of the pressure and temperature of the shale, its porosity and the fraction of porosity which is gas-filled. In contrast, the contribution of adsorbed gas to total gas in place (GIP), although estimated as being as high as 50-60% in some shales³, is still poorly constrained. Not only are there relatively few detailed studies of methane sorption on shales⁴⁻¹², but also adsorption on shale is complex because it is a heterogeneous mixture of organic and inorganic matter, which results in wide variations in surface chemistry and pore shapes/sizes. Previous studies have shown that the amount and type of both organic matter and clay minerals influence the methane sorptive capacity of shales, as does moisture content, pressure and temperature.⁴⁻⁸

Gas is generated from the organic matter of shales at temperatures in the range 370-550 K, with a gas-rich phase typically generated above *ca.* 430 K.¹³ Most of the gas is expelled from the source rock, but some is retained, partly as a result of sorption, to become a potential shale gas resource. Gas sorption capacity measurements are however restricted by the low uptake of shales and no methane sorption data have been published at temperatures above 338 K.⁸ Temperature is a main factor influencing gas sorption capacity and the heat of adsorption can be used to quantify its impact. However, extrapolations from data obtained at 300 – 338 K to geologically relevant temperatures, especially generation temperatures above *ca.* 430 K, have considerable limitations. Thus, gas sorption measurements are needed under laboratory conditions, which are as close as possible to geological conditions.

Adsorption experiments measure the surface excess amount. This is defined as the difference between the amount of gas present in the dead (unoccupied) volume of the apparatus in the event of adsorption and the amount of gas that would otherwise be present in its absence.¹⁴⁻¹⁷ The actual adsorbed layer is represented by the absolute amount and this is the quantity that is crucial for the understanding and analysis of experimental data.¹⁸ The

difference between surface excess and absolute amount adsorbed is non-negligible at pressures exceeding 1 MPa.¹⁸

Since high pressure adsorption measurements give the surface excess, methods are required for calculating the absolute isotherm from the surface excess. Firstly, high-pressure sorption characteristics, for example, the volume and density of the adsorbed phase and, consequently, amounts of absolute adsorbed gas, can be compared with petrophysical data such as porosity, mineral composition and total organic carbon content (TOC), to gain insight into possible relationships between gas stored in shale and mineralogical and geological characterization data. Secondly, to extract absolute sorption characteristics from high-pressure isotherms, models such as the Langmuir or the Dubinin-Radushkevich (DR) must be applied. The Langmuir model is based on a homogenous distribution of sorption sites and monolayer formation on an open surface, while the DR model is based on the Polanyi potential theory and applies when the adsorption process follows a pore filling mechanism. These models were originally established for subcritical adsorption. However, since both methane and carbon dioxide are in the supercritical state under geological subsurface conditions (critical temperatures: methane 190.6 K; carbon dioxide 304.1 K)¹⁹, a relative pressure is not available for use in isotherm equations. Isotherm models, which use relative pressure as a parameter, such as the DR equation, must be modified to give semi-empirical versions of the models for use with shale gas storage under supercritical conditions.

Previous studies of supercritical gas sorption have shown that gas is sorbed in micropores (pores with a diameter < 2 nm) due to increased adsorption potentials in narrow pores.⁴ In mesopores (2-50 nm), mainly monolayers of sorbed gas are formed at most, since supercritical fluids are not able to condense.²⁰ This is consistent with positive correlations observed between micropore volumes, TOC and sorbed gas capacity for shales from the Western Canada Sedimentary Basin.⁴ The volume of the adsorbed phase is thus only a fraction of the total shale pore volume, and homogeneous free gas phase occurs in larger pores, which can contribute to the total gas in shale reservoirs.

The main constituents of shale are anhydrous minerals such as quartz and calcite, hydrous aluminosilicates (clay minerals) and organic matter (kerogen). Since (a) methane is sorbed mainly by clay minerals and kerogens⁴ and (b) kerogen shares chemical characteristics with coal, models used successfully to describe adsorption on coal, such as the Langmuir isotherm model, the Toth-equation and a modified version of the Dubinin-Radushkevich model^{21,22} are rational choices for modelling shale isotherms. Both Gasparik *et al.* and Zhang *et al.* used the Langmuir equation to parameterize shale excess isotherms up to 338 K^{7,8}, obtaining good fits for the Langmuir model. Gasparik *et al.* used 2-3 fitting parameters (maximum absolute sorption uptake, the Langmuir pressure and either a fixed or variable

value for the adsorbed phase density) per isotherm, obtaining reasonable parameters for both approaches.⁸ Zhang *et al.* do not specify their fitting approach, for example the number of fitting parameters.⁷ However, they report differences in the calculated Langmuir pressure with kerogen type (Type I > Type II > Type III), concluding that higher aromaticity results in more sorption sites.

An alternative to semi-empirical models such as DR and Langmuir is the development of more sophisticated models based on density functional theory.²³ Chareonsuppanimit *et al.* measured nitrogen, methane and carbon dioxide sorption on New Albany shale samples from the Illinois Basin and successfully applied a simplified local-density (SLD) approach to model adsorption data at temperatures and pressures between 303 – 358 K and 0.3 - 27 MPa, respectively.¹⁰ However, the applicability of the SLD model was not demonstrated at temperatures above 373 K and absolute isotherms were not reported. Also, the development of such models is complex and the validity of the data has not been assessed.

The surface excess isotherm is a measurement of the difference between the amount of gas present in the dead (unoccupied) volume in a manometric apparatus in the event of adsorption and the amount of gas that would otherwise be present in its absence. The absolute isotherm represents the actual adsorbed layer and therefore, it will allow a better understanding of gas present in shale. The assessment of methane in shales further requires knowledge of the adsorption isotherms under a range of simulated geological conditions. In this paper, methane surface excess isotherms for an organic-rich dry shale have been measured at temperatures between 303 - 473 K and pressures up to 14 MPa. The isosteric enthalpy of adsorption has been determined from the van't Hoff equation and the data used to test the suitability of the Langmuir and Dubinin-Radushkevich models for predicting absolute isotherms. The results are compared with absolute isotherms calculated from surface excess using the pore volumes obtained from subcritical gas adsorption. Finally, the results are discussed in terms of variations in the amounts of sorbed gas that are likely to occur at geological pressure and temperature conditions.

4.2 Experimental

4.2.1 Materials

The Alum Shale sample was obtained from the Skelbro-2 well in Bornholm, Denmark at a depth of 9.4 m.²⁴ A representative sample was crushed and a particle size range of 0.5 - 1 mm used for adsorption measurements, while the fraction < 0.5 mm was used for grain density and total organic carbon (TOC) measurements.

Carbon dioxide and nitrogen gases were obtained from BOC with a purity of 99.995% and 99.9995%, respectively. Methane supply with a purity of 99.995% was obtained from Air Products.

4.2.2 High Pressure Adsorption

High pressure methane isotherms (300 – 473 K; up to 14 MPa) and carbon dioxide isotherms (273 K; up to 3 MPa) were measured on a Hiden Isochema Intelligent Manometric Instrument (IMI) (see Chapter 3.5.1.). 5.284 g were loaded on a manometric adsorption analyser with a reference cell of 6.591 cm³ and a sample cell of 16.534 cm³ (the same type but a different machine as described in Chapter 3.5.1). The sample was pre-dried for 24 hours at 200°C. The skeletal volume was measured by helium pycnometry with a helium dosing pressure of 5 MPa and found to be 4.3251 cm³. Equilibration relaxation kinetics were monitored using a computer algorithm based on an exponential decay model. Calculations were carried out in real time with equilibrium uptake value determined when 99.9 % of the predicted value was achieved. Equilibration times were typically < 1 h. The sample temperature was controlled to better than ± 0.1 K using an electrical heating system. Amounts adsorbed were calculated using the equation of state.^{25,26} The isotherms were obtained in series starting with the 473 K isotherm. The method for calculating the surface excess is given in Appendix B. The repeatability of the CH₄ surface excess isotherm measurements was typically ± 1% at 100 bar for a wide range of shales

4.2.3 Low Pressure Adsorption

Adsorption characteristics of methane, nitrogen and carbon dioxide on the shale were investigated using an Intelligent Gravimetric Analyzer (IGA) as described in Chapter 3.4.1. The adsorbent sample (146.32 mg for CO₂ adsorption, 138.22 mg for N₂ adsorption and 102.66 mg for CH₄ adsorption) was outgased to a constant weight (typically for ~4 hours), at < 10⁻⁶ Pa, at 110°C. The subcritical low temperature absolute isotherms were calculated using the buoyancy based on the liquid densities for the adsorbates at the adsorption temperatures. The difference between surface excess and absolute adsorption was negligible under these conditions.

4.2.4 Absolute Isotherms and Surface Excess

In high-pressure sorption experiments measurements the surface excess sorption is significantly smaller than the corresponding absolute amount adsorbed.²⁷⁻³¹ The surface excess is the difference between total gas present and homogeneous bulk gas phase in the pore volume.²⁸ The absolute isotherms diverge from the excess isotherm with increasing

pressure, due to the increasing density of the homogeneous bulk gas phase, and excess isotherms show a maximum.¹⁴ Models such as the Langmuir and the Dubinin-Radushkevich need to be used to calculate the absolute amount adsorbed. These calculations are based on estimations of (a) the adsorbed phase volume or the adsorbed phase density derived from the experimental data, and (b) the adsorption mechanism.²⁷ The adsorbed phase volume in shales under supercritical conditions is not equivalent to the total adsorption pore volume determined under subcritical conditions as sorption under supercritical conditions is limited to monolayers in larger meso and macro pores and pore filling by capillary condensation does not occur.²⁰

4.2.5 Isotherm Models

The Langmuir equation below is used as a standard model to describe vapor isotherms on shales³²:

$$n_{ab} = n_0 \frac{K(T) f}{1 + K(T) f}$$

Equation 4.1 – Langmuir Equation

where

- f fugacity
- K Langmuir parameter
- n_0 maximum amount adsorbed.

The original Dubinin-Radushkevich (DR) equation is a semi-empirical equation for subcritical vapors³³:

$$n_{ab} = n_0 \exp \left[-D \left(\ln \left(\frac{p^0}{p} \right) R T \right)^2 \right]$$

Equation 4.2 – Dubinin Radushkevich Equation

where

- n_{ab} absolute amount adsorbed
- n_0 maximum absolute amount adsorbed
- p^0 saturation pressure
- p pressure
- R ideal gas constant
- T temperature [K]

D interaction constant which is equal to $-1/(\beta E_0)^2$ where β and E_0 are adsorbate characteristic parameters.³⁴

The model is based on the Polanyi potential theory and applies when the adsorption process follows a pore filling mechanism, e.g. sorption in micropores.³⁵

Since the critical temperature for methane is 190.6 K, methane is in the supercritical state in all shale gas reservoirs. Methane does not exhibit a saturated vapour pressure under supercritical conditions. Therefore, the original DR equation, which includes p^0 in Equation 4.2, cannot be used in this case. In order to apply the DR equation to supercritical sorption processes, Sakurovs *et al.* proposed the replacement of the pressure term p^0/p with $\rho_{ads,max}/\rho_b$, where $\rho_{ads,max}$ and ρ_b are maximum adsorbed and bulk gas phase densities, respectively²²:

$$n_{ab} = n_0 \exp \left[-D \left(\ln \left(\frac{\rho_{ads,max}}{\rho_b} \right) R T \right)^2 \right]$$

Equation 4.3 - Supercritical DR Equation

In this supercritical Dubinin-Radushkevich (SDR) equation the adsorbed phase density is the density at maximum uptake ($n_{ab} = n_0$). At maximum absolute uptake the adsorbed phase density is equal to the bulk gas density. The adsorbed phase densities over the pressure range can be calculated assuming a constant adsorbed phase volume.

Both isotherm models are based on the absolute amount adsorbed and modifications are necessary in order to apply them to excess isotherms. Two options have been used for the modification, using either a) the adsorbed phase volume:

$$n_{ex} = n_{ab} - \rho_b V_{ads}$$

Equation 4.4 – Adsorbed Phase Volume

or b) the adsorbed phase density:

$$n_{ex} = n_{ab} \left(1 - \frac{\rho_b}{\rho_{ads}} \right)$$

Equation 4.5 – Adsorbed Phase Density

The problem is that V_{ads} is unknown. In the case of crystalline porous materials, X-ray or neutron diffraction can be used to determine the pore volume, V_{pore} . It is assumed that

$V_{ads} = V_{pore}$, and this approach has been used in the recent literature on hydrogen storage by metal organic framework materials.³⁶ However, the validity of this assumption is questionable. The surface excess n_{ex} reaches a peak at elevated pressures and then decreases as the $V_{ads}\rho_b$ term becomes more significant. The structure of complex heterogeneous materials such as shales cannot be determined by crystallographic methods. The only methods currently available to determine pore volume and pore size distributions in complex materials are based on subcritical gas adsorption and these have their own limitations. Therefore, the use of the assumption $V_{ads} = V_{pore}$ is more problematic for these heterogeneous materials. However, it provides a method of estimating the limits for the absolute isotherms.

4.3 Results

4.3.1 Shale Characterization

The mineralogy of the sample is dominated by illite-smectite and quartz, with significant muscovite (see Table 4.1). Although illite and mixed-layer illite-smectite have been reported separately, the illite-smectite is illitic in composition and these minerals can be effectively considered as one group. The grain density of the shale is 2.592 g cm^{-3} and the total organic carbon content is $6.35 \pm 0.01 \%$ by weight. An equivalent vitrinite reflectance of $R_0 = 2.26\%$ was determined by Schovsbo *et al.*³⁷

Table 4.1: Mineralogical Composition (%) of Alum Shale #1 measured by X-ray powder diffraction.

Quartz	Plagioclase	K-Feldspar	Calcite	Siderite	Pyrite
44.4	1.0	1.3	0.5	0.4	1.4
Marcasite	Muscovite	Illite	Illite/Smectite	Kaolinite	Chlorite
0.8	9.5	5.9	29.9	0.7	4.2

4.3.2 Pore Characterization by Low Pressure Adsorption

Micropore Volume

The N_2 (78 K), CH_4 (112 K) and CO_2 (195 K) absolute isotherms are compared in Figure 4.1. The CH_4 (112 K), CH_4 (173 K) and CO_2 (273 K) surface excess isotherms are shown in Figure 4.2.

Details of total and micropore volumes are given in Table 4.2. The CO_2 and CH_4 isotherms obtained by both gravimetric and manometric methods are similar on a relative pressure basis. The CO_2 low-pressure gravimetric data (0.1 MPa) and high pressure manometric isotherm data (3 MPa) obtained at 273 K agree in the overlap region and this

validates the measurements obtained. It is evident that the groups of isotherms shown in both figures are very similar and are Type I in the IUPAC classification scheme.³⁸ The CH₄ subcritical absolute isotherm is a useful comparison for the supercritical isotherms obtained from various models described later because it represents an upper limit for adsorption. The CH₄ subcritical isotherms are difficult to measure because of the unavailability of suitable cryogenic liquids in the temperature range between the boiling point (112 K) and the critical temperature (190 K). The similarity of the CH₄, CO₂ and N₂ isotherms indicates that the use of CO₂ and N₂ adsorption for characterising pore volumes as described later is justified.

The subcritical DR theory (Equation 4.2) was applied to the 273 K isotherms to calculate the DR micropore volume. The DR micropore volume calculated from the low-pressure isotherms (up to 0.1 MPa) accounts for ultramicropores (pore width < 0.7 nm)³⁹ and was $0.0129 \pm 0.0008 \text{ cm}^3 \text{ g}^{-3}$. The DR micropore volume from the high-pressure isotherm (up to 3 MPa at 273 K) is linear indicating a Gaussian pore size distribution. The DR micropore volume was $0.0127 \pm 0.0003 \text{ (cm}^3 \text{ g}^{-1}\text{)}$, suggesting that there is only a small amount of porosity in the range of 0.7 to 2 nm diameter. This is in agreement with the pore size distribution (see Figure 4.3).

The DR micropore volume is larger than micropore volumes of Devonian-Mississippian (D-M) shales ($0.003 - 0.012 \text{ cm}^3 \text{ g}^{-1}$) of the same maturity ($R_0 = 1.6 - 2.5\%$) measured by Ross and Bustin.⁴ This is possibly due to the higher TOC of the Alum Shale (6.35% by weight) compared to the D-M shales (0.2- 4.9% by weight), since DR micropore volumes appear to increase with TOC in thermally-mature shales.⁴

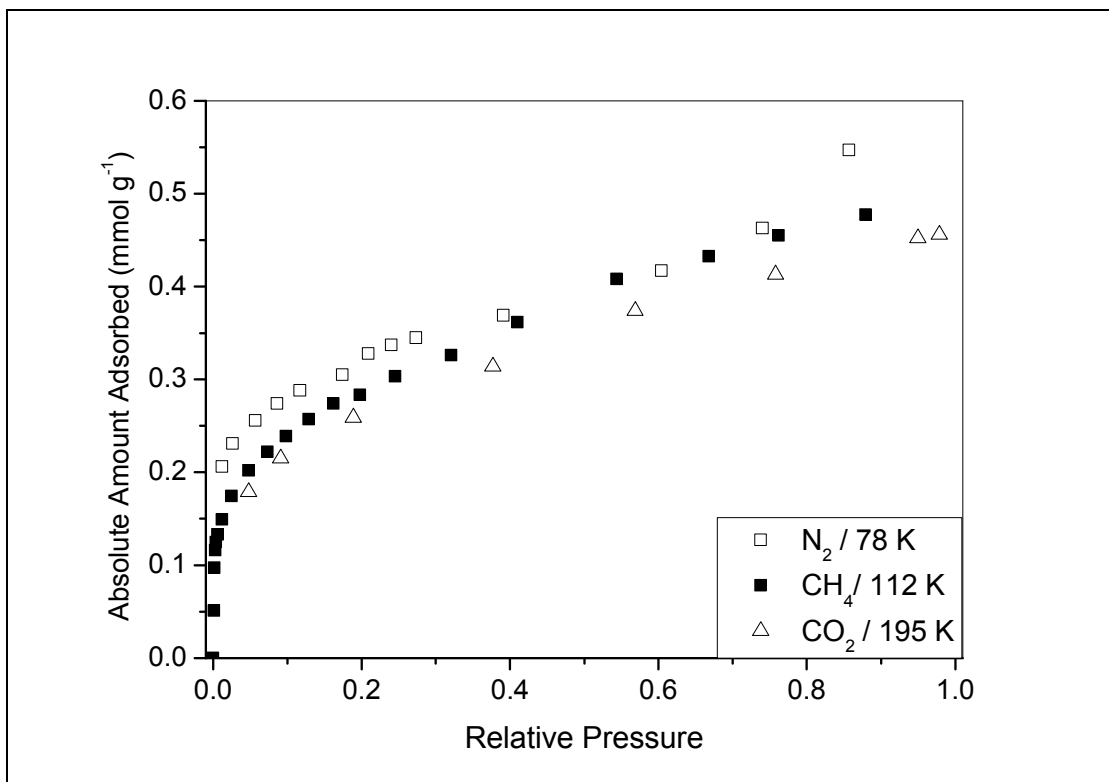


Figure 4.1: Subcritical Isotherms for Alum Shale #1: N₂ (78 K), CO₂ (195 K) and CH₄ (112 K) absolute isotherms on a relative pressure basis.

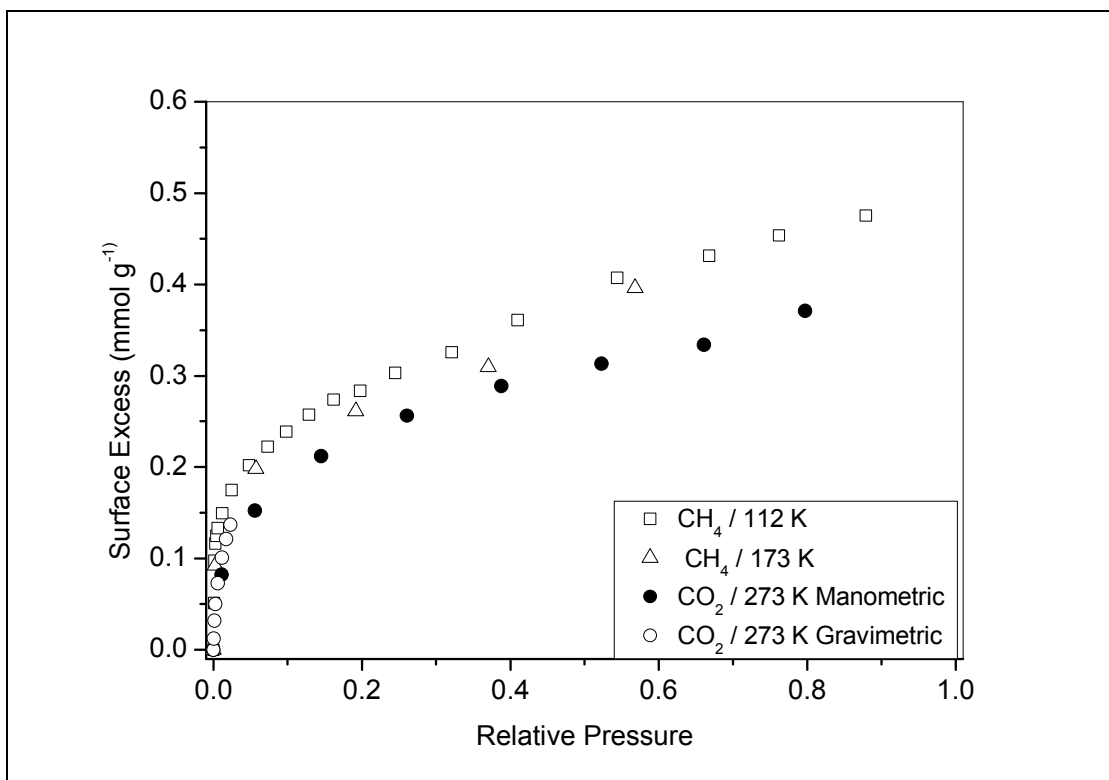


Figure 4.2: Subcritical Isotherms for Alum Shale #1: Surface excess CH₄ (112 K), CH₄ (173 K) and CO₂ (273 K).

Total Sorption Pore Volumes

The pore volume obtained by converting the maximum uptake at $p/p_0 \sim 1$ is the total sorption pore volume under subcritical conditions. The total pore volumes calculated from N_2 isotherm at 78 K and CH_4 at 112 K agree within a few percent (see Table 4.2), in accordance with the Gurvitch Rule.⁴⁰ The CO_2 isotherms at 195 K and 273 K give slightly lower pore volumes. The similarity between the CO_2 isotherms at 195 and 273 K and N_2 isotherms at 78 K shows the absence of significant activated diffusion effects at higher temperatures (see Figure 4.1). The small upward curvature in the N_2 (78 K) isotherm above $p/p^0 = 0.7$ as shown in Figure 4.1 is probably due to some capillary condensation in mesopores. Details of the calculations can be found in the Appendix B. The total sorption pore volume ($0.017 \text{ cm}^3 \text{ g}^{-1}$) is within the range $0.002 - 0.05 \text{ cm}^3 \text{ g}^{-1}$ reported for North American shales.⁴¹

BET Surface Area

The BET surface area calculated from the linear region ($p/p^0 : 0.05 - 0.35$) of the N_2 (78 K) isotherm was $22.8 \pm 1.6 \text{ m}^2 \text{ g}^{-1}$. Previous studies have shown that North American shales have BET surface areas in the range $2 - 17 \text{ m}^2 \text{ g}^{-1}$ ⁴¹ and $1 - 9 \text{ m}^2 \text{ g}^{-1}$.⁴

Table 4.2: Ultrapore-, micropore- and pore volumes determined by low pressure adsorption.

	Method	Gas	Temp. [K]	Specific Pore Volume [$\text{cm}^3 \text{ g}^{-3}$]
Ultramicropore Vol. (pore width > 0.7 nm)	DR (up to 0.1 MPa)	CO_2	273	0.0129 ± 0.0008
Micropore Vol. (pore width > 2nm)	DR (up to 3 MPa)	CO_2	273	0.0127 ± 0.0003
Pore Volume	$p/p^0 \sim 1$	N_2	78	0.0176 ± 0.0020
	$p/p^0 \sim 1$	CO_2	195	0.0168 ± 0.0004
	$p/p^0 \sim 1$	CO_2	273	0.0161 ± 0.0004
	$p/p^0 = 0.879$	CH_4	112	0.0180

Micropore Size Distribution

A nonlocal density functional theory (NLDFT) equilibrium model assuming slit pores⁴² was used to calculate the pore size distribution (PSD) from CO_2 adsorption data at 273 K (see Figure 4.3). The CO_2 isotherm was chosen because it was closest to the temperature range of

the supercritical CH₄ isotherms. The pore size distribution shows an abundance of pores below ~0.9 nm diameter with a cumulative pore volume of 0.0095 cm³ g⁻¹. This shows that ultramicroporosity below ~ 0.9 nm is a major component of the porosity for gas adsorption. The NDLFT model cannot correctly account for pores with a pore width of around 1 and 2 nm and NDLFT PSDs typically show gaps in these regions.^{43,44}

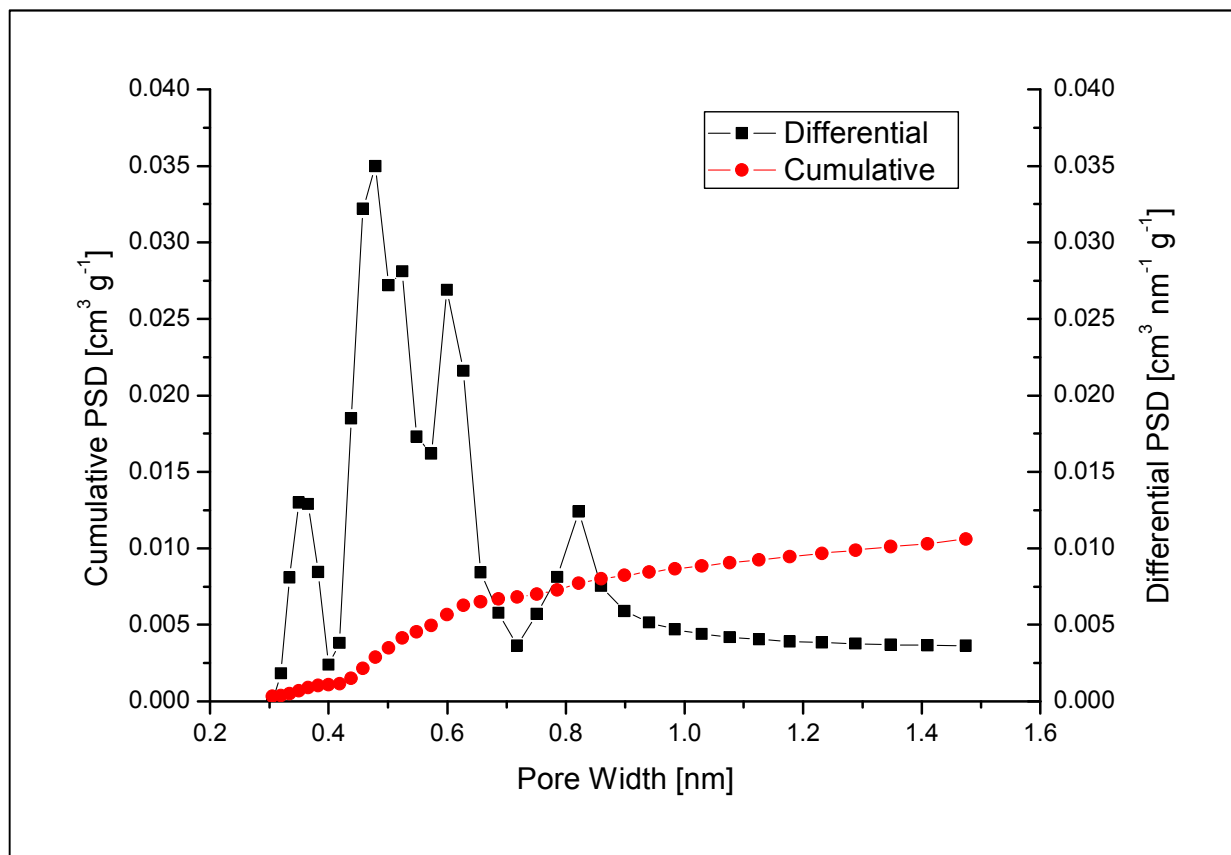


Figure 4.3: Micropore size distribution of Alum Shale #1. The pore size distribution was determined by fitting the CO₂ isotherms at 273 K to a slit pore nonlocal density functional theory equilibrium model. Cumulative pore volume (V) and differential pore volume (dV(w)) are shown.

4.3.3 Methane Isotherms

Low Temperature CH₄ Absolute and Surface Excess Isotherm

The CH₄ isotherm for the shale at 112 K is shown in Figure 4.1 and Figure 4.2. This isotherm represents an upper limit for supercritical adsorption. The absolute uptake conversion factor from the surface excess at 1 bar for the 112 K isotherm is ~1.004. The methane surface excess at 173 K is slightly lower than the 112 K isotherm (see Figure 4.2) and this trend is the same as observed for supercritical methane adsorption discussed later. It is evident that the CO₂ (195 K) isotherm is similar to the CH₄ (112 K) isotherm and the N₂ (78 K) isotherm is slightly higher (see Figure 4.1). The total adsorption pore volumes obtained from CH₄ (112 K), N₂ (78 K) and CO₂ (195 K) were similar (see Table 4.2).

High Pressure Surface Excess Isotherms

Figure 4.4 shows methane shale surface excess isotherms measured over the temperature range 300 – 473 K. The methane uptakes are low compared to coal^{21,45-47}, but similar to previous studies on shale.^{4,5,7-10,48} The methane isotherms follow the trend of decreasing amounts adsorbed with increasing temperature, as expected for physisorption. The maximum uptakes in the surface excess isotherms shift to lower pressure with increasing temperature. The maximum CH₄ surface excess has a good linear relationship with 1/Temperature with $R^2 = 0.989$ for the supercritical methane adsorption (300-473 K) as shown in Figure 4.5. This has potential for estimating maximum surface excess values for other temperatures. The supercritical surface excess CH₄ isobars also have good linear relationships for the surface excess with 1/Temperature over the temperature range 300-473 K and pressure range 5-13 MPa ($R^2 = 0.989 - 0.997$), as shown in Figure 4.6. This is consistent with the correlation for maximum surface excess with 1/T.

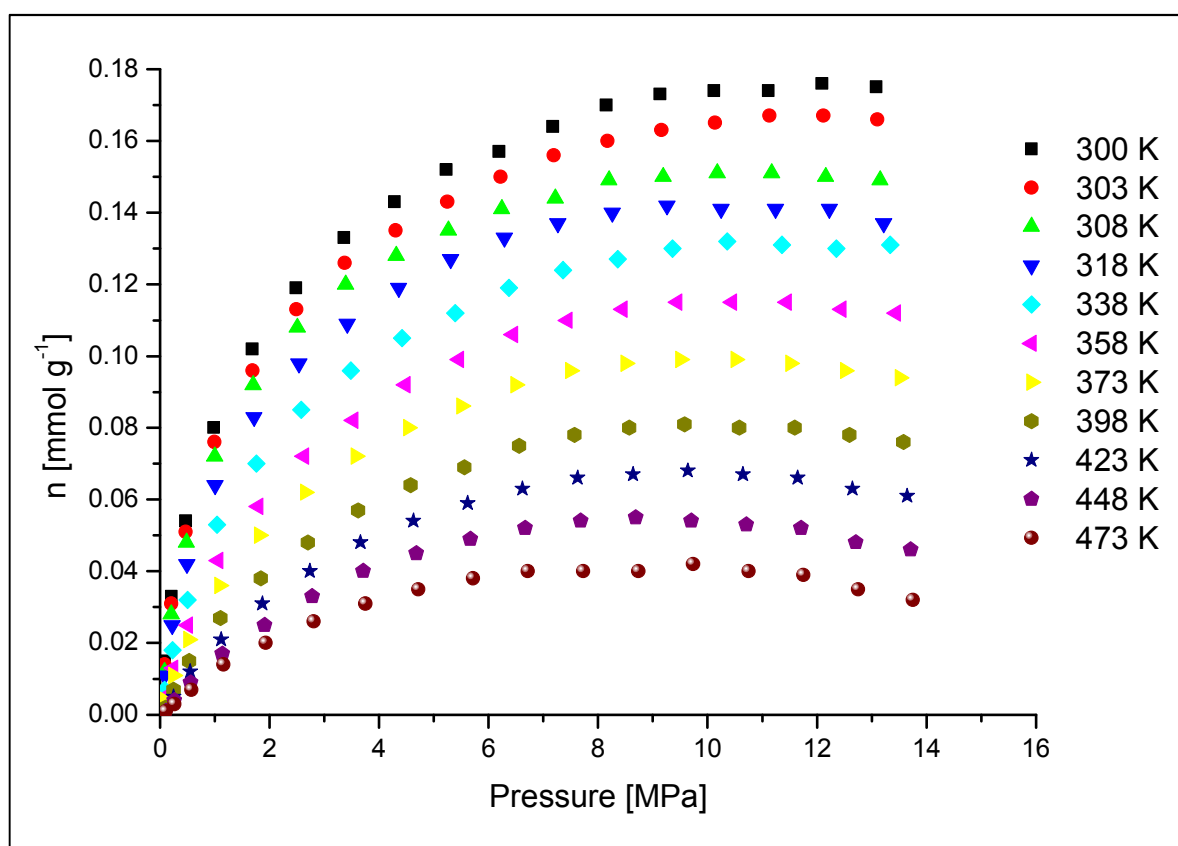


Figure 4.4: Methane surface excess adsorption for Alum Shale #1: Isotherms for temperature range (300 – 473 K).

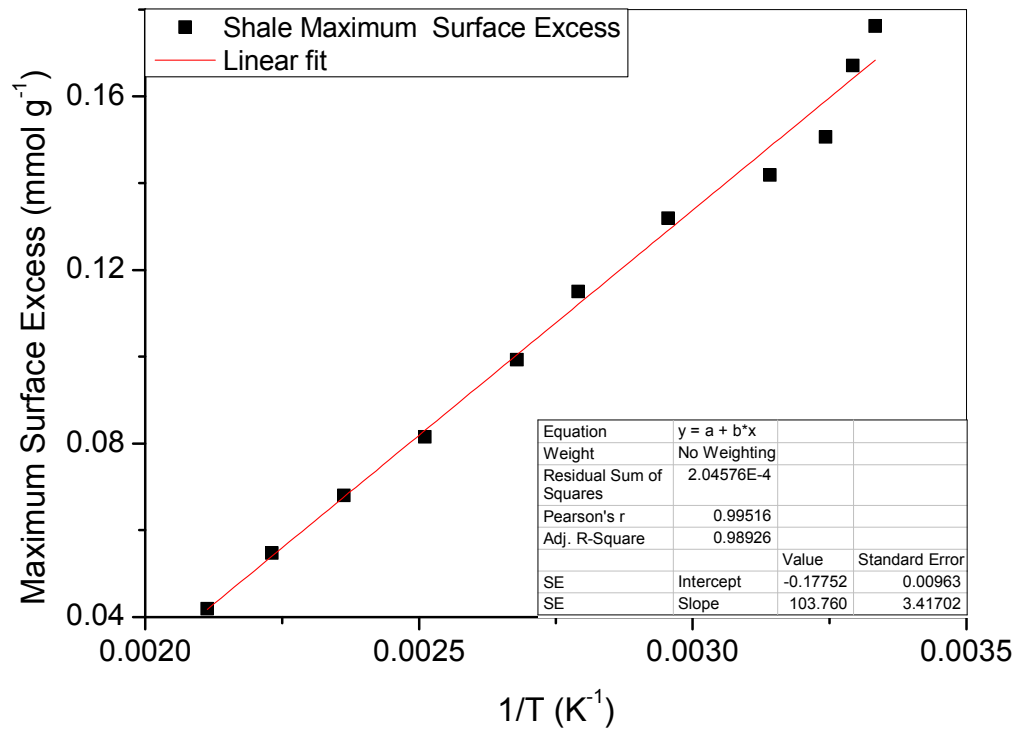


Figure 4.5: Methane surface excess adsorption for Alum Shale #1: The variation of maximum surface excess with 1/Temperature (K^{-1}).

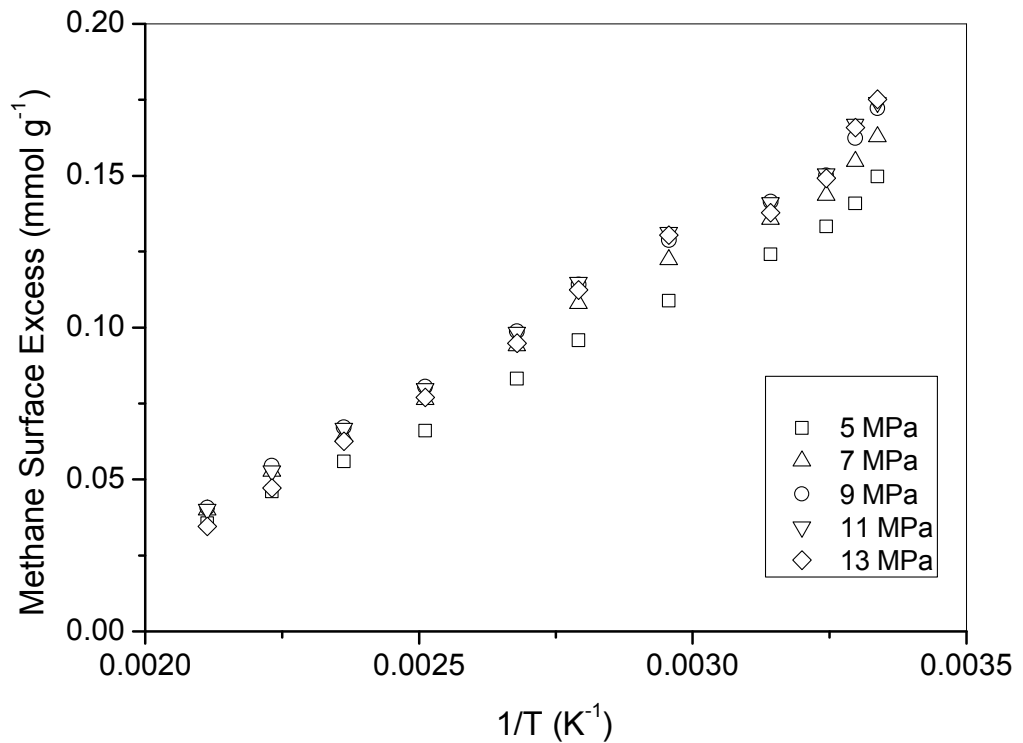


Figure 4.6: Methane surface excess adsorption for Alum Shale #1: The variation of surface excess with 1/Temperature (K^{-1}) for isobars at 5, 7, 9, 11 and 13 MPa.

4.3.4 Modelling of Isotherms

Model Variants

The DR and Langmuir equations are used to parameterize the high-pressure methane isotherm on shale. The maximum absolute uptake and the affinity constants (D and K , respectively) are used as fitting parameters. It is questionable whether the adsorbed phase density should be used as a fitting parameter or should be estimated, although good results for both options have been achieved in previous studies.⁸ Ambrose *et al*⁴⁹ determined an adsorbed phase methane density on shale of 0.37 g cm^{-3} at 353 - 403 K by molecular simulation. This value is slightly lower than the density of liquid CH_4 (0.4251 g cm^{-3} at -161.49°C and 101.3 KPa).⁵⁰ As far as we are aware no information is available on the density of liquid CH_4 as a function of temperature. However, the information available for other liquefied gases indicates that liquid density decreases with increasing temperature.⁵⁰ Therefore, since the temperature range used in this study is much wider (300-473 K), the variation in adsorbate density is also a possibility. However, overfitting with too many parameters will result in a poorly constrained model and give poor results. Here, we have examined the models both with and without the adsorbed phase density (constant and variable with temperature) as a fitting parameter, in order to determine the best option. Furthermore, the Langmuir equation can either be transferred by Equation 4.4 or Equation 4.5 into an excess isotherm equation. Here, both options have been used to fit the experimental data, so that a total of 9 variants are tested overall (see Table 4.3). Details of the fitting for the variants which provided the poorer descriptions of the data are presented in Appendix B.

For variants 2 and 5 the adsorbed phase density of 0.37 g cm^{-3} published by Ambrose *et al*⁴⁹ was used. For variant 8 it was assumed that the volume of the adsorbed phase is equal to the micropore volume measured by CO_2 adsorption. This option was chosen because previous studies have found that sorption under supercritical conditions fills micropores and, at most, builds up monolayers in larger pores.²⁰

Table 4.3: Variants of the SDR and Langmuir isotherm models tested. Column “Version” refers to the option of constant adsorbed phase density or adsorbed phase volume discussed in the experimental section (see Equation 4.4 and Equation 4.5).

Variant	Model	Version	Fitting parameters	No of fitting Parameter
1	DR	b	$n_o(T), D, \rho_{ads}(T)$	21
2	DR	b	$n_o(T), D$	11
3	DR	b	$n_o(T), D, \rho_{ads}$	12
4	Langmuir	b	$n_o(T), K(T), \rho_{ads}(T)$	30
5	Langmuir	b	$n_o(T), K(T)$	20
6	Langmuir	b	$n_o(T), K(T), \rho_{ads}$	21
7	Langmuir	a	$n_o(T), K(T), V_{ads}(T)$	30
8	Langmuir	a	$n_o(T), K(T), V_{ads}$	21
9	Langmuir	a	$n_o(T), K(T)$	20

Table 4.4: Fitting parameters for the optimal DR (Variant 1) and the optimal Langmuir fit (Variant 8). The table shows all parameter calculated by the models for pressure < 14 MPa and temperatures in the range 300 – 448 K.

Temp [K]	Supercritical Dubinin-Radushkevich			Langmuir		
	n_o [mmol g ⁻¹]	ρ_{ads} [kg m ⁻³]	D [mol ² kJ ⁻²]	n_o [mmol g ⁻¹]	K [MPa ⁻¹]	V_{ads} [cm ³ g ⁻¹]
300	0.252	574	0.0093	0.213	0.606	0.0015
303	0.240	548		0.202	0.596	
308	0.219	458		0.182	0.665	
318	0.208	429		0.174	0.595	
338	0.199	422		0.169	0.435	
358	0.178	357		0.151	0.384	
373	0.155	299		0.130	0.384	
398	0.129	258		0.110	0.327	
423	0.110	206		0.092	0.323	
448	0.090	159		0.072	0.353	

Supercritical DR Equation

The fitting for the SDR model for variant 1 is shown in Figure 4.7 with calculated parameters in Table 4.4 and the other variants are given in Appendix B. Model variants 2 and 3 produce good fits for isotherms in the region of 308–338 K but fail to describe all isotherms outside this temperature range. The overall best fit was obtained using the SDR equation with maximum uptake and maximum adsorbed phase density as temperature-variant parameters (variant 1). The maximum absolute uptake and the calculated maximum adsorbed phase density decrease with increasing temperature (see Figure 4.7). Both n_0 and adsorbed phase density have linear correlations with $1/T$ (K^{-1}). The maximum surface excess decreases with increasing temperature and has a linear correlation with $1/T$ (K^{-1}). The trends for n_0 and maximum surface excess are probably related to the density of the adsorbed phase and extent of filling of the micropores decreasing with increasing temperature. The pore size distribution of the shale shows that the pores are mainly < 0.9 nm. Generally, larger pores have lower excess density compared to smaller pores. The change in adsorbed phase density is consistent with molecular simulations of CH_4 on porous carbon systems such as coal and the kerogen organic matrix of gas shales, which show that the adsorbed phase density to pressure response is negligible when the pore width is larger than 1.2 nm.⁵¹ However, at high pressure, the adsorption capacities of 0.6 nm pores decrease to below those of the wider pores.

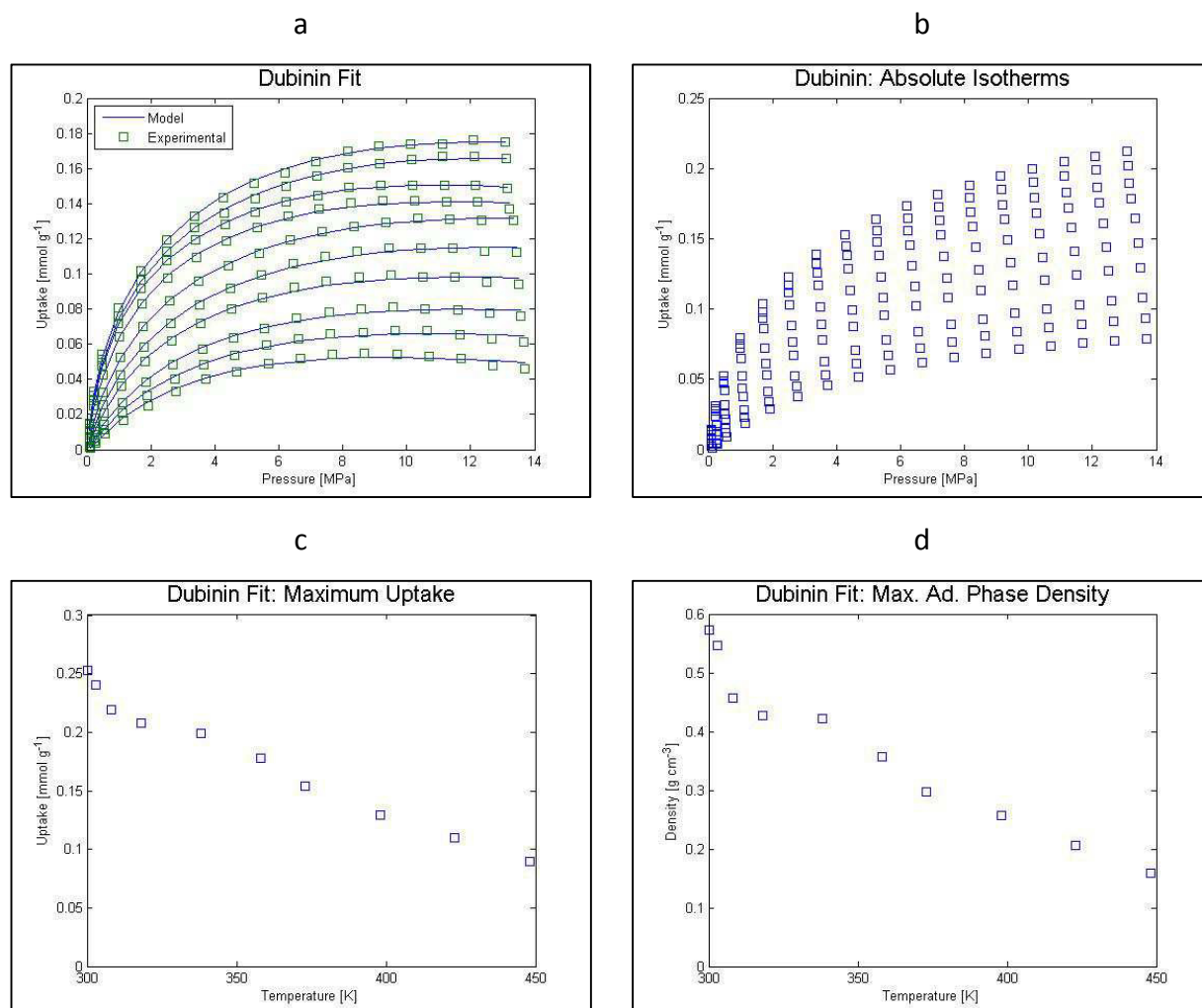


Figure 4.7: Optimal Supercritical Dubinin-Radushkevich (SDR) (Variant 1) fit a) SDR fit to the excess data (squares); b) Absolute Isotherms calculated from the fit; c) Maximum uptake calculated from the fit; d) The adsorbed phase densities modelled from the SDR fit.

Langmuir Equation

The best Langmuir model (Variant 8) for the experimental data is shown in Figure 4.8 and the parameters are given in Table 4.4. The graphs and parameters for the other Langmuir model variants are given in Appendix B. Other Langmuir model variants produce good fits to the experimental data with 30 parameters (Variants 4 and 7). However, the calculated maximum uptake n_0 increases with increasing temperature, indicating that the application of 30 fitting parameters overfits the data and that no physically meaningful parameters are calculated. Variant 5 fits the isotherms at temperatures of 318 - 373 K well, but fails to fit isotherms at low (300 - 308 K) and high temperatures (398 - 448 K). Variant 6 fails to produce good fits at high temperatures (358 - 448 K), whilst variant 9 describes isotherms in the high temperature range (358 - 448 K) well, but fails to model isotherms below 358 K. Compared to the other Langmuir variants, variant 8 produces the best results in terms of both fitting the

isotherms and the reasonability of both the absolute uptake and the Langmuir parameter K (both parameters decrease with increasing temperature) (see Figure 4.8).

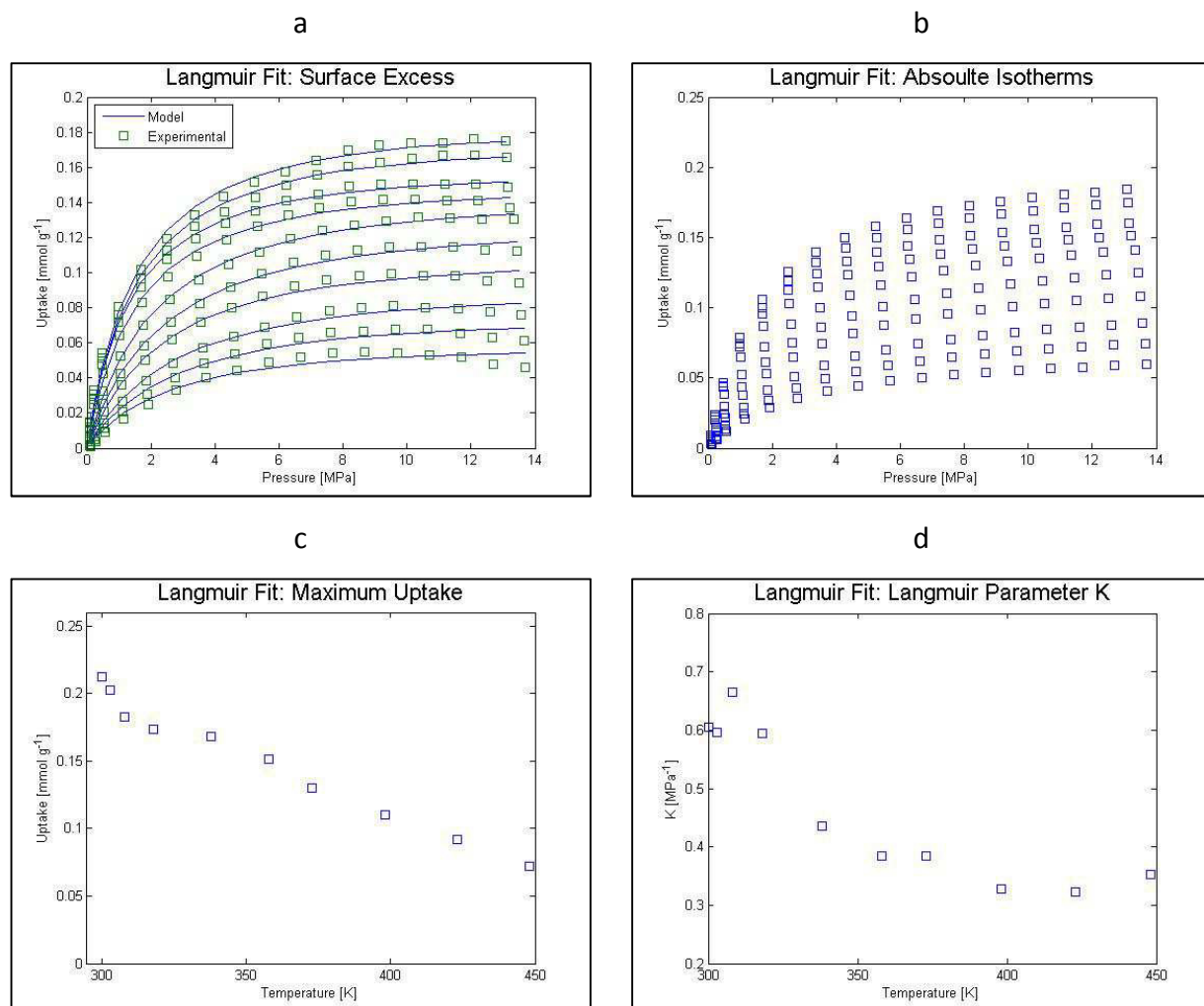


Figure 4.8: Optimal Langmuir fit (Variant 8). a) Langmuir fit to the excess data (squares). b) Absolute Isotherms calculated from the fit. c) Maximum uptake calculated from the fit. d) Langmuir parameter K calculated from the fit.

Adsorbed Phase Densities

The extent of filling of the microporosity may vary with temperature. By assuming a constant adsorbed phase volume over the whole pressure range, the adsorbed phase densities are calculated for Fitting Variant 1 (SDR equation, best fit) (see Figure 4.9). Except for the 300 and 303 K isotherms, the densities are all below the liquid density of methane at boiling point.⁵⁰ The liquid density at low temperature represents a reasonable limit for the adsorbed phase density for high pressure isotherms in the temperature range 300 – 473 K, due to the incompressibility of most liquids.

The adsorbed phase volume calculated (0.0015 cm³ g⁻¹) by the Langmuir equation (Variant 8, best fit) is much less than the micropore volume measured by CO₂ adsorption at 273 K (0.0127 cm³ g⁻¹). The adsorbed phase densities calculated by using Equation 4.4 and Equation

4.5 are almost entirely above the liquid density of methane at boiling point and so the values can be regarded as physically unreasonable.

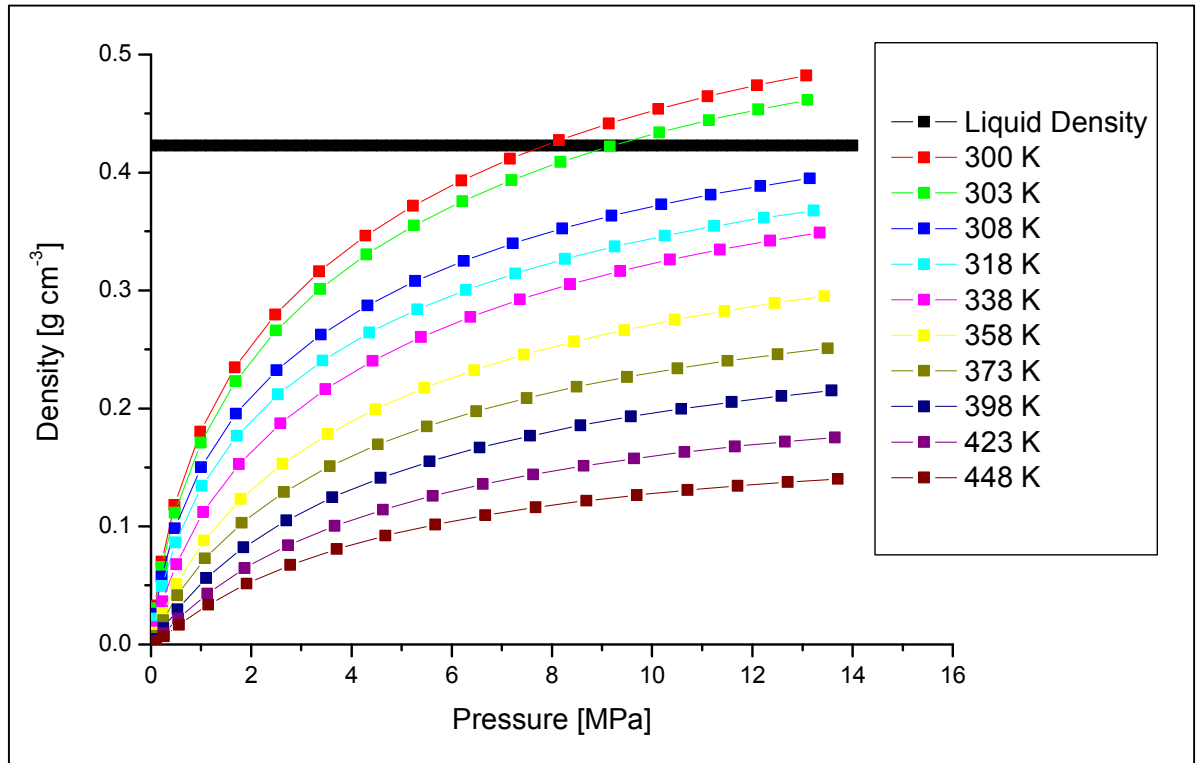


Figure 4.9: Adsorbed phase densities calculated from the SDR model and equation 7. All the adsorbed phase densities are below the liquid density of methane at boiling point (0.425 g cm^{-3}) except the densities at 300 K and 303 K.

4.3.5 Isosteric Enthalpy of Adsorption

The isosteric enthalpy of adsorption of methane adsorption is derived from the van't Hoff equation:

$$\left(\frac{\partial \ln P}{\partial T}\right)_n = \frac{\Delta H}{R T^2}$$

Equation 4.6 – van't Hoff Isochore

where

P pressure in kPa

T temperature in K

n absolute sorption uptake at constant surface coverage

R ideal gas constant in $\text{kJ mol}^{-1} \text{ K}$ and

ΔH enthalpy of adsorption in kJ mol^{-1} .

Isosteric enthalpies are usually obtained from absolute adsorption isotherms, but thermodynamic parameters can be obtained from excess isotherms.^{14,52} An adsorption

isostere was obtained from the excess isotherms at an uptake of $0.025 \text{ mmol g}^{-1}$, where the difference between excess and absolute sorption is negligible. The isosteric heat of adsorption (Q_{st}) calculated from the slope of the isostere is $19.2 \pm 0.1 \text{ kJ mol}^{-1}$ (see Figure 4.10). Adsorption isosteres at uptakes of 0.05 mmol g^{-1} and 0.1 mmol g^{-1} were also calculated from absolute isotherms obtained from the DR model (see Figure 4.7; variant 1, best fit), giving isosteric heats of adsorption of 17.2 kJ mol^{-1} and $19.8 \pm 0.1 \text{ kJ mol}^{-1}$, respectively.

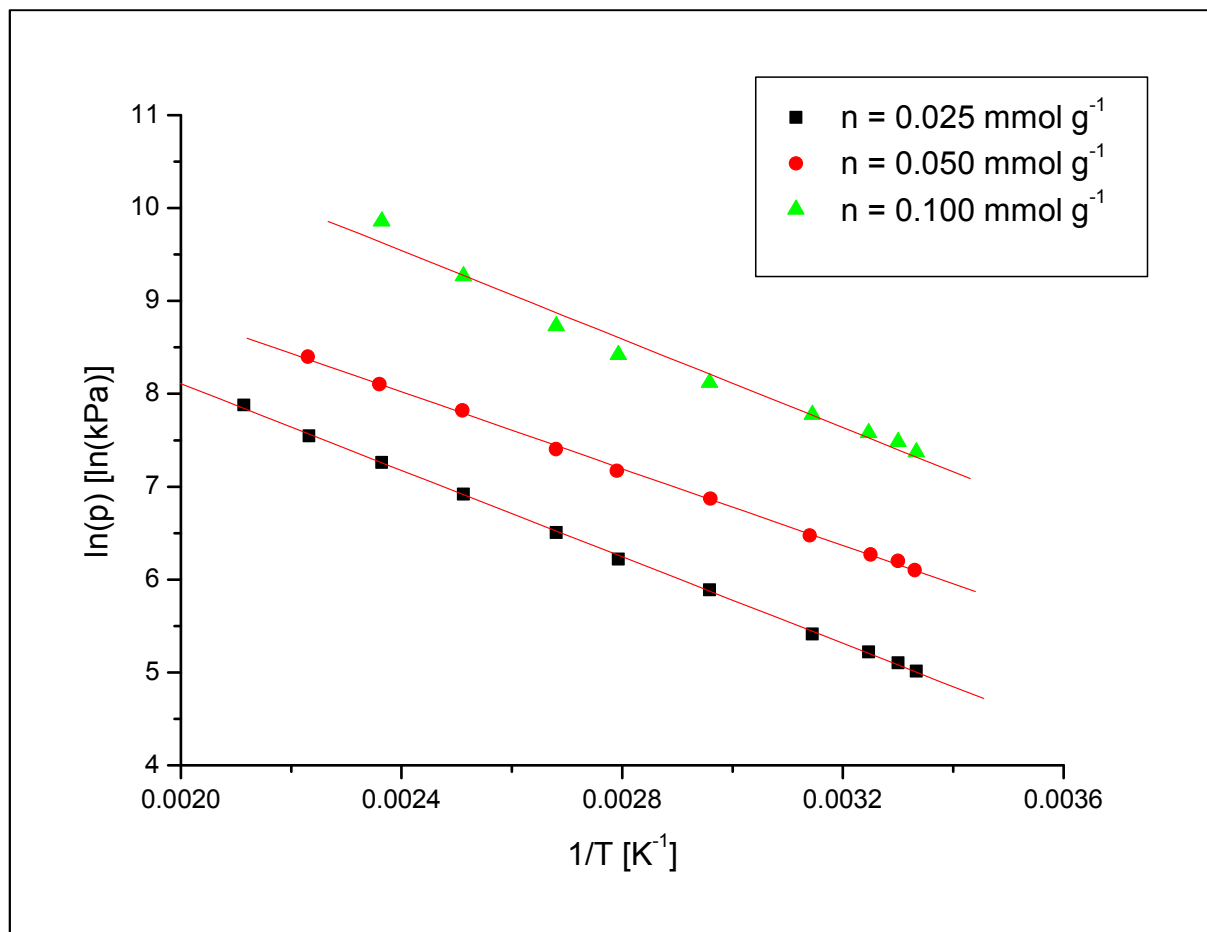


Figure 4.10: Adsorption isosteres for methane adsorption on Alum Shale #1. The adsorption isostere at $0.025 \text{ mmol g}^{-1}$ was calculated from linear regression using the excess isotherms as the difference between excess and absolute uptake was negligible. The other two isosteres are calculated from the absolute isotherms.

4.4 Discussion

As far as storage and exploitation of CH_4 in shales are concerned, the absolute adsorption isotherm is in equilibrium with the homogenous free gas phase in larger macropores, which contribute only marginally to the sorption capacity and function as transport pores for sorption and desorption. These larger macropores may be quantified by microscopy and mercury porosimetry, although these methods have their own limitations. CH_4 adsorption mainly occurs in the micropores and to a lesser extent in the mesopores in the matrix porosity and this describes the total amount of sorbed gas available. The absolute

adsorption isotherm is useful for the understanding of gas sorption on shale. The surface excess is the experimentally measured parameter and is the amount adsorbed, which exceeds gas phase density. The amount of the sorbed phase layer is described by the absolute isotherm. Models can calculate the absolute isotherm from the surface excess and the validation of these models is necessary using experimental data measured under the wide range conditions of pressure and temperature appropriate for geological conditions. The porous structure characterization parameters (total sorption pore volume, micropore volume, surface area etc) can be measured under subcritical conditions to provide data for calculating adsorbed phase density, etc. However, the pore size, which can be filled under supercritical adsorption conditions, and adsorbed phase densities, may decrease with increasing temperature. The correlations between maximum surface excess with $1/T$ (Figure 4.5) and surface excess at specific pressures with $1/T(K)$ (Figure 4.6) are consistent with decreases in adsorbed phase density and pore size that can be filled with CH_4 with increasing temperature.

The DR ultramicropore volume from CO_2 was $0.0129 \text{ cm}^3 \text{ g}^{-1}$ based on density, $\rho_{CO_2} = 1.032 \text{ g cm}^{-3}$ (see Table 4.2). The CO_2 , N_2 and CH_4 total pore volumes obtained under subcritical conditions are similar and about 30% higher than the DR micropore volume. This indicates that significant sorption occurs in larger pores under subcritical conditions. The pore volumes can be used to calculate absolute isotherms by using the homogeneous bulk gas phase in the total gas adsorption pore volume plus the surface excess sorption measured experimentally (see section 2.5.3). Calculation of the absolute isotherm using the subcritical total pore volume represents an upper limit for the isotherm. Comparison of absolute isotherms at (a) 318 K and (b) 448 K using the SDR and Langmuir models and the absolute isotherms based on surface excess and assuming adsorption takes place in either the carbon dioxide DR micropore volume ($0.013 \text{ cm}^3 \text{ g}^{-1}$), the NLDFT micropore volume ($0.0095 \text{ cm}^3 \text{ g}^{-1}$) or the subcritical total pore volume ($0.0161 \text{ cm}^3 \text{ g}^{-1}$), provides an insight into a range of values that are likely for the absolute isotherm (see Figure 4.11). Comparisons for other isotherm temperatures are given in Appendix B. The absolute isotherm calculated from the total pore volume obtained from subcritical gas adsorption gives a maximum for the absolute isotherm. The Langmuir model is very similar to the surface excess up to 10 MPa and is significantly lower than predictions by the other methods. The similarity between the supercritical DR model for (a) the CH_4 absolute and (b) the absolute isotherms calculated from surface excess and the CO_2 micropore volume does not necessarily validate the supercritical DR absolute isotherm model, but suggests that it is better than the Langmuir model for this particular shale. The supercritical DR model not only gives good agreement over the entire temperature range, but also reasonable values for adsorbate density, with the exception of adsorbed phase densities at 300 and 303 K, which exceed the liquid density of CH_4 (0.425 g cm^{-3} at 112 K).

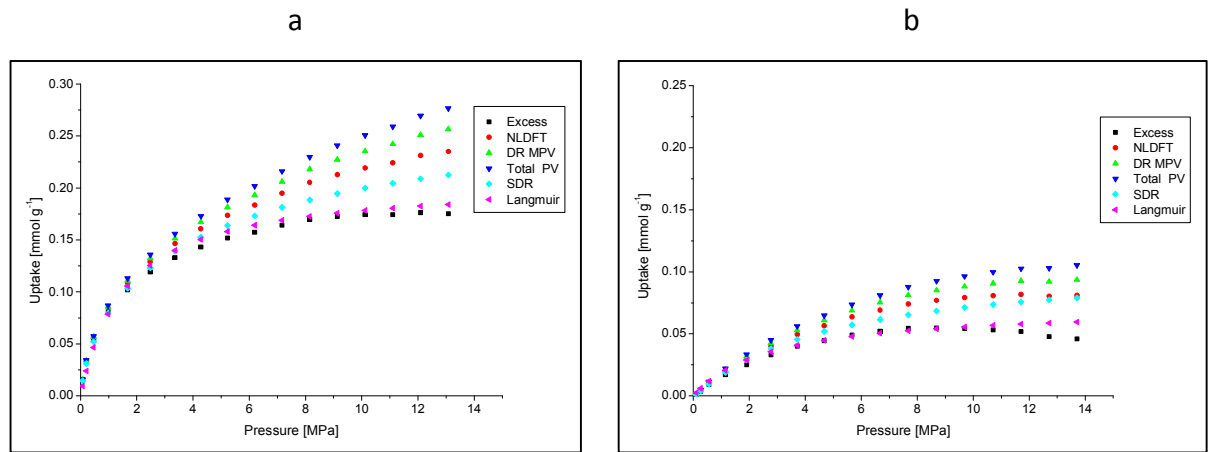


Figure 4.11: Methane excess isotherm and absolute isotherms based on different models at a) 318 K and b) 448 K. The DR and Langmuir absolute isotherms are based on the parameters obtained in this study. The NLDFT absolute isotherms is the combination of the excess isotherm and the compressed gas in the pore volume obtained from the NLDFT model ($0.0095 \text{ cm}^3 \text{ g}^{-1}$). Accordingly, the micropore and the total pore volume are the excess isotherm plus the compressed gas in the micropore volume ($0.0129 \text{ cm}^3 \text{ g}^{-1}$) and in the total sorption pore volume ($0.0161 \text{ cm}^3 \text{ g}^{-1}$).

The isosteric enthalpy of adsorption of $\sim 19 \text{ kJ mol}^{-1}$ is in agreement with values measured on a Barnett Shale from the gas window ($R_0 = 2.01\%$, $Q_{\text{st}} = 18.4 \text{ kJ mol}^{-1}$) by Zhang *et al.*⁷. Pre-gas window shales from the same study have lower isosteric enthalpies of adsorption ($Q_{\text{st}} = 7.3 - 15.3 \text{ kJ mol}^{-1}$). Moreover, the isosteric enthalpy is within the range of values measured on activated carbon ($Q_{\text{st}} = 9 - 20 \text{ kJ mol}^{-1}$)⁵³⁻⁵⁵ and coal ($Q_{\text{st}} = 10 - 22 \text{ kJ mol}^{-1}$).^{56,57} This implies that the strength of interaction of methane with the pore walls of thermally-mature shale is similar to other materials and the reason for low uptake of methane on the shale is the low amounts of micro- and mesoporosity.

Using assumed pressure and temperature gradients, the experimental data have been used to estimate excess and absolute sorbed gas capacities versus depth (see Figure 4.12). Sorption capacity naturally decreases with increasing depth/temperature. At temperatures above *ca.* $160 \text{ }^\circ\text{C}$ (433 K), at which petroleum source rocks are generating gas with little liquid, the absolute amount of adsorbed methane is less than 0.1 mmol g^{-1} , equivalent to around 71 scf t^{-1} . If gas was retained in the shale by sorption alone, this would represent an upper limit to the potential resource; indeed, a lower value may be more realistic since our experiments were performed on dry shale and some of the sorbed gas will be associated with clay minerals.⁴ It is plausible that in the subsurface, the clay matrix of shale is water-filled such that only the organic phases in the shale will adsorb gas; this requires further study. Field data suggest that some shales store gas in excess of 100 scf t^{-1} ⁵⁸, suggesting that the adsorbed gas may be smaller than the homogeneous free bulk gas phase stored in meso- and macroporosity within organic matter.⁵⁹ Since commercial gas shales are often located at 1-2

km burial depth (pressures of 10-20 MPa, temperatures of 40-80 °C), their capacity to adsorb gas will increase during exhumation, such that the fraction of adsorbed gas will increase at the expense of the homogeneous gas phase.

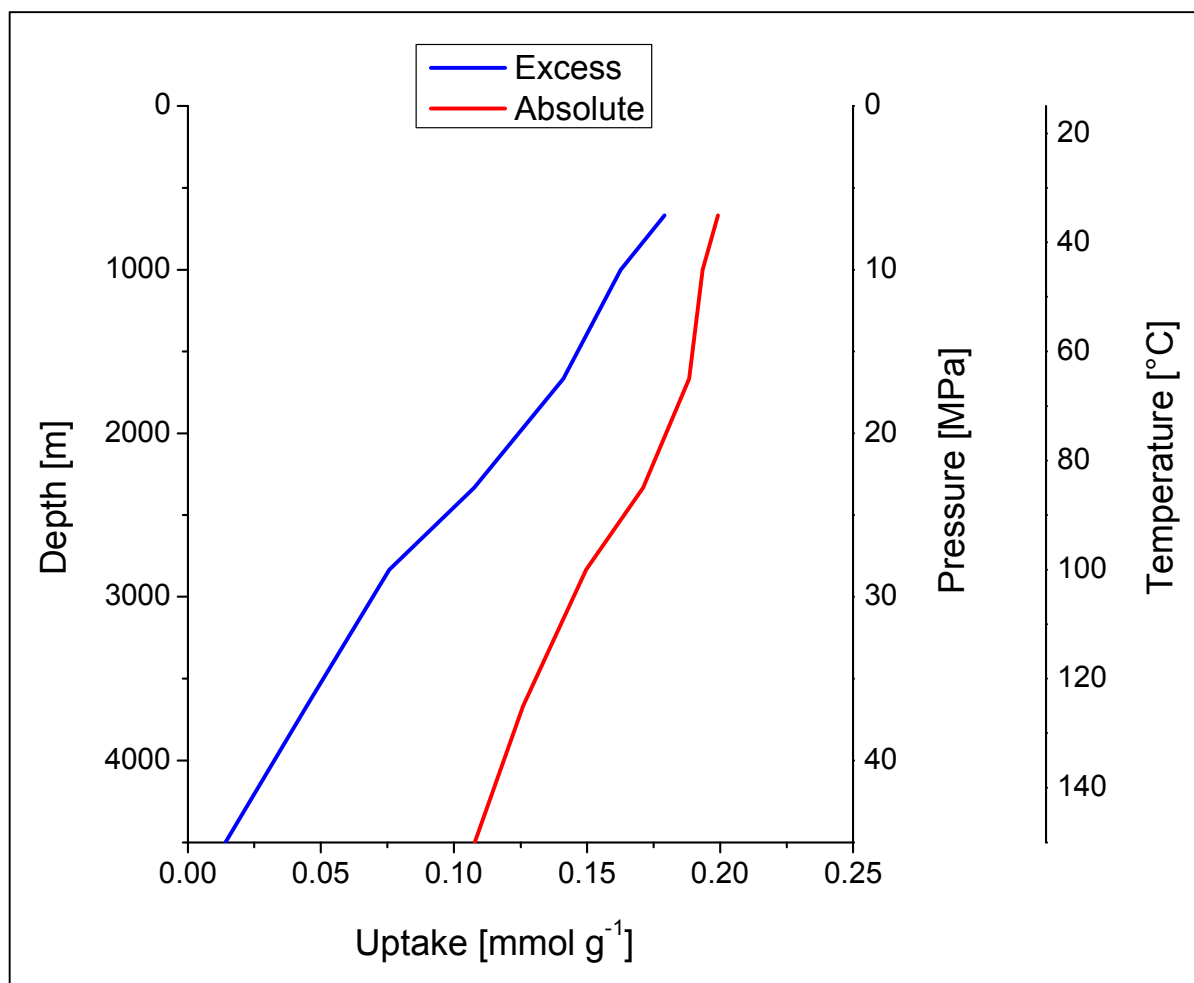


Figure 4.12: Predicted amounts of excess and absolute adsorbed methane based on Alum Shale sorption data presented in this paper. A temperature gradient of 30 °C km⁻¹ and a hydrostatic pressure gradient are assumed. Absolute amounts are based on the SDR model. Note that 0.1 mmol g⁻¹ is equivalent to approximately 71 scf t⁻¹.

4.5 Conclusions

Supercritical methane adsorption data was obtained over a wide temperature range (300 K – 473 K) on an organic-rich shale from an Alum Shale Formation. The gas sorption porosity in this shale is very low and similar to other shales. However, consistent data have been obtained, which gave linear van't Hoff graphs over a wide temperature range (300 - 473 K). The enthalpy of adsorption at low coverage (0.025 mmol g⁻¹) was 19.2 ± 0.1 kJ mol⁻¹ and this is consistent with literature values for methane adsorption on a wide range of materials. Maximum methane excess uptakes decrease from 0.176 mmol g⁻¹ (126 scf t⁻¹) at 300 K to 0.042 mmol g⁻¹ (30 scf t⁻¹) at 473 K and have a linear relationship with reciprocal of temperature (K). This phenomenological model may be useful for predictive purposes. The

model is consistent with decreases in adsorbed phase density and pore size that can be filled with methane with increasing temperature, under supercritical conditions. The applicability of the semi-empirical, supercritical Dubinin-Radushkevich isotherm model is consistent with the calculations based on micropore volumes obtained from subcritical adsorption and has advantages compared with the supercritical Langmuir model. However, more sophisticated models may be required to improve on semi-empirical models and ensure that all model parameters are physically reasonable over a wide temperature range. These results have quantitative implications for the mechanisms by which gas is retained during gas generation and stored in shale reservoirs.

Associated Content

Appendix B

Acknowledgement

The authors would like to thank Dr Sihai Yang and for calculating the pore size distribution and Amin Ghanizadeh and Matus Gasparik for supplying the shale sample. This work was supported by the GASH project funded by Bayerngas, ExxonMobil, GdFSuez, Marathon, Repsol, Schlumberger, Statoil, Total, Vermilion and Wintershall.

References

- (1) Frantz Jr, J. H.; Jochen, V. *Schlumberger White Paper*, 2006.
- (2) Annual Energy Review 2011. [Online Early Access]. Published Online: 2012.
<http://www.eia.gov/>.
- (3) Montgomery, S. L.; Jarvie, D. M.; Bowker, K. A.; Pollastro, R. M. *AAPG Bull.* **2005**, *89*, 155.
- (4) Ross, D. J. K.; Bustin, R. M. *Mar. Pet. Geol.* **2009**, *26*, 916.
- (5) Chalmers, G. R. L.; Bustin, R. M. *Bull. Can. Pet. Geol.* **2008**, *56*, 1.
- (6) Weniger, P.; Kalkreuth, W.; Busch, A.; Krooss, B. M. *Int. J. Coal Geol.* **2010**, *84*, 190.
- (7) Zhang, T. W.; Ellis, G. S.; Ruppel, S. C.; Milliken, K.; Yang, R. S. *Org. Geochem.* **2012**, *47*, 120.
- (8) Gasparik, M.; Ghanizadeh, A.; Bertier, P.; Gensterblum, Y.; Bouw, S.; Krooss, B. M. *Energy Fuels* **2012**, *26*, 4995.
- (9) Lu, X. C.; Li, F. C.; Watson, A. T. *Fuel* **1995**, *74*, 599.
- (10) Chareonsuppanimit, P.; Mohammad, S. A.; Robinson, R. L.; Gasem, K. A. M. *Int. J. Coal Geol.* **2012**, *95*, 34.
- (11) Chalmers, G. R. L.; Bustin, R. M. *Bull. Can. Pet. Geol.* **2008**, *56*, 22.
- (12) Chalmers, G. R. L.; Bustin, R. M. *Int. J. Coal Geol.* **2007**, *70*, 223.
- (13) Pepper, A. S.; Corvi, P. J. *Mar. Pet. Geol.* **1995**, *12*, 291.
- (14) Sircar, S. *Ind. Eng. Chem. Res.* **1999**, *38*, 3670.
- (15) Myers, A. L.; Monson, P. A. *Langmuir* **2002**, *18*, 10261.
- (16) Neimark, A. V.; Ravikovitch, P. I. *Langmuir* **1997**, *13*, 5148.
- (17) Ravikovitch, P. I.; Haller, G. L.; Neimark, A. V. *Advances in Colloid and Interface Science* **1998**, *76–77*, 203.
- (18) Myers, A.; Monson, P. *Adsorption* **2014**, *20*, 591.
- (19) *CRC Handbook of Chemistry and Physics*; 74th ed.; The Chemical Rubber Co.: Boca Raton, Florida, 1993.
- (20) Zhou, L.; Bai, S. P.; Su, W.; Yang, J.; Zhou, Y. P. *Langmuir* **2003**, *19*, 2683.
- (21) Bae, J. S.; Bhatia, S. K. *Energy Fuels* **2006**, *20*, 2599.
- (22) Sakurovs, R.; Day, S.; Weir, S.; Duffy, G. *Energy Fuels* **2007**, *21*, 992.
- (23) Parr, R. G.; Gadre, S. R.; Bartolotti, L. J. *Proc. Natl. Acad. Sci. U. S. A.* **1979**, *76*, 2522.
- (24) Schovsbo, N. H.; Nielsen, A. T.; Klitten, K.; Mathiesen, A.; Rasmussen, P. *Geol. Surv. Den. Greenl. Bull.* **2011**, *9*.
- (25) Lemmon, E. W.; Huber M.L.; McLinden, M. G. *NIST Standard Reference Database 23. NIST Reference Fluid Thermodynamic and Transport Properties—REFPROP Version 8* US Department of Commerce, 2010.

- (26) Setzmann, U.; Wagner, W. *Journal of Physical and Chemical Reference Data* **1991**, *20*, 1061.
- (27) Murata, K.; El-Merraoui, M.; Kaneko, K. *J. Chem. Phys.* **2001**, *114*, 4196.
- (28) Do, D. D.; Do, H. D. *Carbon* **2003**, *41*, 1777.
- (29) Sircar, S. *Ind. Eng. Chem. Res.* **1999**, *38*, 3670
- (30) Zhou, L.; Zhou, Y. P.; Li, M.; Chen, P.; Wang, Y. *Langmuir* **2000**, *16*, 5955.
- (31) Benard, P.; Chahine, R. *Langmuir* **1997**, *13*, 808.
- (32) Langmuir, I. *Journal of the American Chemical Society* **1918**, *40*, 1361.
- (33) Dubinin, M. M. *Zh. Fiz. Khimii* **1965**, 1305.
- (34) White, C. M.; Smith, D. H.; Jones, K. L.; Goodman, A. L.; Jikich, S. A.; LaCount, R. B.; DuBose, S. B.; Ozdemir, E.; Morsi, B. I.; Schroeder, K. T. *Energy Fuels* **2005**, *19*, 659.
- (35) Do, D. D. *Adsorption Analysis: Equilibria and Kinetics*; Imperial College Press, 1998; Vol. 2.
- (36) Furukawa, H.; Miller, M. A.; Yaghi, O. M. *Journal of Materials Chemistry* **2007**, *17*, 3197.
- (37) Schovsbo, N. H. *Gff* **2002**, *124*, 107.
- (38) Gregg, S. J.; Sing, K. S. W. *Adsorption, Surface Area and Porosity*; 2nd ed.; Academic Press: London, 1982.
- (39) Cazorla-Amoros, D.; Alcaniz-Monge, J.; de la Casa-Lillo M.A.; Linares-Solano, A. *Langmuir* **1998**, *14*, 4589.
- (40) Gurvitsch, L. G. *Zhurnal Russkago Fiziko-Khimicheskago Obshchestva* **1915**, *47*, 805.
- (41) Clarkson, C. R.; Freeman, M.; He, L.; Agamalian, M.; Melnichenko, Y. B.; Mastalerz, M.; Bustin, R. M.; Radlinski, A. P.; Blach, T. P. *Fuel* **2012**, *95*, 371.
- (42) Autosorb Version 1.6 ed.; Quantachrome Instruments: 2008.
- (43) Neimark, A. V.; Lin, Y.; Ravikovitch, P. I.; Thommes, M. *Carbon* **2009**, *47*, 1617.
- (44) Ravikovitch, P. I.; Vishnyakov, A.; Russo, R.; Neimark, A. V. *Langmuir* **2000**, *16*, 2311.
- (45) Krooss, B. M.; van Bergen, F.; Gensterblum, Y.; Siemons, N.; Pagnier, H. J. M.; David, P. *Int. J. Coal Geol.* **2002**, *51*, 69.
- (46) Busch, A.; Gensterblum, Y.; Krooss, B. M. *Int. J. Coal Geol.* **2003**, *55*, 205.
- (47) Gensterblum, Y.; van Hemert, P.; Billemont, P.; Battistutta, E.; Busch, A.; Krooss, B. M.; De Weireld, G.; Wolf, K. *Int. J. Coal Geol.* **2010**, *84*, 115.
- (48) Li, D. Y.; Liu, Q. F.; Weniger, P.; Gensterblum, Y.; Busch, A.; Krooss, B. M. *Fuel* **2010**, *89*, 569.
- (49) Ambrose, R. J.; Hartman, R. C.; Diaz-Campos, M.; Akkutlu, I. Y.; Sondergeld, C. H. *Spe J.* **2012**, *17*, 219.
- (50) *Handbook of Compressed Gases, 3rd Edition Van Nostrand Reinhold, New York 1990*; 3rd ed.; Van Nostrand Reinhold: New York, 1990.

- (51) Mosher, K.; He, J.; Liu, Y.; Rupp, E.; Wilcox, J. *Int. J. Coal Geol.* **2013**, *109–110*, 36.
- (52) Sircar, S. *Journal of the Chemical Society-Faraday Transactions I* **1985**, *81*, 1527.
- (53) Himeno, S.; Komatsu, T.; Fujita, S. *J. Chem. Eng. Data* **2005**, *50*, 369.
- (54) Duren, T.; Sarkisov, L.; Yaghi, O. M.; Snurr, R. Q. *Langmuir* **2004**, *20*, 2683.
- (55) Rahman, K. A.; Loh, W. S.; Yanagi, H.; Chakraborty, A.; Saha, B. B.; Chun, W. G.; Ng, K. C. *Journal of Chemical and Engineering Data* **2010**, *55*, 4961.
- (56) Ruppel, T. C.; Grein, C. T.; Bienstoc. *Fuel* **1974**, *53*, 152.
- (57) Xia, X. Y.; Tang, Y. C. *Geochim. Cosmochim. Acta* **2012**, *77*, 489.
- (58) Jarvie, D. M.; Hill, R. J.; Ruble, T. E.; Pollastro, R. M. *AAPG Bull.* **2007**, *91*, 475.
- (59) Loucks, R. G.; Reed, R. M.; Ruppel, S. C.; Jarvie, D. M. *Journal of Sedimentary Research* **2009**, *79*, 848.

High-pressure Methane Adsorption and Characterization of Pores in Posidonia Shales and Isolated Kerogens

Rexer, T. F.; Mathia, E. J.; Aplin, A. C.; Thomas, K. M. *Energy Fuels* **2014**.

Abstract

Sorption capacities and pore characteristics of bulk shales and isolated kerogens have been determined for immature, oil-window and gas-window mature samples from the Lower Toarcian Posidonia Shale formation. Dubinin-Radushkevich (DR) micropore volumes, sorption pore volumes and surface areas of shales and kerogens were determined from CO₂ adsorption isotherms at -78°C and 0°C, and N₂ adsorption isotherms at -196°C. Mercury injection capillary pressure porosimetry, grain density measurements and helium pycnometry were used to determine shale and kerogen densities and total pore volumes. Total porosities of shale decrease through the oil-window and then increase into the gas-window. High-pressure methane isotherms up to 14 MPa were determined at 45, 65 and 85°C on dry shale and at 45 and 65°C on kerogen. Methane excess uptakes at 65°C and 11.5 MPa were in the range 0.056-0.110 mmol g⁻¹ (40-78 scf t⁻¹) for dry Posidonia Shales and 0.36-0.70 mmol g⁻¹ (253-499 scf t⁻¹) for the corresponding dry kerogens. Absolute methane isotherms were calculated by correcting for the gas at bulk gas phase density in the sorption pore volume. The enthalpies of CH₄ adsorption for shales and kerogens at zero surface coverage showed no significant variation with maturity, indicating that the sorption pore volume is the primary control on sorption uptake. The sum of pore volumes measured by a) CO₂ sorption at -78°C and b) mercury injection, are similar to the total porosity for shales. Since mercury in our experiments occupies pores with constrictions larger than ca. 6 nm, we infer that porosity measured by CO₂ adsorption at -78°C in the samples used in this study is largely within pores with effective diameters smaller than 6 nm. The linear correlation between maximum CH₄ surface excess sorption and CO₂ sorption pore volume at -78°C is very strong for both shales and kerogens, and goes through the origin, suggesting that the vast majority of sorbed CH₄ occurs in pores smaller than 6 nm. The DR micropore volume obtained from CO₂ adsorption at 0°C was 40-62% of the corresponding CO₂ sorption pore volume. Sorption mass balances using kerogen and shale isotherms showed that approximately half of the CO₂ sorption in these dry shales is in organic matter, with the rest likely to be associated with the inorganic phase (mainly clay minerals). A similar distribution was observed for supercritical CH₄ adsorption.

Mass balances for adsorption isotherms for kerogen and clay minerals do not always account for the total measured sorbed CH₄ on dry shales, suggesting that some sorption may possibly occur, which is not accounted for by the minerals identified and kerogens in the shales.

5.1 Introduction

Shale gas is a key methane supply resource for the future. In 2010 it accounted for 20 % of the natural gas production in the United States, up from 1 % in 2000.¹ The economic potential of shale gas reservoirs is essentially a function of the Gas-in-Place (GIP) and the rate at which that gas can be supplied from the shale matrix to an induced fracture network connected to a wellbore. At the heart of both factors is the requirement to quantify the nature of the shale pore volume and to understand how variations in pore size distributions affect the location and amounts of both sorbed and homogeneous bulk (“free”) gas.

Pore volumes and size distributions in shales are affected by compaction, maturity, grain size and mineralogy.²⁻⁷ The pore volume of shales can be determined by various techniques such as mercury injection capillary pressure (MICP) porosimetry and grain density/ helium pycnometry, scanning electron microscopy (SEM) images and gas sorption techniques, with each method characterizing a specific pore size range. Ultra small angle neutron scattering and small angle neutron scattering techniques are also useful for the determination of pore connectivity in shales.⁸⁻¹⁰ Sorbed gas in shale is in equilibrium with the homogeneous bulk gas phase (“free gas”) in larger pores. Sorption capacity depends on pressure and temperature, and structural characteristics, such as (micro-) pore volume and organic matter type, maturity and content. Supercritical methane maximum surface excess adsorption decreases linearly with reciprocal of absolute temperature for an Alum shale.¹¹ The hygroscopic moisture content of shales correlates with methane sorption capacity indicating that methane and water compete for the same sorption sites. Also, under geological conditions, moisture may be present leading to reduced methane capacity compared with dry shales.^{12,13,14}

Ross et al have reported positive correlations between maturity and sorption capacity in organic-rich shales, which they attributed to an increased micropore volume (pore width 0.3 – 2 nm).¹⁴ However, they were not able to fully explain variations in sorption capacity by micropore volume and Total Organic Carbon (TOC) content alone. Several authors have reported positive correlations of methane sorption uptake and TOC, implying that much of the sorbed methane in shale is associated with organic matter.^{12,14,15} Gasparik et al. reported no correlation for methane sorption capacity and TOC (0.8-10.5%) for dry shales¹⁶, but found a correlation for another suite of dry shales with TOC (0.4-14.1%).¹³ These results illustrate the

complex nature of the problem when relating composition and structure of shales to methane sorption capacity. Water may also be present under subsurface conditions and methane adsorption studies of moisture-equilibrated shale samples show that competitive adsorption has a detrimental effect on methane sorption capacity.¹³

The differences between surface excess and absolute amounts adsorbed become significant in high pressure isotherms. The surface excess is the difference between the amount of gas present in the system and the amount of gas that would be present if all the accessible volume in the system were occupied by the adsorbate gas in its bulk state. The actual absolute amount adsorbed represents the total amount of gas molecules in the sorbed state.¹⁷⁻¹⁹ Various semi-empirical models such as the Langmuir or the supercritical Dubinin-Radushkevich model are available alongside models based on density functional theory.^{11,16,20} While the Langmuir models have been commonly used to parameterize shale sorption data, the supercritical Dubinin-Radushkevich model has been shown to have good applicability for a predominantly ultra-microporous (< 0.7 nm) high maturity Alum Shale (Ro = 2.26%), for isotherms over a wide temperature range (27-200°C).¹¹ Although sorption data on shales are available, the absolute sorption capacity in shale remains poorly constrained.^{11-16,21-23}

Shales are complex heterogeneous materials with amorphous kerogen and crystalline inorganic phases. The amounts of methane adsorbed on shales are also very low and this is complicated by the fact that the minor kerogen component has a much larger adsorption capacity than the inorganic phase in the shale. Previous studies have concentrated on the correlation of surface excess with geological characterization data, for example, total organic carbon, maturity etc. and this has significant limitations. The aim of this study was to investigate how supercritical methane sorption capacity and pore structural characteristics in shale and kerogen obtained from subcritical adsorption change with maturity. The pore structural characteristics were obtained using subcritical carbon dioxide (-78 and 0°C) and nitrogen (-196°C) adsorption, mercury injection capillary pressure (MICP) porosimetry, helium pycnometry and grain density measurements. Posidonia Shale samples from the early oil window, the oil window and the gas window were studied. The shale sample set is relatively homogeneous in terms of TOC and mineral composition, allowing the impact of maturity on shale and kerogen pore structure and methane capacity to be studied independently of these variables. Kerogen samples were isolated using chemical methods. Furthermore, high-pressure methane sorption isotherms were determined on both shales and isolated organic kerogen matter to investigate the interrelations between high-pressure sorption capacity, maturity, pore structure and the sorbed gas distribution between organic and inorganic phases.

5.1.1 Posidonia Shales

The Lower Toarcian Posidonia Shale is regarded as one of the most widespread and economically important petroleum source rocks of Western Europe. The formation is a reference source rock of Type II kerogen.²⁴⁻²⁶ These black shales were deposited in an epicontinental sea of moderate depth, extending from the Yorkshire Basin (United Kingdom), over the Lower Saxony Basin and the Southwest German Basin into the Paris Basin, during the Lower Toarcian period.^{24,27,28} Recent electron microscopy studies inferred that the formation of nanoporous organic materials occurred due to gaseous hydrocarbon generation in Posidonia Shales of gas window maturity.²⁹ Geological and geochemical history has been reviewed in detail elsewhere.^{24,27-33}

5.2 Experimental

5.2.1 Materials

Posidonia shales were obtained from the Wickensen (WIC), Harderode (HAR) and Hadessen (HAD) boreholes. These boreholes were drilled along the Western flank of the Hils half-graben. The shales progressively increase in maturity from the early oil window Wickensen ($R_o = 0.53\%$), through the mid oil window Harderode ($R_o = 0.89\%$), to the gas window Hadessen ($R_o = 1.45\%$) samples.²⁹

Carbon dioxide and nitrogen gases were obtained from BOC Industrial Gases UK with purities of 99.995% and 99.9995%, respectively. Methane, with a purity of 99.995%, was obtained from Air Products UK and Air Liquide UK.

5.2.2 Rock Eval Pyrolysis

Rock-Eval Pyrolysis was carried out with a Delsi Rock Eval OSA pyrolysis instrument and the following parameters were measured: The S1 value is the amount of free hydrocarbons in the sample and S2 is the amount of hydrocarbons generated through thermal cracking of non-volatile organic matter. T_{max} is the temperature with the maximum generation rate of cracking products. This temperature is an indicator of the maturity of the sample.³⁴

5.2.3 Mercury Injection Porosimetry

Porosimetry measurements were performed using a Micromeritics Autopore IV Mercury Injection Porosimeter. Shale samples were freeze-dried for 48 h and $\sim 1 \text{ cm}^{-3}$ samples were loaded and outgassed under vacuum. The mercury pressure was increased stepwise up to 268.9 MPa. MICP bulk volumes/densities of shale were calculated from the bulk volume of the known mass of sample placed into the MICP equipment and the grain density of the

sample measured by the small pycnometer method. Pore volumes, measured by injected mercury, (MICP_{pv}) were calculated from the difference of the volume of mercury injected at 1.379 MPa and 268.9 MPa, assuming that the small amounts of mercury injected at the lower pressure, only fill surface topography and micro fractures. The macroporosity (1093 - 50 nm) present in some samples, which could act as methane gas storage capacity was included in the total pore volume, but surface topography and micro fractures related to the de-stressing and drying of geological samples were excluded (see Table 5.1). Assuming a contact angle of 141° between mercury, particle surface and air and a surface tension of 0.485 N m^{-1} ,^{3,35,36} the Young-Laplace equation derived for cylindrical pores predicts that at these pressures, mercury penetrates pore throats (constrictions) with equivalent diameters between 1093 nm at 1.379 MPa and 5.6 nm at 268.9 MPa. These diameters should be regarded as equivalent pore diameters because of the variation in pore shape in the heterogeneous shale materials. Details about the measurements are given in Chapter 2.

5.2.4 Kerogen Isolation

Shales (~25 g each) were crushed to powder and treated with 8 mL HCl (0.5 M) to remove carbonates and acidified CrCl_2 (1.0 M) to remove pyrite. The mixture was diluted with degassed water. The shale particles were separated from the solution by centrifuging (15 min, 3500 min^{-1}). The process was repeated 3 times. Samples were then freeze-dried (-25°C). Silicates were removed by treating the decarbonated and depyritized shales with 15 mL HF (0.4 M). The process was repeated twice. The shale-acid mixture was diluted with degassed water and the kerogens were separated by filtering. For Harderode shales no depyritization was conducted as pyrite removal proved inefficient for Wickensen and Hadessen shales. XRD profiles were obtained before and after the demineralization to ensure removal of all minerals except pyrite. Details about the process and chemical reactions are given in Appendix C (Section A). The isolated kerogen samples contained varying amounts of pyrite (see Appendix C, Section A, Table S C1), which were measured by proximate analysis. CO_2 (-78°C) and N_2 (-196°C) adsorption isotherms for pyrite showed that no significant adsorption occurred (see Appendix C, Figure S C2). Therefore, all kerogen adsorption isotherms were corrected for pyrite content.

5.2.5 Pore Characterization by Low Pressure Sorption

Adsorption characteristics of nitrogen and carbon dioxide on the shales and kerogens were investigated using an Intelligent Gravimetric Analyzer (IGA), supplied by Hiden Isochema Ltd., Warrington, UK.

Adsorbent samples were crushed to particle sizes between 500 – 1180 μm , loaded (130 – 160 mg of shales, 40-105 mg of kerogens) in the IGA and out-gassed to a constant weight (typically for ~ 4 hours), at $< 10^{-4}$ Pa, at 110°C. N_2 isotherms were measured at -196°C up to a pressure of 99 kPa. CO_2 isotherms were collected at -78°C and 0°C up to 100 kPa. The saturated vapor pressure (p_0) for CO_2 at 0°C is 3.49 MPa. All adsorption isotherms were measured a minimum of two times and the experimental repeatability was typically ± 1.5 % for CO_2 adsorption uptakes at both -78 and 0°C at 0.1 MPa and ± 1.1 % for N_2 uptakes at -196°C and 0.099 MPa.

5.2.6 High Pressure Methane Sorption

High pressure methane isotherms were measured on a Hiden Isochema Intelligent Manometric Instrument (IMI). System specifications are described in Chapter 2. Crushed shale samples (500 – 1180 μm) and kerogens were pre-dried (typically for ~ 4 hours, at < 500 Pa and at 110°C) in a vacuum oven and loaded (typically ~ 10 g shale, 0.8-1.3 g kerogen) into the IMI sample cell. For kerogens, displacers were employed to reduce the void volume, because only relatively small quantities were available. Prior to the measurements another internal drying was carried out (typically for ~ 4 hours), at $< 10^{-4}$ Pa, at 110°C followed by helium pycnometry (2 MPa dosing pressure at 40°C and ca. 0.7 MPa at equilibrium after dosing) to determine the skeletal volume. The assumption is that helium penetrates all accessible porosity and is not adsorbed.³⁷

Methane isotherms were measured at 45, 65 and 85°C. In between measuring isotherms the system was out-gassed below $< 10^{-6}$ Pa and heated to 110°C. Excess uptake was calculated by a mass balance given in Chapter 2. Isotherm experimental repeatability was typically ± 5.0 % for both shale and kerogens at 10 MPa. In addition, assuming that helium adsorption is negligible, helium isotherms were measured at all temperatures as blank determinations for no adsorption, to leak-test the system and to monitor skeletal densities.

5.3 Results

5.3.1 Total Organic Carbon Content and Grain Densities

The TOC and the grain densities obtained from both buoyancy and helium pycnometry are shown in Table 5.1. TOC values range from 5.8 - 10.9 wt%. Excellent agreement was observed for shale grain densities (2.331 – 2.607 g cm^{-3}) and helium pycnometry (2.297 - 2.614 g cm^{-3}) with measurements for specific samples agreeing within 3%. Kerogen densities were much lower and ranged from 1.024 to 1.368 g cm^{-3} .

Table 5.1: Well depth, TOC, grain and helium densities, mercury injection pore volumes and total porosities for Posidonia Shales and kerogens.

Well + Sample	Depth	TOC	Shale grain density	Shale density (Helium Pycnometry)	Shale Bulk Vol. (MICP)	Shale Specific Total Pore Vol.	Kerogen TOC†	Kerogen density (Helium Pycnometry)
	[m]	[wt%]	[g cm ⁻³]	[g cm ⁻³]	[cm ³ g ⁻¹]	[%]	[wt%]	[g cm ⁻³]
WIC7145	47.4	10.92	2.331	2.321	0.497	13.8	73	1.217
WIC7155	57.8	9.67	2.361	2.297	0.484	12.5	73	1.235
HAR7038	44.5	7.91	2.493	2.468	0.414	3.1	97	1.168
HAR7060	66.8	5.78	2.592	2.550	0.404	4.5	>99	1.024
HAD7090	40.1	7.41	2.572	2.556	0.439	11.4	83	1.342
HAD7119	60.6	7.15	2.607	2.614	0.445	13.7	79	1.368

† The kerogen TOC content is corrected for the residual pyrite content, which could not be removed by the separation process.

5.3.2 Rock Eval Pyrolysis

The bulk geochemical data classifies the Posidonia Shale kerogen as Type II with a maturation trend typical for the marine algal kerogen (see Table 5.2).³⁸ The Rock-Eval analyses showed a decrease of hydrogen index (HI) from ~700 mg HC/g in the early oil window down to ~370 mg HC/g in the peak oil window and 50 mg HC/g in the gas window. The S1 and S2 parameters decrease with increasing maturity.

The Rock Eval T_{max} values of kerogen are slightly lower than for the corresponding shales (see Appendix C, Section A3) with the difference increasing with increasing kerogen maturity. Heat and mass transfer effects are likely to be quite different for isolated kerogens and kerogens embedded in an inorganic shale matrix and these factors will influence T_{max} significantly. However, good linear correlations are observed for S2 peak ($R^2 = 0.9595$) and HI ($R^2 = 0.9977$) parameters for pyrolysis of the kerogen and shales (see Appendix C, Figure S C1). Previous work has shown that S2 and HI parameters are decreased by mineral matrix effects involving retention of pyrolysis products.³⁹ Therefore, it is reasonable to conclude that the kerogen isolation process only had a minimal effect on kerogen properties.

Table 5.2: Rock-Eval pyrolysis results for Posidonia shales. PP= Production Potential, PI=HI= Hydrogen Index (see Chapter 2.2.4)

	S1	S2	T _{MAX}	PP	PI	HI
	[mg g ⁻¹]	[mg g ⁻¹]	[°C]	[mg g ⁻¹]		[mg _{HC} g _{TOC} ⁻¹]
WIC7145	4.2	72.0	425	76.2	0.05	660
WIC7155	3.9	69.4	429	73.3	0.05	718
HAR7038	3.3	30.2	449	33.5	0.10	382
HAR7060	2.0	21.2	447	23.2	0.09	361
HAD7090	0.9	4.2	464	5.1	0.18	56
HAD7119	1.2	3.2	459	4.4	0.28	44

5.3.3 Mineralogy

The bulk mineralogical compositions of these Posidonia samples are similar throughout the whole maturation sequence (see Table 5.3). The most abundant phases are calcite (31-55 wt.%) and phyllosilicates (23-37 wt.%). Within the phyllosilicates group, illite-rich mixed layer illite-smectite is the most prominent component, followed by kaolinite, illite, muscovite and chlorite. In addition, there is a moderate content of quartz (8-16 wt.%) and minor contents of pyrite (4-9 wt.%), feldspars (1-5 wt.%) and dolomite (0.3-6.4 wt.%). Other minerals include siderite, marcasite and anatase, but their content does not exceed 2-3 wt.%. The XRD and microscopic data classify the immature Posidonia Shale as a calcareous nanoplankton-, silt- and clay-bearing mudstone.

Table 5.3: Mineral composition of Posidonia shales in wt%. Other minerals includes Feldspar, Siderite, Anatase, Marcasite, Aragonite and Dickite (not more than 1.5 wt%).

	Quartz	Plagioclase	Calcite	Dolomite	Pyrite	Gypsum	Muscovite	Illite + I-S	Kaolinite	Chlorite	Other
WIC7145	13.2	1.0	46.6	0.3	3.9	2.2	0.0	22.4	5.1	2.0	3.3
WIC7155	8.6	1.4	55.3	0.6	5.4	2.4	0.1	19.4	2.2	1.8	2.8
HAR7038	15.8	2.1	43.5	0.7	5.6	0.0	3.2	18.5	8.9	0.0	1.7
HAR7060	13.0	2.8	30.5	6.4	9.1	0.0	3.7	26.2	6.6	0.0	1.7
HAD7090	16.0	3.0	39.7	1.8	5.0	1.8	1.3	23.9	3.9	0.7	2.9
HAD7119	8.2	4.9	49.9	2.7	4.5	3.8	0.0	19.5	1.1	2.7	2.7

5.3.4 Pore Characterization

Total Pore Volume (TPV) and MICP Pore Volume (MICP_{pv})

The bulk volume obtained from MICP and the skeletal densities from grain density measurements and helium pycnometry were used to calculate the total pore volumes of the Posidonia shales. The total pore volume (< 1093 nm) was obtained from mercury injection at 1.379 MPa and the helium or grain densities. Mercury injection at a pressure of 268.90 MPa measures the accessible pore volume for constrictions with equivalent pore widths > 5.6 nm based on the Young-Laplace equation for cylindrical capillaries. Correcting for conformance/surface roughness using the method of Wang et al³, which, depending on the sample, ranged from 1.379 - 35.2 MPa mercury pressure (corresponding to equivalent pore diameters of 43 to 1093 nm), did not lead to significantly different MICP pore volumes. The maximum pore sizes in the samples obtained from MICP were as follows: WIC7145 (156 nm), WIC7155: (156 nm), HAR7038 (21 nm), HAR 7060 (24 nm), HAD 7090 (156 nm) and HAD7199 (547 nm). These maximum pore sizes decrease through the oil-window and then increase into the gas-window.

Mercury injection volumes were ~80% of total pore volumes in the Wickensen samples, ~40% in the Harderode samples and 50-75% in the Hadessen samples. Total pore volumes and mercury injection volumes show the same trend with maturity (see Table 5.4). There is a decrease in total pore volume from around of 65 to 15 mm³ g⁻¹ for the Wickensen samples (R₀ = 0.53%) to the Harderode samples (R₀ = 0.89 %) and an increase back to about 55 mm³ g⁻¹ for Hadessen (R₀ = 1.45%) shales. A similar trend of pore volume with maturity, with a minimum in the oil window, has been observed previously for coals.⁴⁰

Sorption Pore Volumes

According to the Gurvitch Rule adsorption uptake at $p/p_0 \approx 1$ when expressed as a volume, using the liquid density should be the same for all adsorptives on a given adsorbent.⁴¹⁻⁴³ These sorption pore volumes can thus be calculated from CO₂ isotherms at 0.1 MPa and -78°C or nitrogen adsorption isotherms at 0.1 MPa and -196°C.

Carbon dioxide isotherms for both shales and kerogens at -78°C do not reach plateaus and are therefore classified as Type I/II in the IUPAC Classification Scheme (see Figures 5.1 and 5.2).⁴⁴ Maximum uptake (at $p/p_0 \approx 1$) was 0.23 – 0.44 mmol g⁻¹ on shales and 1.83 – 3.02 mmol g⁻¹ on kerogens (see Figure 5.1 and 5.2). Tabulated isotherm data are given in Appendix C, Section B. Normalizing the isotherms by maximum uptake reveals that all isotherms (shale and kerogen) have very similar isotherm shapes. This indicates that the Posidonia shales and kerogens have similar pore size distributions within the porosity range measured by CO₂ adsorption at -78°C.

Calculated sorption pore volumes from CO₂ isotherms at -78°C (CO₂ SPV) of shale and kerogen are shown in Table 5.4. An adsorbed phase density of 1.177 g cm⁻³ was assumed. There is a range of possible values for densities of adsorbed CO₂ from 1.562 g cm⁻³ for solid at -78°C to 0.762 g cm⁻³ at 21.1°C. The density chosen is in the middle of this range and is the liquid density of CO₂ at the boiling point (-56.6°C).⁴⁵ CO₂ sorption pore volumes range from 8.3 to 16.4 mm³ g⁻¹ on shale and from 68.5 to 113.0 mm³ g⁻¹ on kerogen (see Table 5.4). There is a trend in sorption and MICP pore volumes with maturity with the minimum observed for HAR shales. The sum of the CO₂ sorption pore volumes and MICP pore volumes are very similar to the corresponding total pore volumes calculated from the MICP bulk volume (< 1093 nm) and the grain or helium density with a linear correlation coefficient with R² > 0.97 (see Figure 5.3). Therefore, the CO₂ sorption pore volume and MICP pore volume (5.6 – 1093 nm) account for the total pore volume (< 1093 nm) in this suite of shale samples. Considering that the Young-Laplace equation for cylindrical capillaries predicts that mercury penetrates pore constrictions down to effective pore diameters of approximately 5.6 nm, the good agreement suggests that the CO₂ sorption pore volume accounts for pores up to approximately this pore diameter. This sorption pore volume represents approximately 25% of total pore volume in the Wickensen samples, 46 and 66 % in the Harderode samples and around 21 and 32% in the Hadessen samples (see Table 5.4). However, we note that the high pressures used in mercury injection porosimetry may distort shale samples. Furthermore, MICP measurements were carried out on 1 cm³ chips while sorption measurements were carried out on particles (500 – 1180 μm) and, thus, the accessible pore volume may differ.

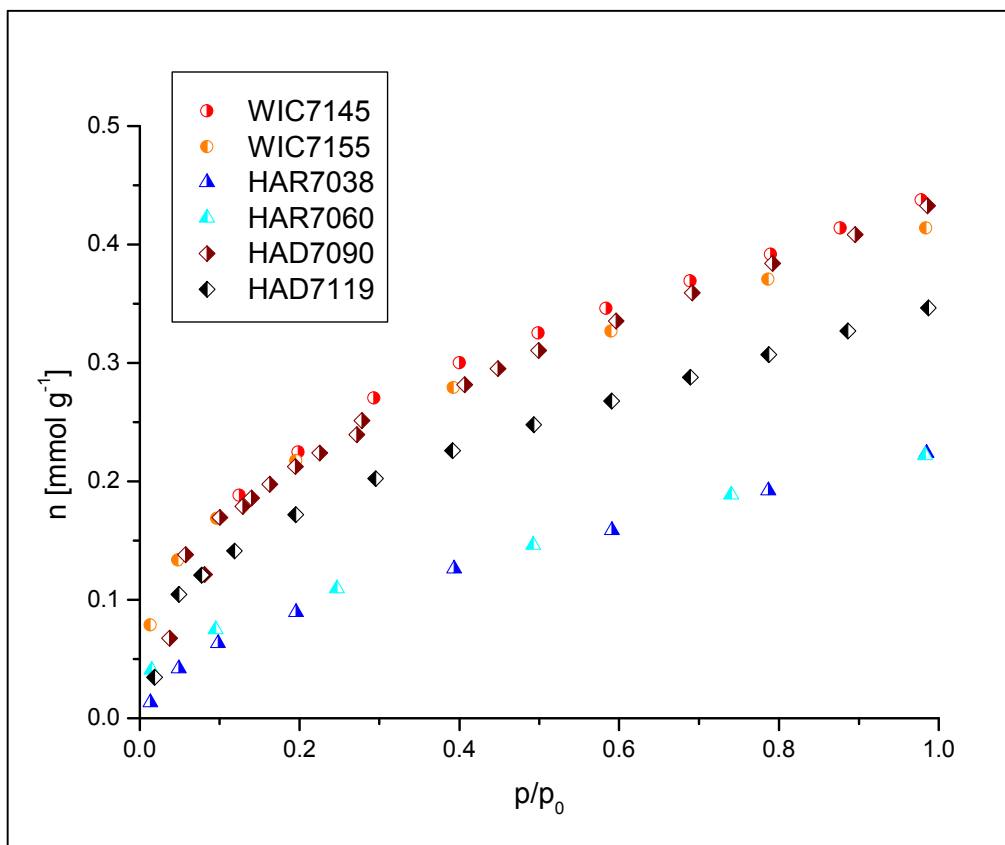


Figure 5.1: CO₂ adsorption isotherms for shales at -78°C.

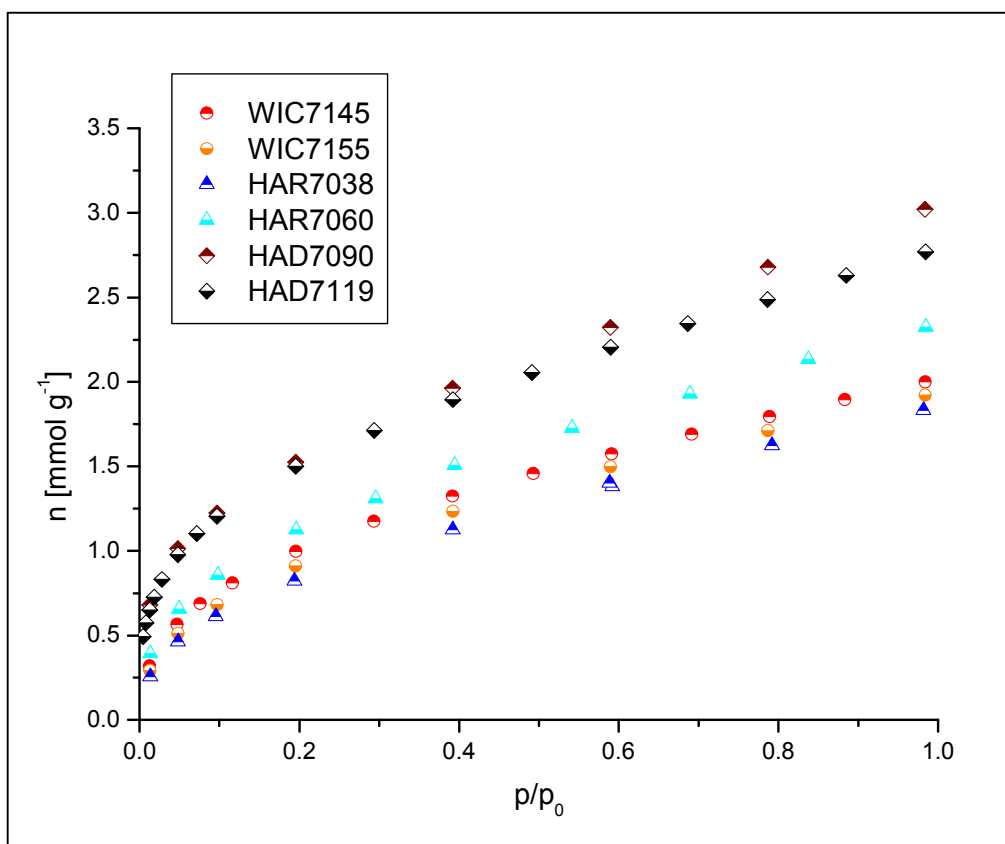


Figure 5.2: CO₂ isotherms for kerogens at -78°C.

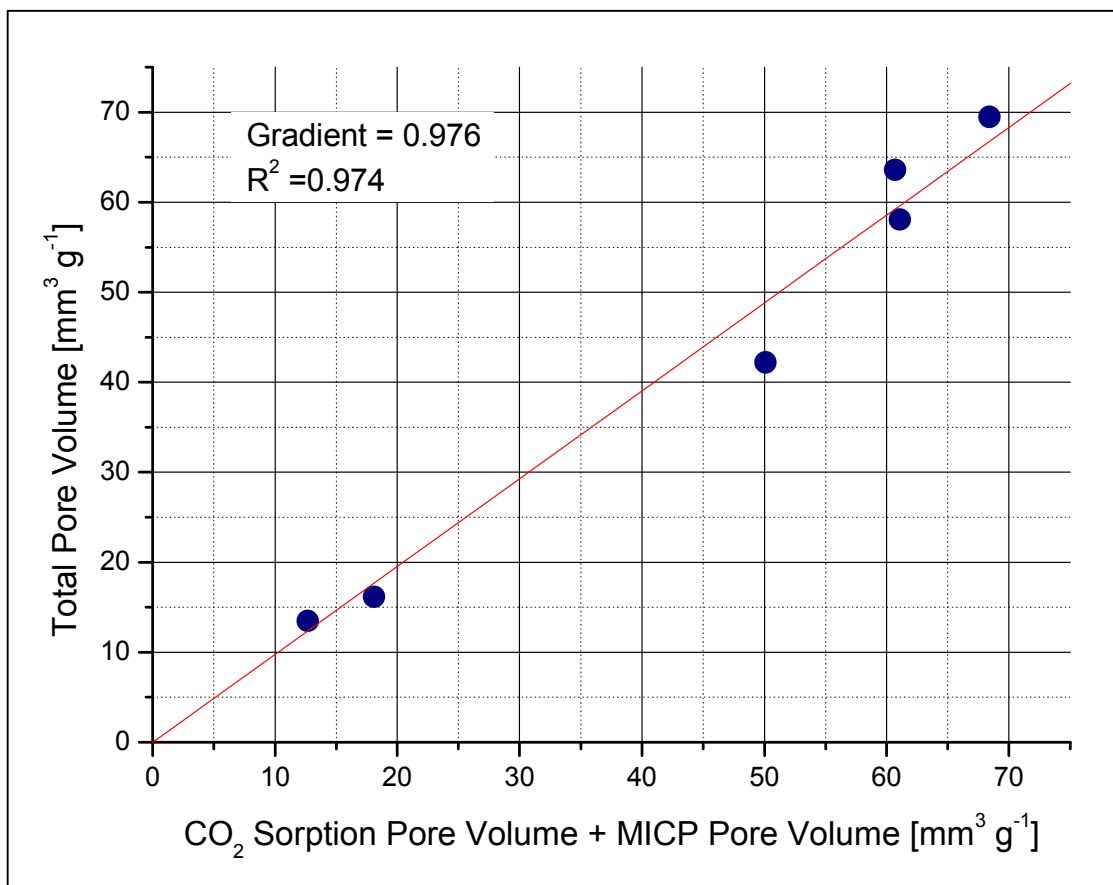


Figure 5.3: Correlation of Total Pore Volume with CO₂ Sorption Pore Volume (-78°C) plus MICP Pore Volume. Pore Volumes were calculated assuming an adsorbed phase density of 1.177 g cm⁻³.

Nitrogen adsorption isotherms of shales and kerogen at -196°C are shown in Figures 5.4 and 5.5, respectively. Tabulated isotherm data are given in Appendix C, Section B. Nitrogen uptakes on Harderode shales were too low to allow measurements of isotherms. This is in contrast to the CO₂ isotherms for the Harderode shales at -78°C, which, although having the lowest uptake, have isotherm shapes consistent with the other samples. This difference in isotherm uptake is attributed to activated diffusion effects for N₂ in ultramicroporosity at -196°C, which is not apparent for CO₂ adsorption at -78°C.^{46,47} The shapes of the N₂ adsorption isotherms indicate micropore filling (up to $p/p_0 \approx 0.2$) and gradual increase for $p/p_0 > 0.2$ and increased upward isotherm curvature close to $p/p_0 = 1$. Maximum uptakes at $p/p_0 \approx 1$ were in the range 0.22 – 0.59 mmol g⁻¹ on shale and 0.32 – 4.0 mmol g⁻¹ on kerogen (see Appendix C, Section B1). Steep uptake of nitrogen isotherms of Hadessen shales and kerogens at -196°C at very low p/p_0 ($p/p_0 < 0.02$) indicates filling of ultramicropores.⁴⁸ Since some activated diffusion effects were observed for N₂ adsorption on HAR shales and kerogens at -196°C, the surface areas were not suitable for comparisons between samples.

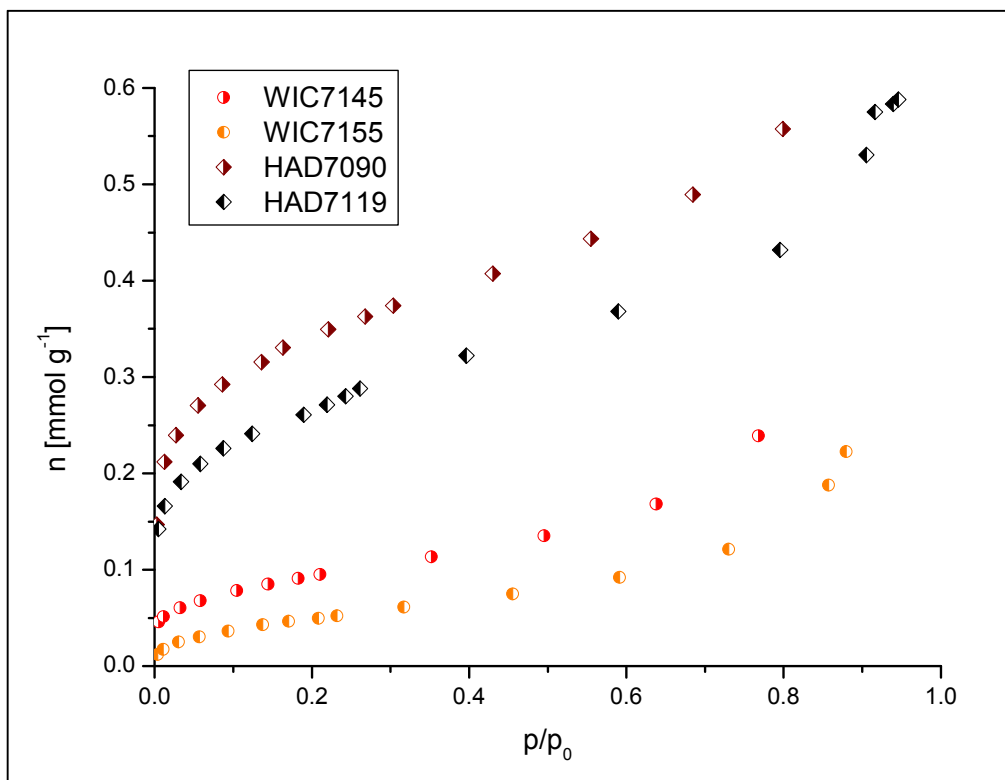


Figure 5.4: N₂ adsorption isotherms at -196°C for Posidonia shales.

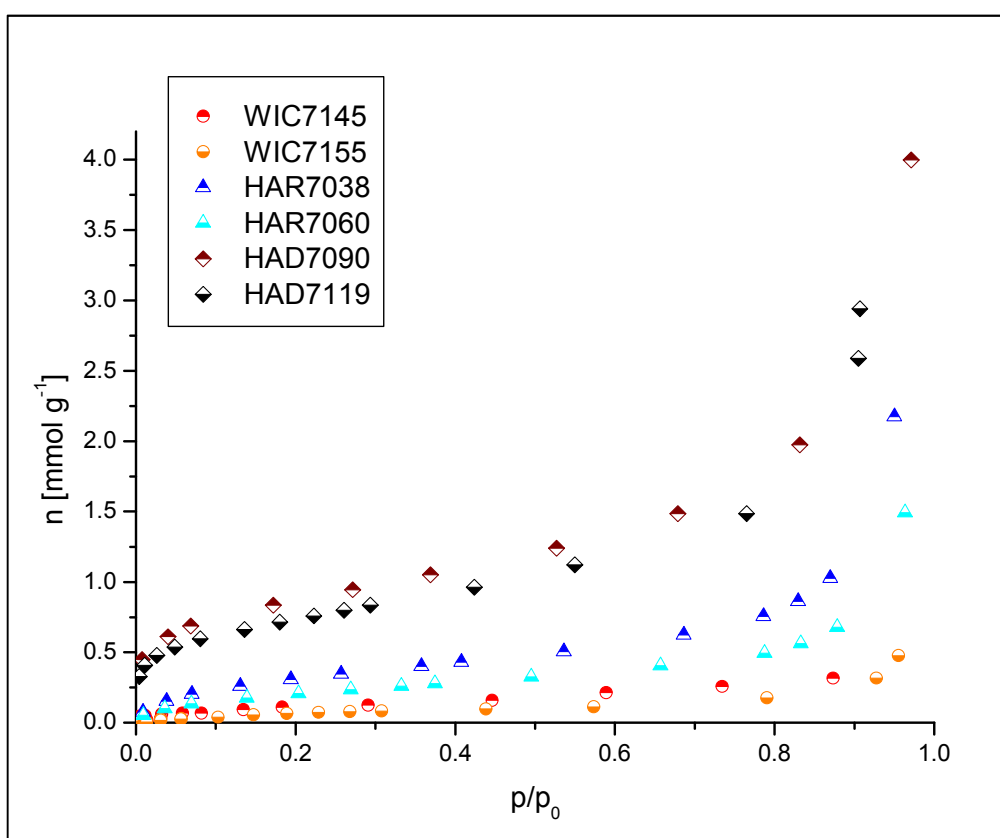


Figure 5.5: N₂ adsorption isotherms at -196°C for Posidonia kerogens.

Micropore Volume

Some authors favor the use of carbon dioxide adsorption at 0°C for the characterization of the microporous structure in activated carbons and coals, because, compared with N₂ at -196°C, the higher temperature for CO₂ adsorption overcomes kinetic limitations due to activated diffusion.^{50,49,50} Carbon dioxide isotherms at 0°C of shale and kerogen are Type I Isotherms (see Appendix C, Section B1 for tabulated data). At these temperature and pressure conditions (< 0.1 MPa), CO₂ sorption is limited to ultramicropores (< ~0.7 nm).^{46,51} Maximum uptakes at $p/p_0 \sim 0.029$ were between 0.06 and 0.12 mmol g⁻¹ for shales and between 0.27 and 0.74 mmol g⁻¹ for kerogens. Thus, CO₂ uptake on kerogen is about 5 times higher than on shales under these conditions.

The Dubinin-Radushkevich (DR) model was used to calculate ultramicropore volumes using a density of 1.032 g cm⁻³ (liquid density of CO₂ at -20°C).⁵² A value of 1.023 g cm⁻³ was used previously in a detailed study of the adsorption of CO₂ on activated carbons.⁴⁶ Additionally, a non-local density functional theory (NLDFT) equilibrium model with a kernel based on slit-shaped pores in carbon was used to calculate pore size distributions (see Appendix C, Section D) and micropore volumes from the isotherms. These pore size distributions (< 5 nm) are shifted to slightly lower pore sizes compared with Eagle Ford shale obtained from nitrogen (-196°C).⁵³ Table 5.4 shows that the ultramicropore volumes in shales, estimated from the DR model range from 4.6 to 8.0 mm³ g⁻¹, or from 4.0 to 7.7 mm³ g⁻¹ estimated from the NLDFT model. Ultramicropores thus represent approximately 12% of total pore volume in Wickensen and Hadessen samples, and 25 and 41% of total pore volume in the Harderode samples. Ultramicropore volumes follow the same trends as CO₂ sorption pore volumes. There is only a weak trend of micropore volume with maturity for the shales.

Ultramicropore volumes in kerogens are much higher than in shales, ranging from 27.0 to 54.6 mm³ g⁻¹, estimated from the DR model, and 21.8 to 50.8 mm³ g⁻¹ according to the NLDFT model (see Table 5.4). Ultramicropore volumes are similar in Wickensen (R₀ = 0.53%) and Harderode (R₀ = 0.89%) samples, but are almost double in the Hadessen (R₀ = 1.45%) samples (see Table 5.4).

Even though the models are entirely different, NDLFT micropore volumes generally agree well with the DR ultramicropore volumes. NDLFT micropore size distributions are shown in Appendix C, Section D. The pore size distribution show very little porosity above a pore width of about 1 nm, confirming that CO₂ at 0°C and 0.1 MPa is limited to ultramicroporosity.

DR micropore volumes were also calculated from nitrogen -196°C isotherms. At low relative pressure nitrogen fills micropores < 2 nm providing there is no activated diffusion or molecular sieving. The N₂ micropore volumes are shown in Table 5.4. For kerogen the N₂ micropore volumes are significantly lower than the CO₂ ultra-micropore volume probably

reflecting some activated diffusion or molecular sieving, as mentioned in section 3.2.2. However, the nitrogen micropore volumes increase with increasing maturity in a similar manner to the CO₂ ultramicropore volumes. This large increase in micropore volume might be due to the generation of slightly larger micropores in kerogen through which nitrogen can diffuse more readily.

Table 5.4: Shale and kerogen pore volumes measured by different techniques.

Sample	Pore Diameter Range [nm]							BET Surface Area
	< 0.7	< 1.5	0.3 – 2		6-1093		SPV+ MICP	
	CO ₂ (0°C) UMP	CO ₂ (0°C) NLDFT	N ₂ (-196°C) MPV	CO ₂ (-78°C) SPV	MICP	TPV		
	mm ³ g ⁻¹							
Shale								
WIC7145	6.7	4.6	2.9	16.4	53.1	68.4	69.5	6.7
WIC7155	8.0	7.7	1.6	15.5	48.1	60.7	63.6	4.3
HAR7038	5.2	4.3	-	8.4	5.1	12.7	13.5	-
HAR7060	4.6	5.7	-	8.3	7.8	18.1	16.1	-
HAD7090	6.4	6.0	11.6	16.2	26.0	50.1	42.2	25.1
HAD7119	6.0	4.0	9.1	13.0	45.1	61.1	58.1	21.0
Kerogen								
WIC7145	32.5	21.8	5.2	74.8				12.5
WIC7155	28.8	24.3	3.7	71.8				7.5
HAR7038	27.0	25.3	11.9	68.5				27.3
HAR7060	33.5	33.1	9.0	87.0				17.9
HAD7090	50.6	42.4	34.6	113.0				68.1
HAD7119	54.6	50.8	24.2	103.6				56.1

UMP = Ultramicropore Volume determined using the DR equation and CO₂ sorption at 0°C; NLDFT = Pore volume determined by applying a Non-Local Density Functional Theory model to Carbon Dioxide 0°C isotherms, N₂ MPV = Micropore volume determined by the DR equation from -196°C nitrogen isotherms; SPV = Sorption pore volume based on Gurvitch's Rule and calculated from CO₂ isotherms at -78°C; MICP = Pore Volume from mercury injection capillary pressure porosimetry, the estimated pore constriction sizes were derived from Young-Laplace equation for cylindrical capillaries (see Chapter 2); TPV = Total pore volume from equation 2 using mercury bulk density and Grain Density/Helium Pycnometry (skeletal volume); Total Porosity = 1 – Mercury bulk density / (Grain or He density), equation 3 ; SPV+MICP = sum of CO₂ -78°C sorption pore volume and MICP pore volume, equation 4.

5.3.5 Methane Sorption

Shale

Shale isotherms were measured at 45, 65 and 85°C and up to ~14 MPa. Excess shale isotherms are shown in Figures 5.6 and 5.7. Tabulated isotherm data are given in Appendix C, Section B2. Isotherms at 45°C for HAR7060 and HAD7090 show a distinct excess maximum, while the other isotherms show plateaus. Maximum surface excess uptakes are between 0.096 and 0.119 mmol g⁻¹ for Wickensen and Hadessen shales while uptake on Harderode shales were lower, with maxima of 0.054 and 0.070 mmol g⁻¹ (Appendix C, Section B2). Maximum methane surface excess uptake decreases with increasing temperature for all shales. Furthermore, at 65°C and 85°C the isotherms do not have a distinct maximum in the pressure range used in this study.

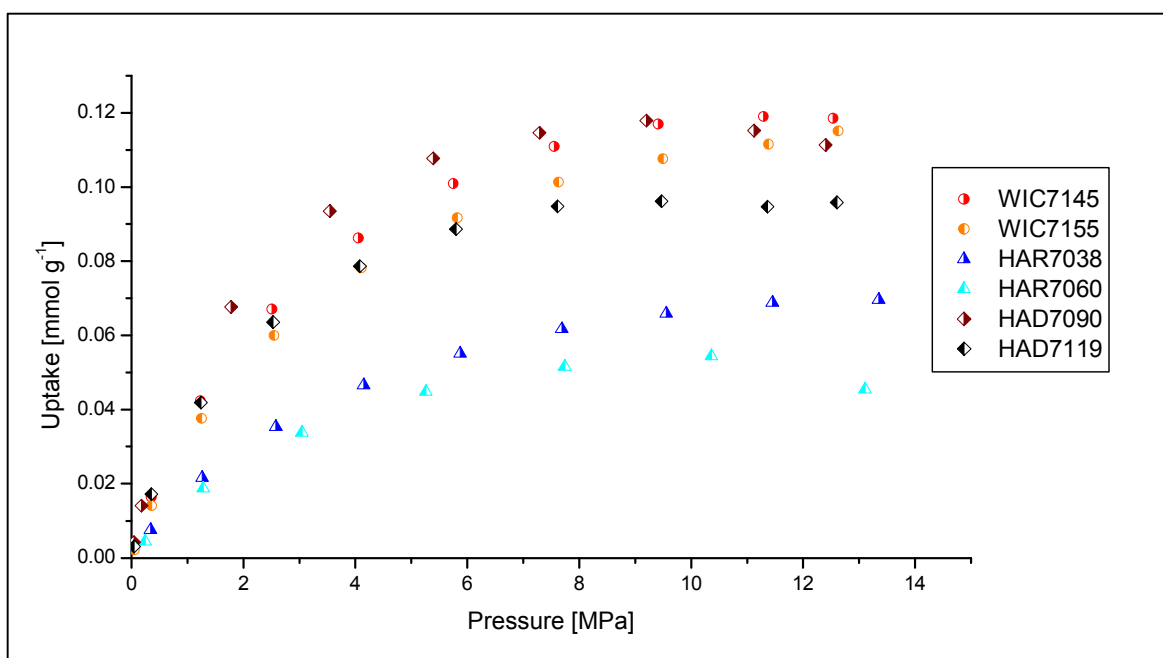


Figure 5.6: Methane surface excess adsorption isotherms at 45°C on Posidonia shales.

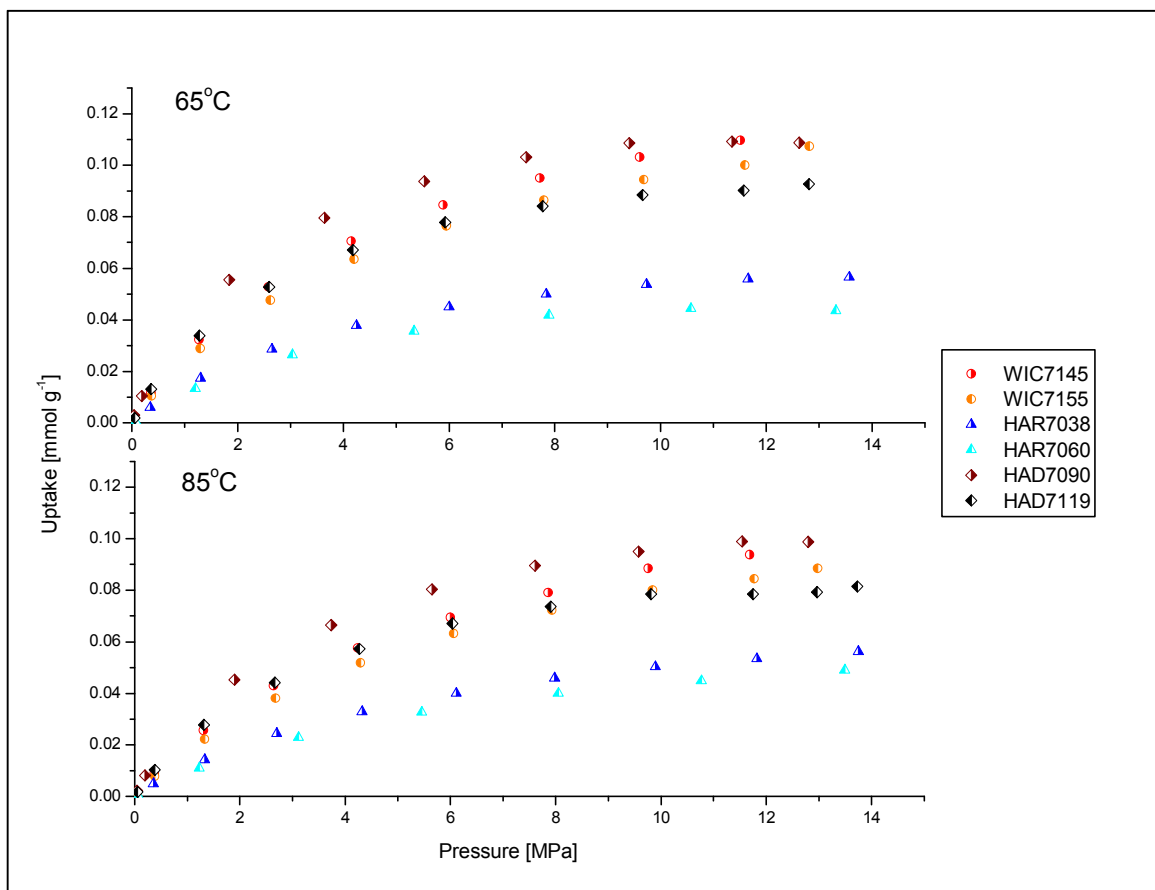


Figure 5.7: Methane surface excess adsorption isotherms at 65°C and 85°C on Posidonia shales.

Kerogen

Methane sorption isotherms on isolated kerogens were measured at 45 and 65°C and up to ~14 MPa. The surface excess isotherms are shown in Figures 5.8 and 5.9 and tabulated data are given in Appendix C, Section B2. The pressure range is not large enough for the isotherms to reach the excess maximum or plateau. WIC and HAR kerogens take up between 0.45 - 0.58 mmol g⁻¹ at ~13.5 MPa and 45°C, which is similar to Pennsylvanian coals of various rank (VR = 0.72 – 1.56%R₀).⁵⁴ Maximum uptake on HAD kerogens (R₀ = 1.45%) was higher (0.90 - 0.95 mmol g⁻¹ at 45°C and ~14 MPa) than on WIC (R₀ = 0.53%) and HAR (R₀ = 0.89%) kerogens. This shows the increase in adsorption capacity at the onset of the gas window.

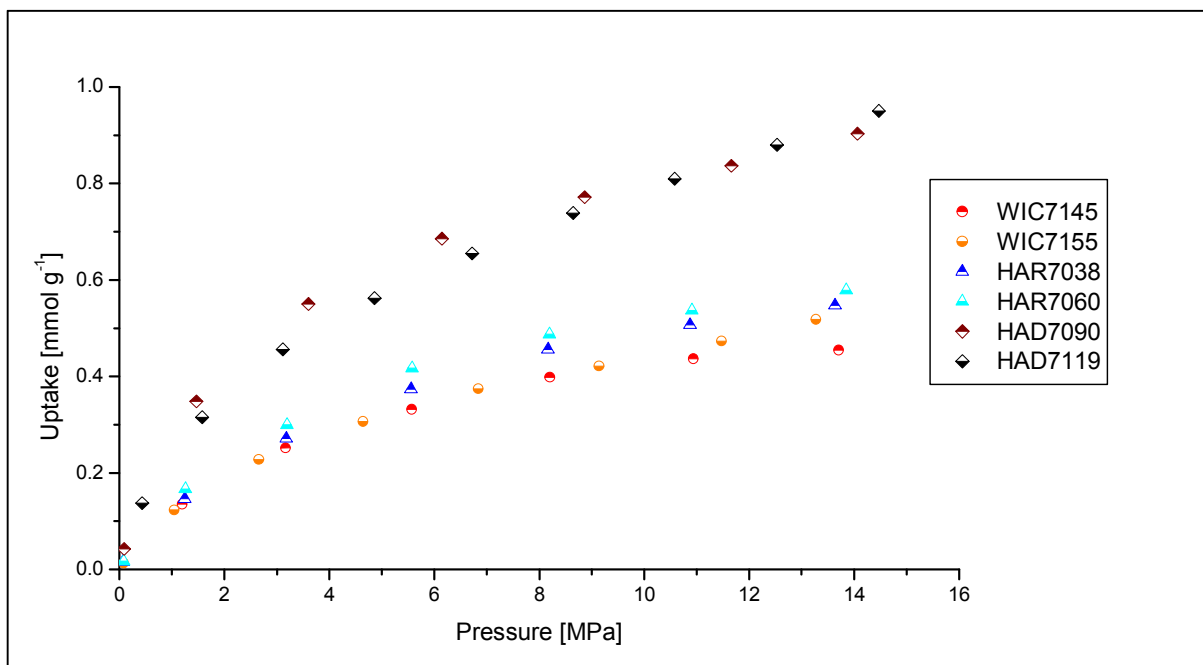


Figure 5.8: Methane surface excess isotherms for Posidonia kerogens at 45°C.

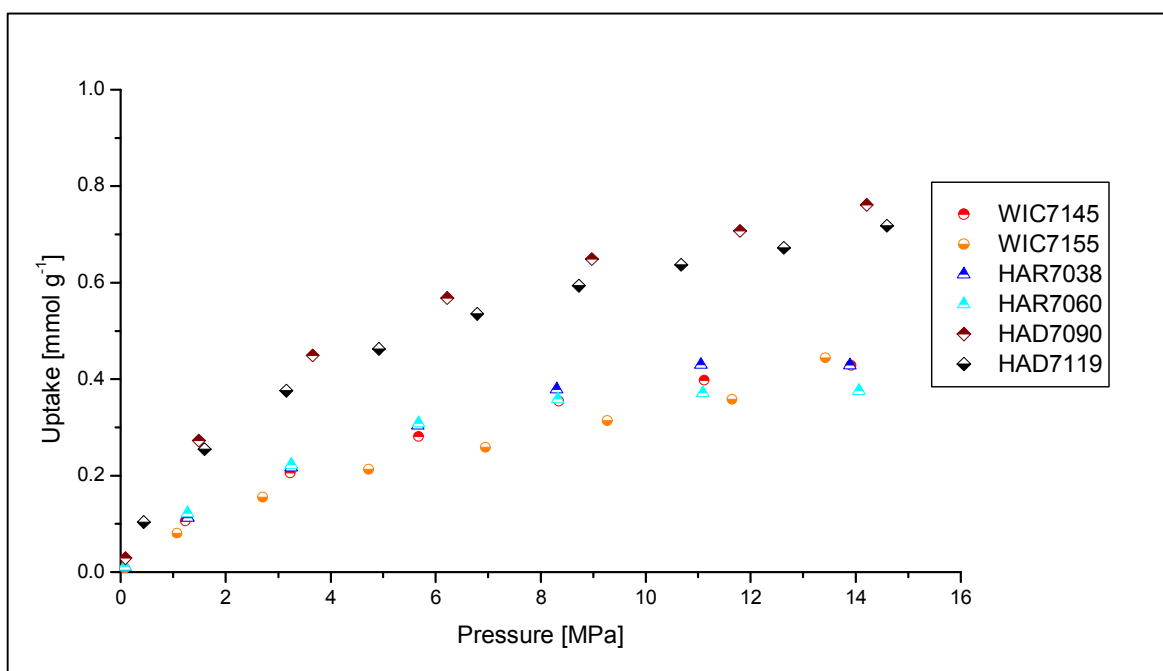


Figure 5.9: Methane surface excess adsorption isotherms for Posidonia kerogens at 65°C.

Methane Sorption and Pore Volumes

There is only a weak correlation ($R^2=0.48$) of maximum excess uptake at 45°C on shale and TOC (see Figure 5.10). However, there is a very strong correlation of methane uptake and CO₂ sorption pore volume. Figure 5.11 shows methane uptake on shale and kerogen at 45°C and 10.0 MPa against the CO₂ sorption pore volume, with a regression line which goes through the origin. A strong correlation also exists between methane uptake at 65°C and 11.5 MPa and CO₂ sorption pore volume (see Figure 5.12). Similar correlations are obtained at lower pressures and also at 85°C (see Appendix C, Section E). The correlations suggest that

supercritical methane sorption on Posidonia shales and kerogens mainly takes place in pore volumes as measured by CO₂ sorption at -78°C. Both the CO₂ subcritical and methane supercritical adsorption studies show that kerogens have much larger adsorption than for the corresponding shales (see Figures 5.11 and 5.12). Comparison of kerogen and shale isotherms with TOC measurements indicate that the shale adsorption exceeds that which can be accounted for by the kerogen alone, indicating that significant adsorption occurs in the inorganic phase of the shale. The Sorption mass balances for kerogens and inorganic phase materials (clays etc.) are discussed later.

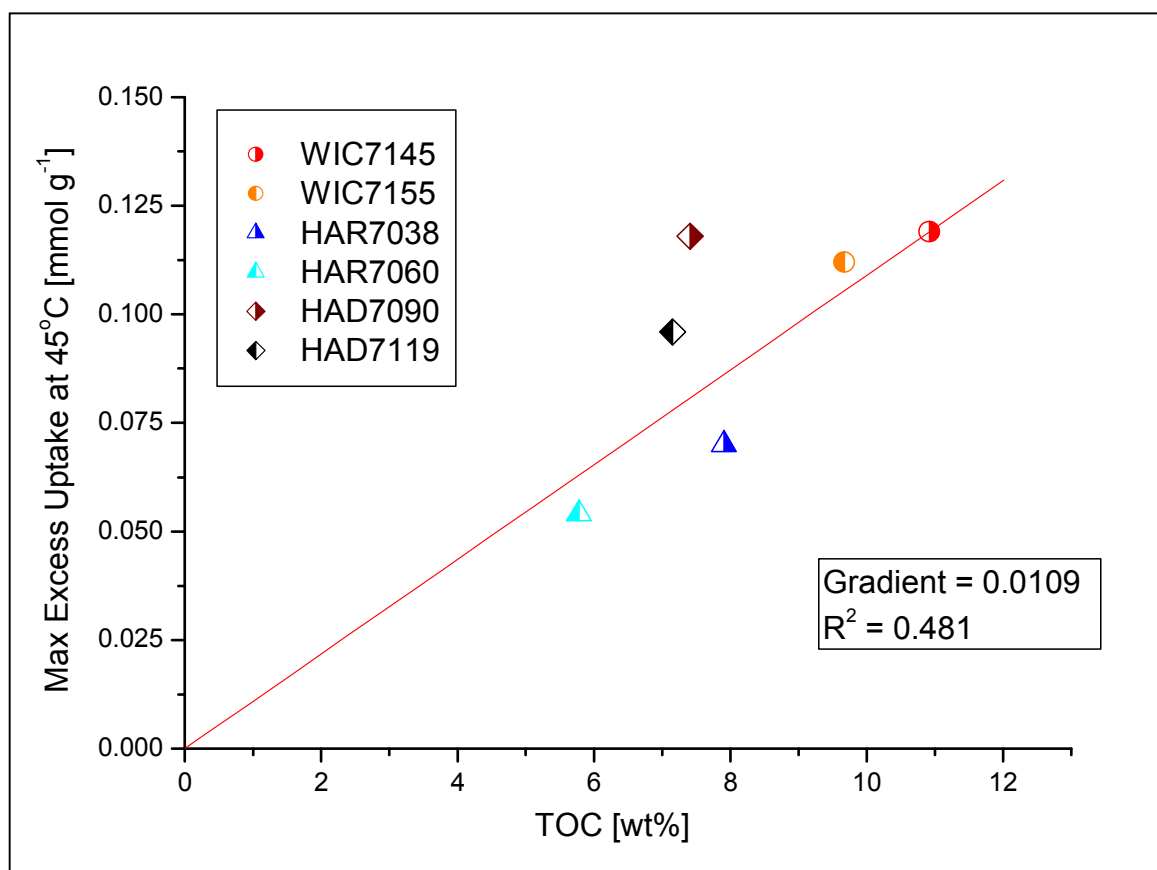


Figure 5.10: Plot of Maximum methane surface excess uptake at 45°C versus TOC.

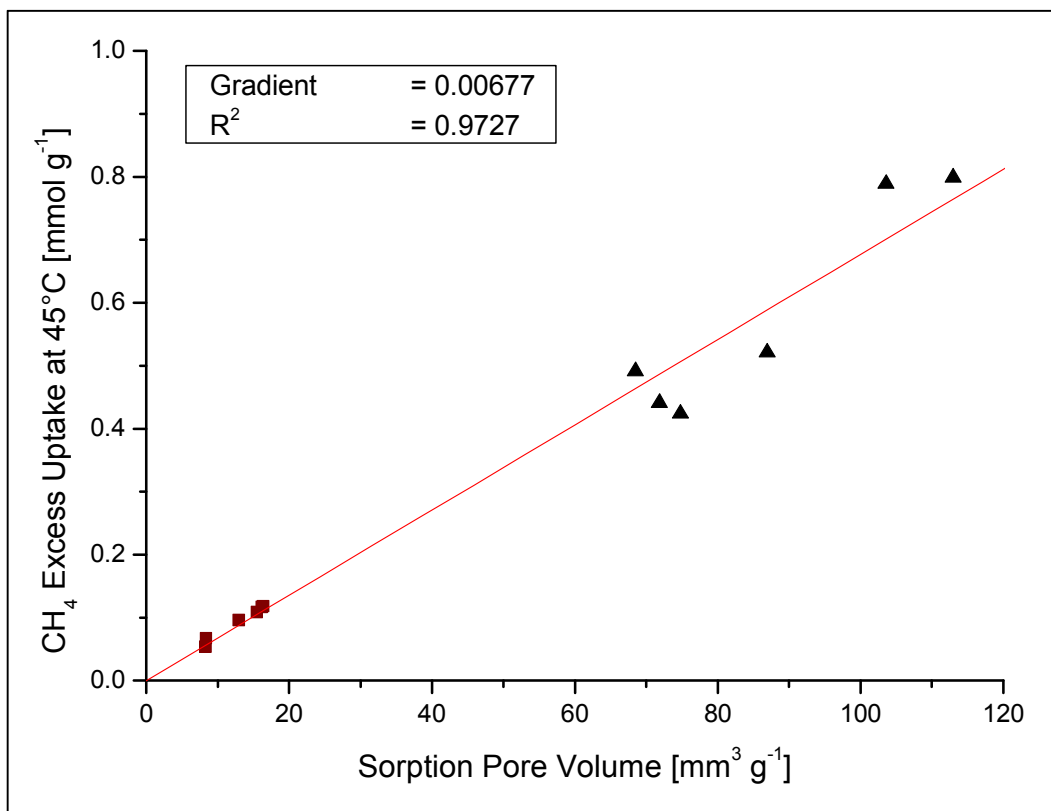


Figure 5.11: Graph of CH₄ maximum excess uptake at 45°C and 10 MPa on shale (squares) and kerogen (triangles) versus CO₂ sorption pore volume (-78°C).

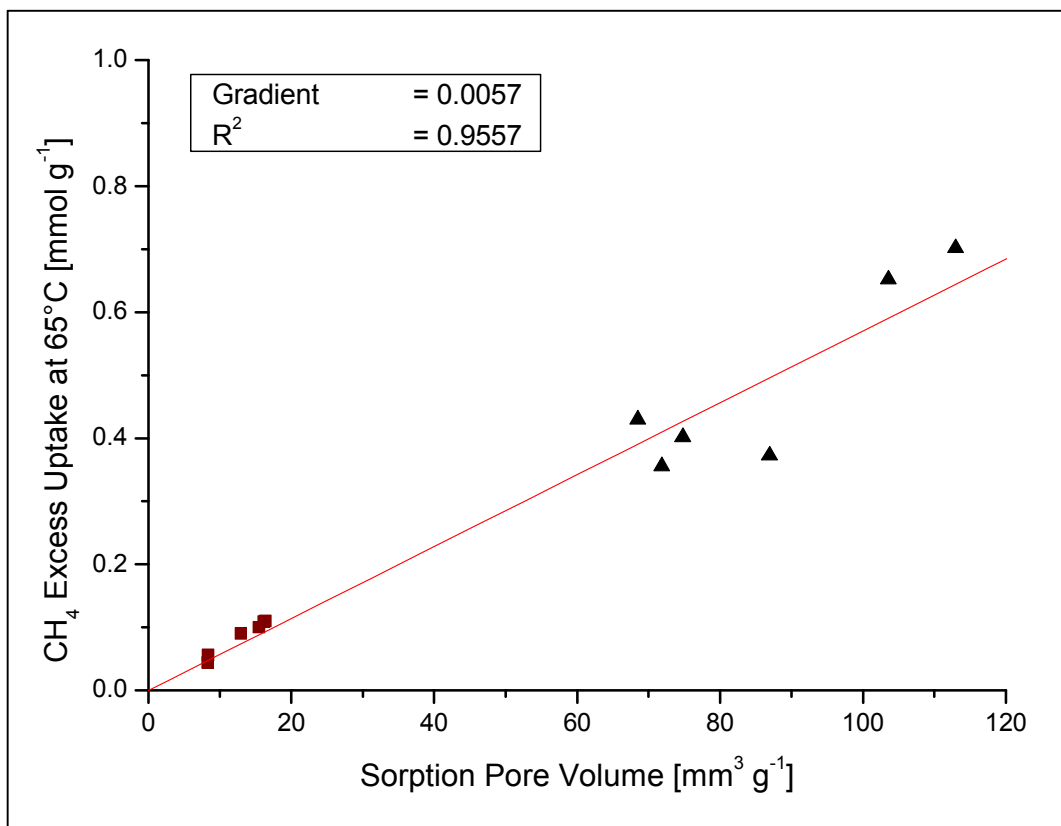


Figure 5.12: Graph of CH₄ excess uptake at 65°C and 11.5 MPa on shale (squares) and kerogen (triangles) versus CO₂ sorption pore volume (-78°C).

Absolute isotherms and parameterization

The absolute isotherm can be calculated from the excess isotherm using the following equation

$$n_{ab} = n_{ex} + \rho_b * V_{ad}$$

Equation 5.1 – Absolute and Excess Sorption

Where n_{ex} is the excess amount adsorbed, ρ_b is bulk gas phase density and V_{ad} is the adsorption pore volume. Equation 1 has been used for crystalline zeolites and metal organic frameworks, where the structure can be determined from X-ray or neutron diffraction studies. Good agreement has been observed between total pore volumes from crystallographic data and pore volumes measured by gas adsorption for microporous metal organic framework materials.^{55,56} In these materials, V_{ad} is assumed to be equal to the (crystallographic) total pore volume, which is an inherent property of the adsorbent.^{57,58} However, for heterogeneous materials, such as shales, which have a wide pore size distribution, this assumption is more problematic since adsorption in the larger pores may not be significant.⁵⁹ In the shales used in this study, the subcritical CO₂ sorption pore volumes were 21-32% of the total pore volume for the WIC and HAD shale samples and 46-66% of the total pore volume for the HAR shale samples (see Table 5.4). It is evident that in these materials, V_{ad} is significantly lower than the total pore volume. Studies of a high maturity Alum shale showed that subcritical pore volumes obtained from adsorption of CO₂ (-78°C and 0°C), N₂ (-196°C) and CH₄ (-161°C) agreed within $\pm 5\%$.¹¹ Hence, the CO₂ sorption pore volume at -78°C is a reasonable estimate for an upper limit for V_{ad} . Therefore, in this study, a sorption volume balance for the shales was investigated by measuring the total pore volume (< 1093 nm) from helium pycnometry, grain density and mercury bulk density; mercury injection capillary pressure porosimetry and gas sorption pore volumes.

The Young-Laplace equation for cylindrical capillaries indicates that mercury enters pores with constrictions with equivalent diameters > 1093 nm at 1.379 MPa. Therefore, at 1.379 MPa, $1/\rho_{HgBulk}$ will be equal to the volume of the shale and pores < 1093 nm, where ρ_{HgBulk} is the mercury bulk density of the shale. Assuming helium enters all accessible pores and is not adsorbed; $1/\rho_{He}$ is equal to the volume of shale, where ρ_{He} is the density of the shale measured by helium pycnometry. Therefore, the total pore volume (< 1093 nm) is given by the following equation.

$$Total\ Specific\ Pore\ Volume\ (< 1093\ nm) = \frac{1}{\rho_{HgBulk}} - \frac{1}{\rho_{He}}$$

Equation 5.2 – Total Pore Volume

and the Total Porosity (< 1093 nm)

$$Total\ Porosity\ (< 1093\ nm) = 1 - \frac{\rho_{HgBulk}}{\rho_{He}}$$

Equation 5.3 – Total Pore Volume

Alternatively, since the helium and grain densities are similar within experimental error, ρ_{He} can be replaced by ρ_{Grain} in equations 2 and 3.

Figure 5.3 shows that a graph of Total Pore Volume (< 1093 nm) versus CO₂ sorption pore volume (CO_2SPV) + mercury injection pore volume ($MICP_{PV}$) corresponding to equation (4) below, has good linearity ($R^2 = 0.974$) for the 6 shales studied, which vary markedly in maturity.

$$Total\ Pore\ Volume(< 1093\ nm) = CO_2\ SPV + MICP_{PV}$$

Equation 5.4 – Pore Volume Balance in Shales

The $MICP_{PV}$ corresponds to the difference between the mercury injected at 1.379 and 268.9 MPa. The $CO_2\ SPV$ is the pore volume obtained from CO₂ adsorption at 0.1 MPa and -78°C using a CO₂ adsorbed phase density of 1.177 g cm⁻³. The $CO_2\ SPV$ characterizes the microporosity and some mesoporosity where gas adsorption predominates, while the $MICP_{PV}$ characterizes the mesoporosity > 5.6 nm and macroporosity up to 1093 nm. The upper size limit for significant CO₂ adsorption is unknown, but the linear relationship in Figure 5.3 indicates that it is approximately 5-6 nm. However, there will be very small amounts of adsorption in larger pores. The linearity of the relationship indicates that all the accessible porosity < 1093 nm has been taken into account by the combination of CO₂ sorption and mercury injection. It is not possible to use mercury injection porosimetry for isolated kerogens. The strong linear ($R^2 = 0.9557$ and 0.9727) correlation between CH₄ sorption uptake and CO₂ sorption pore volume for both shales and kerogens used in this study suggest that supercritical methane sorption in shales and kerogen takes place in the CO₂ sorption pore volume (see Figures 5.11 and 5.12). These correlations support the use of the CO₂ sorption

pore volume (-78°C) for V_{ad} to estimate absolute isotherms and thus quantify the sorbed phases in shales. Also, it provides an estimate of adsorbed phase versus bulk “free” gas phase contributions to methane stored in shale.

The absolute isotherms of shales and kerogen are shown in Figure 5.13 and Figure 5.14. Absolute amounts on HAD shales at ~13 MPa and 85°C are 0.14 and 0.18 mmol g⁻¹. HAD kerogens exhibit much higher absolute amounts adsorbed of 1.21 and 1.31 mmol g⁻¹ (at 13 MPa and 65°C). Mass balance calculations between the shale and kerogen data obtained by normalizing these uptakes with TOC and comparison with the uptake on shale under the same conditions, shows that approximately 50% of the methane uptake in HAD shales is within the kerogen.

The Dubinin-Radushkevich and Langmuir equations can be used as semi-empirical equations to parameterize the methane absolute isotherms. The supercritical Dubinin-Radushkevich equation has been shown to describe methane isotherms more accurately than the Langmuir equation over a wide temperature range (27-200 °C) for an Alum Shale sample.¹¹ The DR micropore volume was 77 % of the CO₂ sorption pore volume in the Alum Shale and this is significantly higher than the shales used in this study, which were in the range 40-62%. However, the Posidonia Shale and kerogen absolute and excess isotherms for 45, 65 and 85°C were described more accurately by a modified version of the Langmuir equation:

$$n_{ab} = n_{ab,max} \frac{K(T) f}{1 + K(T) f}$$

Equation 5.5 – Langmuir Equation

where $n_{ab,max}$ is the maximum absolute amount adsorbed, $K(T)$ is the Langmuir parameter, f is fugacity. One fitting parameter can be eliminated by using $n_{ab,max} = CO_2SPV * \rho_{ad,max}$ where CO_2SPV is the CO₂ sorption pore volume and $\rho_{ad,max}$ is the maximum adsorbed phase density.

The shale and kerogen absolute and excess isotherms were fitted to Equation 5 with 2 fitting parameters for shales and kerogens, the temperature-dependent Langmuir parameter $K(T)$ and the maximum adsorbed phase density ($\rho_{ad,max}$). Due to the narrow temperature range (45-85°C for shale and 45-65°C for kerogen) $\rho_{ad,max}$ was assumed to be independent of temperature. Other studies on shale sorption have used pressure instead of fugacity in the Langmuir model.^{12,16} The use of pressure instead of fugacity gave almost identical results to those presented in Table 5.4.

Table 5.5: Parameters calculated by fitting the Langmuir equation to the shale methane sorption data. The error column shows the accumulated error (residuals sum of squares) of the fit. The adsorbed phase density is assumed to be constant over the (relatively small) temperature range.

Sample	ρ_{ad}	K(45)	K(65)	K(85)	SPV	Error
	kg m ⁻³	MPa ⁻¹				
Shale						
WIC 7145	371	0.112	0.087	0.068	16.4	1.3E-04
WIC 7155	388	0.099	0.077	0.061	15.5	8.5E-05
HAR 7038	415	0.102	0.074		8.4	3.2E-05
HAR 7060	340	0.115	0.084		8.3	4.7E-06
HAD 7090	293	0.193	0.152	0.118	16.2	1.5E-04
HAD 7119	299	0.188	0.147	0.114	13.0	8.1E-05
Kerogen						
WIC 7145	478	0.058	0.048		74.8	2.0E-03
WIC 7155	503	0.057	0.040		71.8	2.7E-03
HAR 7038	516	0.064	0.048		68.5	2.0E-03
HAR 7060	441	0.069	0.047		87.0	4.5E-03
HAD 7090	356	0.118	0.089		113.0	9.6E-03
HAD 7119	614	0.054	0.040		103.6	4.5E-02

Good fits were obtained for shale and kerogen isotherms. The calculated parameters are shown in Table 5.5 and the fits of the model to the absolute isotherms at 65°C are shown in Figure 5.13 for shale and Figure 5.14 for kerogen. The corresponding CH₄ adsorption data at 45°C and 85°C are given in Appendix C, Section C. The adsorbed phase densities of methane on shale are all below the liquid density of methane (425.1 kg m⁻³ at boiling point: -161.49°C and 101.3 kPa).⁵² The hypothesis is that adsorbed phase densities in the pores do not exceed the liquid density of the sorptive. The adsorbed phase densities of WIC and HAR shales are within 11% of the methane adsorbed phase density on shale determined by molecular simulations (370 kg m⁻³) by Ambrose et al.⁶⁰ The adsorbed phase densities calculated for HAD shales (~ 290 kg m⁻³) are lower. This could be due to wider pores in the HAD gas window shales ($R_0 = 1.45\%$), as indicated earlier. The Langmuir constants and adsorbed phase densities are similar to the values determined by Gasparik et al. on Aalburg and Sleen shale samples at 65°C ($K(65) = 0.064 - 0.104 \text{ MPa}^{-1}$; 295 – 332 kg m⁻³).¹⁶ The calculated adsorbed phase densities for all kerogens with the exception of HAD7090 are above the liquid methane density suggesting that the Langmuir model may have significant limitations for determining physically reasonable sorption parameters or possibly, there are sorption-induced volumetric changes.

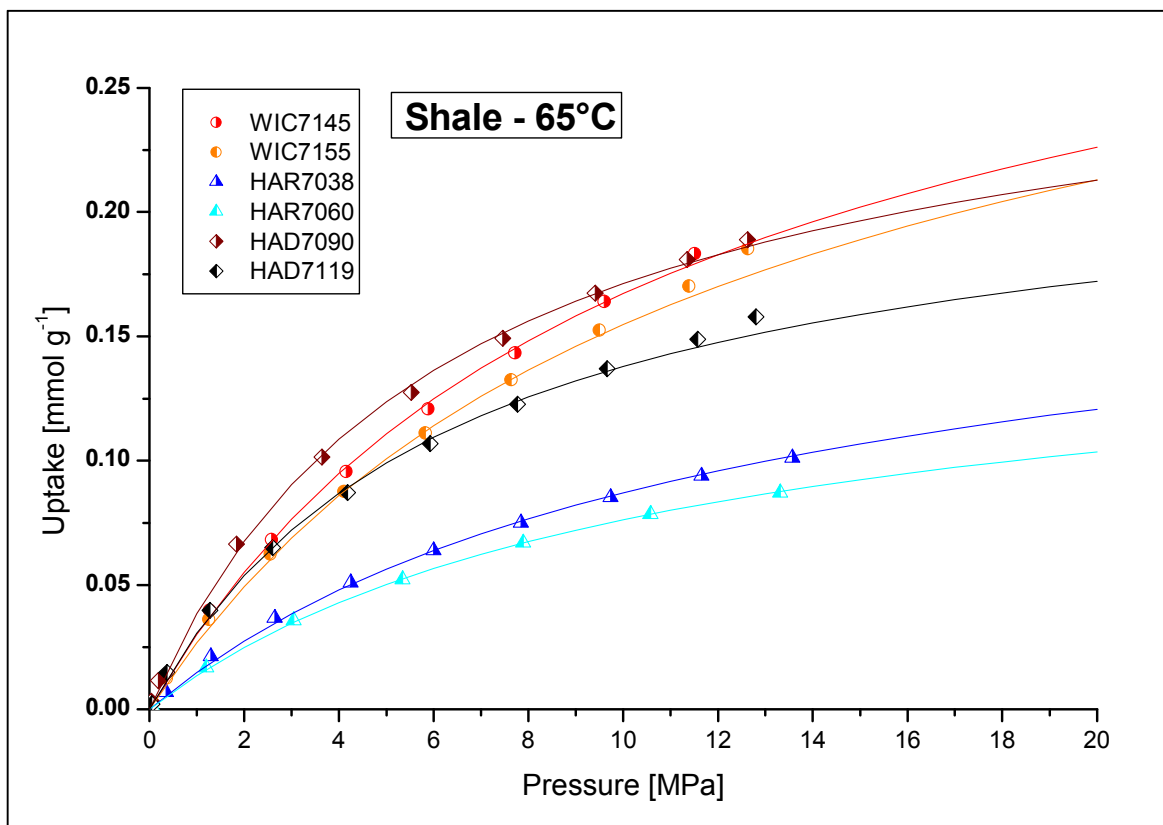


Figure 5.13: Absolute methane isotherms on shale at 65°C. It is assumed that the volume of the adsorbed phase is equal to the CO₂ sorption pore volume. The lines represent the Langmuir fit to the absolute and excess data (simultaneous fit).

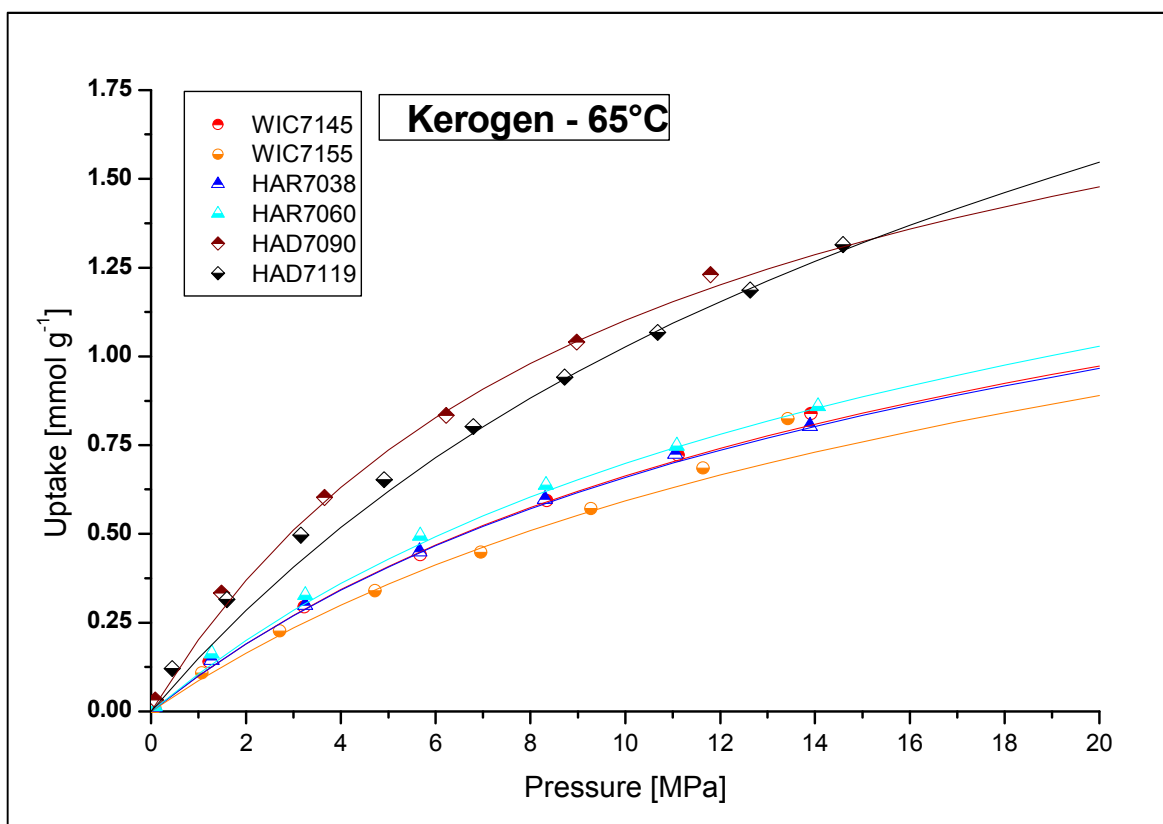


Figure 5.14: Absolute methane isotherms on kerogen at 65°C. It is assumed that the volume of the adsorbed phase is equal to the CO₂ sorption pore volume. The lines represent the Langmuir fit to the absolute and excess data (simultaneous fit).

Distribution of high-pressure methane sorption

Mass balances of methane sorption on shales were determined to investigate the distribution of sorption sites between kerogen plus clay minerals and the organic-inorganic interface. Methane sorption on clay minerals has been studied previously.^{61,62} Ji et al⁶¹ have measured methane sorption at 65°C up to around 10 MPa on montmorillonite, kaolinite, chlorite and illite at 65°C while Liu et al⁶² measured methane sorption on montmorillonite, kaolinite and illite at 60°C and up to 18 MPa. The clay sorption data and kerogen sorption data were normalized by the XRD data and TOC, respectively, and compared against shale isotherm at 65°C. Results are shown in Figure 5.15. Around 45 – 60% and 60 – 70% of the methane sorption can be attributed to clays and kerogen in WIC and HAD shales, respectively, whereas kerogen and clay minerals can account for the entire sorption capacity measured on HAR shales.

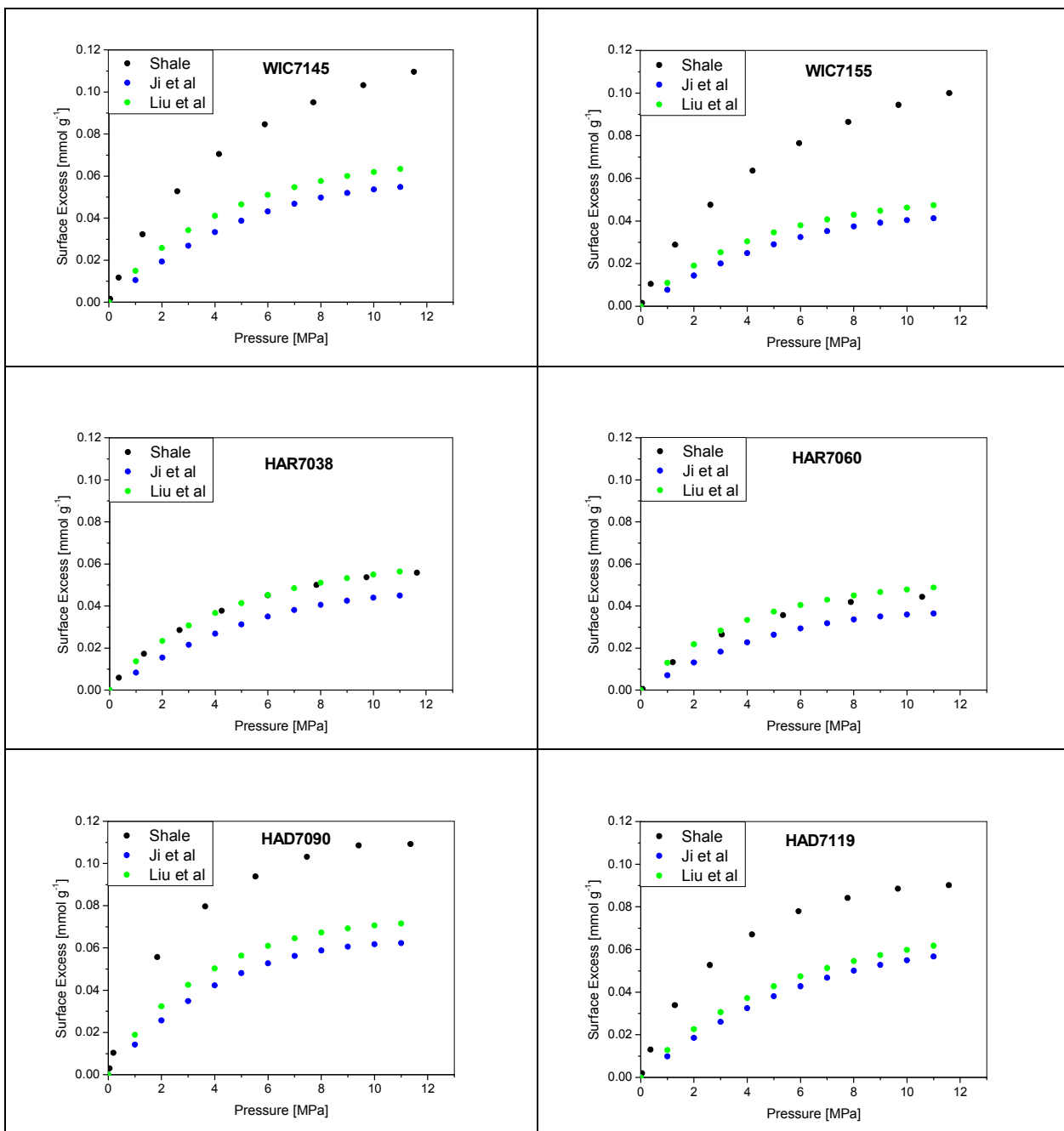


Figure 5.15: Mass balances of methane surface excess sorption on shale at 65°C. The experimental shale excess isotherms (black) are compared to mass balance isotherms calculated from the sorption excess data for kerogen, TOC and mineral composition determined in this study and sorption data for clay minerals reported by Ji et al⁶¹ (blue) and Liu et al (green).⁶² The isotherms were obtained by fitting kerogen and clay mineral data to the Langmuir equation and components were normalized and summed for comparisons with the experimental shale isotherms.

Enthalpies of Adsorption

The isosteric enthalpies of adsorption can be calculated for a pure gas using the equation below.⁶³

$$Q_{st,n} = RT^2 \left[\frac{\delta \ln P}{\delta T} \right]_n$$

Equation 5.6 – van't Hoff Equation

where $Q_{st,n}$ is the isosteric enthalpy of adsorption at a surface excess loading n , P is pressure, T is temperature and R is the gas constant. The surface excess is approximately equal to the absolute amount adsorbed at low pressure. The isosteric enthalpy of adsorption at zero surface coverage ($Q_{st,n=0}$) is a fundamental measure of the adsorbate interaction with the adsorbent. At the zero surface coverage adsorption limit, the isosteric enthalpies of adsorption derived from surface excess and absolute isotherms should be identical.

The methane absolute isotherms were calculated using equation 1 and the CO₂ sorption pore volume (-78°C). The isosteric enthalpies of adsorption of methane on shale and kerogen were calculated at zero surface coverage by two methods (Myers and Monson⁶⁴ and virial equation^{65,66}). The virial equation at low surface coverage is given below:

$$\ln\left(\frac{n_{ab}}{p}\right) = A_0 + A_1 n_{ab}$$

Equation 5.7 – Virial Equation

where n_{ab} is the absolute amount adsorbed (mmol g⁻¹), p is pressure (Pa), A_0 and A_1 are virial parameters. The slope of the graph of A_0 against T^{-1} gives ($Q_{st,n=0}/R$). The Henry's Law constant is given by the equation below:

$$K_H = \exp(A_0)$$

Equation 5.8 – Virial Equation and Henry's Law Constant

The $Q_{st,n=0}$ was also determined using the Langmuir equation 5, which provide a good fit for the experimental data. Myers and Monson define the absolute uptake as the amount of gas inside the pore volume and use the Langmuir equation to derive Q_{st} .⁶⁴ In the case of shales, which have a significant amount of meso- and macroporosity, the sorption pore volume is the volume of increased density due to sorption. The equation derived is:

$$C = \frac{1}{P^0} \exp\left(\frac{A}{R}\right) \exp\left(\frac{-B}{RT}\right)$$

Equation 5.9 – Myers and Monson

where C is the constant in the Langmuir equation, which is a function of temperature; B is the enthalpy of adsorption (kJ mol^{-1}), and $P^0 = 1 \text{ bar}$ is the pressure at the perfect-gas reference state. The temperature-independent component $\exp(A/R)$ is an entropic factor.

The enthalpies of CH_4 adsorption at zero surface coverage on shales and kerogens calculated by both methods are shown in Table 5.6. The enthalpies of adsorption for shales and kerogen are very similar for calculations by both methods. The average values for $Q_{st, n=0}$ for shale are $14.4 \pm 1.6 \text{ kJ mol}^{-1}$ (Virial Method⁶⁵) $12.2 \pm 1.0 \text{ kJ mol}^{-1}$ (Myers and Monson Method⁶⁴) while the values for kerogens are $13.1 \pm 1.9 \text{ kJ mol}^{-1}$ (Virial Method⁶⁵) and $13.4 \pm 3.0 \text{ kJ mol}^{-1}$ (Myers and Monson Method⁶⁴). No clear trend with maturity was observed. The $Q_{st, n=0}$ values are slightly lower than the corresponding enthalpy of $19.2 \pm 0.1 \text{ kJ mol}^{-1}$ determined at $0.025 \text{ mmol g}^{-1}$ for an Alum shale, which had a greater proportion of ultramicroporosity. Similar results have been obtained for a Barnett shale from the gas window ($R_0 = 2.01\%$, $Q_{st} = 18.4 \text{ kJ mol}^{-1}$).¹² Shales from the pre-gas window had lower isosteric enthalpies of adsorption ($Q_{st} = 7.3 - 15.3 \text{ kJ mol}^{-1}$).¹² The range of isosteric enthalpies obtained for CH_4 adsorption on other porous materials are similar (activated carbon ($Q_{st} = 9-20 \text{ kJ mol}^{-1}$)⁶⁷⁻⁶⁹ and coal ($Q_{st} = 10-22 \text{ kJ mol}^{-1}$)^{70,71}). It is apparent that the strength of interactions of methane with porosity in various shales are similar and also similar to CH_4 adsorption on carbonaceous materials. There are, at most, small differences in adsorption enthalpy with maturity or uptake for the samples studied. The thermodynamics discussed above and the correlation of supercritical CH_4 adsorption uptake with CO_2 sorption pore volume (-78°C) for shales suggest that the amount adsorbed is controlled by the available porosity ($< \sim 6 \text{ nm}$) rather than the strength of the interaction of CH_4 with the pore walls in shales.

Table 5.6: Isothermic Enthalpies of Adsorption of CH₄ on shales and kerogens at zero surface coverage ($Q_{st,n=0}$).

Calculation Method	Shale $Q_{st,n=0}$ (kJ mol ⁻¹)					
	Virial	15.1 ± 0.1	15.7 ± 2.8	11.8 ± 0.4	12.9 ± 2.4	15.7 ± 0.8
Monson & Myers	11.7 ± 0.1	11.2 ± 0.4	14.0 ± 0.5	12.7 ± 1.9	11.7 ± 0.1	12.1 ± 0.3
	Kerogen $Q_{st,n=0}$ (kJ mol ⁻¹)					
Virial	11.2		14.5	12.8	15.7	11.5
Myers & Monson	8.5 ± 1.3	15.8 ± 2.8	12.9	17.2 ± 1.4	12.6 ± 1.7	13.4 ± 0.8

1: The Virial equation was used to calculate the enthalpy at zero surface coverage (ZSC) $Q_{st,n=0}$ from the absolute isotherm. 2: The method of Myers and Monson was used to calculate $Q_{st,n=0}$. Kerogen WIC7155: sorption data did not give a suitable fit to the Virial equation.

5.4 Discussion

Comparison of the subcritical CO₂ isotherms for Posidonia shales and the corresponding kerogen isotherms shows that they have similar shapes. Both the DR micropore volumes (CO₂, 0°C) and sorption pore volumes (CO₂, -78°C) increase with increasing total pore volumes and have approximately linear trends for the shales (see Appendix C, Section E). The DR micropore volumes (CO₂, 0°C) and sorption pore volumes (CO₂, -78°C) have a similar trend for the kerogens and better linearity ($R^2 = 0.8893$) (see Appendix C, Section G). However, no specific trends are expected between these parameters. The DR micropore volumes (CO₂, 0°C) and sorption pore volumes (CO₂, -78°C) for the kerogens are 3.6-9.1 and 4.6-10.5 times larger than the corresponding shales indicating the potential importance of the kerogen in determining CH₄ storage capacity. Comparison of the DR micropore volumes (CO₂, 0°C) and sorption pore volumes (CO₂, -78°C) for shales and kerogens shows no correlation suggesting that adsorption in the inorganic phase (clays etc.) makes a significant contribution to subcritical adsorption (see Appendix C, Section G). Comparison of the supercritical high pressure methane isotherms for the Posidonia kerogens and shales shows that similar trends to the CO₂ subcritical isotherms are observed, with the kerogen uptakes being ~ 3.6 – 8.4 times greater than the corresponding shale at 11.5 MPa and 65°C. However, the TOC values for the samples studied are in the range 5.78 -10.92%, and therefore, the inorganic phase is >89% of the shales. The sorption mass balance between kerogen and shale indicates that methane storage in the inorganic phase of dry shales is also significant.

Posidonia kerogens have DR micropore volumes which are at the lower end of the range of micropore volumes measured on various coals ($0.014 - 0.057 \text{ cm}^3 \text{ g}^{-1}$).⁷²⁻⁷⁴ A trend of DR micropore volume with maturity for coals has been reported with DR micropore volume decreasing from high volatile to medium volatile bituminous coals and then increasing with further coalification.^{40,72,75} The decrease in micropore volumes was attributed to the filling of pores by low-volatile hydrocarbons and the subsequent increase to the cracking of the occluded oils with coalification.^{40,75} Similar trends were observed in DR micropore and sorption pore volumes in this study, suggesting that there is pore generation and/or pore opening by cracking of occluded oil in gas-window Posidonia kerogens. Micropore 'blocking' by bitumen in the oil-window kerogens (HAR) may take place, similar to coal. The presence of low-volatile bitumen is suggested by the relatively low helium densities of HAR kerogens compared with HAD kerogens, which had the highest densities (see Table 5.1). The shale CO₂ DR micropore and sorption pore volumes reach a minimum in the oil window. However, kerogens do not show a well-defined minimum in the oil window. There is no significant change from WIC to HAR, but an increase to HAD. It is apparent that changes in the microporosity of kerogen are probably controlling changes in the microporosity of shales into the gas-window.

The shale pore volume is comprised of contributions from inorganic materials (including phyllosilicates, etc), kerogens and the interface region between these materials. The contribution of the kerogen component to the shale porosity can be determined by normalizing the kerogen pore volume with TOC. This shows that approximately half of the CO₂ sorption pore volume for a given shale is within the organic matter for all Posidonia shale samples. The other part of the porosity cannot be attributed to any specific mineral type as comparisons of mineral composition with pore volumes do not show any correlations. However, previous publications have concluded that micropores are present in clay but not in quartz,¹⁴ although the clay content variation in Posidonia shales (illite/smectite ranging from only 18.5 – 26.2 wt%, kaolinite 1.1 – 8.9 wt%) is too small to show any trend with pore volume. The role of clays for sorption in dry shales is consistent with the similar shapes of kerogen and clay mineral isotherms.¹⁴

Since the sum of porosity measured by (a) CO₂ adsorption at -78°C and (b) mercury injection is very similar to total porosity, and since mercury injection measures pore constrictions larger than approximately ~6 nm, we infer that most of the CO₂ sorption porosity is in pores smaller than ~6 nm. The very strong correlation between CH₄ maximum excess uptake and CO₂ sorption volume suggests that most CH₄ is sorbed in pores which are smaller than ~ 6 nm and associated with both kerogen and clay minerals. Grand canonical Monte Carlo simulations of methane adsorption have been carried out for graphitic surfaces, as

models for kerogens, across a range of pore sizes for various temperature and pressure conditions. The results suggest that adsorbed methane density changes non-monotonically with increasing pore width, and decreases to a minimum in 1.2 nm pores at 12 MPa.⁷⁶ Cai et al⁷⁷ suggested that the pore volume, with pore widths in the range 2 – 5 nm, was the primary control for methane adsorption capacity of coals from Northeastern China.

Methane isotherms for shales and kerogens normalized to TOC are shown in Appendix C, Section F. It is apparent that the TOC normalized isotherms for shales are always higher than the corresponding kerogen isotherms. This indicates significant methane adsorption in the inorganic component of the shale. A mass balance for CH₄ sorption based on the kerogen isotherms measured in this study and the illite or smectite isotherms published by Ji et al⁶¹ and Liu et al⁶² suggests that for HAR shales, all the CH₄ sorption can be accounted for by uptake on clay minerals and kerogen. However, only 45-60% of the sorption of WIC shales and 60-70% of the sorption of HAD shales can be accounted for by a mass balance of sorption by kerogen and clay minerals (Figure 5.15).^{61,62} Sorption mass balances determined using kerogen and shale isotherms suggest that in dry natural shales possibly significant sorption also occurs at interfaces between kerogen and clay minerals for the WIC and HAD shales. Also, the kerogen separation process may modify its adsorption characteristics, and some other inorganic materials not accounted for in the sorption mass balance may increase sorption.

We note that since water is present in natural subsurface shales, pores associated with clay minerals may be at least partly water-filled, in which case they will not contribute to the sorption pore volume. The adsorbed phase in porous systems is in equilibrium with the homogeneous bulk gas phase in meso- and macropores. Fracturing shale and releasing gas from the bulk gas phase allows the sorbed gas to desorb. The amount of gas released (sorbed + bulk gas) at reservoir temperatures can be estimated from the excess isotherms and total pore volumes. The amount of gas desorbed can be visualized directly from the absolute isotherms. Absolute CH₄ sorption on dry Posidonia shales at 65°C and 15 MPa ranges from 0.092 - 0.202 mmol g⁻¹ (66 – 144 scf t⁻¹) on dry shale, and from 0.76 - 1.32 mmol g⁻¹ (540 – 942 scf t⁻¹) on dry kerogen. Absolute amounts adsorbed at 85°C and 15 MPa are 103 and 127 scf t⁻¹ in dry Hadessen shales. The shapes of the absolute shale and kerogen isotherms indicate that only small amounts of gas will desorb at high pressure. This is not only because most sorbed gas is within pores smaller than approximately 6 nm, but also, comparison of the DR micropore volumes obtained from CO₂ adsorption at 0°C suggests that 40 – 62 % of the sorption pore volumes in shales and 39 – 53 % in kerogen are ultramicroporous. Gas in ultramicropores is strongly sorbed due to the proximity of the walls and the resulting high sorption potential. Furthermore, there is no significant variation of enthalpies of adsorption determined from high-pressure methane isotherms, indicating that the interactions of the

pore surfaces and the methane molecules are similar in all these Posidonia samples and is not affected by maturity.

Although N₂ isotherms at -196°C are often used to characterize porosity they can be misleading.⁷⁸ The narrowest ultramicroporosity cannot be accessed by nitrogen molecules at -196°C, due to activated diffusion. Furthermore, microporous solids may give rise to unrealistically high BET surface areas as micropore filling may occur. Both issues have been pointed out on coal previously.⁷⁹

While the supercritical Dubinin-Radushkevich equation produced good fits for CH₄ sorption in a previous study on Alum shale, Posidonia shale are more accurately described by the Langmuir equation.⁸ In comparison to the Posidonia shales, the Alum shale has a larger proportion of ultra-microporosity (DR CO₂ ultramicropore volume of 12.9 and CO₂ sorption pore volume of 16.8 mm³ g⁻¹).¹⁴ The DR model is based on micropore filling and, thus, it produced good results on ultra microporous shales. The Posidonia shales have a much greater fraction of larger pores as shown by the ratio of the CO₂ -78°C sorption pore volume to the CO₂ (0°C) DR micropore volume (see Table 5.4) and this may be the reason for the Langmuir model providing a better fit than the DR equation for the Posidonia isotherm data.

5.5 Conclusions

Methane sorption capacities and pore characteristics of bulk shales and isolated kerogens have been determined for immature, oil-window and gas-window samples from the Lower Toarcian Posidonia Shale formation. Total porosities and CO₂ sorption volumes (-78°C) of organic-rich Posidonia shales decrease through the oil-window and then increase into the gas-window. This implies that part of the sorption porosity is blocked by bitumen and then regenerated as a result of gas generation from bitumen and/or kerogen. Since (a) the sum of porosities measured by CO₂ at -78°C and mercury injection are very similar to the corresponding total pore volume (< 1093 nm) thereby accounting for all the available shale porosity and (b) mercury at 268.9 MPa occupies pores with constrictions larger than ca. 6 nm, we infer that porosity measured by CO₂ adsorption at -78°C is largely within pores smaller than 6 nm. The CO₂ sorption pore volume represents 21 to 66 % of the total pore volume in these shales, with 10 to 41 % of the total pore volume in DR micropore pore (<~0.7 nm) volume. Porosity information from subcritical nitrogen sorption at -196°C is not applicable due to activated diffusion effects.

A modified Langmuir model including the sorption pore volume fits the absolute and surface excess CH₄ isotherms well and this provides a useful parameterization of the data. Methane is sorbed strongly in ultramicropores and will only be desorbed at low pressure.

Enthalpies of methane adsorption on dry shales range from 11.2 - 15.7 kJ mol⁻¹ and from 8.5 - 17.2 kJ mol⁻¹ on kerogen, and are not related to maturity. The linear correlation between maximum CH₄ sorption and CO₂ sorption pore volume (-78°C) is very strong for both shales and kerogens, and suggests that the vast majority of sorbed CH₄ occurs in pores smaller than 6 nm, with around half of that within ultramicroporosity in the shales studied. Shale and kerogen mass balance considerations indicate that approximately half of the CH₄ sorption on dry shales takes place within the organic matter and this indicates the significance of the inorganic phase, including the role of clays and possibly the organic-inorganic interface as sorption sites in dry shales. However, caution is required in extrapolating these results to the subsurface, where water may occur.

References

- (1) *Annual Energy Outlook 2013*, U.S. Department of Energy, 2013.
- (2) Borst, R. L. *Sedimentology* **1982**, *29*, 291.
- (3) Yang, Y. L.; Aplin, A. C. *Mar. Pet. Geol.* **1998**, *15*, 163.
- (4) Cartwright, J. A.; Dewhurst, D. N. *Geological Society of America Bulletin* **1998**, *110*, 1242.
- (5) Loucks, R. G.; Reed, R. M.; Ruppel, S. C.; Jarvie, D. M. *Journal of Sedimentary Research* **2009**, *79*, 848.
- (6) Loucks, R. G.; Reed, R. M.; Ruppel, S. C.; Hammes, U. *AAPG Bull.* **2012**, *96*, 1071.
- (7) Milliken, K. L.; Rudnicki, M.; Awwiller, D. N.; Zhang, T. W. *AAPG Bull.* **2013**, *97*, 177.
- (8) Clarkson, C. R.; Freeman, M.; He, L.; Agamalian, M.; Melnichenko, Y. B.; Mastalerz, M.; Bustin, R. M.; Radliński, A. P.; Blach, T. P. *Fuel* **2012**, *95*, 371.
- (9) Mastalerz, M.; He, L.; Melnichenko, Y. B.; Rupp, J. A. *Energy Fuels* **2012**, *26*, 5109.
- (10) Ruppert, L. F.; Sakurovs, R.; Blach, T. P.; He, L.; Melnichenko, Y. B.; Mildner, D. F. R.; Alcantar-Lopez, L. *Energy Fuels* **2013**, *27*, 772.
- (11) Rexer, T. F. T.; Benham, M. J.; Aplin, A. C.; Thomas, K. M. *Energy Fuels* **2013**, *27*, 3099.
- (12) Zhang, T. W.; Ellis, G. S.; Ruppel, S. C.; Milliken, K.; Yang, R. S. *Org. Geochem.* **2012**, *47*, 120.
- (13) Gasparik M.; Bertier P.; Gensterblum Y.; Ghanizadeh A.; Krooss B. M.; Littke R. *Int J Coal Geology* **2014**, *123*, 34.
- (14) Ross, D. J. K.; Bustin, R. M. *Mar. Pet. Geol.* **2009**, *26*, 916.
- (15) Weniger, P.; Kalkreuth, W.; Busch, A.; Krooss, B. M. *Int. J. Coal Geol.* **2010**, *84*, 190.
- (16) Gasparik, M.; Ghanizadeh, A.; Bertier, P.; Gensterblum, Y.; Bouw, S.; Krooss, B. M. *Energy Fuels* **2012**, *26*, 4995.
- (17) Neimark, A. V.; Ravikovitch, P. I. *Langmuir* **1997**, *13*, 5148.
- (18) Myers, A.; Monson, P. *Adsorption* **2014**, *20*, 591.
- (19) Sircar, S. *Ind. Eng. Chem. Res.* **1999**, *38*, 3670.
- (20) Chareonsuppanimit, P.; Mohammad, S. A.; Robinson, R. L.; Gasem, K. A. M. *Int. J. Coal Geol.* **2012**, *95*, 34.
- (21) Lu, X. C.; Li, F. C.; Watson, A. T. *Fuel* **1995**, *74*, 599.
- (22) Chalmers, G. R. L.; Bustin, R. M. *Bull. Can. Pet. Geol.* **2008**, *56*, 22.
- (23) Chalmers, G. R. L.; Bustin, R. M. *Int. J. Coal Geol.* **2007**, *70*, 223.
- (24) Littke, R.; Baker, D. R.; Leythaeuser, D. *Org. Geochem.* **1988**, *13*, 549.
- (25) Vandenbroucke, M.; Behar, F.; Santorcuato, A.; Rullkotter, J. *Org. Geochem.* **1993**, *20*, 961.
- (26) Vandenbroucke, M.; Largeau, C. *Org. Geochem.* **2007**, *38*, 719.

- (27) Rullkotter, J.; Leythaeuser, D.; Horsfield, B.; Littke, R.; Mann, U.; Muller, P. J.; Radke, M.; Schaefer, R. G.; Schenk, H. J.; Schwochau, K.; Witte, E. G.; Welte, D. H. *Org. Geochem.* **1988**, *13*, 847.
- (28) Littke, R.; Baker, D. R.; Leythaeuser, D.; Rullkotter, J. *KEYS TO THE DEPOSITIONAL HISTORY OF THE POSIDONIA SHALE (TOARCIAN) IN THE HILS SYNCLINE, NORTHERN GERMANY*; Geological Soc Publishing House: Bath, 1991.
- (29) Bernard, S.; Horsfield, B.; Schulz, H.-M.; Wirth, R.; Schreiber, A.; Sherwood, N. *Mar. Pet. Geol.* **2012**, *31*, 70.
- (30) Schmid-Rohl, A.; Rohl, H. J.; Oschmann, W.; Frimmel, A.; Schwark, L. *Geobios* **2002**, *35*, 13.
- (31) Schwark, L.; Frimmel, A. *Chemical Geology* **2004**, *206*, 231.
- (32) Rohl, H. J.; Schmid-Rohl, A. In *Deposition of Organic-Carbon-Rich Sediments: Models, Mechanisms, and Consequences*; Harris, N. B., Ed.; S E P M - Soc Sedimentary Geology: Tulsa, 2005; Vol. 82, p 165.
- (33) Munoz, Y. A.; Littke, R.; Brix, M. R. *Geofluids* **2007**, *7*, 335.
- (34) Espitalie, J. *Rev. IFP* **1977**, *32*, 23.
- (35) Lapiere, C.; Leroueil, S.; Locat, J. *Can. Geotech. J.* **1990**, *27*, 761.
- (36) Heling, D. *Sedimentology* **1970**, *15*, 247.
- (37) Lowell, S.; Shields, J. E. *Powder surface area and porosity*; Chapman and Hall: London, New York, 1991.
- (38) van Krevelen, D.; Schuyer, J. *Coal science*; Elsevier, 1957.
- (39) Wilhelms, A.; Larter, S. R.; Leythaeuser, D. *Org. Geochem.* **1991**, *17*, 351.
- (40) Laxminarayana, C.; Crosdale, P. J. *Int. J. Coal Geol.* **1999**, *40*, 309.
- (41) Gurvitch, L. *J. Phys. Chem. Soc. Russ.* **1915**, *47*, 805.
- (42) Marsh, H. *Carbon* **1987**, *25*, 49.
- (43) Fletcher, A. J.; Thomas, K. M.; Rosseinsky, M. J. *Journal of Solid State Chemistry* **2005**, *178*, 2491.
- (44) Sing, K. S. W.; Everett, D. H.; Haul, R. A. W.; Moscou, L.; Pierotti, R. A.; Rouquerol, J.; Siemieniewska, T. *Pure and Applied Chemistry* **1985**, *57*, 603.
- (45) Lemmon, E. W.; Huber, M. L.; McLinden, M. O. *NIST Reference Fluid Thermodynamic and Transport Properties - REFPROP*, U.S. Department of Commerce, 2010.
- (46) Garrido, J.; Linares-Solano, A.; Martin-Martinez, J. M.; Molina-Sabio, M.; Rodriguez-Reinoso, F.; Torregrosa, R. *Langmuir* **1987**, *3*, 76.
- (47) Marsh, H.; Wynne-Jones, W. F. K. *Carbon* **1964**, *1*, 269.
- (48) Sing, K. S. W.; Williams, R. T. *Particle & Particle Systems Characterization* **2004**, *21*, 71.
- (49) Lamond, T. G.; Metcalfe, J. E. I.; Walker, P. L. J. *Carbon* **1965**, *3*, 59.

- (50) Rodriguez-Reinoso, F.; Linares-Solano, A. In *Chemistry and Physics of Carbon*; Thrower, P. A., Ed.; New York: Marcel Dekker, 1989; Vol. 21, p 1.
- (51) Cazorla-Amoros, D.; Alcaniz-Monge, J.; de la Casa-Lillo, M. A.; Linares-Solano, A. *Langmuir* **1998**, *14*, 4589.
- (52) *Handbook of Compressed Gases, 3rd Edition Van Nostrand Reinhold, New York 1990*; 3rd ed.; Van Nostrand Reinhold: New York, 1990.
- (53) Firouzi, M.; Rupp, E. C.; Liu, C. W.; Wilcox, J. *Int. J. Coal Geol.* **2014**, *121*, 123.
- (54) Krooss, B. M.; van Bergen, F.; Gensterblum, Y.; Siemons, N.; Pagnier, H. J. M.; David, P. *Int. J. Coal Geol.* **2002**, *51*, 69.
- (55) Xiao, B.; Wheatley, P. S.; Zhao, X.; Fletcher, A. J.; Fox, S.; Rossi, A. G.; Megson, I. L.; Bordiga, S.; Regli, L.; Thomas, K. M.; Morris, R. E. *J. Am. Chem. Soc.* **2007**, *129*, 1203.
- (56) Lin, X.; Telepeni, I.; Blake, A. J.; Dailly, A.; Brown, C. M.; Simmons, J. M.; Zoppi, M.; Walker, G. S.; Thomas, K. M.; Mays, T. J.; Hubberstey, P.; Champness, N. R.; Schroder, M. *J. Am. Chem. Soc.* **2009**, *131*, 2159.
- (57) Furukawa, H.; Miller, M. A.; Yaghi, O. M. *Journal of Materials Chemistry* **2007**, *17*, 3197.
- (58) Murray, L. J.; Dinca, M.; Long, J. R. *Chem. Soc. Rev.* **2009**, *38*, 1294.
- (59) Broom, D. P.; Thomas, K. M. *MRS Bull.* **2013**, *38*, 412.
- (60) Ambrose, R. J.; Hartman, R. C.; Diaz-Campos, M.; Akkutlu, I. Y.; Sondergeld, C. H. *Spe J.* **2012**, *17*, 219.
- (61) Ji, L. M.; Zhang, T. W.; Milliken, K. L.; Qu, J. L.; Zhang, X. L. *Appl. Geochem.* **2012**, *27*, 2533.
- (62) Liu, D.; Yuan, P.; Liu, H. M.; Li, T.; Tan, D. Y.; Yuan, W. W.; He, H. P. *Applied Clay Science* **2013**, *85*, 25.
- (63) Sircar, S. *Ind. Eng. Chem. Res.* **1992**, *31*, 1813.
- (64) Myers, A. L.; Monson, P. A. *Langmuir* **2002**, *18*, 10261.
- (65) Cole, J. H.; Everett, D. H.; Marshall, C. T.; Paniago, A. R.; Powl, J. C.; Rodriguez-Reinoso, F. *J. Chem. Soc. Faraday Trans.* **1974**, *70*, 2154.
- (66) Czepirski, L.; Jagiello, J. *Chemical Engineering Science* **1989**, *44*, 797.
- (67) Himeno, S.; Komatsu, T.; Fujita, S. *J. Chem. Eng. Data* **2005**, *50*, 369.
- (68) Duren, T.; Sarkisov, L.; Yaghi, O. M.; Snurr, R. Q. *Langmuir* **2004**, *20*, 2683.
- (69) Rahman, K. A.; Loh, W. S.; Yanagi, H.; Chakraborty, A.; Saha, B. B.; Chun, W. G.; Ng, K. C. *Journal of Chemical and Engineering Data* **2010**, *55*, 4961.
- (70) Ruppel, T. C.; Grein, C. T.; Bienstoc. *Fuel* **1974**, *53*, 152.
- (71) Xia, X. Y.; Tang, Y. C. *Geochim. Cosmochim. Acta* **2012**, *77*, 489.
- (72) Gurdal, G.; Yalcin, M. N. *Int. J. Coal Geol.* **2001**, *48*, 133.
- (73) Clarkson, C. R.; Bustin, R. M. *Fuel* **1996**, *75*, 1483.

- (74) Clarkson, C. R.; Bustin, R. M.; Levy, J. H. *Carbon* **1997**, *35*, 1689.
- (75) Levine, J. R. *Coalification: The Evolution of Coal as Source Rock and Reservoir Rock for Oil and Gas*; AAPG, 1993.
- (76) Mosher, K.; He, J.; Liu, Y.; Rupp, E.; Wilcox, J. *Int. J. Coal Geol.* **2013**, *109–110*, 36.
- (77) Cai, Y. D.; Liu, D. M.; Pan, Z. J.; Yao, Y. B.; Li, J. Q.; Qiu, Y. K. *Fuel* **2013**, *103*, 258.
- (78) Sing, K. *Colloids and Surfaces A: Physicochemical and Engineering Aspects* **2001**, *187–188*, 3.
- (79) Mahajan, O. P. *Carbon* **1991**, *29*, 735.

Chapter 6

Conclusions

Recent research on sorption capacities of gas shales has mainly focused on determining the influence of geological characterization parameters. It has been found that along pressure and temperature, TOC, clay content, maturity and the moisture content are the main variables, which enable first approximations of gas in place in shale from well-logging data.¹⁻⁵ However, there is still much uncertainty about the quantitative contribution of these parameters and there is contradictory evidence in literature regarding, for example, the sorption capacity of specific clay minerals and the role of the organic matrix in gas retention.^{6,7} This is further complicated by the very low gas uptake of shales, which makes gas sorption capacities difficult to measure. As the reproducibility of isotherms has not been assessed, it is uncertain to what extent the published isotherms are representative.

Furthermore, the aim of the work presented in this thesis was to better understand the occurrence and retention of gas in shales by establishing standard techniques and, thus, ensuring reproducibility of sorption capacity measurements. Moreover, the multiple effects of maturity on sorption capacity, that is the role of temperature, pressure and pore evolution with maturation, specifically in the organic matrix, were the focus of this research. Measurements were carried out on Posidonia shales and isolated kerogens ranging from early-oil window to gas window maturity, showing little variation in mineral composition, plus one Alum Shale sample of dry gas window maturity.

Manometric equipment has been calibrated and modified for CH₄ and CO₂ sorption measurements on shale. In order to validate the equipment and to assess the reproducibility and identify sources of errors an interlaboratory comparison study among seven institutes on two carbonaceous shales (low (VR = 0.5%R_O) and high maturity (VR = 2.0%R_O) has been conducted together with the Energy and Mineral Resources Group of the RWTH Aachen. The results show that a high degree of intralaboratory repeatability is achievable. Interlaboratory discrepancies of methane isotherms measured on the high-maturity sample are within an adequate range of discrepancies (0.02 mmol g⁻¹ at 15 MPa) whereas there are larger discrepancies (0.08 mmol g⁻¹ at 15 MPa) for the low maturity sample. Likely contributors are varying residual moisture content due to different pretreatment procedures, errors in void volume measurements, unaccounted leakage from the system and insufficient equilibration times. Recommendations are given accordingly for the second phase of the interlaboratory comparison study. Methane isotherms measured by our group on a high-maturity shale

sample agree well with isotherms measured at the RWTH Aachen and are within the satisfactory range of discrepancies observed between isotherms of other institutes.

For accurate determination of subcritical CO₂ isotherms residual moisture needs to be removed from the gas supply (CO₂ purity 99.995%). Thus, zeolite bed (70 cm³) filled with sodium aluminium silicate, was interposed between gas supply and the sample cells of the gravimetric equipment. Isotherms measured before and after interposing the zeolite bed showed around 30% less uptake.

Shales exhibit low porosities compared to coals and the pores are heterogeneous in terms of surface chemistry, shape and size – ranging from below 0.7 nm to pores larger than 1000 µm. Thus, characterization of pores in shale is difficult and requires the application of multiple methods. Scanning Electronic Microscopy (SEM) can visualize pores down to 20 nm but quantification is time-consuming and is based on statistical estimation methods. Mercury Injection Capillary Porosimetry (MICP) measures pore volumes and pore size distributions (PSD).⁸ However, the shale porous network might be affected by high-pressures (> 100 MPa) used, e.g. in this study repeated attempts to measure the pore volume by MICP on the Alum Shale sample failed. Furthermore, PSD's from MICP are calculated from the Washburn equation and, thus, PSD's refer to pore constrictions rather than pore bodies. It has been suggested before that sorption on shale and coal occurs mainly in the micropore size (pore diameter < 3 nm) region. Quantification of pores in this size region relies on low-pressure sorption and its models, such as Brunauer, Emmett and Teller's (BET) theory⁹, Dubinin-Radushkevich (DR) model¹⁰⁻¹² and Gurvitch Rule^{13,14}. Each model relies on different idealised sorption mechanisms, such as multilayer formation on an energetically homogeneous surface (BET) and micropore filling derived from Polanyi's potential theory (DR), or on empirical findings (Gurvitch Rule).^{15,16} Thus, each model will only determine an 'equivalent pore volume/surface area' and three pore probing methods were applied in this study to get best possible insight.¹⁷

The sum of the CO₂ sorption pore volume (measured at – 78°C) and the MICP pore volume show good agreement with the total pore volume as measured by mercury bulk density and grain density or helium pycnometry measurements. Thus, these 'equivalent' pore volumes can be assumed to represent pore volumes of pores with diameter below 6 nm. This pore size is inferred, since according to the Washburn equation, mercury can penetrate pore constrictions down to about this diameter at 268.9 MPa.⁸ To calculate sorption pore volumes, the uptake at p/p_0 is converted into a pore volume in accordance with the Gurvitch Rule. This involves multiplying the uptake by the reciprocal of the adsorbed phase density that is the liquid density of the adsorbate. Thus, it becomes clear that CO₂ sorption pore volumes

represent an approximation only, as the pore size distribution and the surface chemistry affect the adsorbed phase density.^{15,18}

An estimation of total gas capacities of shales can be calculated by adding excess sorption and the amount of free gas in the shale pore volume and by accounting for the water saturation of the gas reservoir. However, from a scientific point of view, determining absolute isotherms, which describe the actual adsorbed phase volume, is of interest as these can be compared against petrophysical data to allow a deeper insight into the occurrence of gas in shale under subsurface conditions. These comparisons include the interdependencies between absolute capacities, kerogen type, TOC, mineral compositions, shale fabric, maturity and pore size distributions. However, a much larger data set needs to be collected to constrain these interdependencies. In this study we have calculated absolute isotherms for Posidonia shales ranging from early oil window to the gas window maturity based on the good correlation between sorption pore volume (pore diameter < 6 nm) and excess sorption capacity at a range of temperature (45- 85°C) and pressure.

Posidonia kerogens chemically isolated from shales exhibit around ~7 times higher CH₄ sorption capacities (at 10 Mpa) than the corresponding shale. Sorption pore volumes of kerogen are 5 – 10 times larger than shale pore volumes. Mass balances for adsorption show that kerogen and clay minerals (sorption data by Ji et al⁷ and Liu et al⁶) cannot account for the sorption of the corresponding shales in all cases, implying some sorption in the organic-inorganic interface. Alternatively, kerogen modification during the isolation process occurs or there is adsorption on unidentified minerals. Furthermore, CH₄ excess uptake on Posidonia shales (at a range of pressure and temperature) show strong correlations with sorption pore volumes (< 6 nm) indicating that a large part of the methane sorption takes place within pores of diameters below 6 nm. Similar observations were made for coal.¹⁹ However, the same correlations cannot be seen for the Namurian, Alum and Posidonia outcrop shale (see Figure 6.1).

The absolute amount adsorbed (actual adsorbed phase) is the total amount of gas present in the pore volume of increased gas density due to sorption. To estimate absolute amounts adsorbed in our work we have used the supercritical DR and the Langmuir model, respectively.^{20,21} These models were originally derived for subcritical sorption and are based on micropore filling and monolayer sorption, respectively. For the Alum Shale sample (R₀ = 2.26%) isotherms were obtained over a wide range of temperature (27 – 200°C). The DR model gave better fits to the data over the Langmuir model and calculated reasonable adsorbed phase densities. This possibly reflects the – in comparison to the Posidonia shales - large (DR) ultramicropore fraction of the CO₂ sorption pore volume. For Posidonia shales the

Langmuir model gave better fits than the DR model. The actual adsorbed phase was assumed to be equivalent to the sorption pore volume based on experimental evidence. According to the $n_{ab} = n_{ex} + \rho_b \times V_{ad}$, this means the “calculated” adsorbed phase density needs to increase linearly with fugacity. However, how the ‘actual’ sorbed phase density changes with fugacity is not known and there are local differences in the density depending on the pore size.¹⁸ Consequently, the Langmuir model is limited to estimate an “average maximum adsorbed phase density” from the isotherm. We have termed this density “maximum density” as we have substituted the Langmuir capacity n_{max} with $n_{max} = \rho_{ad} \times V_{ad}$, thus assuming it is the density at maximum sorption capacity. However, if this calculated density provides any physical insight cannot be determined based on our data. However, it should be noted that the calculated adsorbed phase densities are close to adsorbed phase densities calculated on shale by molecular simulation.²² Moreover, the pore widening in the < 6nm range from WIC to HAD seems to be reflected in the calculated “maximum adsorbed phase densities” which are lower for HAD than for WIC shales as expected for wider pores.¹⁸ However, one should be aware that these densities are fitting parameter and that experimental error will also have impact on the calculated parameters.

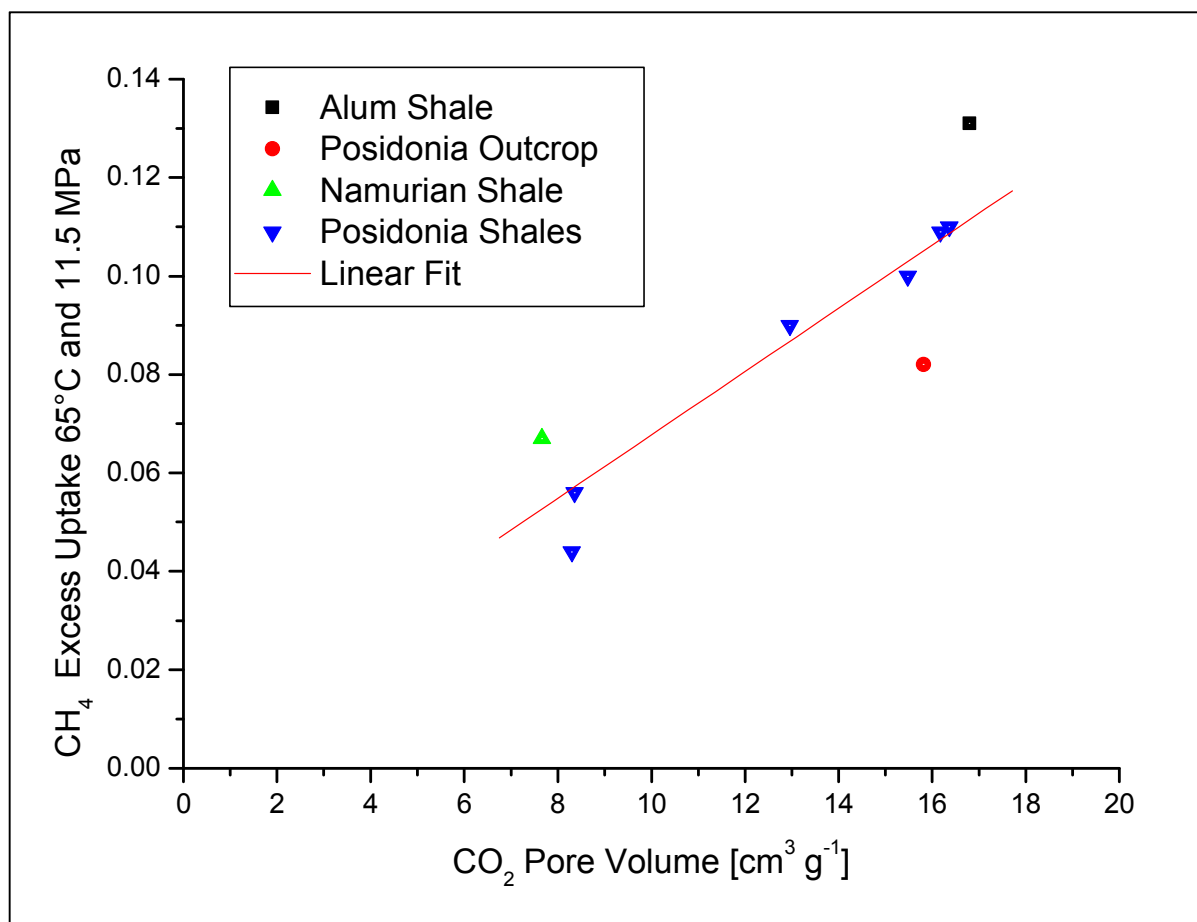


Figure 6.1: Correlation of methane excess uptake at 65°C and 11.5 MPa with the CO₂ sorption pore volume of Posidonia shales, an Alum Shale, Namurian Shale and Posidonia Outcrop Shale.

Future work should focus on further improving the interlaboratory reproducibility of CH₄, CO₂, C₂H₆ and other relevant gas isotherms on shale. Recommendations for a second Round Robin study are given in chapter 3. Furthermore, for improved gas in place estimations competitive sorption of gases on shale should be focused on in future. We recommend to examine and quantify pore volumes of shales by low pressure sorption techniques as shown in this thesis in addition to high-pressure methane isotherms. As shown, pores of diameters below 6 control the sorption capacity of Posidonia shales. Thus, we think constraining the interdependencies between micropore/sorption pore volumes and mineral composition, organic matrix and maturity of shale will eventually help to understand the retention of gas in shale.

References

- (1) Lu, X. C.; Li, F. C.; Watson, A. T. *Fuel* **1995**, *74*, 599.
- (2) Ross, D. J. K.; Bustin, R. M. *Mar. Pet. Geol.* **2009**, *26*, 916.
- (3) Zhang, T. W.; Ellis, G. S.; Ruppel, S. C.; Milliken, K.; Yang, R. S. *Org. Geochem.* **2012**, *47*, 120.
- (4) Gasparik, M.; Ghanizadeh, A.; Bertier, P.; Gensterblum, Y.; Bouw, S.; Krooss, B. M. *Energy Fuels* **2012**, *26*, 4995.
- (5) Gasparik, M.; Bertier, P.; Gensterblum, Y.; Ghanizadeh, A.; Krooss, B. M.; Littke, R. *Int. J. Coal Geol.*
- (6) Liu, D.; Yuan, P.; Liu, H.; Li, T.; Tan, D.; Yuan, W.; He, H. *Applied Clay Science* **2013**, *85*, 25.
- (7) Ji, L.; Zhang, T.; Milliken, K. L.; Qu, J.; Zhang, X. *Applied Geochemistry* **2012**, *27*, 2533.
- (8) Leon, C. *Advances in Colloid and Interface Science* **1998**, *76*, 341.
- (9) Brunauer, S.; Emmett, P. H.; Teller, E. *Journal of the American Chemical Society* **1938**, *60*, 309.
- (10) Dubinin, M. M.; Zaverina, E. D.; Serpinsky, V. V. *Journal of the Chemical Society (Resumed)* **1955**, 1760.
- (11) Marsh, H.; Rand, B. *Journal of Colloid and Interface Science* **1970**, *33*, 101.
- (12) Sing, K. *Colloids and Surfaces A: Physicochemical and Engineering Aspects* **2001**, *187–188*, 3.
- (13) Gurvitch, L. *J. Phys. Chem. Soc. Russ.* **1915**, *47*, 805.
- (14) Fletcher, A. J.; Thomas, K. M.; Rosseinsky, M. J. *Journal of Solid State Chemistry* **2005**, *178*, 2491.
- (15) Gregg, S. J.; Sing, K. S. W.; Academic Press Inc: London, 1982; Vol. 2.
- (16) Do, D. D.; Do, H. D. *Carbon* **2003**, *41*, 1777.
- (17) Marsh, H. *Carbon* **1987**, *25*, 49.
- (18) Mosher, K.; He, J.; Liu, Y.; Rupp, E.; Wilcox, J. *Int. J. Coal Geol.* **2013**, *109–110*, 36.
- (19) Cai, Y. D.; Liu, D. M.; Pan, Z. J.; Yao, Y. B.; Li, J. Q.; Qiu, Y. K. *Fuel* **2013**, *103*, 258.
- (20) Sakurovs, R.; Day, S.; Weir, S.; Duffy, G. *Energy Fuels* **2007**, *21*, 992.
- (21) Gensterblum, Y.; van Hemert, P.; Billefont, P.; Battistutta, E.; Busch, A.; Krooss, B. M.; De Weireld, G.; Wolf, K. *Int. J. Coal Geol.* **2010**, *84*, 115.
- (22) Ambrose, R. J.; Hartman, R. C.; Diaz-Campos, M.; Akkutlu, I. Y.; Sondergeld, C. H. *Spe J.* **2012**, *17*, 219.

Appendix A

A. Micropore Volume (CO₂ at 273 K)

Table S A1: CO₂ isotherms at 273 K.

Namurian Shale				Posidonia Outcrop			
Uptake	Pressure	p/p_0^{-1}	Temp	Uptake	Pressure	p/p_0^{-1}	Temp
mmol g ⁻¹	kPa		°C	mmol g ⁻¹	kPa		°C
0.025	6.71	0.002	-0.01	0.011	1.20	0.000	-0.09
0.038	11.70	0.003	-0.01	0.028	3.06	0.001	-0.07
0.055	21.66	0.006	-0.04	0.034	5.15	0.001	-0.07
0.066	31.71	0.009	-0.03	0.040	10.07	0.003	-0.09
0.076	41.66	0.012	-0.02	0.053	19.86	0.006	-0.07
0.083	51.67	0.015	-0.04	0.069	39.65	0.011	-0.08
0.090	61.68	0.018	-0.05	0.083	59.80	0.017	-0.11
0.096	71.68	0.021	-0.04	0.094	79.97	0.023	-0.11
0.101	81.62	0.023	-0.02	0.105	100.24	0.029	-0.17
0.105	91.59	0.026	-0.02	0.117	149.96	0.043	-0.09
0.110	101.67	0.029	-0.01	0.130	200.13	0.057	-0.08
				0.166	400.08	0.115	-0.10
				0.192	599.68	0.172	-0.07
				0.211	799.89	0.229	-0.07

B. Sorption Pore Volumes (CO₂ at 195 K)

Table S A2: CO₂ isotherm at 194.5 K.

Namurian Shale			Posidonia Outcrop		
Uptake	Pressure	p/p_0^{-1}	Uptake	Pressure	p/p_0^{-1}
mmol g ⁻¹	kPa		mmol g ⁻¹	kPa	
0.037	1.05	0.010	0.093	1.39	0.014
0.080	4.81	0.047	0.147	5.13	0.051
0.106	9.76	0.096	0.183	10.14	0.100
0.130	19.80	0.195	0.227	20.12	0.199
0.156	39.77	0.393	0.287	40.08	0.396
0.175	59.77	0.590	0.334	60.13	0.594
0.191	79.70	0.787	0.377	80.21	0.792
0.208	99.74	0.985	0.423	100.29	0.990

C. BET Surface Areas (N₂ at 77 K)

Table S A3: N₂ isotherms at 77 K in tabular form.

Namurian Shale				Posidonia Outcrop			
Uptake	Pressure	p/p_0^{-1}	Temp	Uptake	Pressure	p/p_0^{-1}	Temp
mmol g ⁻¹	kPa		°C	mmol g ⁻¹	kPa		°C
0.076	0.59	0.004	-191.84	0.022	1.08	0.006	-191.41
0.092	1.23	0.007	-190.37	0.030	2.79	0.018	-191.81
0.100	2.92	0.017	-191.32	0.039	5.74	0.041	-193.05
0.107	5.92	0.037	-191.74	0.049	9.77	0.071	-193.17
0.113	9.92	0.060	-191.39	0.059	14.76	0.122	-194.30
0.118	14.92	0.083	-190.70	0.068	19.80	0.163	-194.27
0.129	20.04	0.178	-194.89	0.076	24.78	0.219	-194.88
0.133	24.91	0.217	-194.74	0.083	29.82	0.261	-194.77
0.140	29.96	0.279	-195.33	0.090	34.79	0.299	-194.62
0.144	34.94	0.320	-195.17	0.098	39.89	0.360	-195.04
0.149	39.84	0.363	-195.14	0.122	54.75	0.514	-195.38
0.185	69.93	0.695	-195.87	0.152	69.82	0.673	-195.60
0.227	84.96	0.844	-195.87	0.203	84.80	0.831	-195.75
0.457	98.99	0.982	-195.85	0.318	95.89	0.937	-195.73
				0.438	98.94	0.973	-195.78

D. High-Pressure Methane Isotherms

Namurian Shale

Table S A4: Namurian Shale CH₄ isotherms.

Uptake	Pressure	Sample Temp	Density
mmol g⁻¹	MPa	K	kg m⁻³
Isotherm 1			
0.0084	0.198	338.27	3.1242
0.0235	0.832	338.17	13.397
0.0378	1.969	338.16	33.016
0.0473	3.442	338.17	61.203
0.0543	5.122	338.18	98.373
0.0581	6.932	338.18	147.02
0.0599	8.807	338.17	212.24
0.0600	10.709	338.17	303.44
Isotherm 2			
0.0126	0.344	338.18	5.4457
0.0224	0.748	338.18	12.004
0.0342	1.551	338.17	25.608
0.0442	2.614	338.16	44.934
0.0518	3.848	338.18	69.631
0.0568	5.194	338.15	100.13
0.0606	6.600	338.18	137.24
0.0630	8.038	338.17	183.15
0.0644	9.498	338.17	241.83
0.0665	10.964	338.18	318.05
0.0676	12.436	338.18	411.01

Posidonia Outcrop

Table S A5: Posidonia Outcrop CH₄ isotherms.

Uptake	Pressure	Sample Temp	Density
mmol g⁻¹	MPa	K	kg m⁻³
Isotherm 1			
0.0085	0.347	338.23	5.4928
0.0281	1.449	338.15	23.837
0.0465	3.077	338.15	53.892
0.0609	5.040	338.18	96.402
0.0725	7.197	338.16	155.17
0.0786	9.466	338.17	240.38
0.0826	11.775	338.17	368.16
0.0849	13.943	338.16	502.57
Isotherm 2			
0.0082	0.339	338.19	5.3654
0.0278	1.445	338.17	23.766
0.0445	2.892	338.15	50.271
0.0588	4.548	338.19	84.953
0.0684	6.337	338.12	129.85
0.0761	8.196	338.19	188.79
0.0817	10.100	338.19	270.72
0.0842	12.018	338.17	383.86
0.0860	14.101	338.16	510.95

E. High-Pressure Carbon Dioxide Isotherms

Posidonia Outcrop

Table S A6: Posidonia Outcrop CO₂ isotherms.

Uptake	Pressure	Sample Temp	Density
mmol g⁻¹	MPa	K	kg m⁻³
Isotherm 1			
0.0207	0.151	334.17	0.0207
0.0722	1.003	334.19	0.0722
0.1173	2.342	334.13	0.1173
0.1519	4.152	334.17	0.1519
Isotherm 2			
0.0217	0.152	334.16	0.0217
0.0538	0.595	334.16	0.0538
0.0853	1.257	334.19	0.0853
0.1135	2.069	334.32	0.1135
0.1400	2.984	334.18	0.1400
0.1596	3.983	334.17	0.1596
0.1715	5.046	334.15	0.1715
0.1823	6.195	334.17	0.1823

Appendix B

Table S B1: CO₂ Isotherms at 194.5 K in tabular form.

Run 1			Run 2		
Uptake	Pressure	p/p_0	Uptake	Pressure	p/p_0
mmol g ⁻¹	kPa		mmol g ⁻¹	kPa	
0.179	5.02	0.048	0.19	4.924	0.05
0.215	9.59	0.091	0.23	9.809	0.09
0.259	19.94	0.189	0.27	19.809	0.19
0.314	39.63	0.377	0.32	39.661	0.38
0.374	59.90	0.569	0.36	60.039	0.57
0.413	79.73	0.758	0.40	79.728	0.76
0.452	100.03	0.950	0.44	100.012	0.95
0.456	103.03	0.979	0.44	102.886	0.98

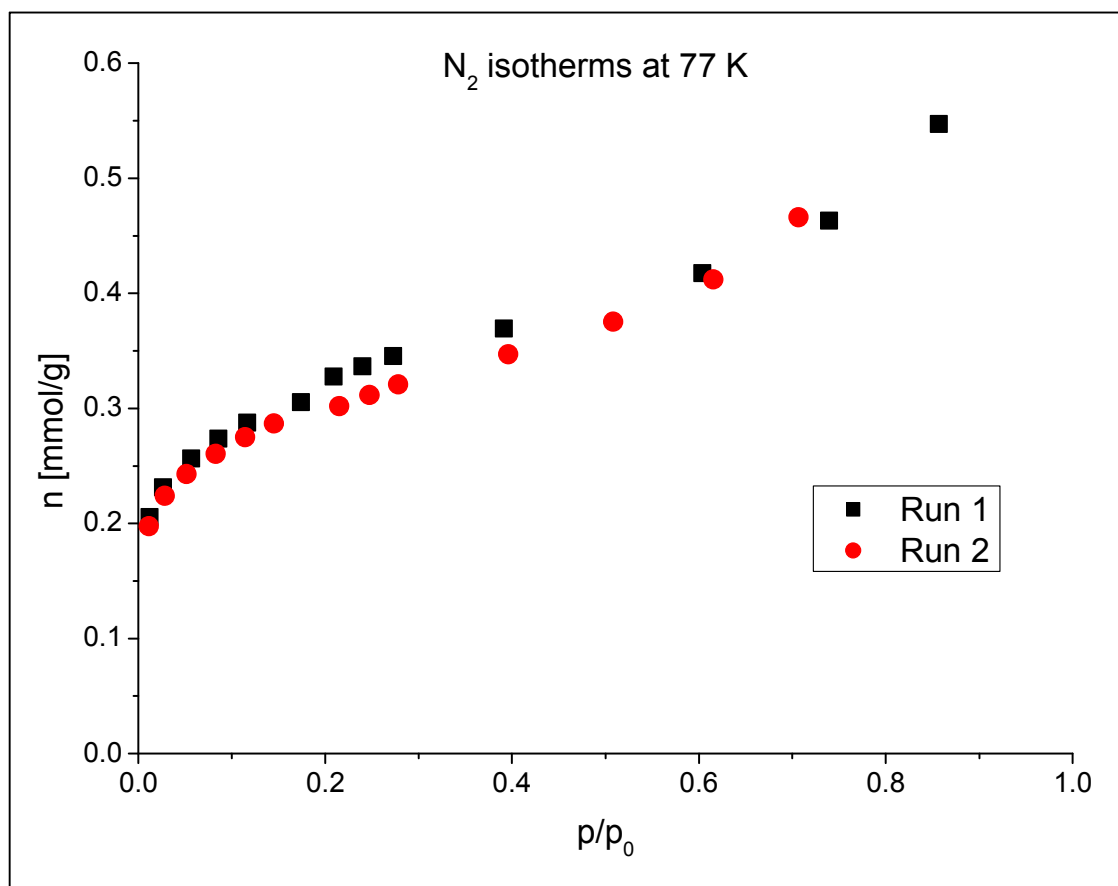


Figure S B1: Nitrogen adsorption isotherms on Alum Shale #1 at 77 K.

Table S B2: N₂ Isotherms at 77 K in tabular form.

Run 1				Run 2			
Uptake	Pressure	$p p_0^{-1}$	Temp	Uptake	Pressure	$p p_0^{-1}$	Temp
mmol g ⁻¹	kPa		K	mmol g ⁻¹	kPa		K
0.206	2.80	0.012	84.96	0.198	2.83	0.011	85.75
0.231	5.80	0.026	84.45	0.224	5.83	0.028	83.82
0.256	9.82	0.057	82.12	0.243	9.84	0.052	83.06
0.274	14.79	0.086	82.09	0.261	14.82	0.083	82.43
0.288	19.83	0.117	81.94	0.275	19.84	0.114	82.15
0.305	24.80	0.174	80.32	0.287	24.85	0.145	82.02
0.328	29.83	0.209	80.32	0.302	29.90	0.215	80.09
0.337	34.79	0.240	80.47	0.311	34.85	0.248	80.21
0.345	39.80	0.273	80.53	0.321	39.83	0.278	80.36
0.369	54.30	0.391	80.08	0.347	54.83	0.396	80.06
0.417	69.77	0.604	78.47	0.375	69.81	0.508	79.99
0.463	84.83	0.740	78.40	0.412	84.93	0.615	80.03
0.547	98.78	0.857	78.44	0.466	98.79	0.707	80.15

Excess Isotherms in tabular form

Table S B3: CO₂ Isotherms at 273 K.

Gravimetric				Manometric			
Uptake	Pressure	p/p_0	Temp	Uptake	Pressure	p/p_0	Temp
mmol g ⁻¹	kPa		K	mmol g ⁻¹	MPa		K
0.0121	1.62	0.000	273.05	0.0821	0.04	0.011	273.14
0.0317	5.29	0.002	273.08	0.1524	0.20	0.056	273.12
0.0501	9.97	0.003	273.07	0.2119	0.51	0.145	273.14
0.0730	19.92	0.006	273.07	0.2562	0.91	0.261	273.12
0.1008	40.04	0.011	273.06	0.2888	1.36	0.388	273.13
0.1211	59.79	0.017	273.03	0.3132	1.83	0.523	273.11
0.1369	79.84	0.023	273.03	0.3338	2.31	0.661	273.13
0.1500	99.80	0.029	272.97	0.3709	2.78	0.797	273.14

Methane Excess Isotherms

Table S B4: CH₄ excess isotherm data 300 K.

Uptake	Pressure	Sample Temp	Density	Fugacity
mmol g⁻¹	MPa	K	kg m⁻³	MPa
0.0152	0.08	299.42	0.50	0.08
0.0330	0.21	299.39	1.36	0.21
0.0543	0.47	299.35	3.03	0.46
0.0804	0.98	299.36	6.45	0.97
0.1018	1.68	299.36	11.12	1.63
0.1191	2.48	299.40	16.69	2.38
0.1330	3.36	299.44	22.92	3.17
0.1432	4.28	299.53	29.64	3.98
0.1518	5.23	299.55	36.78	4.79
0.1574	6.19	299.58	44.24	5.59
0.1640	7.17	299.70	51.93	6.37
0.1698	8.15	299.77	59.87	7.14
0.1726	9.13	299.81	68.01	7.88
0.1741	10.12	299.87	76.24	8.61
0.1741	11.11	299.91	84.57	9.32
0.1762	12.09	299.99	92.88	10.01
0.1751	13.08	300.05	101.19	10.69

Table S B5: CH₄ excess isotherm data 303 K.

Uptake	Pressure	Sample Temp	Density	Fugacity
mmol g⁻¹	MPa	K	kg m⁻³	MPa
0.0143	0.08	303.21	0.50	0.08
0.0310	0.21	303.19	1.36	0.21
0.0515	0.47	303.22	3.03	0.47
0.0762	0.99	303.26	6.42	0.98
0.0965	1.69	303.22	11.03	1.64
0.1131	2.49	303.24	16.53	2.40
0.1262	3.37	303.27	22.67	3.20
0.1347	4.30	303.28	29.31	4.01
0.1430	5.25	303.29	36.33	4.83
0.1496	6.22	303.30	43.64	5.64
0.1559	7.19	303.26	51.20	6.43
0.1604	8.17	303.30	58.96	7.20
0.1628	9.16	303.32	66.90	7.95
0.1651	10.14	303.35	74.94	8.69
0.1671	11.13	303.37	83.06	9.41
0.1667	12.12	303.32	91.23	10.11
0.1657	13.10	303.33	99.34	10.80

Table S B6: CH₄ excess isotherm data 308 K.

Uptake	Pressure	Sample Temp	Density	Fugacity
mmol g⁻¹	MPa	K	kg m⁻³	MPa
0.0120	0.08	308.14	0.48	0.08
0.0280	0.21	308.13	1.33	0.21
0.0477	0.48	308.16	3.00	0.47
0.0716	1.00	308.20	6.34	0.98
0.0916	1.70	308.27	10.90	1.65
0.1077	2.51	308.24	16.30	2.41
0.1195	3.39	308.26	22.33	3.22
0.1283	4.32	308.33	28.83	4.05
0.1353	5.27	308.25	35.69	4.87
0.1410	6.24	308.30	42.81	5.69
0.1444	7.22	308.26	50.19	6.50
0.1494	8.20	308.25	57.74	7.28
0.1503	9.19	308.27	65.43	8.05
0.1506	10.18	308.30	73.23	8.81
0.1505	11.17	308.30	81.08	9.54
0.1504	12.16	308.36	88.93	10.27
0.1489	13.15	308.31	96.78	10.97

Table S B7: CH₄ excess isotherm data 318 K.

Uptake	Pressure	Sample Temp	Density	Fugacity
mmol g⁻¹	MPa	K	kg m⁻³	MPa
0.0106	0.08	318.12	0.49	0.08
0.0247	0.22	318.05	1.34	0.22
0.0425	0.49	318.11	2.97	0.48
0.0644	1.01	318.16	6.23	1.00
0.0830	1.72	318.17	10.67	1.68
0.0979	2.54	318.22	15.91	2.45
0.1094	3.42	318.25	21.71	3.27
0.1188	4.36	318.21	27.96	4.11
0.1266	5.31	318.28	34.50	4.96
0.1327	6.29	318.33	41.29	5.80
0.1368	7.27	318.32	48.29	6.62
0.1403	8.26	318.28	55.44	7.44
0.1418	9.26	318.34	62.69	8.24
0.1414	10.25	318.32	70.03	9.02
0.1410	11.24	318.29	77.36	9.79
0.1408	12.23	318.28	84.73	10.54
0.1369	13.22	318.29	92.07	11.28

Table S B8: CH₄ excess isotherm data 338 K.

Uptake	Pressure	Sample Temp	Density	Fugacity
mmol g⁻¹	MPa	K	kg m⁻³	MPa
0.0068	0.08	338.16	0.48	0.08
0.0179	0.23	338.15	1.30	0.23
0.0324	0.50	338.16	2.87	0.50
0.0527	1.04	338.21	5.99	1.03
0.0702	1.76	338.21	10.20	1.72
0.0847	2.58	338.23	15.14	2.52
0.0962	3.48	338.23	20.58	3.36
0.1048	4.42	338.26	26.37	4.23
0.1116	5.39	338.26	32.42	5.11
0.1192	6.37	338.29	38.63	5.98
0.1242	7.36	338.27	45.01	6.85
0.1273	8.36	338.27	51.49	7.71
0.1296	9.36	338.27	58.02	8.55
0.1319	10.36	338.35	64.55	9.39
0.1309	11.36	338.28	71.14	10.21
0.1303	12.35	338.27	77.70	11.02
0.1306	13.34	338.33	84.19	11.82

Table S B9: CH₄ excess isotherm data 358 K.

Uptake	Pressure	Sample Temp	Density	Fugacity
mmol g⁻¹	MPa	K	kg m⁻³	MPa
0.0049	0.09	358.20	0.48	0.09
0.0133	0.24	358.14	1.27	0.24
0.0253	0.51	358.14	2.77	0.51
0.0427	1.06	358.22	5.76	1.05
0.0584	1.79	358.20	9.77	1.76
0.0716	2.63	358.21	14.44	2.57
0.0824	3.53	358.21	19.52	3.43
0.0917	4.48	358.30	24.95	4.33
0.0995	5.46	358.26	30.59	5.23
0.1057	6.45	358.28	36.37	6.14
0.1099	7.44	358.27	42.22	7.04
0.1130	8.45	358.30	48.14	7.93
0.1150	9.45	358.31	54.09	8.82
0.1147	10.45	358.32	60.06	9.69
0.1149	11.45	358.31	66.00	10.55
0.1128	12.45	358.26	71.96	11.41
0.1121	13.44	358.28	77.83	12.26

Table S B10: CH₄ excess isotherm data 373 K.

Uptake	Pressure	Sample Temp	Density	Fugacity
mmol g⁻¹	MPa	K	kg m⁻³	MPa
0.0038	0.09	373.18	0.48	0.09
0.0105	0.24	373.18	1.25	0.24
0.0209	0.52	373.18	2.71	0.52
0.0361	1.08	373.23	5.60	1.07
0.0499	1.81	373.21	9.46	1.79
0.0620	2.65	373.26	13.96	2.61
0.0718	3.57	373.19	18.87	3.49
0.0800	4.53	373.29	24.04	4.40
0.0864	5.50	373.27	29.38	5.32
0.0921	6.49	373.26	34.84	6.24
0.0958	7.49	373.26	40.37	7.16
0.0981	8.50	373.24	45.96	8.08
0.0993	9.50	373.25	51.56	8.98
0.0985	10.51	373.24	57.16	9.88
0.0984	11.51	373.28	62.74	10.78
0.0955	12.51	373.25	68.30	11.66
0.0941	13.51	373.28	73.81	12.54

Table S B11: CH₄ excess isotherm data 398 K.

Uptake	Pressure	Sample Temp	Density	Fugacity
mmol g⁻¹	MPa	K	kg m⁻³	MPa
0.0016	0.10	398.17	0.46	0.10
0.0066	0.25	398.19	1.20	0.25
0.0146	0.53	398.13	2.57	0.53
0.0269	1.10	398.13	5.36	1.09
0.0384	1.84	398.19	9.01	1.83
0.0483	2.70	398.23	13.23	2.66
0.0572	3.62	398.18	17.81	3.56
0.0639	4.58	398.21	22.62	4.49
0.0689	5.56	398.21	27.56	5.43
0.0746	6.56	398.27	32.60	6.38
0.0784	7.57	398.19	37.68	7.33
0.0799	8.57	398.19	42.77	8.27
0.0815	9.58	398.25	47.88	9.22
0.0801	10.58	398.20	52.98	10.15
0.0796	11.59	398.26	58.04	11.08
0.0776	12.59	398.24	63.05	12.00
0.0761	13.58	398.21	68.04	12.92

Table S B12: CH₄ excess isotherm data 423 K.

Uptake	Pressure	Sample Temp	Density	Fugacity
mmol g⁻¹	MPa	K	kg m⁻³	MPa
0.0012	0.10	423.17	0.44	0.10
0.0051	0.25	423.16	1.16	0.25
0.0115	0.55	423.17	2.50	0.55
0.0210	1.12	423.22	5.13	1.12
0.0310	1.87	423.19	8.57	1.86
0.0402	2.74	423.22	12.57	2.71
0.0484	3.66	423.25	16.88	3.62
0.0538	4.63	423.21	21.38	4.57
0.0594	5.62	423.29	25.97	5.53
0.0630	6.62	423.22	30.65	6.50
0.0660	7.63	423.25	35.36	7.47
0.0668	8.64	423.25	40.06	8.44
0.0680	9.64	423.26	44.76	9.41
0.0675	10.65	423.26	49.44	10.37
0.0656	11.65	423.23	54.09	11.33
0.0632	12.65	423.27	58.71	12.29
0.0613	13.65	423.23	63.27	13.23

Table S B13: CH₄ excess isotherm data 448 K.

Uptake	Pressure	Sample Temp	Density	Fugacity
mmol g⁻¹	MPa	K	kg m⁻³	MPa
0.0008	0.10	448.08	0.44	0.10
0.0037	0.26	448.13	1.13	0.26
0.0090	0.56	448.11	2.41	0.56
0.0170	1.14	448.11	4.94	1.14
0.0252	1.91	448.13	8.24	1.90
0.0330	2.78	448.19	12.02	2.76
0.0400	3.71	448.19	16.07	3.69
0.0445	4.68	448.14	20.28	4.64
0.0490	5.67	448.20	24.59	5.61
0.0520	6.67	448.17	28.96	6.60
0.0544	7.68	448.16	33.34	7.59
0.0547	8.69	448.19	37.71	8.57
0.0542	9.70	448.22	42.07	9.56
0.0532	10.71	448.19	46.43	10.55
0.0518	11.71	448.19	50.74	11.53
0.0478	12.71	448.12	55.01	12.51
0.0459	13.71	448.20	59.23	13.49

Table S B14: CH₄ excess isotherm data 473 K.

Uptake	Pressure	Sample Temp	Density	Fugacity
mmol g⁻¹	MPa	K	kg m⁻³	MPa
0.0005	0.10	473.15	0.41	0.10
0.0028	0.26	473.08	1.08	0.26
0.0071	0.57	473.10	2.31	0.57
0.0137	1.16	473.15	4.74	1.16
0.0202	1.93	473.21	7.89	1.93
0.0263	2.81	473.29	11.48	2.80
0.0314	3.75	473.19	15.32	3.74
0.0347	4.72	473.23	19.31	4.71
0.0381	5.72	473.23	23.37	5.69
0.0398	6.72	473.16	27.46	6.69
0.0405	7.73	473.21	31.56	7.69
0.0403	8.74	473.25	35.66	8.69
0.0419	9.74	473.19	39.72	9.69
0.0403	10.75	473.20	43.78	10.69
0.0395	11.75	473.23	47.80	11.70
0.0354	12.75	473.17	51.77	12.69
0.0318	13.75	473.20	55.73	13.69

Fitting of the experimental data to sorption models

Supercritical Dubinin-Radushkevich model

Variant 1 (best fit)

This variant represents the best fit in terms of fitting performance and reasonability of the calculated parameters. The results are shown in the main manuscript.

Variant 2

Variables: $D, n_0(T)$

No. of Fitting Parameters: 10

Variant 2 fails to fit the experimental data.

Table S B15: All parameters calculated by fitting the SDR model (Variant 2) to the experimental data.

Temperature	n_0	ρ_{ads}	D	v
K	mmol g^{-1}	kg m^{-3}	$\text{mol}^2 \text{kJ}^{-2}$	-
300	0.245	370	0.010	1.326
303	0.234			
308	0.220			
318	0.210			
338	0.200			
358	0.185			
373	0.167			
398	0.147			
423	0.134			
448	0.118			

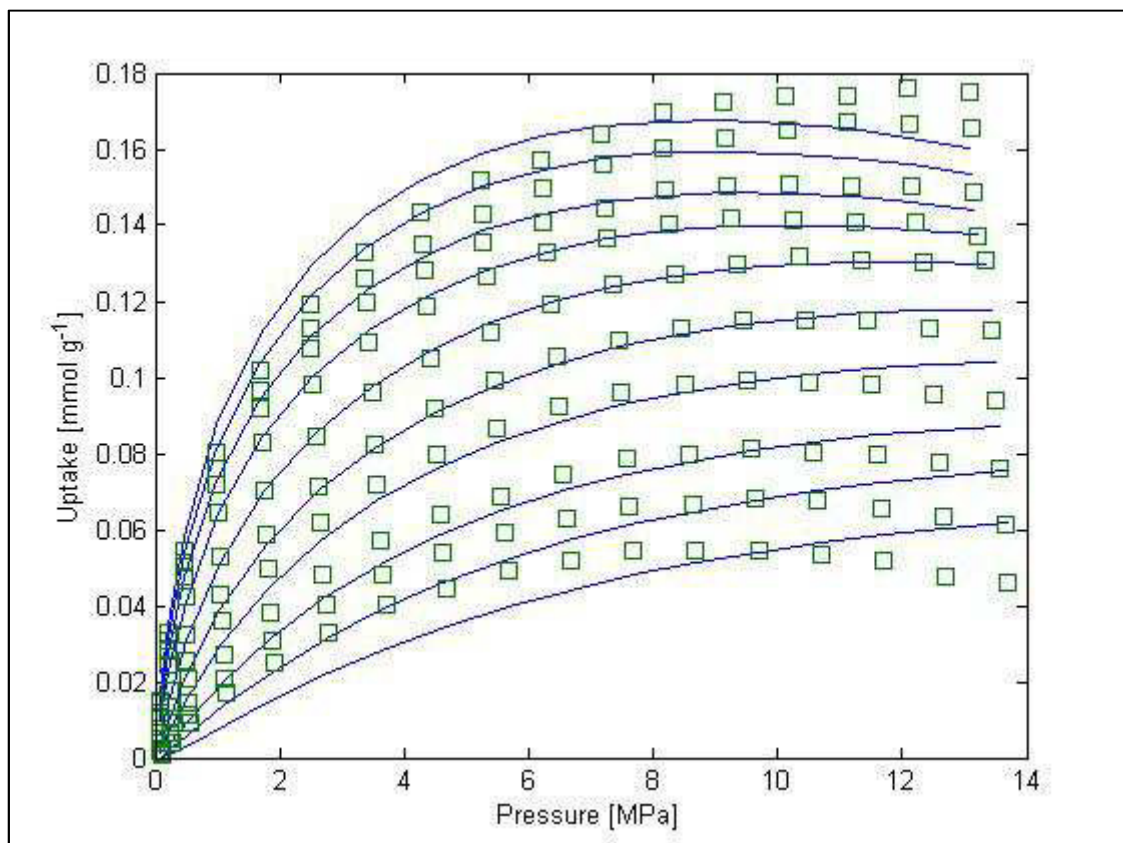


Figure S B2: Fit of the SDR model (Variant 2) to the experimental data. Green squares represent the experimental data, blue lines represent the fit of the model.

Variant 3

Variables: $D, n_0(T), \rho_{\text{ads}}$

No. of Fitting Parameters: 10

Variant 3 fails to fit the experimental data.

Table S B16: All parameters calculated by fitting the SDR model (Variant 3) to the experimental data.

Temperature	n_0	ρ_{ads}	D	v
K	mmol g ⁻¹	kg m ⁻³	mol ² kJ ⁻²	-
300	0.239	540	0.008	1.079
303	0.228			
308	0.214			
318	0.205			
338	0.198			
358	0.184			
373	0.167			
398	0.148			
423	0.137			
448	0.121			

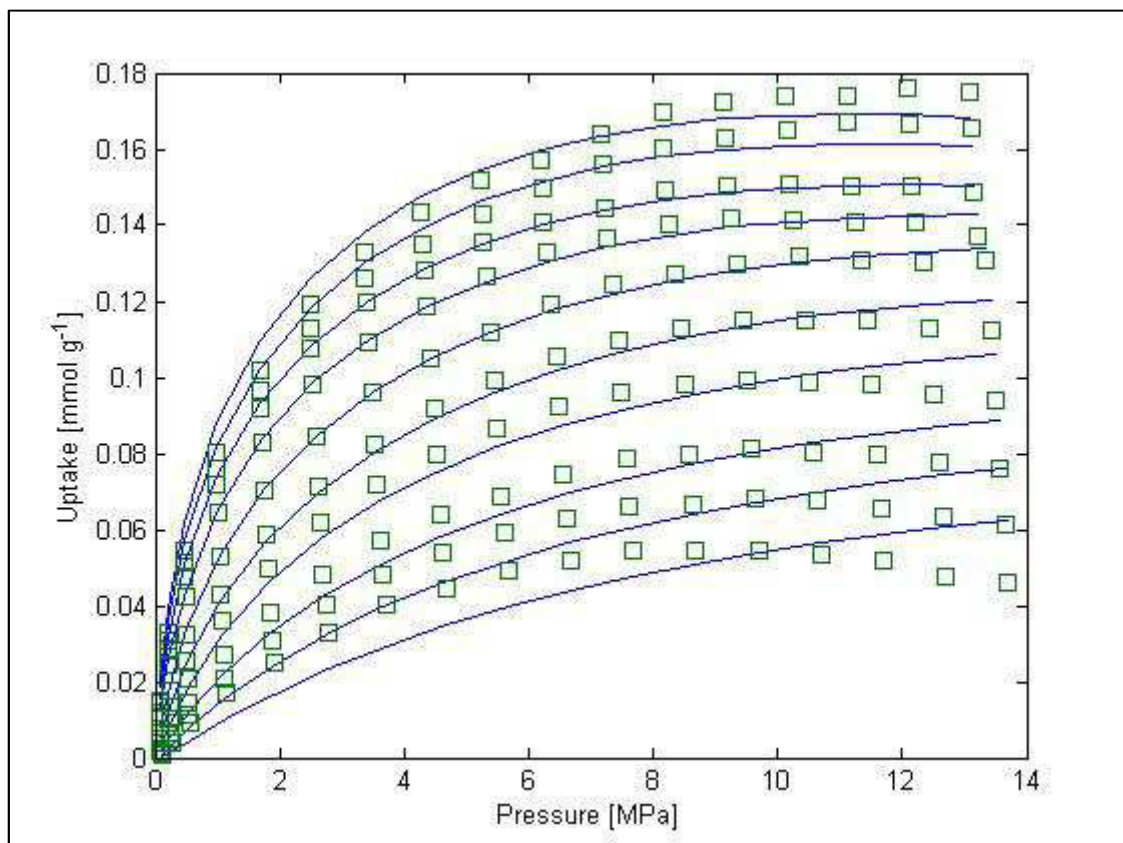


Figure S B3: Fit of the SDR model (Variant 3) to the experimental data. Green squares represent the experimental data, blue lines represent the fit of the model.

Langmuir model

Variant A4

Variables: $n_0(T)$, $k(T)$, $\rho_{\text{ads}}(T)$

No. of Fitting Parameters: 30

Variant 4 fails to fit the experimental data.

Table S B17: All parameters calculated by fitting the Langmuir model (Variant 4) to the experimental data.

Temp	n_0	k	ρ_{ads}	v
K	mmol g ⁻¹		kg m ⁻³	
300	0.201	0.673	2234300	0.2324
303	0.191	0.664	1713000	
308	0.175	0.716	5486	
318	0.176	0.574	1369	
338	0.169	0.428	1496	
358	0.186	0.269	384	
373	0.188	0.212	246	
398	0.191	0.143	180	
423	0.218	0.095	129	
448	0.244	0.066	99	

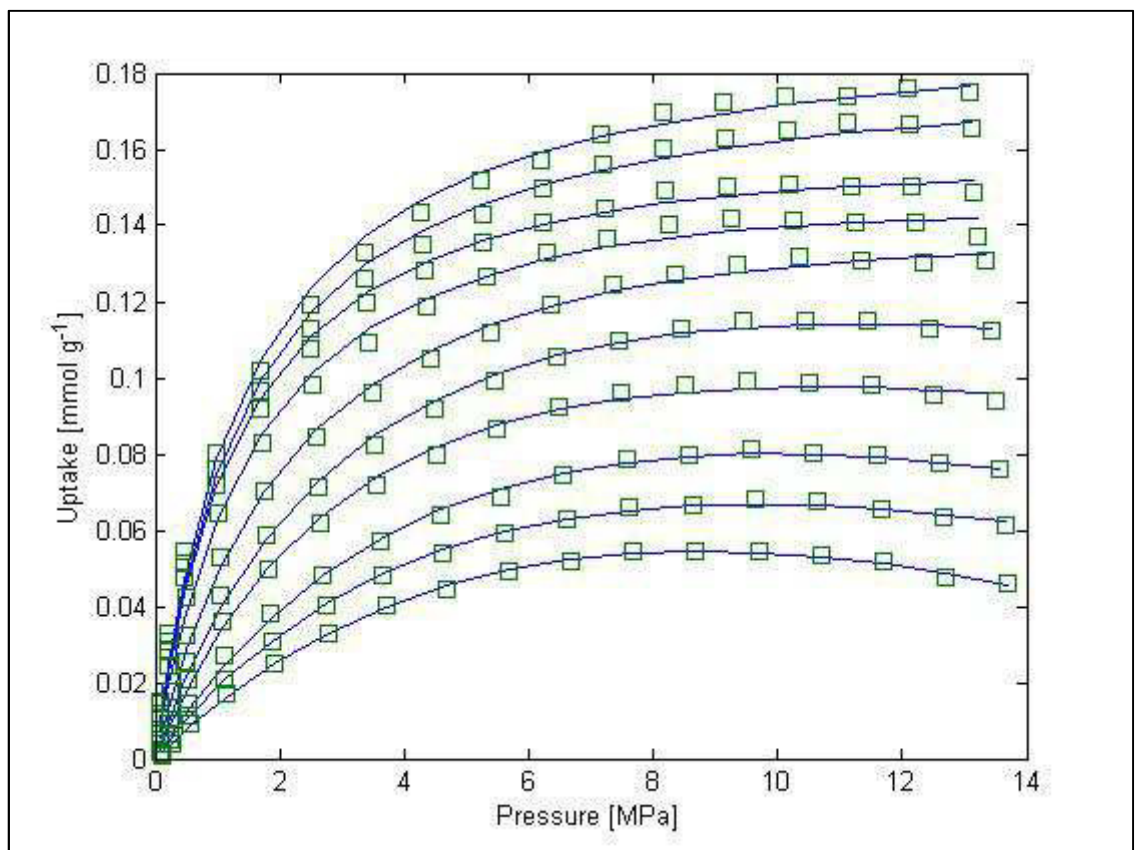


Figure S B4: Fit of the Langmuir model (Variant 4) to the experimental data. Green squares represent the experimental data, blue lines represent the fit of the model.

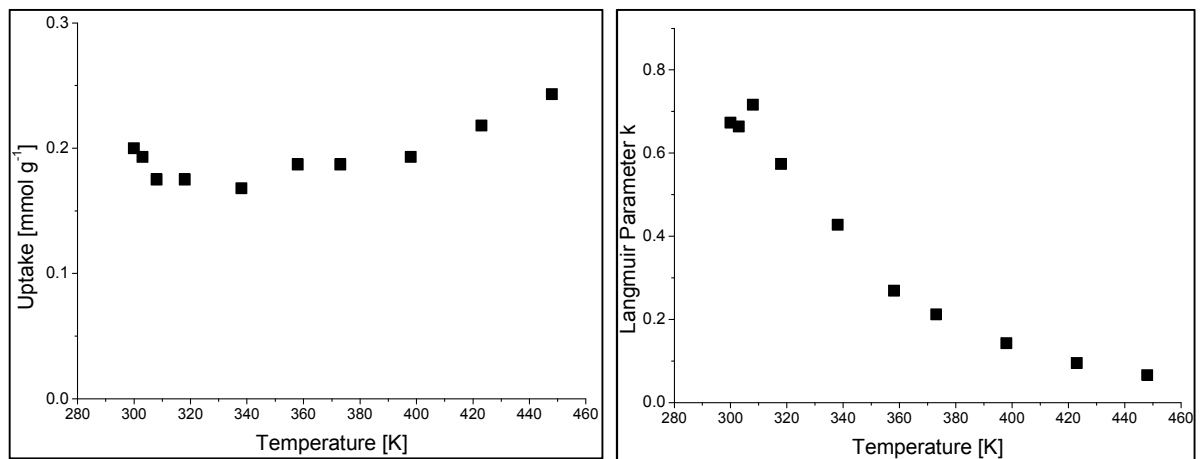


Figure S B5: Parameter calculated by the Langmuir model (Variant 4) a) Maximum absolute uptake and b) Langmuir constant plotted against temperature.

Variant 5Variables: $n_0(T)$, $k(T)$

No. of Fitting Parameters: 20

Variant 5 fails to fit the experimental data in the high temperature area (373 K, 398 K, 423 K, 448 K) and in the low temperature area (300 K, 303 K).

Table S B18: All parameters calculated by fitting the Langmuir model (Variant 5) to the experimental data.

Temp	n_0	k	ρ_{ads}	v
K	mmol g^{-1}		kg m^{-3}	
300	0.290	0.333	370	0.957
303	0.273	0.334		
308	0.238	0.393		
318	0.224	0.365		
338	0.216	0.282		
358	0.189	0.264		
373	0.158	0.277		
398	0.130	0.248		
423	0.105	0.257		
448	0.079	0.296		

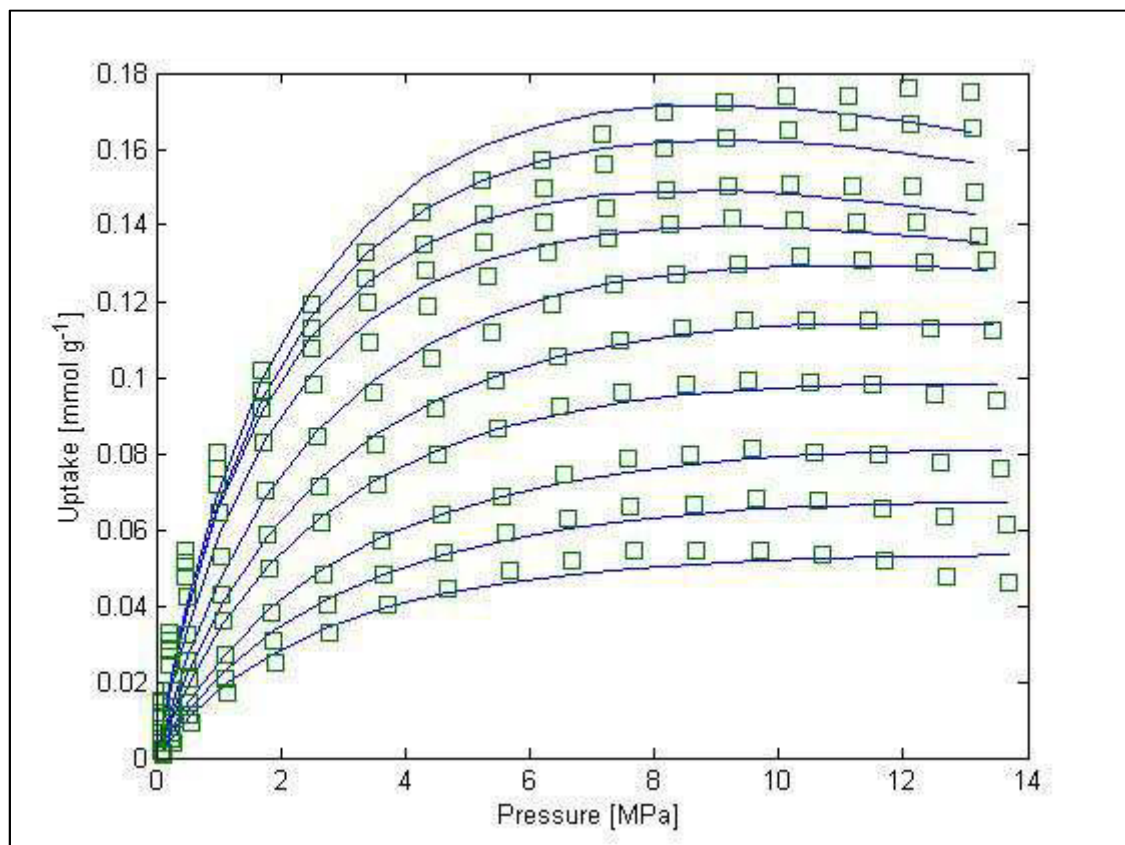


Figure S B6: Fit of the Langmuir model (Variant 5) to the experimental data. Green squares represent the experimental data, blue lines represent the fit of the model.

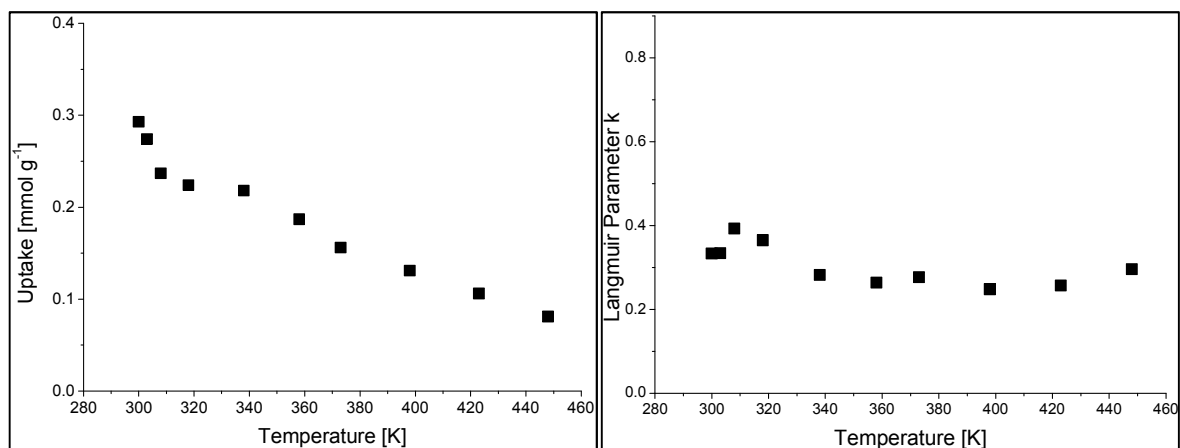


Figure S B7: Parameter calculated by the Langmuir model (Variant 5) a) Maximum absolute uptake and b) Langmuir constant plotted against temperature.

Variant 6Variables: $n_0(T)$, $k(T)$, ρ_{ads}

No. of Fitting Parameters: 21

Variant 6 fails to fit isotherms below 358 K.

Table S B19: All parameters calculated by fitting the Langmuir model (Variant 6) to the experimental data.

Temp	n_0	k	ρ_{ads}	v
K	mmol g ⁻¹		kg m ⁻³	
300	0.205	0.644	4992	0.453
303	0.195	0.636		
308	0.176	0.713		
318	0.167	0.638		
338	0.161	0.466		
358	0.144	0.411		
373	0.123	0.415		
398	0.103	0.356		
423	0.085	0.354		
448	0.066	0.394		

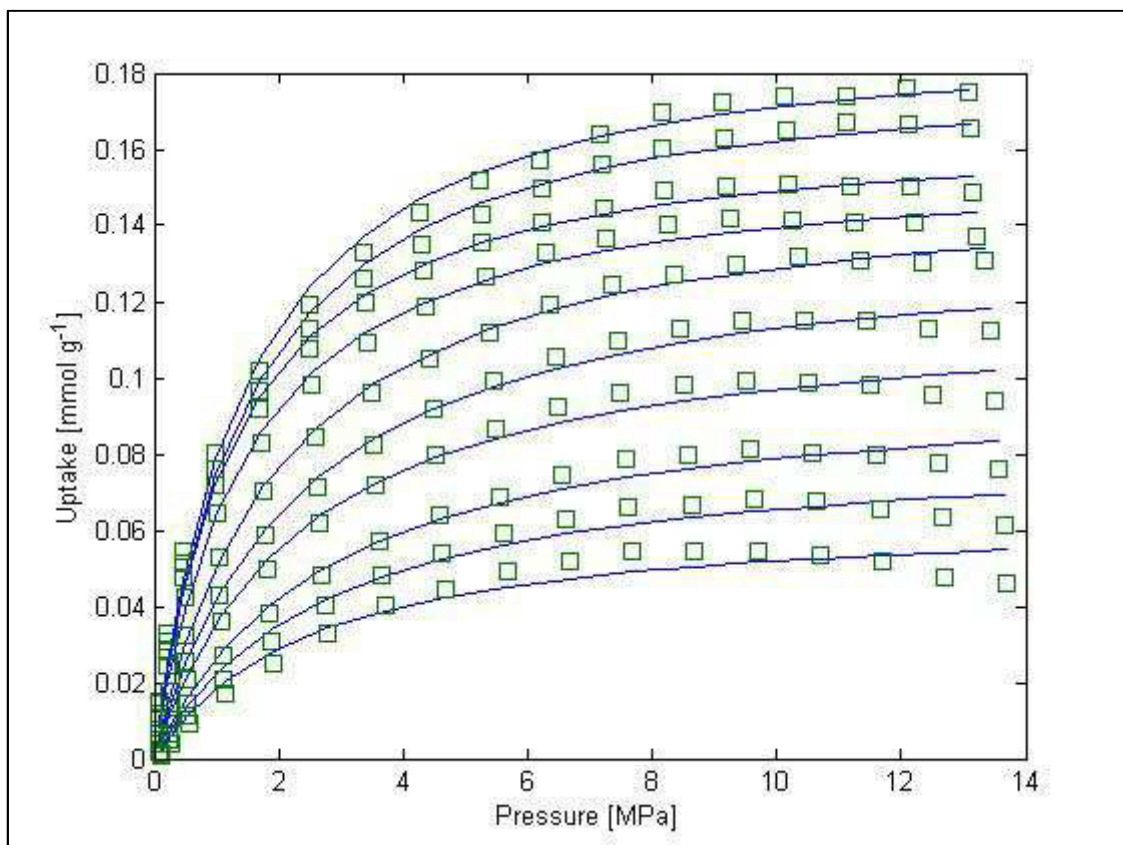


Figure S B8: Fit of the Langmuir model (Variant 6) to the experimental data. Green squares represent the experimental data, blue lines represent the fit of the model.

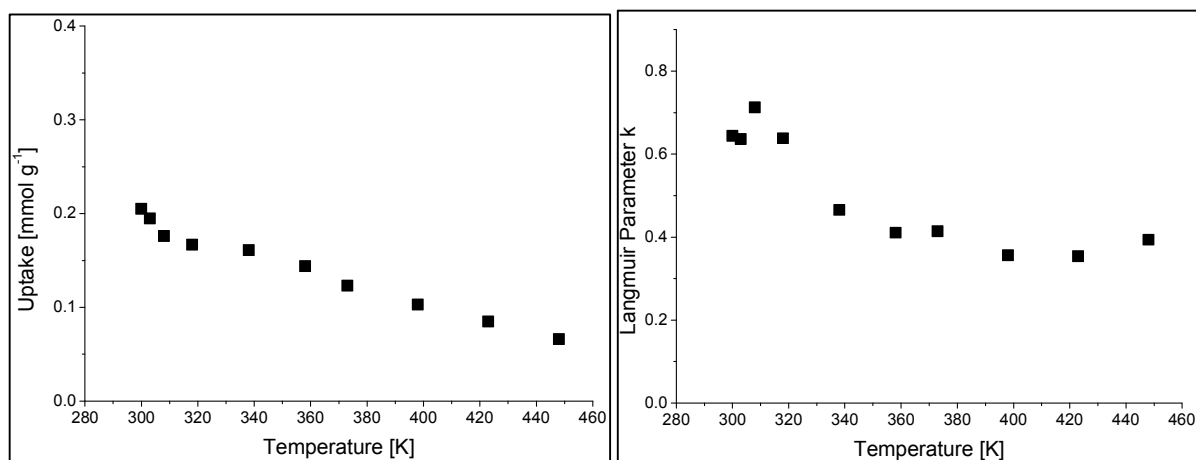


Figure S B9: Parameter calculated by the Langmuir model (Variant 6) a) Maximum absolute uptake and b) Langmuir constant plotted against temperature.

Variant 7

Variables: $n_0(T)$, $k(T)$, V_{ads}

No. of Fitting Parameters: 30

Variant 7 fits the isotherm well. However, the calculated parameters are physically unreasonable, e.g. increasing absolute maximum uptake with increasing temperature and negative adsorbed phase Volumes at 300 and 303 K. Thus, it can be said that this variant with 30 fitting parameters provides a poorly constrained model.

Table S B20: All parameters calculated by fitting the Langmuir model (Variant 7) to the experimental data.

Temp	n_0	k	V_{ads}	v
K	mmol g^{-1}		kg m^{-3}	
300	0.180	0.839	-0.0029	0.2084
303	0.172	0.812	-0.0026	
308	0.174	0.729	0.0003	
318	0.180	0.555	0.0024	
338	0.169	0.433	0.0016	
358	0.200	0.261	0.0079	
373	0.203	0.216	0.0114	
398	0.236	0.137	0.0174	
423	0.348	0.084	0.0308	
448	0.253	0.097	0.0260	

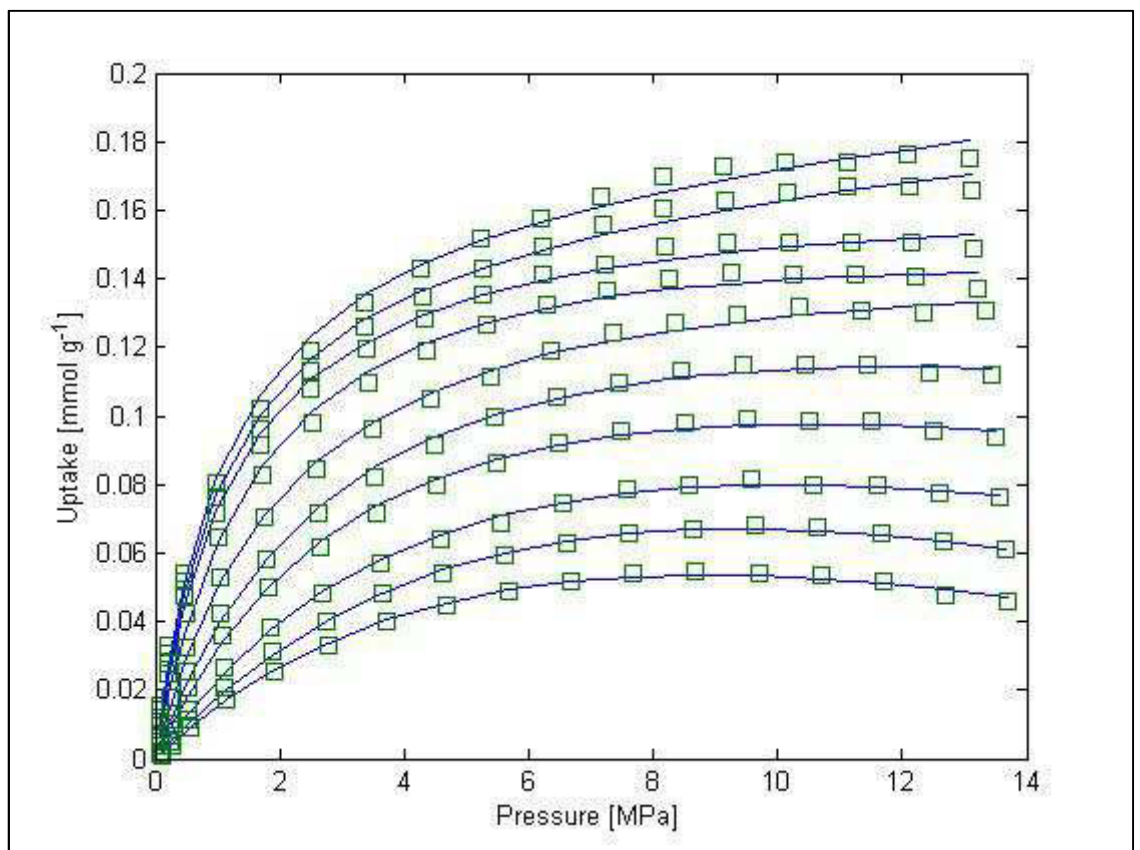


Figure S B10: Fit of the Langmuir model (Variant 7) to the experimental data. Green squares represent the experimental data, blue lines represent the fit of the model.

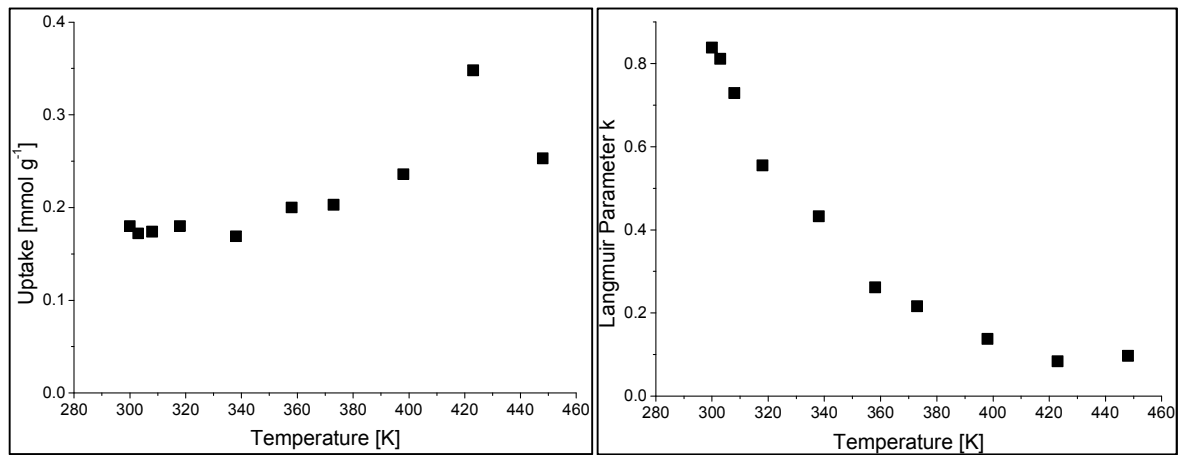


Figure S B11: Parameter calculated by the Langmuir model (Variant 7) a) Maximum absolute uptake and b) Langmuir constant plotted against temperature.

Variant 8 (best Langmuir fit)

This variant represents the best Langmuir fit in terms of fitting performance and reasonability of the calculated parameters. The results are shown in the main manuscript.

Variant 9

Variables: $n_0(T)$, $k(T)$

No. of Fitting Parameters: 20

Variant 9 fails to fit isotherms at temperatures above 338 K.

Table S B21: All parameters calculated by fitting the Langmuir model (Variant 8) to the experimental data.

Temp	n_0	k	V_{ads}	v
K	mmol g^{-1}	MPa^{-1}	kg m^{-3}	
300	0.374	0.243	0.0017	1.481
303	0.362	0.234		
308	0.328	0.256		
318	0.315	0.237		
338	0.311	0.188		
358	0.285	0.172		
373	0.255	0.167		
398	0.232	0.14		
423	0.204	0.134		
448	0.172	0.136		

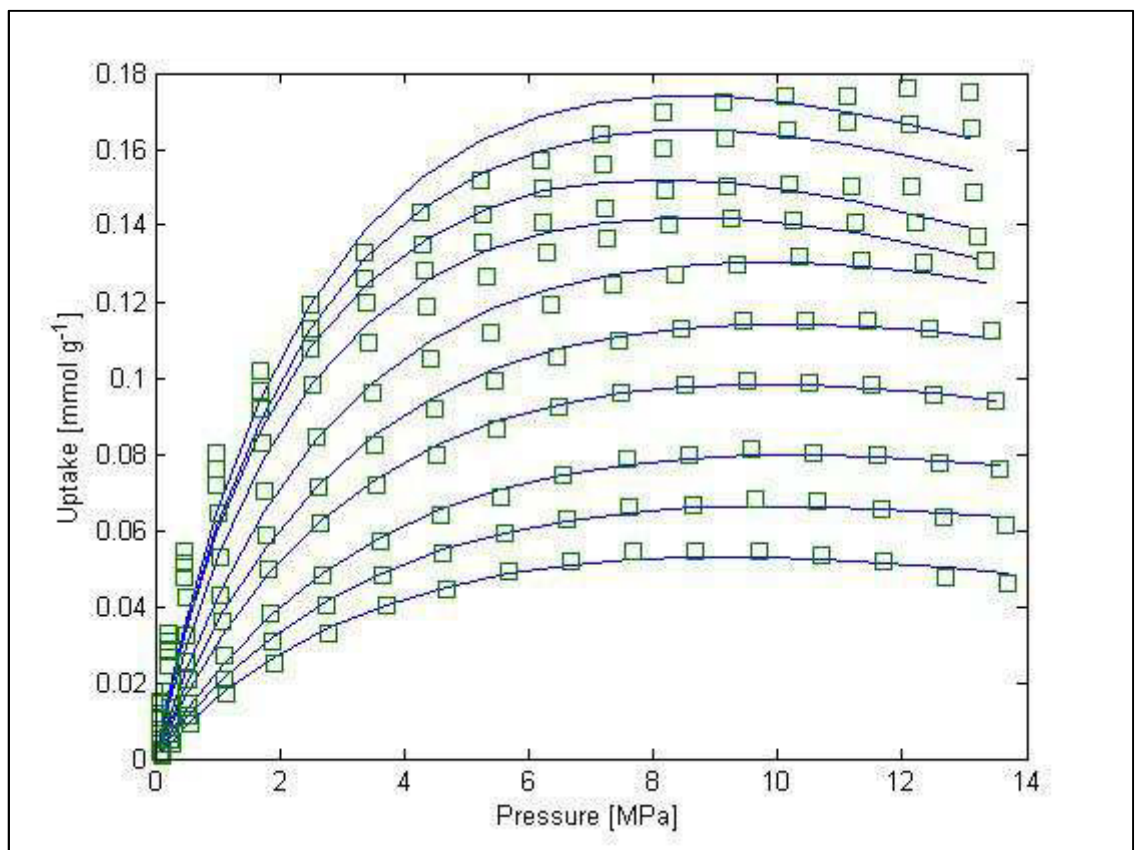


Figure S B12: Fit of the Langmuir model (Variant 9) to the experimental data. Green squares represent the experimental data, blue lines represent the fit of the model.

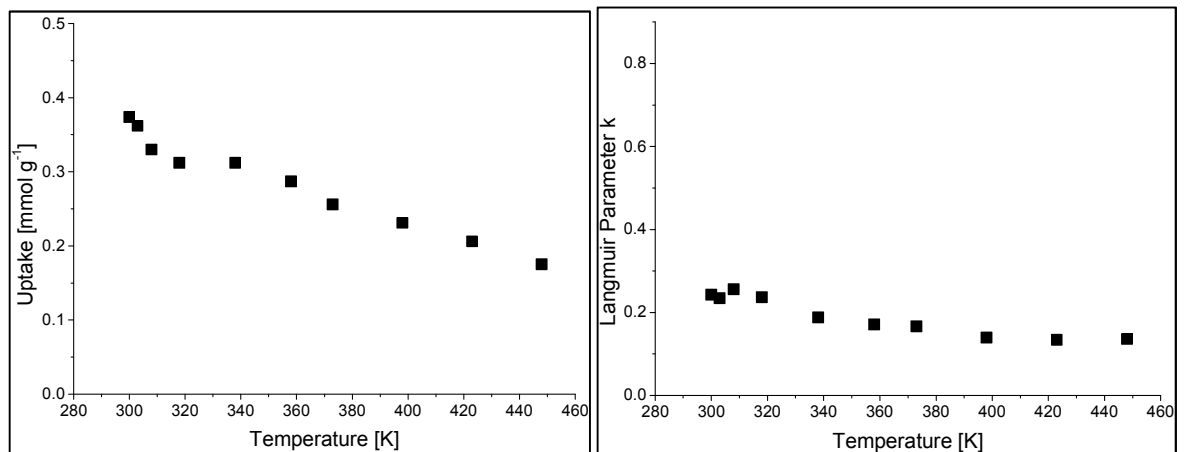
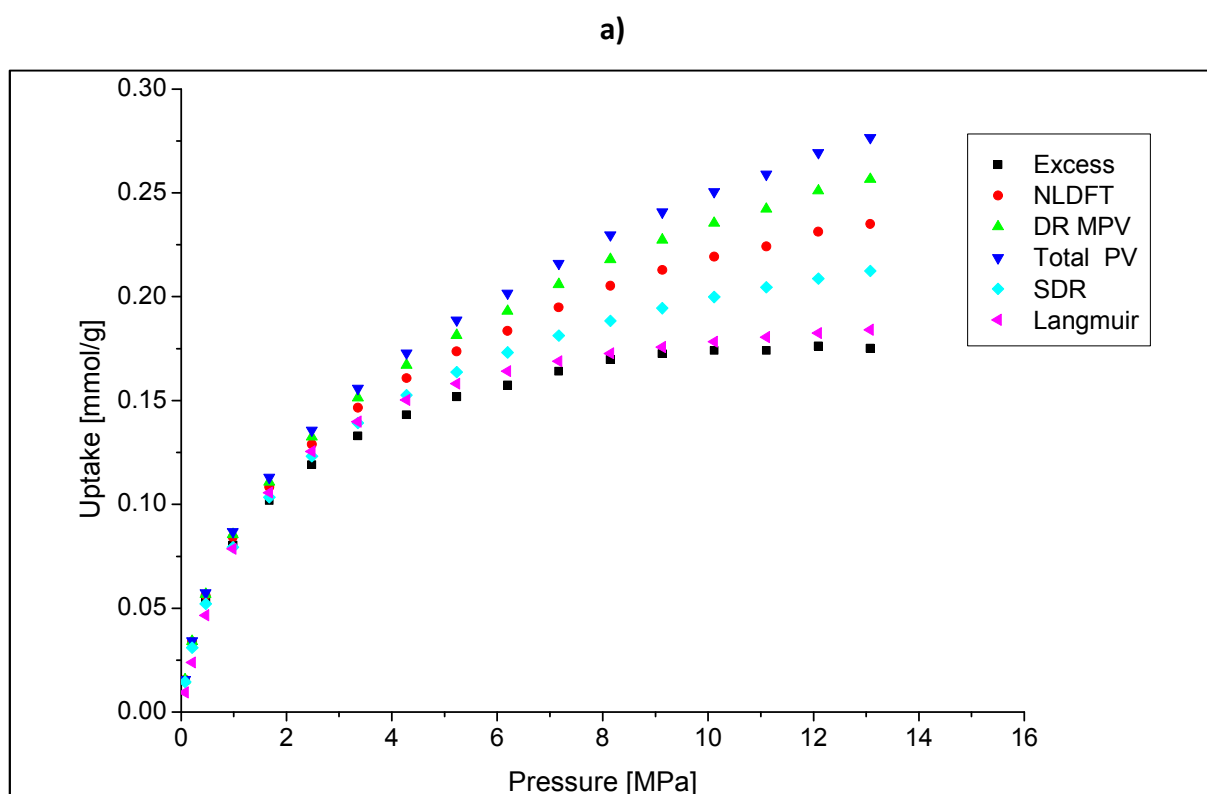


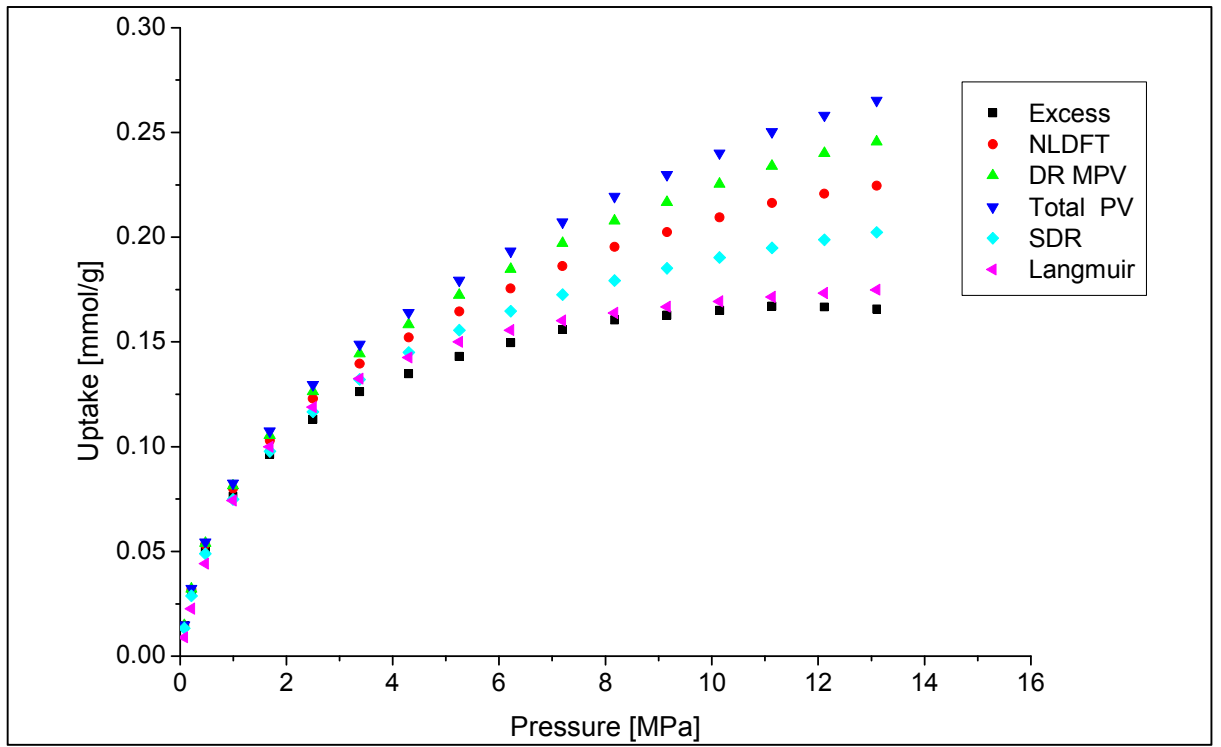
Figure S B13: Parameter calculated by the Langmuir model (Variant 9) a) Maximum absolute uptake and b) Langmuir constant plotted against temperature.

Comparisons of Methane excess isotherm and absolute isotherms

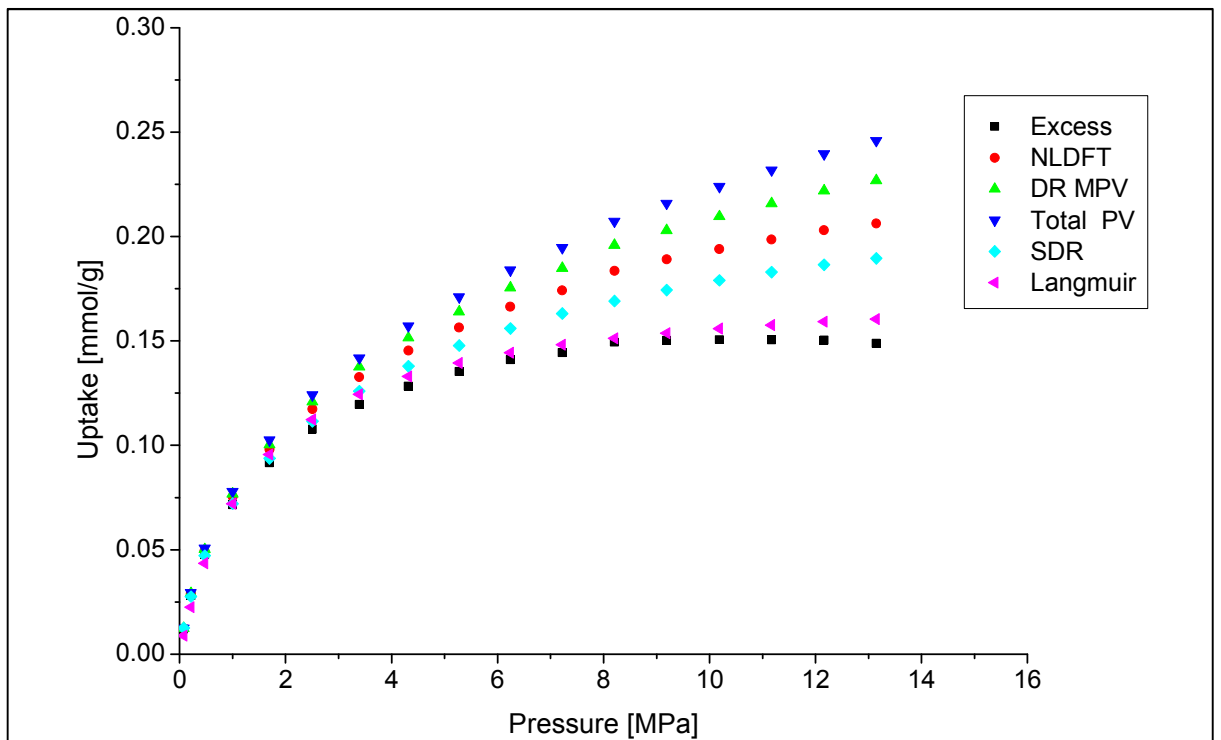
The SDR and Langmuir absolute isotherms are based on the parameters obtained in this study. The NLDFT absolute isotherms is the combination of the excess isotherm and the compressed gas in the pore volume obtained from the NDLFT model ($0.0095 \text{ cm}^3 \text{ g}^{-1}$). Accordingly, the micropore and the total pore volume are the excess isotherm plus the compressed gas in the micropore volume ($0.0129 \text{ cm}^3 \text{ g}^{-1}$) and in the total pore volume ($0.0161 \text{ cm}^3 \text{ g}^{-1}$). The latter values was chosen because it is the closest to the range of temperatures used for methane adsorption.



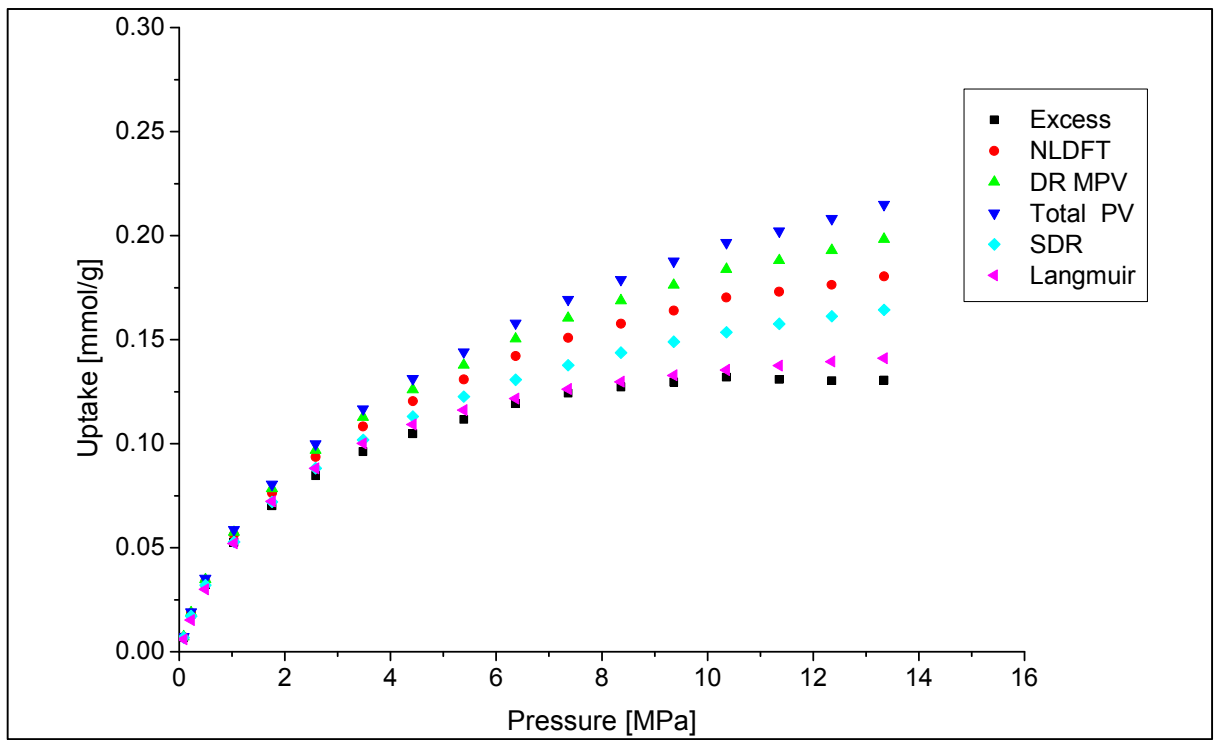
b)



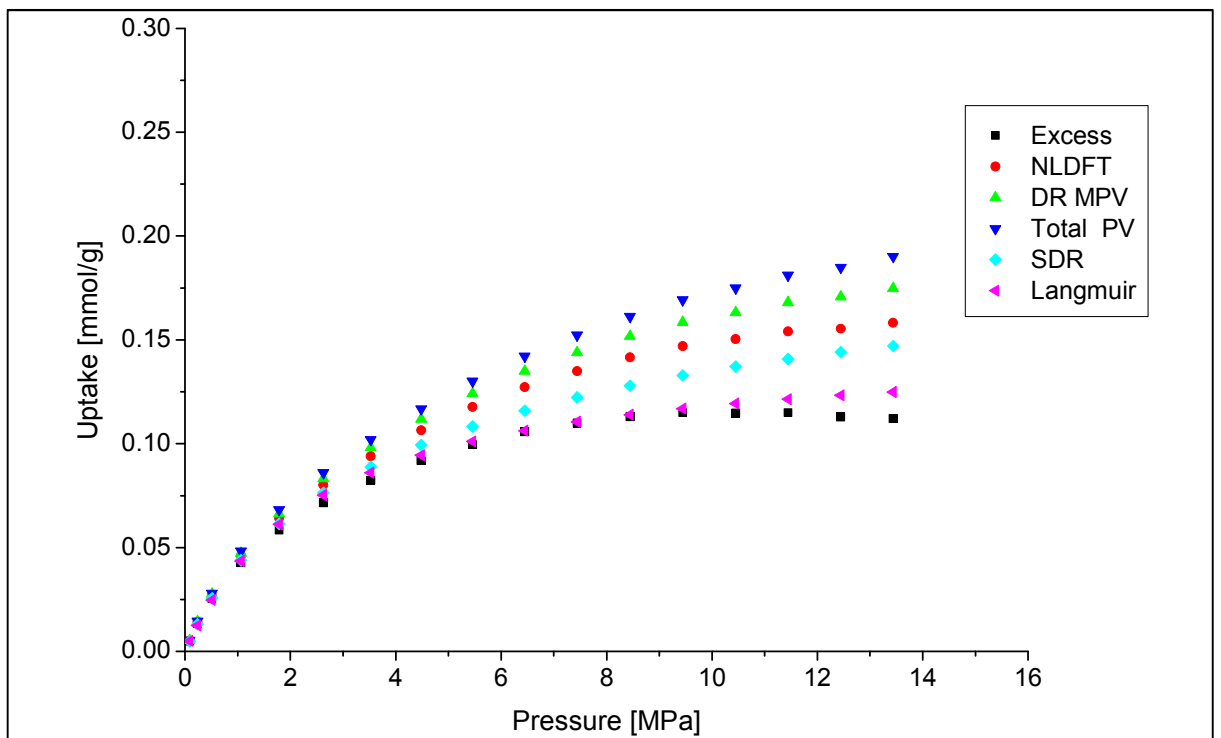
c)



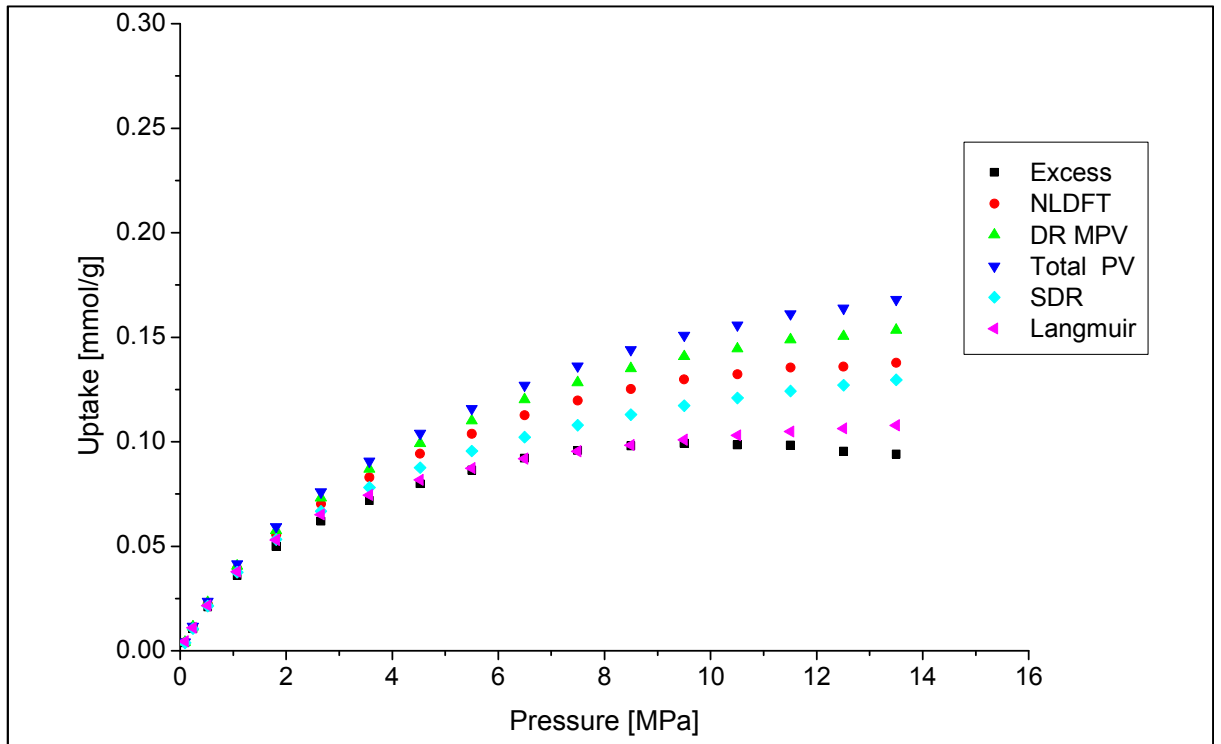
d)



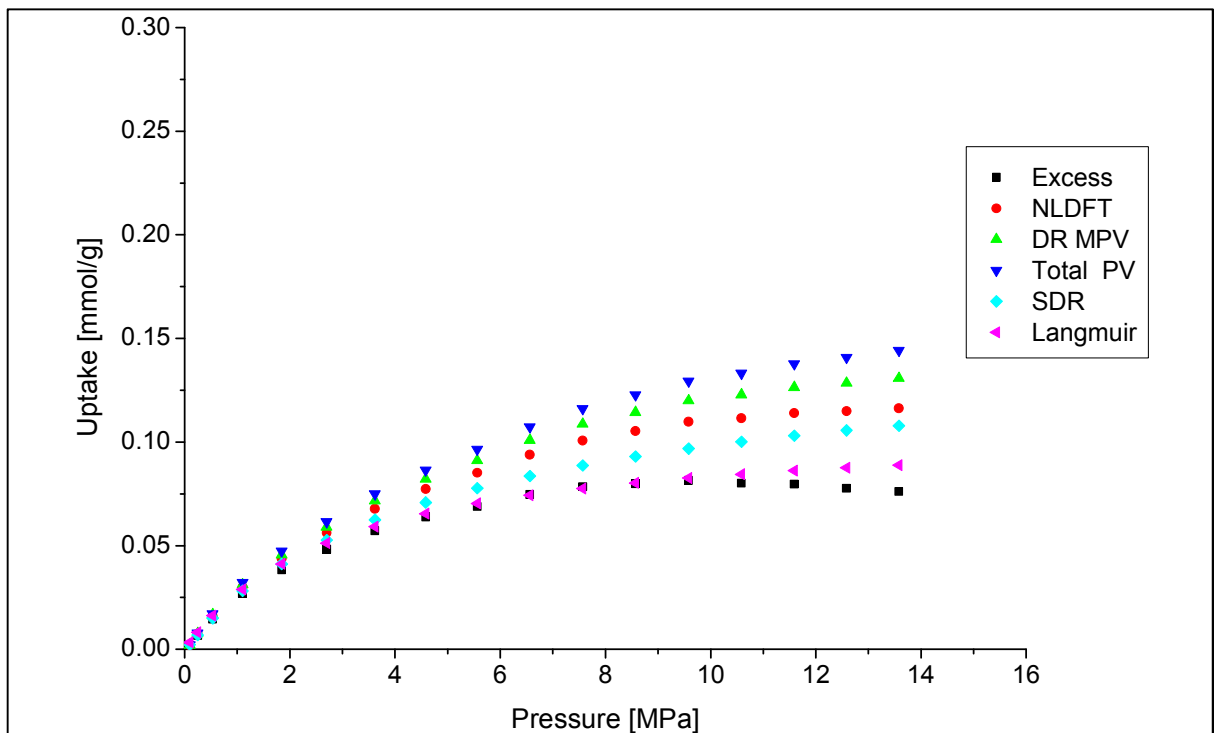
e)



f)



g)



h)

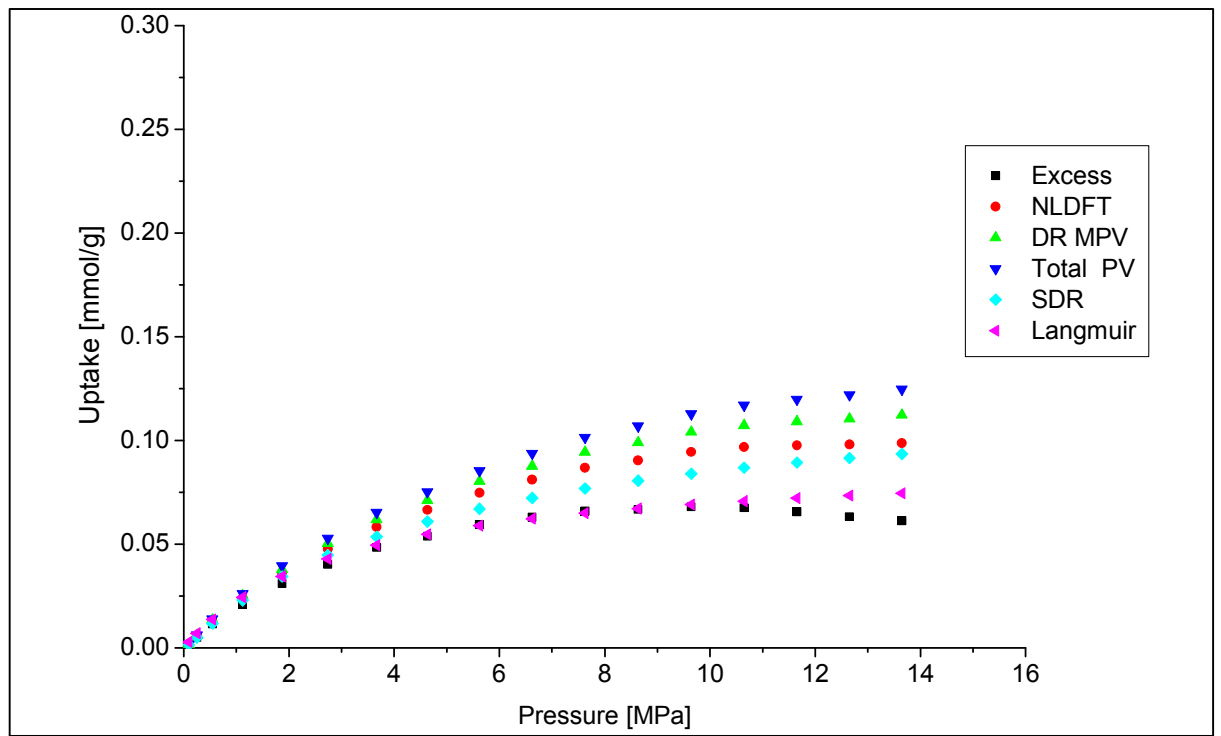


Figure S B14: Methane excess and absolute isotherms based on different models over a range of temperature a) 300K, b) 303 K, c) 308 K, d) 338 K, e) 358 K f) 373 K, g) 398 K, h) 423 K.

Example calculation of isotherms based on the parameter in Table 4 for 358 K

Dubinin

1. Choose Temperature and Pressure range

$$T = 358 \text{ K and } P = 2 - 16 \text{ MPa}$$

2. Parameters and Equations (see Table 4)

Parameter:

$$n_0 = 0.178 \text{ mmol g}^{-1}$$
$$\rho_{ads} = 357 \text{ kg m}^{-3}$$
$$D = 0.0093 \text{ mol}^2 \text{ kJ}^{-2}$$
$$R = 0.008315 \text{ kJ mol}^{-1} \text{ K}^{-1}$$

Equation (excess): $n_{ex} = n_0 \exp \left[-D \left(\ln \left(\frac{\rho_{ads,max}}{\rho_b} \right) R T \right)^2 \right] \left(1 - \frac{\rho_b}{\rho_{ads}} \right)$

Equation (absolute): $n_{ab} = n_0 \exp \left[-D \left(\ln \left(\frac{\rho_{ads,max}}{\rho_b} \right) R T \right)^2 \right]$

3. Stepwise calculation

Pressure	Density	$\ln \left(\frac{\rho_{ads,max}}{\rho_b} \right)$	$\left(\ln \left(\frac{\rho_{ads,max}}{\rho_b} \right) R T \right)^2$	Absolute calculated	Excess calculated
MPa	kg m ⁻³			mmol g ⁻¹	mmol g ⁻¹
2	10.953	3.4841	107.554	0.0655	0.0635
4	22.229	2.7763	68.294	0.0943	0.0884
6	33.782	2.3578	49.256	0.1126	0.1019
8	45.548	2.0590	37.561	0.1255	0.1095
10	57.443	1.8269	29.573	0.1352	0.1134
12	69.373	1.6382	23.779	0.1427	0.1150
14	81.231	1.4804	19.419	0.1486	0.1148
16	92.913	1.3461	16.054	0.1533	0.1134

Units applied as shown here.

Langmuir

1. Choose Temperature and Pressure range

$$T = 358 \text{ K and } P = 2 - 16 \text{ MPa}$$

2. Parameters and Equations (see Table 4)

$$n_0 = 0.151 \text{ mmol g}^{-1}$$

$$k = 0.384 \text{ MPa}^{-1}$$

$$V_{\text{ads}} = 0.0015 \text{ cm}^3 \text{ g}^{-1}$$

$$M = 16.04 \text{ g mol}^{-1}$$

$$\text{Equation (excess): } n_{ab} = n_0 \frac{K(T) f}{1+K(T) f} - (\rho_b V_{\text{ads}} M^{-1})$$

$$\text{Equation (absolute): } n_{ab} = n_0 \frac{K(T) f}{1+K(T) f}$$

3. Stepwise calculation

Pressure	Density	Fugacity	Absolute calculated	Excess calculated
MPa	kg m ⁻³	MPa	mmol g ⁻¹	mmol g ⁻¹
2	10.953	1.97	0.0650	0.0640
4	22.229	3.88	0.0903	0.0882
6	33.782	5.73	0.1038	0.1006
8	45.548	7.53	0.1122	0.1080
10	57.443	9.30	0.1180	0.1126
12	69.373	11.02	0.1221	0.1157
14	81.231	12.72	0.1253	0.1177
16	92.913	14.40	0.1279	0.1192

Units applied as shown here.

Appendix C

Contents

A. Kerogen Isolation	172
A.1 Kerogen isolation by HF and HCl.....	172
A.2 Kerogen purity, characterization and comparison with kerogen in shale.....	173
A.3 Pyrite corrections.....	178
B. Isotherms in tabular form	179
B.1 Low pressure adsorption data	179
B.2 High Pressure Methane Isotherms	187
C. Langmuir Parameterization	197
D. Micropore Size Distributions.....	199
E. Comparison of methane surface excess at specific pressures with CO ₂ sorption pore volume....	205
F. Comparison of High Pressure Methane Isotherms Normalized to TOC	207
G. Comparison of Porosity Characteristics determined from Subcritical Low Pressure/Temperature Adsorption	210

A. Kerogen Isolation

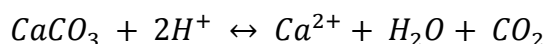
A.1 Kerogen isolation by HF and HCl

The aim of kerogen isolation was to separate the inorganic phase of the shale from the organic matter without altering the structure or generating newly formed solvent soluble organic material.¹ Hydrochloric acid (HCl) reacts with carbonates, some sulfides, oxides and hydroxides and hydrofluoric acid (HF) reacts with quartz, silicate and clay minerals. There are various techniques described in the literature for the removal of pyrite.² Shales vary in composition and, thus, the isolation process is tuned for each shale sample set. Demineralization is described in detail below:

Elimination of carbonates, sulfides, oxides and hydroxides by HCl:

Carbonates, sulfides and oxides react with HCl and the products are in solution.³

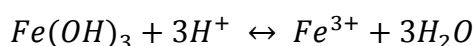
Carbonates:



Sulfides:



Oxides and Hydroxides:



HCl can hydrolyze organic matter. Durand and Nicaise have shown that this effect is insignificant for kerogens.²

Elimination of quartz, silicate and clays by HF:

Quartz, silicates and clay minerals react with HF. To avoid the formation of insoluble fluorides concentrated HCl is added before adding HF (40%).³

Quartz:



HF reacts with certain organic functional groups, e.g. condensation reactions of unsaturated hydrocarbons. However, it was shown that these reactions only slightly change the composition, e.g. increase the fluorine content of the sample.³

Pyrite removal:

Pyrite (FeS_2) is often closely associated with organic matter in shale. Treatment with nitric acid (HNO_3) and lithium aluminum hydride (LiAlH_4) have been proposed as methods to eliminate pyrite. However, HNO_3 can oxidize or nitrate kerogen and LiAlH_4 can reduce carboxylic acids, esters and ketones to alcohols.^{2,3}

For this study chromium(II) chloride (CrCl_2) in an acid solution and an inert nitrogen environment was used to remove pyrite.¹ Canfield et al used CrCl_2 to remove and quantify sulfur species present in a sediment to relate it to the type of diagenetic environment in which they were deposited.⁴ CrCl_2 reduces sulfur species to H_2S . CrCl_2 does not reduce or liberate either organic sulfur or sulfate sulfur.^{4,5} As CrCl_2 is non-oxidizing, it does not oxidize organic kerogen matter.

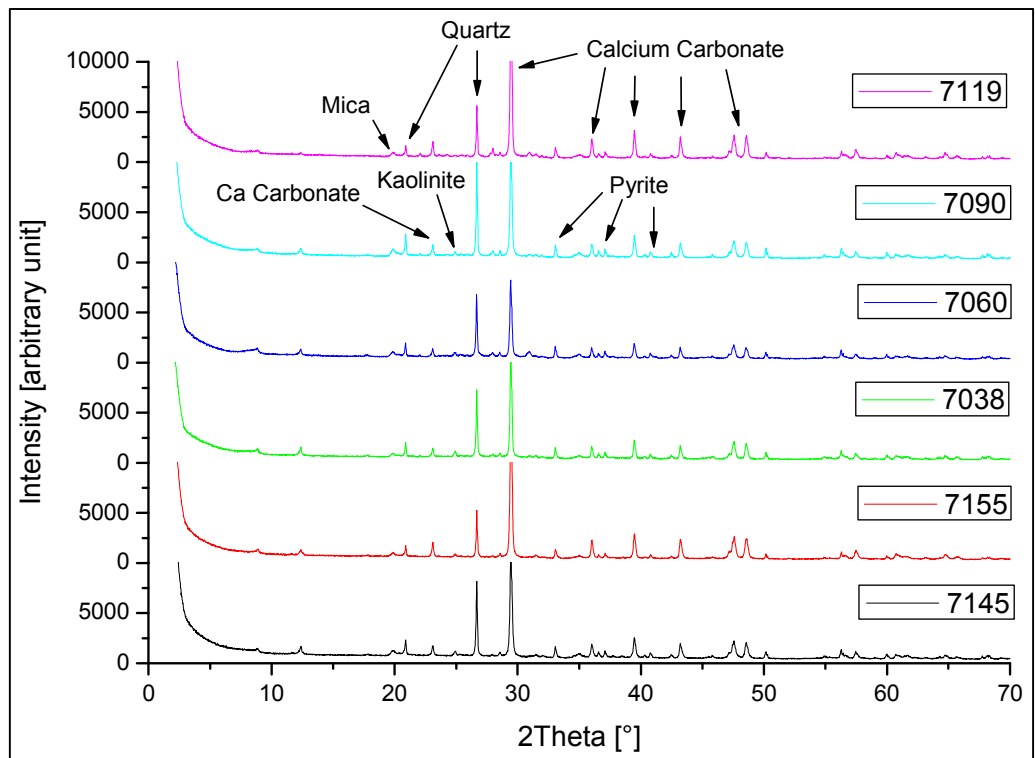
A.2 Kerogen purity, characterization and comparison with kerogen in shale

i) Verification of kerogen isolation purity by X-ray Diffraction

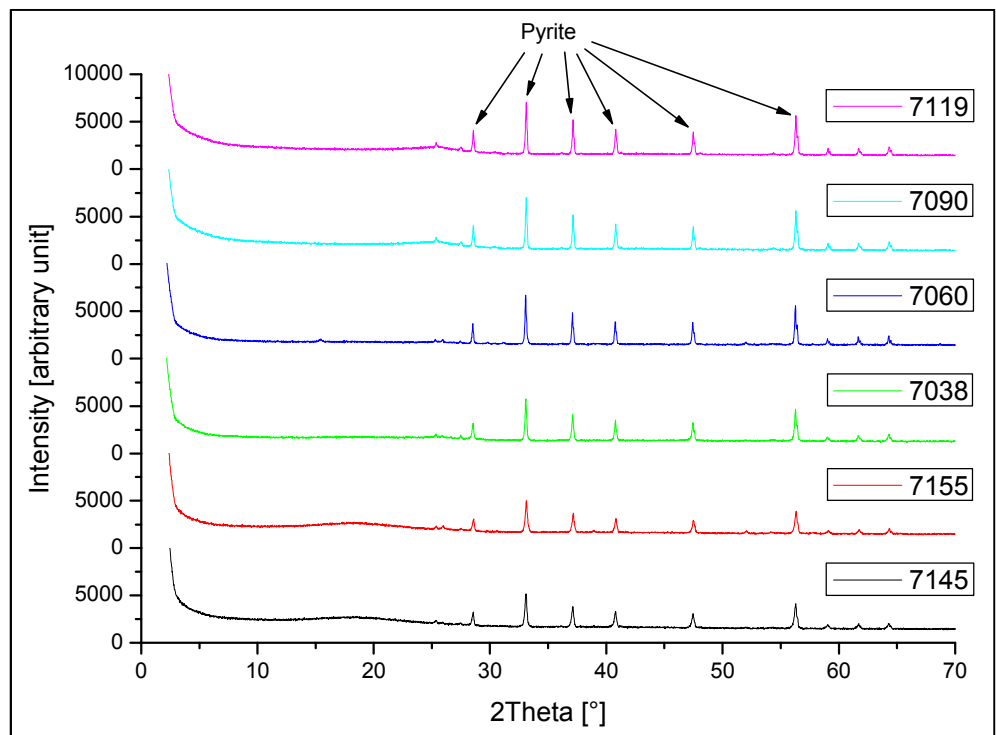
XRD profiles were measured on the samples before and after the isolation process (see Figure S C1) on a PANalytical X'Pert Pro MPD, combined with a Philips PW3040/60 X-ray generator and fitted with an X'Celerator detector. Diffraction data were acquired by exposing powder samples to $\text{Cu-K}\alpha$ X-ray radiation, which has a characteristic wavelength (λ) of 1.5418 Å. X-rays were generated from a Cu anode supplied with 40 kV and a current of 40 mA. Phase identification was carried out by means of the X'Pert accompanying software program PANalytical High Score Plus in conjunction with the ICDD Powder Diffraction File 2 Database (1999), ICDD Powder Diffraction File 4 - Minerals (2012), the American Mineralogist Crystal Structure Database (March 2010) and the Crystallography Open Database.

The disappearance of the mineral peaks in the kerogen samples confirms complete removal of the minerals with the exception of pyrites, which is present in all samples (see Figure S C1a and b).

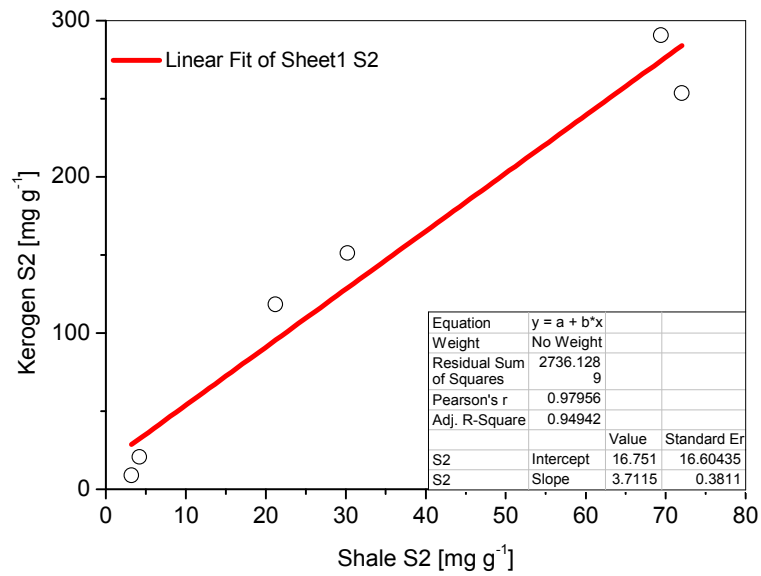
a)



b)



c)



d)

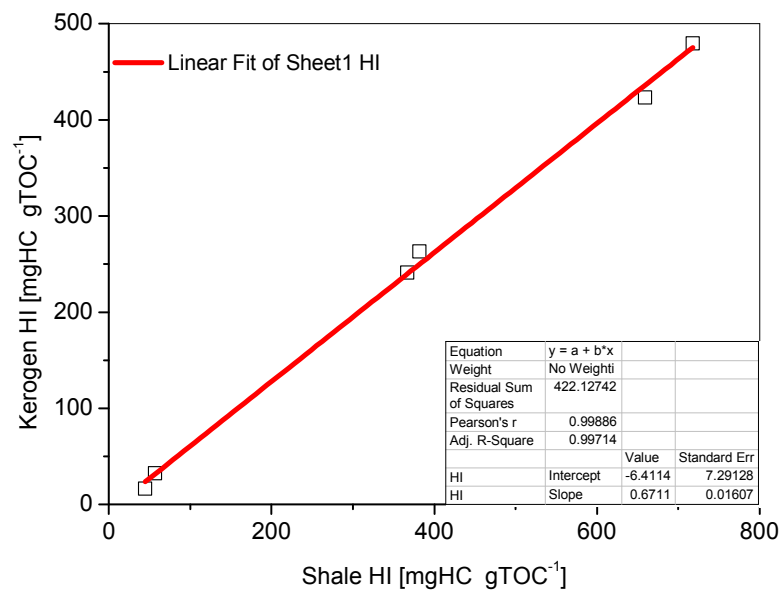


Figure S C1: Characterization data for kerogens and shale s a) XRD profiles of shales, b) XRD profiles kerogens after the isolation, c) comparison of Rock Eval S2 parameters for kerogens and shales, d)) comparison of Rock Eval HI parameters for kerogens and shales.

ii) Proximate analysis of isolated kerogens

In comparison to other minerals pyrite could not be removed completely from the isolated kerogens. Thus, the pyrite content was determined by thermal gravimetric analysis (TGA). The procedure was as follows

1. Load ~ 10-20 mg of kerogen in a TGA and take initial weight measurement
2. Heat to and hold at 110°C under continuous nitrogen stream of 50 mL min⁻¹ to constant weight (typically 30 min)
3. Heat to and hold at 900°C to constant weight (typically 30 min)
4. Cool to and hold at 800°C under 50 mL min⁻¹ in a gas stream (20% Argon, 80% Oxygen) to constant weight
5. Cool to room temperature and final weight measurement(m_f)

Moisture, volatile matter and fixed carbon were determined by a thermogravimetric method, which gave the same results as British Standards for proximate analysis.⁶⁻⁹ Results are show in Table S C1.

Pyrite (FeS_2) is oxidized to Ferric Oxide (Fe_2O_3) in the process at 800°C.¹⁰ Thus, the pyrite content is calculated by converting m_f to mass of pyrite.

iii) Comparison of isolated kerogens and kerogens in shale using Rock Eval Methods

The correlations for the Rock Eval characteristics of shales and isolated kerogens are shown in Figures S C1c and d and Table S C1. It is evident that there are good linear correlations between the kerogen S2 and HI characteristic parameters in shale and the isolated kerogens. This indicates that the kerogen isolation process only has a minimal effect on the kerogen properties.

Table S C1: Isolated Posidonia kerogen characterization data a) composition determined by proximate analysis b) Rock-Eval pyrolysis results.

a)

Sample	Run	Isolated Kerogen Composition in wt%				
		Moisture	Volatiles	Pyrite	Fixed C	Pyrite content of dry mass
7145	1	1.55	58.09	17.35	23.01	17.62
7145	2	1.08	58.18	17.22	23.52	17.41
7155	1	1.20	59.22	16.18	23.40	16.38
7155	2	1.26	61.46	17.01	20.27	17.23
7038	1	0.4	35.9	40.5	23.3	40.6
7060	1	0.5	33.9	55.3	10.3	55.5
7090	1	1.16	23.52	24.94	50.38	25.23
7090	2	1.13	23.53	22.10	53.24	22.35
7119	1	1.41	23.03	29.69	45.87	30.11
7119	2	1.29	24.15	29.64	44.92	30.03

b)

	S1	S2	T _{MAX}	HI
	[mg g ⁻¹]	[mg g ⁻¹]	[°C]	[mg _{Hc} g _{TOC} ⁻¹]
WIC7145	8.91	253.6	416	423
WIC7155	7.18	290.75	428	480
HAR7038	5.77	151.17	435	263
HAR7060	8.45	118.34	430	241
HAD7090	1.67	20.67	437	33
HAD7119	1.77	9.03	422	16

S1 = Free hydrocarbon, S2 = Generated hydrocarbon through thermal cracking of non-volatile organic matter, T_{MAX} = Temperature of maximum release of cracked hydrocarbons, HI = Hydrogen Index

A.3 Pyrite corrections

Pyrite could not be removed completely and, thus, the sorption data were corrected for the pyrite content. Sorption measurements on pure pyrite show no significant gas uptake. CO₂ isotherms (-78°C, up to 1 bar) and N₂ (-196°C, up to 1 bar) were measured on pure pyrite from Huancayo, Peru. There was no detectable gas uptake on pyrite (see Figure S C2). All the sorption data were corrected for pyrite content in accordance with Table S C1.

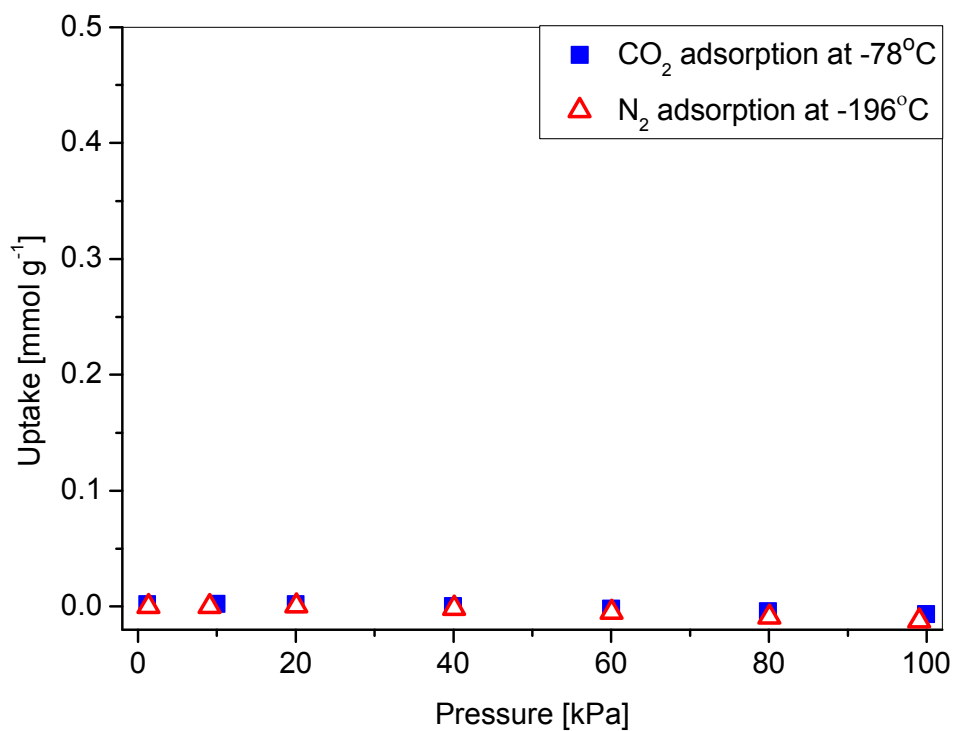


Figure S C2: Carbon dioxide (-78°C) and nitrogen (-196°C) adsorption isotherms for pyrite.

B. Isotherms in tabular form

B.1 Low pressure adsorption data

Table S C2: Low pressure isotherms for CO₂ adsorption on shales and kerogens at 273K.

Shales

WIC7145				WIC7155			
Pressure	Uptake	Temp	p/p ₀	Pressure	Uptake	Temp	p/p ₀
[mbar]	[mmol g ⁻¹]	[°C]		[mbar]	[mmol g ⁻¹]	[°C]	
117.1	0.013	-0.10	0.003	31.3	0.026	-0.11	0.001
197.4	0.022	-0.11	0.006	51.7	0.033	-0.10	0.001
300.7	0.029	-0.05	0.009	100.9	0.044	-0.08	0.003
397.7	0.035	-0.05	0.011	196.9	0.059	-0.13	0.006
498.8	0.040	-0.06	0.014	401.1	0.080	-0.06	0.012
599.1	0.045	-0.09	0.017	599.6	0.096	-0.10	0.017
698.5	0.049	-0.09	0.020	798.1	0.108	-0.05	0.023
799.1	0.052	-0.07	0.023	1001.3	0.118	-0.07	0.029
898.5	0.056	-0.07	0.026				
1000.8	0.060	-0.07	0.029				

HAR7038				HAR7060			
Pressure	Uptake	Temp	p/p ₀	Pressure	Uptake	Temp	p/p ₀
[mbar]	[mmol g ⁻¹]	[°C]		[mbar]	[mmol g ⁻¹]	[°C]	
15.1	0.003	-0.08	0.000	15.1	0.005	0.19	0.000
26.8	0.007	0.05	0.001	29.9	0.009	-0.06	0.001
34.8	0.013	-0.10	0.001	52.5	0.016	-0.05	0.002
50.3	0.018	-0.18	0.001	100.4	0.019	-0.09	0.003
77.4	0.020	-0.11	0.002	198.8	0.025	-0.11	0.006
98.0	0.024	-0.14	0.003	298.4	0.030	-0.13	0.009
197.3	0.033	0.04	0.006	400.3	0.034	-0.10	0.011
297.4	0.038	-0.13	0.009	503.1	0.039	-0.01	0.014
399.7	0.043	-0.22	0.011	600.0	0.043	-0.13	0.017
500.8	0.048	-0.10	0.014	701.7	0.049	-0.11	0.020
601.9	0.053	-0.21	0.017	801.5	0.055	-0.23	0.023
701.8	0.059	-0.25	0.020	900.0	0.066	-0.04	0.026
801.5	0.062	0.05	0.023	998.2	0.069	-0.15	0.029
898.1	0.063	-0.13	0.026				
996.9	0.067	-0.35	0.029				

HAD7090				HAD7119			
Pressure	Uptake	Temp	p/p ₀	Pressure	Uptake	Temp	p/p ₀
[mbar]	[mmol g ⁻¹]	[°C]		[mbar]	[mmol g ⁻¹]	[°C]	
55.7	0.013	-0.26	0.002	18.7	0.001	-0.20	0.001
121.9	0.011	-0.12	0.003	48.2	0.006	-0.03	0.001
199.3	0.023	-0.18	0.006	78.0	0.011	-0.10	0.002
411.3	0.038	-0.07	0.012	119.6	0.016	-0.02	0.003
596.2	0.056	-0.12	0.017	198.4	0.021	-0.05	0.006
798.1	0.065	-0.11	0.023	298.2	0.028	-0.08	0.009
999.5	0.077	-0.14	0.029	398.9	0.035	-0.14	0.011
1210.3	0.084	-0.11	0.035	502.0	0.039	-0.05	0.014
2004.6	0.105	-0.11	0.058	598.9	0.044	-0.10	0.017
4003.4	0.134	-0.10	0.115	699.7	0.048	-0.05	0.020
6003.4	0.152	-0.11	0.172	798.9	0.051	-0.07	0.023
8006.4	0.159	-0.13	0.230	898.6	0.054	-0.08	0.026
				1000.7	0.057	-0.03	0.029

Kerogens

WIC7145				WIC7155			
Pressure	Uptake	Temp	p/p ₀	Pressure	Uptake	Temp	p/p ₀
[mbar]	[mmol g ⁻¹]	[°C]		[mbar]	[mmol g ⁻¹]	[°C]	
11.5	0.003	-0.16	0.000	11.9	0.008	-0.10	0.000
46.8	0.032	-0.09	0.001	30.4	0.022	-0.14	0.001
77.7	0.046	-0.07	0.002	48.6	0.036	-0.05	0.001
116.6	0.065	0.05	0.003	101.7	0.063	-0.07	0.003
197.8	0.098	-0.08	0.006	198.4	0.102	-0.07	0.006
296.9	0.130	-0.05	0.009	396.5	0.159	0.01	0.011
397.6	0.155	-0.11	0.011	598.6	0.204	-0.05	0.017
498.8	0.180	-0.08	0.014	798.5	0.241	-0.08	0.023
597.6	0.202	-0.08	0.017	998.8	0.290	-0.03	0.029
698.8	0.223	-0.06	0.020	1198.9	0.366	-0.12	0.034
797.7	0.242	-0.07	0.023	1503.0	0.360	-0.07	0.043
898.9	0.258	-0.11	0.026	2000.7	0.414	-0.07	0.057
997.4	0.273	-0.08	0.029	4000.4	0.583	0.03	0.115
				6000.8	0.710	-0.12	0.172
				8000.3	0.812	-0.06	0.230

HAR7038				HAR7060			
Pressure	Uptake	Temp	p/p ₀	Pressure	Uptake	Temp	p/p ₀
[mbar]	[mmol g ⁻¹]	[°C]		[mbar]	[mmol g ⁻¹]	[°C]	
12.1	0.024	-0.04	0.000	19.5	0.039	-0.08	0.001
29.4	0.053	-0.06	0.001	28.9	0.068	-0.02	0.001
50.2	0.079	-0.03	0.001	49.1	0.094	-0.02	0.001
99.8	0.104	-0.05	0.003	99.1	0.133	-0.02	0.003
100.1	0.099	-0.08	0.003	199.2	0.190	-0.03	0.006
199.7	0.156	0.01	0.006	299.2	0.237	-0.04	0.009
299.9	0.196	-0.03	0.009	398.7	0.278	-0.08	0.011
399.9	0.229	-0.08	0.011	499.3	0.318	-0.05	0.014
500.7	0.251	-0.05	0.014	599.3	0.351	-0.05	0.017
600.7	0.274	-0.03	0.017	699.4	0.376	-0.02	0.020
700.5	0.300	-0.04	0.020	799.8	0.409	-0.04	0.023
800.5	0.324	-0.04	0.023	899.1	0.437	-0.03	0.026
900.5	0.342	-0.03	0.026	999.6	0.459	-0.03	0.029
999.7	0.358	-0.04	0.029				

HAD7090				HAD7119			
Pressure	Uptake	Temp	p/p ₀	Pressure	Uptake	Temp	p/p ₀
[mbar]	[mmol g ⁻¹]	[°C]		[mbar]	[mmol g ⁻¹]	[°C]	
13.2	0.036	0.25	0.000	15.0	0.077	0.02	0.000
30.5	0.085	0.24	0.001	31.7	0.149	-0.05	0.001
50.8	0.126	0.20	0.001	52.8	0.199	-0.03	0.002
100.2	0.191	0.19	0.003	102.0	0.269	0.02	0.003
201.1	0.277	0.27	0.006	202.3	0.369	-0.04	0.006
402.0	0.395	0.29	0.012	302.3	0.440	-0.03	0.009
601.0	0.484	0.17	0.017	401.6	0.499	-0.08	0.012
801.4	0.556	0.17	0.023	501.6	0.548	-0.05	0.014
1001.5	0.615	0.23	0.029	602.7	0.597	-0.01	0.017
				701.6	0.643	-0.05	0.020
				801.7	0.681	0.01	0.023
				902.2	0.711	-0.05	0.026
				1001.9	0.742	0.04	0.029

Table S C3: Low pressure isotherms for CO₂ adsorption on shales and kerogens at 195 K.**Shales**

WIC7145		WIC7155		HAR7038	
Pressure	Uptake	Pressure	Uptake	Pressure	Uptake
[mbar]	[mmol g⁻¹]	[mbar]	[mmol g⁻¹]	[mbar]	[mmol g⁻¹]
126.6	0.188	13.0	0.079	13.5	0.013
201.4	0.225	48.2	0.134	49.6	0.042
297.2	0.271	97.7	0.169	99.6	0.063
406.1	0.300	198.2	0.217	198.4	0.090
505.8	0.326	398.0	0.279	399.3	0.126
592.3	0.346	598.2	0.327	599.5	0.159
698.8	0.369	797.7	0.371	798.4	0.192
800.8	0.392	998.0	0.414	999.1	0.224
889.3	0.414			1028.4	0.231
992.3	0.438				

HAR7060		HAD7090		HAD7119	
Pressure	Uptake	Pressure	Uptake	Pressure	Uptake
[mbar]	[mmol g⁻¹]	[mbar]	[mmol g⁻¹]	[mbar]	[mmol g⁻¹]
14.8	0.041	37.9	0.068	19.0	0.034
96.5	0.075	58.0	0.138	49.7	0.105
250.7	0.109	82.2	0.121	78.3	0.121
500.0	0.146	101.8	0.170	120.2	0.141
751.1	0.189	130.6	0.179	198.0	0.172
997.1	0.222	142.0	0.186	299.3	0.202
1030.1	0.230	165.3	0.198	397.2	0.226
		197.8	0.213	500.4	0.248
		228.7	0.224	599.1	0.268
		275.8	0.239	699.1	0.288
		282.5	0.252	798.7	0.307
		412.6	0.282	898.9	0.327
		454.7	0.295	1001.5	0.346
		506.2	0.310	1029.6	0.353
		605.1	0.335		
		701.6	0.359		
		803.8	0.384		
		908.2	0.408		
		1000.3	0.433		

Kerogens

WIC7145		WIC7155		HAR7038	
Pressure	Uptake	Pressure	Uptake	Pressure	Uptake
[mbar]	[mmol g ⁻¹]	[mbar]	[mmol g ⁻¹]	[mbar]	[mmol g ⁻¹]
13.0	0.320	13.1	0.292	13.8	0.255
47.6	0.565	48.7	0.511	48.9	0.462
77.2	0.687	98.5	0.681	97.0	0.612
117.8	0.811	198.2	0.911	196.8	0.824
198.7	0.996	397.9	1.234	398.1	1.125
297.6	1.174	598.5	1.499	600.7	1.382
397.4	1.324	798.3	1.712	597.0	1.402
500.0	1.458	998.2	1.921	803.4	1.623
599.7	1.574			996.2	1.831
701.2	1.690				
800.5	1.795				
896.2	1.896				
998.2	2.000				

HAR7060		HAD7090		HAD7119	
Pressure	Uptake	Pressure	Uptake	Pressure	Uptake
[mbar]	[mmol g ⁻¹]	[mbar]	[mmol g ⁻¹]	[mbar]	[mmol g ⁻¹]
13.8	0.392	12.9	0.679	4.6	0.494
50.1	0.655	48.3	1.012	8.1	0.575
99.6	0.855	98.1	1.224	12.9	0.651
199.2	1.126	198.1	1.525	18.5	0.727
299.7	1.309	397.7	1.962	28.1	0.832
400.1	1.507	598.0	2.322	48.5	0.979
549.5	1.726	798.1	2.680	72.8	1.104
699.1	1.929	997.8	3.022	98.1	1.206
849.8	2.132			198.2	1.501
999.2	2.326			298.2	1.714
				398.0	1.896
				498.4	2.056
				598.5	2.204
				696.6	2.346
				797.9	2.487
				898.0	2.630
				998.5	2.770
				1027.8	2.817

Table S C4: Low pressure isotherms for N₂ adsorption on shales and kerogens at 77 K.**Shales**

WIC7145				WIC7155			
Pressure	Uptake	Temp	p/p ₀	Pressure	Uptake	Temp	p/p ₀
[mbar]	[mmol g ⁻¹]	[°C]		[mbar]	[mmol g ⁻¹]	[°C]	
13.8	0.046	-186.9	0.005	12.4	0.012	-185.0	0.004
29.9	0.051	-186.7	0.011	29.5	0.017	-186.0	0.011
59.8	0.060	-190.3	0.032	59.7	0.025	-189.8	0.031
99.7	0.068	-191.0	0.058	99.7	0.030	-190.8	0.057
149.6	0.078	-192.8	0.105	149.6	0.036	-191.7	0.093
199.9	0.085	-193.0	0.144	200.6	0.043	-192.6	0.138
249.8	0.091	-193.2	0.183	249.4	0.046	-192.5	0.170
289.5	0.095	-193.1	0.211	298.8	0.049	-192.7	0.208
459.3	0.113	-193.6	0.352	348.4	0.052	-192.3	0.232
630.2	0.135	-193.8	0.496	399.3	0.061	-193.9	0.317
799.4	0.168	-193.9	0.638	549.0	0.075	-194.3	0.455
960.0	0.239	-194.0	0.768	699.3	0.092	-194.5	0.592
				849.5	0.121	-194.6	0.730
				989.2	0.188	-194.7	0.857
				1039.4	0.222	-194.5	0.879

HAD7090				HAD7119			
Pressure	Uptake	Temp	p/p ₀	Pressure	Uptake	Temp	p/p ₀
[mbar]	[mmol g ⁻¹]	[°C]		[mbar]	[mmol g ⁻¹]	[°C]	
9.9	0.147	-182.2	0.003	11.0	0.142	-187.9	0.005
27.9	0.212	-188.4	0.013	27.6	0.166	-189.0	0.013
57.2	0.240	-189.0	0.027	57.5	0.191	-191.0	0.034
96.9	0.271	-190.8	0.055	97.9	0.210	-191.2	0.058
146.0	0.292	-191.2	0.086	147.7	0.226	-191.2	0.087
197.1	0.315	-192.6	0.136	198.0	0.241	-191.7	0.124
247.2	0.331	-192.2	0.163	247.5	0.261	-193.6	0.189
298.0	0.349	-193.3	0.221	298.3	0.271	-193.2	0.219
347.6	0.363	-193.6	0.268	347.5	0.280	-192.7	0.243
397.2	0.374	-193.6	0.303	397.1	0.288	-192.2	0.261
547.1	0.408	-193.8	0.430	548.4	0.322	-193.1	0.396
697.4	0.443	-193.9	0.555	697.9	0.368	-194.5	0.590
847.6	0.490	-194.1	0.684	848.0	0.432	-195.4	0.796
987.3	0.558	-194.1	0.799	988.0	0.531	-195.2	0.905
				1037.4	0.575	-194.8	0.916
				1088.1	0.583	-194.6	0.939
				1138.2	0.588	-194.3	0.946

Kerogens

WIC7145				WIC7155			
Pressure	Uptake	Temp	p/p ₀	Pressure	Uptake	Temp	p/p ₀
[mbar]	[mmol g ⁻¹]	[°C]		[mbar]	[mmol g ⁻¹]	[°C]	
11.7	0.006	-189.1	0.006	28.8	0.004	-188.8	0.013
27.5	0.017	-189.5	0.014	58.9	0.017	-189.9	0.031
57.5	0.033	-190.2	0.031	99.2	0.028	-190.8	0.056
132.1	0.068	-191.7	0.082	149.0	0.040	-192.6	0.103
202.2	0.093	-192.3	0.134	199.5	0.057	-193.2	0.147
273.3	0.111	-192.4	0.183	249.1	0.067	-193.5	0.189
342.6	0.125	-194.5	0.291	299.5	0.074	-193.6	0.229
508.1	0.160	-194.8	0.446	349.0	0.079	-193.6	0.268
667.3	0.214	-194.8	0.589	399.0	0.083	-193.6	0.308
826.9	0.258	-194.9	0.734	548.9	0.098	-194.0	0.438
987.4	0.318	-194.9	0.873	698.1	0.114	-194.2	0.573
				849.3	0.177	-195.3	0.790
				989.1	0.317	-195.4	0.927
				1039.2	0.476	-195.2	0.955

HAR7038				HAR7060			
Pressure	Uptake	Temp	p/p ₀	Pressure	Uptake	Temp	p/p ₀
[mbar]	[mmol g ⁻¹]	[°C]		[mbar]	[mmol g ⁻¹]	[°C]	
13.7	0.077	-191.7	0.009	14.1	0.053	-191.8	0.009
51.7	0.153	-193.2	0.038	51.5	0.102	-192.8	0.036
90.9	0.204	-193.6	0.070	90.9	0.134	-193.5	0.069
160.6	0.260	-194.1	0.130	160.5	0.176	-194.7	0.139
231.8	0.306	-194.4	0.194	231.5	0.208	-194.8	0.204
301.7	0.345	-194.5	0.257	301.2	0.235	-194.9	0.269
371.1	0.401	-195.6	0.358	371.3	0.259	-195.0	0.332
421.8	0.431	-195.6	0.408	421.1	0.277	-194.9	0.375
551.4	0.506	-195.7	0.536	550.3	0.326	-195.0	0.495
700.9	0.623	-195.7	0.686	701.2	0.405	-195.4	0.657
801.6	0.756	-195.7	0.786	800.4	0.493	-195.8	0.787
851.5	0.861	-195.7	0.829	850.7	0.563	-195.7	0.833
901.1	1.026	-195.6	0.870	900.9	0.677	-195.7	0.878
991.5	2.173	-195.5	0.950	990.9	1.493	-195.7	0.963

HAD7090				HAD7119			
Pressure	Uptake	Temp	p/p ₀	Pressure	Uptake	Temp	p/p ₀
[mbar]	[mmol g ⁻¹]	[°C]		[mbar]	[mmol g ⁻¹]	[°C]	
11.9	0.448	-191.5	0.007	10.6	0.330	-186.1	0.004
59.3	0.612	-192.4	0.040	28.0	0.409	-187.0	0.011
98.3	0.688	-192.7	0.069	58.4	0.479	-188.3	0.026
199.1	0.835	-194.6	0.172	98.2	0.539	-189.5	0.049
299.2	0.945	-195.1	0.271	147.8	0.597	-190.3	0.080
398.7	1.051	-195.2	0.369	198.4	0.664	-192.5	0.136
548.4	1.241	-195.6	0.527	247.6	0.714	-193.1	0.180
698.7	1.485	-195.7	0.679	298.3	0.758	-193.4	0.223
849.0	1.974	-195.7	0.831	348.8	0.798	-193.3	0.260
988.7	3.998	-195.8	0.971	397.9	0.834	-193.2	0.293
				547.7	0.962	-193.7	0.424
				697.4	1.122	-193.8	0.550
				848.4	1.486	-195.0	0.765
				987.8	2.589	-195.2	0.905
				1038.5	2.940	-194.7	0.907

B.2 High Pressure Methane Isotherms

Table S C5: High Pressure CH₄ Isotherms for shales and Kerogens.

Shales

WIC7145				
Excess Uptake	Pressure	Temperature	Density	Absolute U.
[mmol g⁻¹]	[MPa]	[K]	[kg m⁻³]	[mmol g⁻¹]
45°C				
0.003	0.048	318.20	0.29	0.003
0.016	0.354	318.15	2.16	0.019
0.042	1.233	318.18	7.60	0.050
0.067	2.512	318.19	15.75	0.083
0.086	4.053	318.17	25.93	0.113
0.101	5.754	318.21	37.58	0.139
0.111	7.556	318.17	50.36	0.162
0.117	9.412	318.28	63.85	0.182
0.119	11.295	318.27	77.80	0.198
0.119	12.542	318.15	87.11	0.207
65°C				
0.002	0.050	338.20	0.28	0.002
0.012	0.368	338.18	2.1088	0.014
0.032	1.273	338.18	7.3591	0.040
0.053	2.581	338.18	15.119	0.068
0.070	4.151	338.17	24.692	0.096
0.085	5.886	338.17	35.555	0.121
0.095	7.719	338.17	47.315	0.143
0.103	9.603	338.15	59.623	0.164
0.110	11.511	338.12	72.205	0.183
85°C				
0.001	0.051	358.12	0.28	0.002
0.009	0.379	358.17	2.05	0.011
0.026	1.307	358.19	7.11	0.033
0.043	2.642	358.14	14.53	0.058
0.058	4.239	358.14	23.59	0.082
0.070	6.001	358.17	33.77	0.104
0.079	7.856	358.16	44.67	0.125
0.089	9.759	358.15	55.97	0.146
0.094	11.687	358.14	67.47	0.163

WIC7155				
Excess Uptake	Pressure	Temperature	Density	Absolute U.
[mmol g⁻¹]	[MPa]	[K]	[kg m⁻³]	[mmol g⁻¹]
45°C				
0.002	0.050	318.16	0.301	0.002
0.014	0.363	318.17	2.210	0.016
0.038	1.256	318.17	7.745	0.045
0.060	2.551	318.19	16.005	0.075
0.078	4.107	318.20	26.286	0.104
0.092	5.823	318.16	38.062	0.128
0.101	7.634	318.18	50.921	0.150
0.108	9.498	318.15	64.524	0.170
0.112	11.387	318.15	78.522	0.187
0.115	12.628	318.18	87.733	0.200
65°C				
0.002	0.050	338.28	0.286	0.002
0.010	0.374	338.28	2.143	0.013
0.029	1.295	338.15	7.491	0.036
0.048	2.620	338.16	15.357	0.062
0.064	4.205	338.16	25.029	0.088
0.076	5.952	338.18	35.978	0.111
0.086	7.793	338.18	47.798	0.133
0.094	9.681	338.18	60.130	0.152
0.100	11.593	338.16	72.733	0.170
0.107	12.817	338.16	80.799	0.185
85°C				
0.001	0.052	358.15	0.282	0.001
0.008	0.386	358.12	2.084	0.010
0.022	1.329	358.13	7.237	0.029
0.038	2.680	358.19	14.741	0.052
0.052	4.291	358.16	23.880	0.075
0.063	6.062	358.16	34.126	0.096
0.072	7.925	358.13	45.085	0.116
0.080	9.838	358.18	56.442	0.134
0.084	11.769	358.13	67.960	0.150
0.088	12.981	358.05	75.190	0.161

HAR7038				
Excess Uptake	Pressure	Temperature	Density	Absolute U.
[mmol g⁻¹]	[MPa]	[K]	[kg m⁻³]	[mmol g⁻¹]
45°C				
0.008	0.341	318.16	2.077	0.009
0.022	1.263	318.18	7.792	0.026
0.035	2.581	318.16	16.202	0.044
0.047	4.152	318.19	26.587	0.060
0.055	5.875	318.18	38.425	0.075
0.062	7.692	318.17	51.338	0.089
0.066	9.559	318.17	64.969	0.100
0.069	11.452	318.17	79.004	0.110
0.070	13.354	318.15	93.128	0.118
65°C				
0.006	0.354	338.15	2.027	0.007
0.017	1.302	338.16	7.532	0.021
0.029	2.649	338.19	15.528	0.037
0.038	4.248	338.17	25.290	0.051
0.045	6.000	338.15	36.284	0.064
0.050	7.842	338.16	48.118	0.075
0.054	9.736	338.17	60.495	0.085
0.056	11.654	338.19	73.125	0.094
0.057	13.570	338.17	85.734	0.101
85°C				
0.005	0.359	358.18	1.940	0.006
0.014	1.330	358.17	7.244	0.018
0.024	2.700	358.16	14.857	0.032
0.033	4.326	358.14	24.084	0.045
0.040	6.111	358.10	34.422	0.058
0.046	7.983	358.14	45.422	0.069
0.050	9.894	358.12	56.784	0.080
0.053	11.824	358.14	68.285	0.089
0.056	13.756	358.15	79.745	0.098

HAR7060				
Excess Uptake	Pressure	Temperature	Density	Absolute U.
[mmol g⁻¹]	[MPa]	[K]	[kg m⁻³]	[mmol g⁻¹]
45°C				
0.004	0.247	318.17	1.500	0.005
0.019	1.286	318.17	7.936	0.023
0.034	3.048	318.17	19.247	0.044
0.045	5.265	318.15	34.186	0.063
0.052	7.743	318.17	51.709	0.078
0.054	10.361	318.18	70.890	0.091
0.045	13.110	318.18	91.307	0.093
65°C				
0.001	0.074	338.08	0.424	0.001
0.013	1.204	338.19	6.959	0.017
0.026	3.043	338.17	17.911	0.036
0.036	5.342	338.17	32.121	0.052
0.042	7.894	338.17	48.450	0.067
0.044	10.573	338.15	66.010	0.078
0.044	13.315	338.16	84.068	0.087
85°C				
0.000	0.077	358.28	0.415	0.000
0.011	1.235	358.18	6.719	0.014
0.023	3.117	358.15	17.208	0.032
0.033	5.456	358.14	30.601	0.048
0.040	8.051	358.14	45.825	0.064
0.045	10.767	358.13	61.987	0.077
0.049	13.493	358.15	78.191	0.089

HAD7090				
Excess Uptake	Pressure	Temperature	Density	Absolute U.
[mmol g⁻¹]	[MPa]	[K]	[kg m⁻³]	[mmol g⁻¹]
45°C				
0.004	0.044	318.17	0.268	0.005
0.014	0.184	318.25	1.119	0.015
0.068	1.779	318.18	11.049	0.079
0.094	3.543	318.17	22.518	0.116
0.108	5.394	318.18	35.081	0.143
0.115	7.289	318.19	48.439	0.164
0.118	9.204	318.20	62.342	0.181
0.115	11.123	318.19	76.547	0.192
0.111	12.405	318.12	86.106	0.198
65°C				
0.003	0.047	338.11	0.270	0.003
0.010	0.192	338.10	1.098	0.011
0.056	1.840	338.20	10.703	0.066
0.080	3.644	338.21	21.570	0.101
0.094	5.531	338.13	33.319	0.127
0.103	7.459	338.09	45.648	0.149
0.109	9.406	338.18	58.323	0.167
0.109	11.353	338.21	71.137	0.181
0.109	12.622	338.13	79.528	0.189
85°C				
0.002	0.049	358.10	0.265	0.002
0.008	0.199	358.19	1.074	0.009
0.045	1.894	358.12	10.362	0.056
0.066	3.734	358.11	20.707	0.087
0.080	5.652	358.14	31.739	0.112
0.090	7.605	358.16	43.184	0.133
0.095	9.572	358.21	54.850	0.150
0.099	11.538	358.19	66.567	0.166
0.099	12.794	358.12	74.061	0.173

HAD7119				
Excess Uptake	Pressure	Temperature	Density	Absolute U.
[mmol g⁻¹]	[MPa]	[K]	[kg m⁻³]	[mmol g⁻¹]
45°C				
0.003	0.047	318.16	0.284	0.003
0.017	0.353	318.17	2.152	0.019
0.042	1.238	318.12	7.638	0.048
0.064	2.529	318.18	15.866	0.076
0.079	4.084	318.13	26.137	0.100
0.089	5.799	318.13	37.901	0.119
0.095	7.610	318.16	50.752	0.136
0.096	9.473	318.17	64.335	0.148
0.095	11.362	318.16	78.336	0.158
0.096	12.604	318.17	87.561	0.167
65°C				
0.002	0.050	338.22	0.284	0.002
0.013	0.368	338.18	2.107	0.015
0.034	1.280	338.23	7.399	0.040
0.053	2.599	338.12	15.231	0.065
0.067	4.182	338.15	24.888	0.087
0.078	5.928	338.18	35.824	0.107
0.084	7.770	338.18	47.649	0.123
0.089	9.661	338.18	59.999	0.137
0.090	11.575	338.17	72.616	0.149
0.093	12.804	338.19	80.703	0.158
85°C				
0.002	0.053	358.19	0.283	0.002
0.010	0.382	358.08	2.063	0.012
0.028	1.316	358.23	7.165	0.034
0.044	2.660	358.12	14.637	0.056
0.057	4.268	358.15	23.754	0.076
0.067	6.039	358.15	33.994	0.095
0.074	7.903	358.16	44.946	0.110
0.078	9.814	358.14	56.305	0.124
0.079	11.745	358.12	67.823	0.133
0.079	12.964	358.14	75.059	0.140
0.081	13.732	358.13	79.610	0.146

Kerogens

Kerogen - WIC7145					
Excess Uptake	Ex normalized	Pressure	Temperature	Density	Absolute U.
[mmol g ⁻¹]	[mmol g ⁻¹]	[MPa]	[K]	[kg m ⁻³]	[mmol g ⁻¹]
45°C					
0.135	0.015	1.200	318.17	7.40	0.170
0.252	0.028	3.167	318.18	20.03	0.345
0.332	0.037	5.572	318.16	36.32	0.502
0.399	0.045	8.203	318.16	55.04	0.656
0.437	0.049	10.936	318.19	75.16	0.787
0.455	0.051	13.707	318.17	95.72	0.901
0.475	0.053	15.956	318.16	112.07	0.997
65°C					
0.106	0.012	1.230	338.24	7.11	0.140
0.206	0.023	3.233	338.15	19.06	0.294
0.282	0.031	5.677	338.16	34.24	0.441
0.354	0.040	8.345	338.18	51.39	0.594
0.398	0.044	11.116	338.17	69.59	0.722
0.429	0.048	13.916	338.16	88.00	0.839

Kerogen - WIC7155					
Excess Uptake	Ex normalized	Pressure	Temperature	Density	Absolute U.
[mmol g ⁻¹]	[mmol g ⁻¹]	[MPa]	[K]	[kg m ⁻³]	[mmol g ⁻¹]
45°C					
0.014	0.002	0.081	318.16	0.494	0.016
0.123	0.014	1.049	318.16	6.450	0.152
0.228	0.026	2.655	318.19	16.684	0.303
0.307	0.034	4.643	318.17	29.919	0.441
0.375	0.042	6.840	318.17	45.235	0.577
0.422	0.047	9.137	318.16	61.867	0.699
0.474	0.053	11.477	318.17	79.186	0.828
0.518	0.058	13.273	318.13	92.541	0.933
65°C					
0.008	0.001	0.084	338.16	0.478	0.010
0.081	0.009	1.074	338.23	6.197	0.109
0.155	0.017	2.709	338.15	15.894	0.227
0.213	0.024	4.726	338.15	28.262	0.339
0.259	0.029	6.953	338.14	42.378	0.448
0.314	0.035	9.273	338.18	57.451	0.571
0.358	0.040	11.644	338.16	73.071	0.685
0.444	0.050	13.427	338.21	84.781	0.824

Kerogen – HAR7038					
Excess Uptake	Ex normalized	Pressure	Temperature	Density	Absolute U.
[mmol g ⁻¹]	[mmol g ⁻¹]	[MPa]	[K]	[kg m ⁻³]	[mmol g ⁻¹]
45°C					
0.016	0.001	0.078	318.17	0.476	0.018
0.146	0.012	1.245	318.17	7.680	0.179
0.272	0.021	3.185	318.17	20.151	0.358
0.374	0.030	5.557	318.18	36.208	0.529
0.456	0.036	8.168	318.21	54.771	0.690
0.507	0.040	10.878	318.17	74.732	0.826
0.547	0.043	13.637	318.16	95.212	0.954
65°C					
0.011	0.001	0.082	338.18	0.467	0.013
0.113	0.009	1.282	338.16	7.413	0.145
0.217	0.017	3.254	338.18	19.189	0.299
0.305	0.024	5.662	338.17	34.137	0.450
0.379	0.030	8.306	338.18	51.130	0.597
0.430	0.034	11.056	338.18	69.189	0.725
0.429	0.034	13.893	338.16	87.845	0.804

Kerogen – HAR7060					
Excess Uptake	Ex normalized	Pressure	Temperature	Density	Absolute U.
[mmol g⁻¹]	[mmol g⁻¹]	[MPa]	[K]	[kg m⁻³]	[mmol g⁻¹]
45°C					
0.017	0.001	0.081	318.15	0.491	0.020
0.167	0.010	1.259	318.17	7.762	0.209
0.300	0.017	3.196	318.16	20.224	0.409
0.417	0.024	5.581	318.17	36.376	0.614
0.488	0.028	8.196	318.16	54.992	0.787
0.537	0.031	10.911	318.18	74.977	0.944
0.579	0.034	13.854	318.17	96.808	1.104
65°C					
0.012	0.001	0.081	338.17	0.464	0.014
0.123	0.007	1.277	338.17	7.383	0.163
0.223	0.013	3.254	338.16	19.191	0.327
0.309	0.018	5.674	338.15	34.214	0.495
0.359	0.021	8.327	338.17	51.271	0.637
0.372	0.022	11.087	338.15	69.401	0.748
0.376	0.022	14.065	338.20	88.955	0.858

Kerogen – HAD7090					
Excess Uptake	Ex normalized	Pressure	Temperature	Density	Absolute U.
[mmol g⁻¹]	[mmol g⁻¹]	[MPa]	[K]	[kg m⁻³]	[mmol g⁻¹]
45°C					
0.043	0.003	0.087	318.18	0.527	0.047
0.349	0.026	1.465	318.19	9.060	0.412
0.551	0.041	3.603	318.17	22.919	0.712
0.686	0.051	6.143	318.16	40.303	0.970
0.772	0.057	8.864	318.19	59.857	1.194
0.837	0.062	11.659	318.17	80.544	1.405
0.904	0.067	14.063	318.15	98.356	1.597
65°C					
0.029	0.002	0.090	338.22	0.514	0.033
0.273	0.020	1.488	338.19	8.622	0.334
0.450	0.033	3.659	338.17	21.665	0.602
0.568	0.042	6.220	338.17	37.683	0.834
0.650	0.048	8.973	338.18	55.482	1.040
0.708	0.052	11.797	338.18	74.075	1.230
0.761	0.056	14.208	338.15	89.905	1.394

Kerogen – HAD7119					
Excess Uptake	Ex normalized	Pressure	Temperature	Density	Absolute U.
[mmol g ⁻¹]	[mmol g ⁻¹]	[MPa]	[K]	[kg m ⁻³]	[mmol g ⁻¹]
45°C					
0.137	0.009	0.436	318.17	2.657	0.155
0.315	0.022	1.575	318.18	9.756	0.378
0.456	0.031	3.114	318.15	19.684	0.583
0.563	0.038	4.862	318.16	31.420	0.765
0.656	0.045	6.725	318.17	44.414	0.942
0.739	0.050	8.642	318.17	58.236	1.115
0.810	0.055	10.581	318.17	72.526	1.279
0.880	0.060	12.528	318.15	87.007	1.442
0.951	0.065	14.470	318.15	101.330	1.605
1.019	0.070	16.424	318.10	115.430	1.765
65°C					
0.104	0.007	0.444	338.23	2.543	0.121
0.255	0.017	1.597	338.18	9.265	0.315
0.376	0.026	3.154	338.16	18.581	0.496
0.463	0.032	4.915	338.17	29.440	0.653
0.536	0.037	6.793	338.16	41.347	0.803
0.594	0.041	8.725	338.17	53.863	0.941
0.637	0.044	10.677	338.16	66.692	1.068
0.673	0.046	12.629	338.15	79.565	1.187
0.718	0.049	14.593	338.18	92.392	1.315
0.775	0.053	16.541	338.18	104.880	1.452

C. Langmuir Parameterization

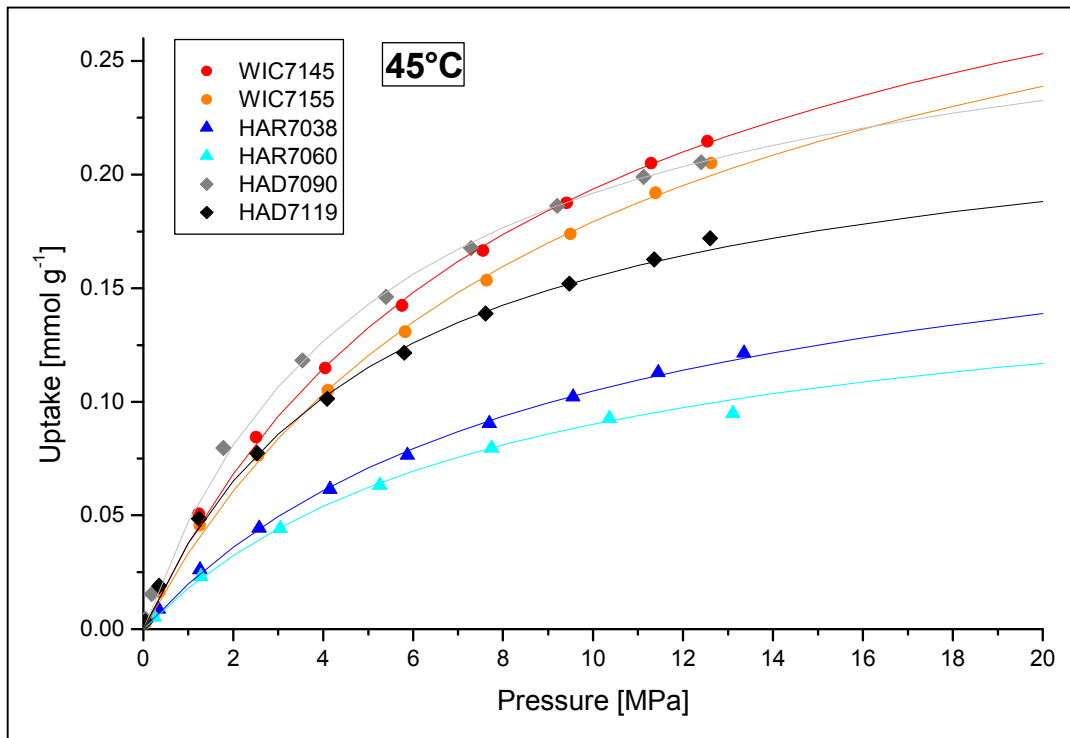


Figure S C3: Absolute methane isotherms on shale at 45°C (points). The absolute isotherms were calculated by assuming an adsorbed phase volume equal to the pore volume as measured by CO₂ sorption at 195 K. The lines represent a Langmuir fit to the sorption data.

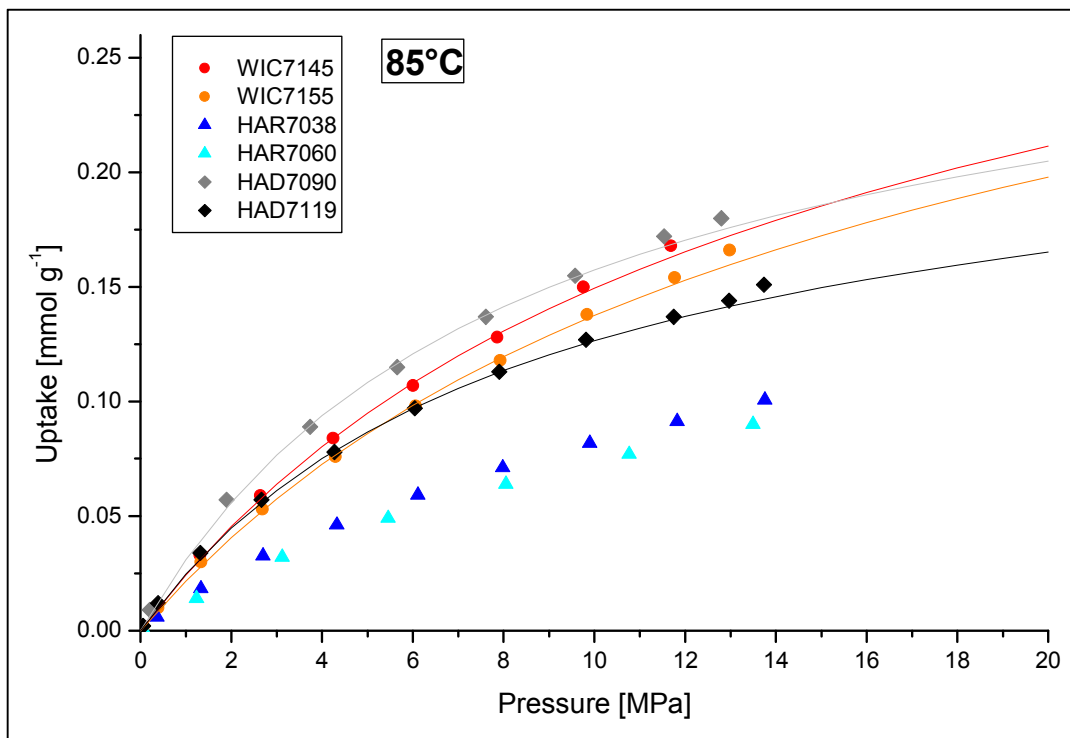


Figure S C4: Absolute methane isotherms on shale at 85°C (points). The absolute isotherms were calculated by assuming an adsorbed phase volume equal to the pore volume as measured by CO₂ sorption at 195 K. The lines represent a Langmuir fit to the sorption data.

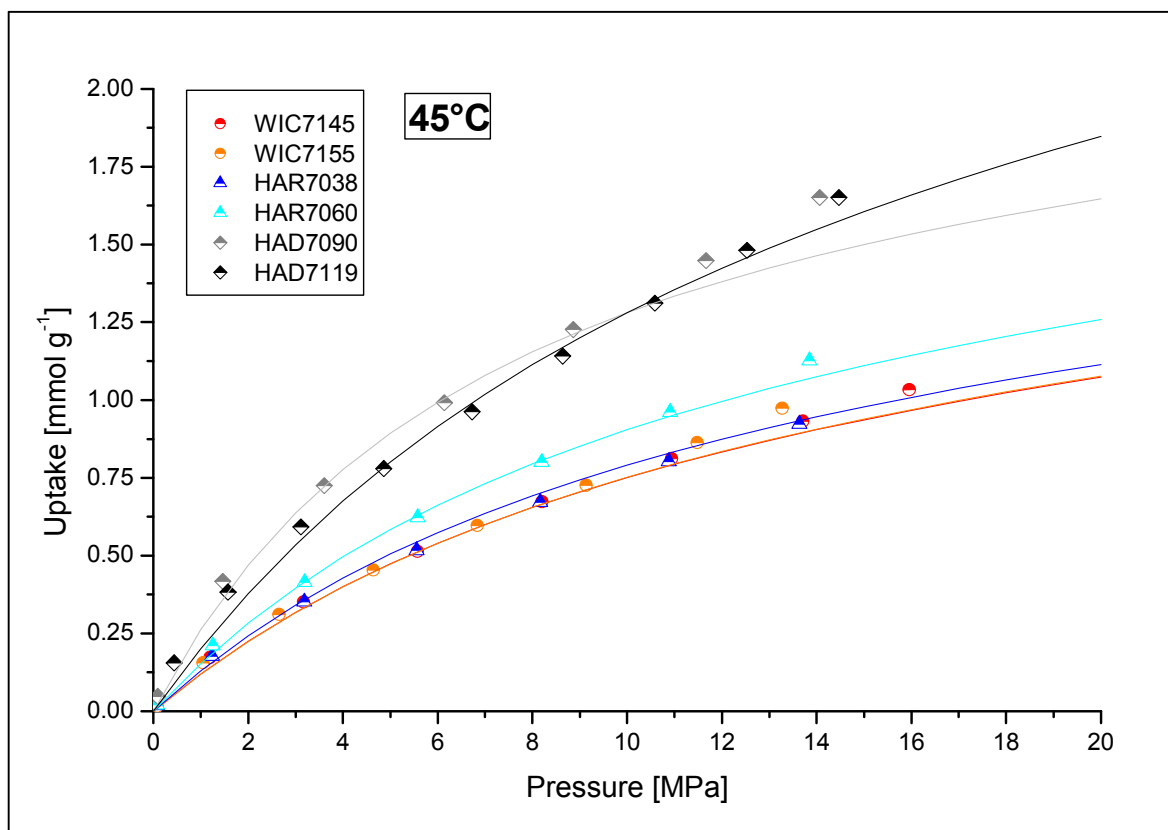
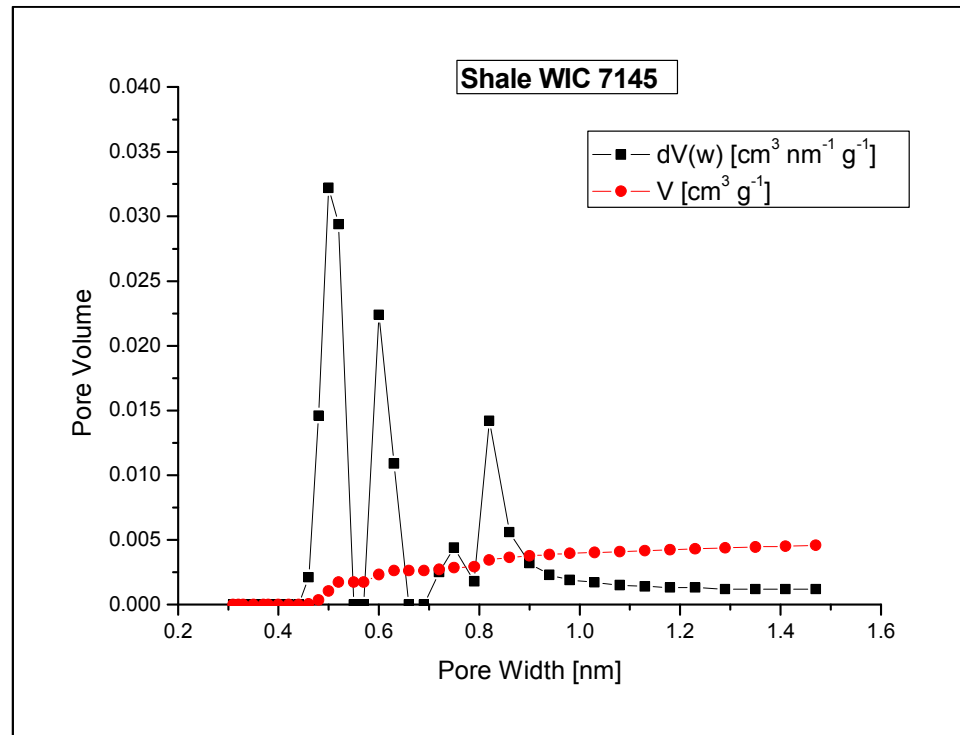


Figure S C5: Absolute methane isotherms on kerogen at 45°C (points). The absolute isotherms were calculated by assuming an adsorbed phase volume equal to the pore volume as measured by CO₂ sorption at 195 K. The lines represent a Langmuir fit to the sorption data.

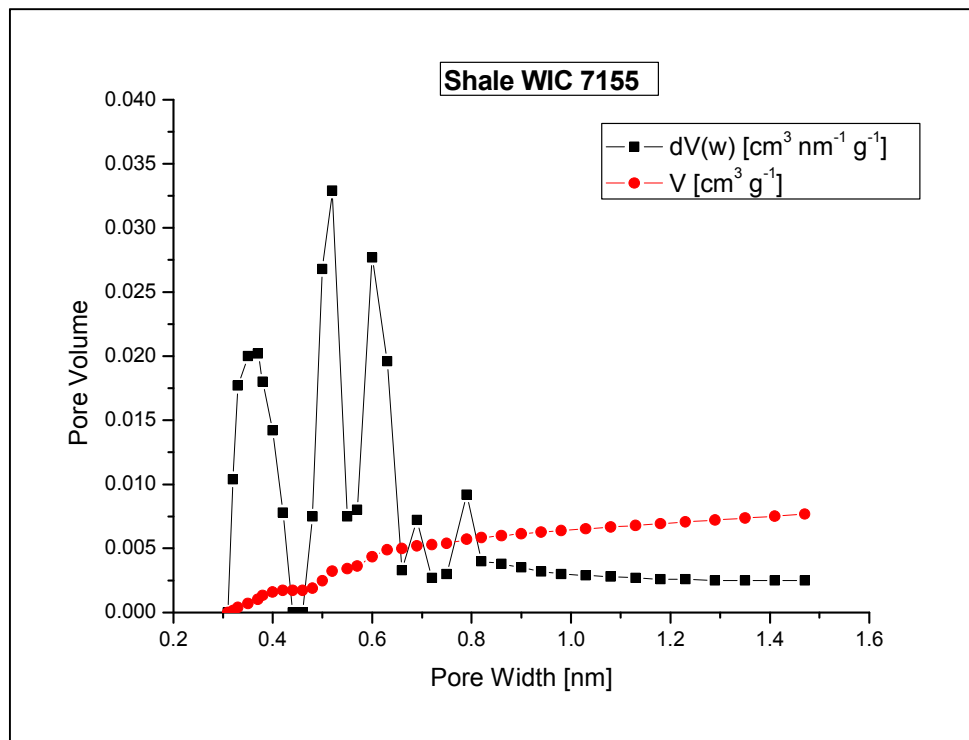
D. Micropore Size Distributions

Shales

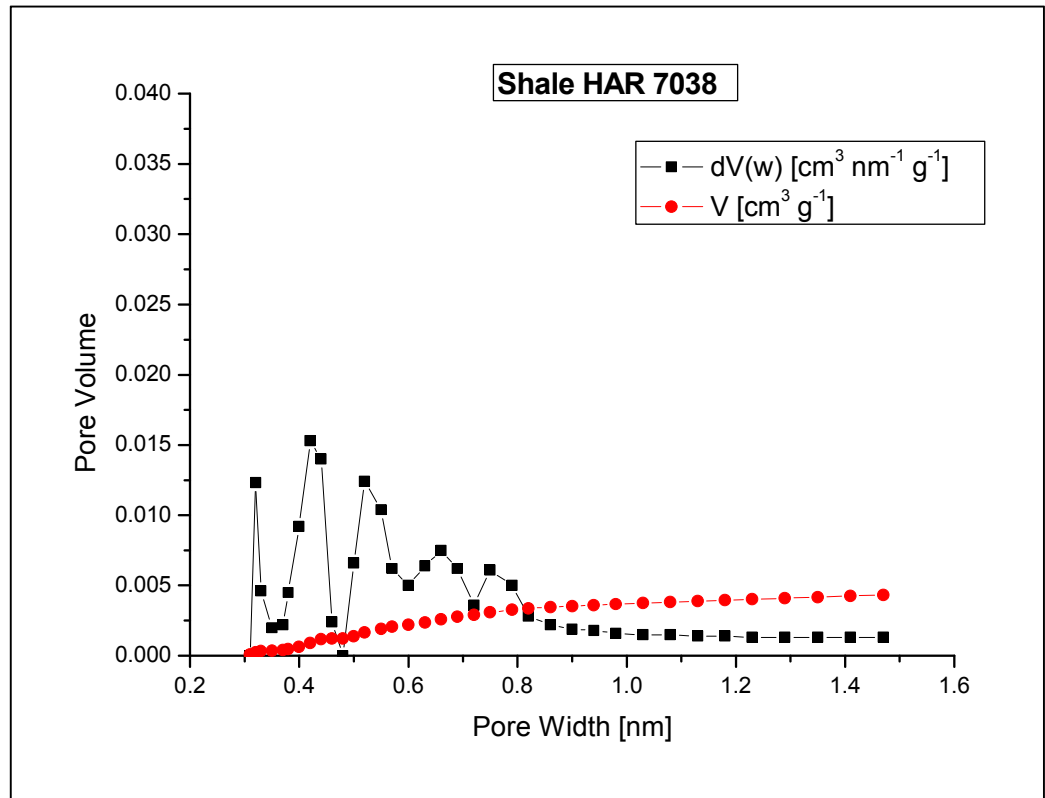
a)



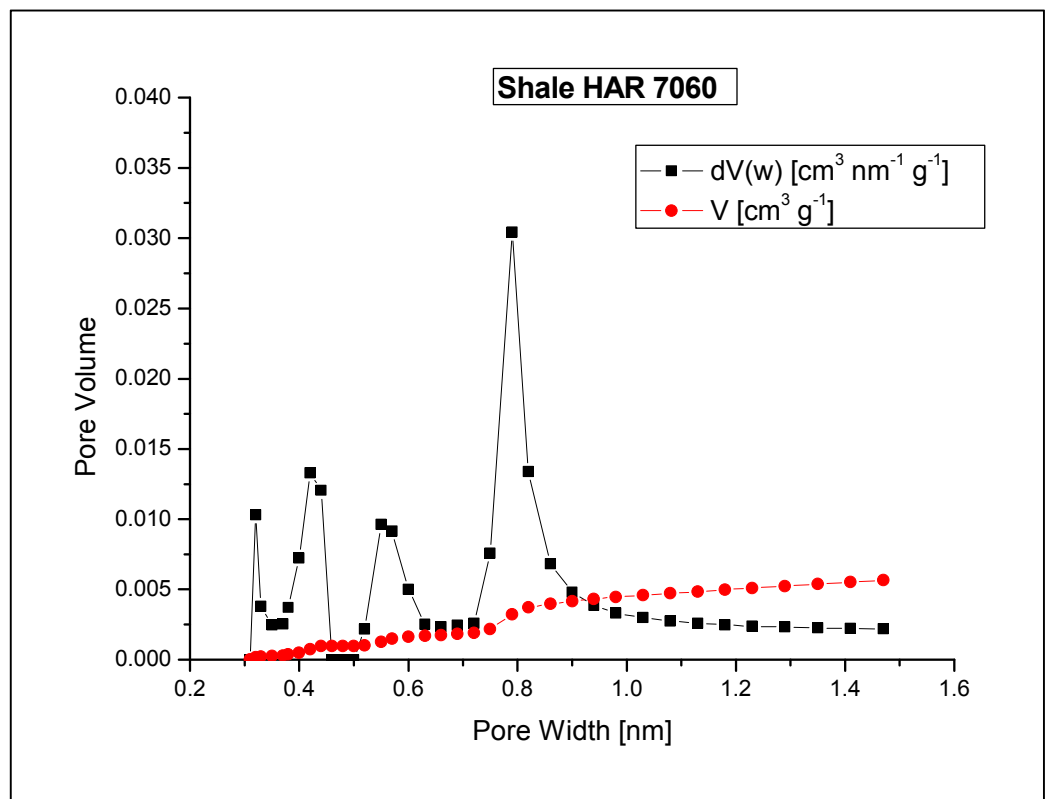
b)



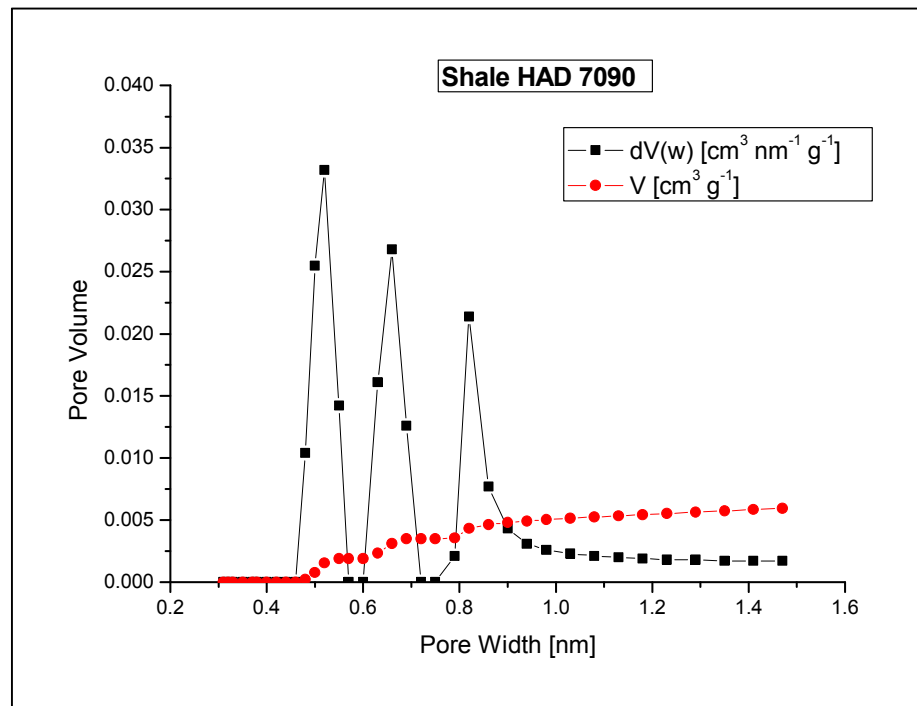
c)



d)



e)



f)

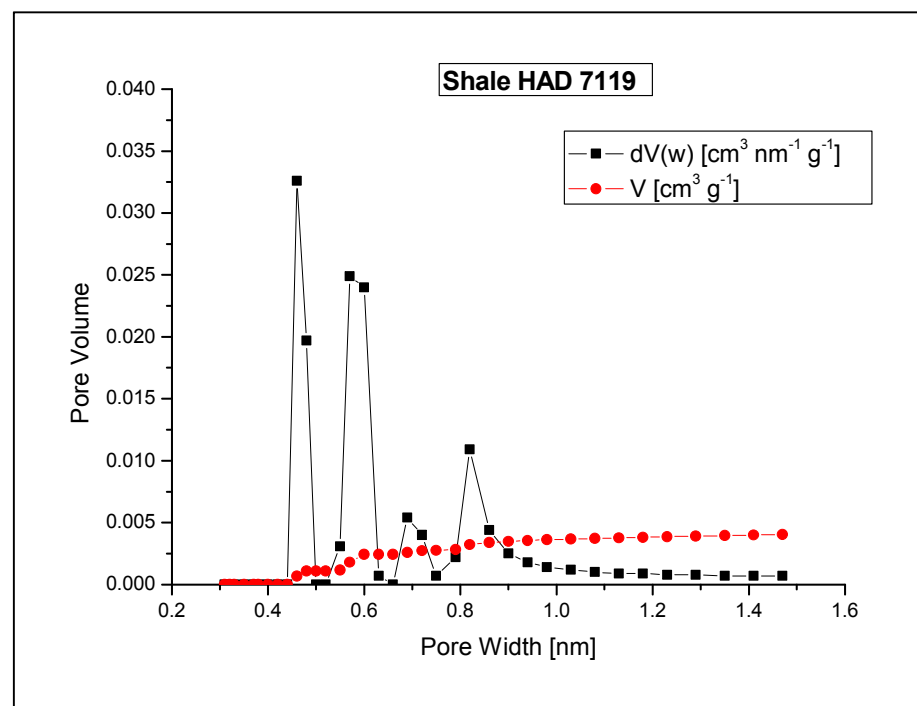
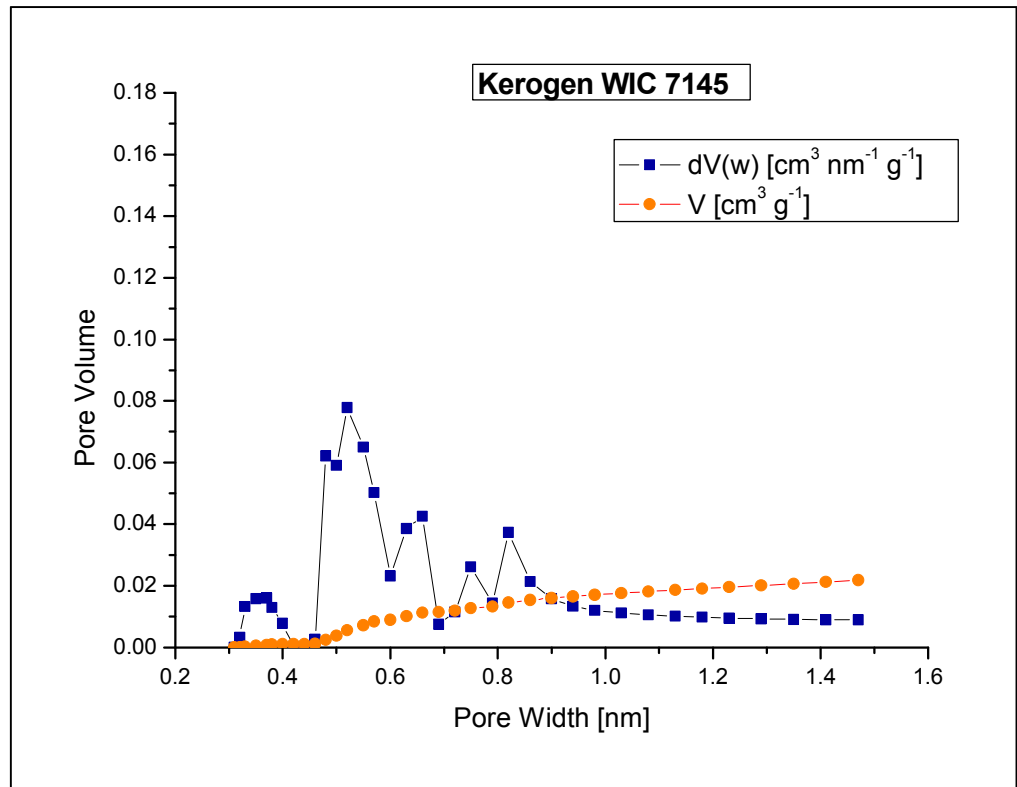


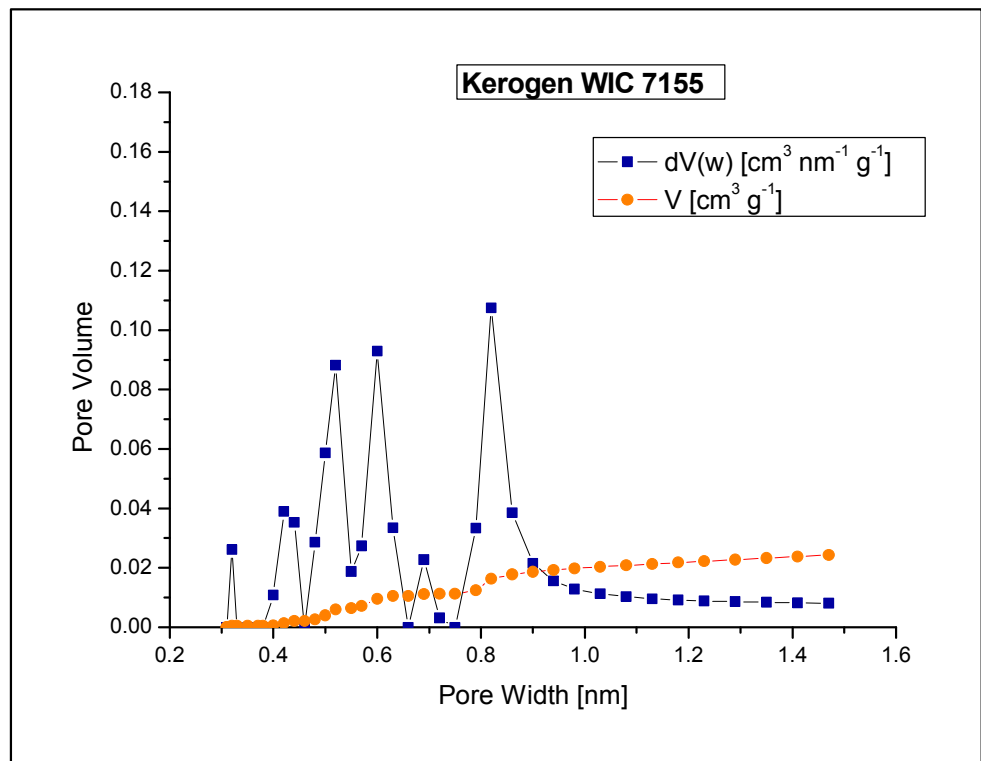
Figure S C6: Micropore Size Distributions on shale calculated from CO_2 adsorption at 273 K by a NDFT equilibrium model with a kernel based on slit-shaped pores in carbon. a) WIC7145; b) WIC7155; c) HAR7038; d) HAR7060; e) HAD7090; f) HAD7119.

Kerogen

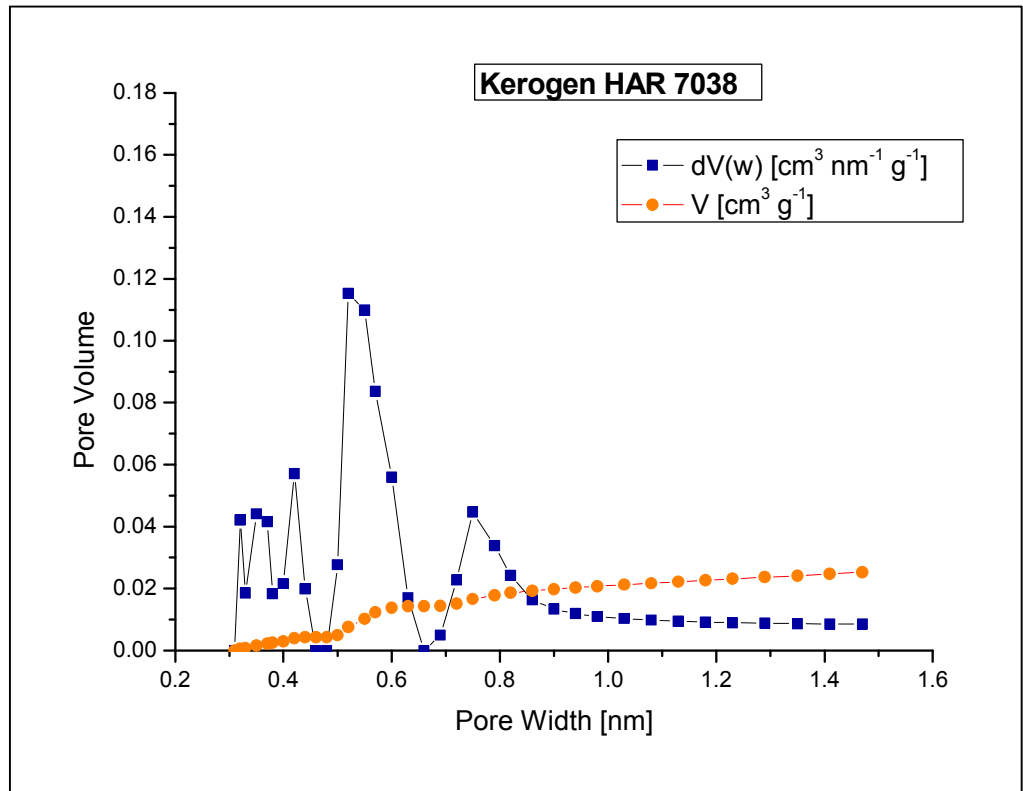
a)



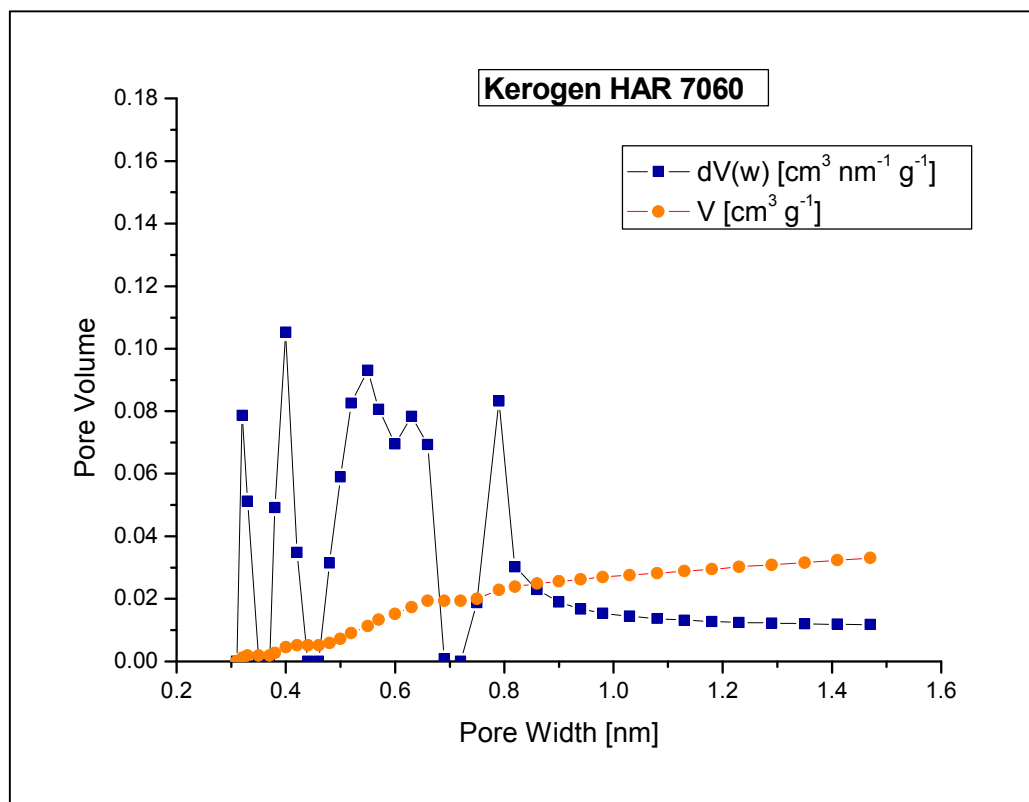
b)



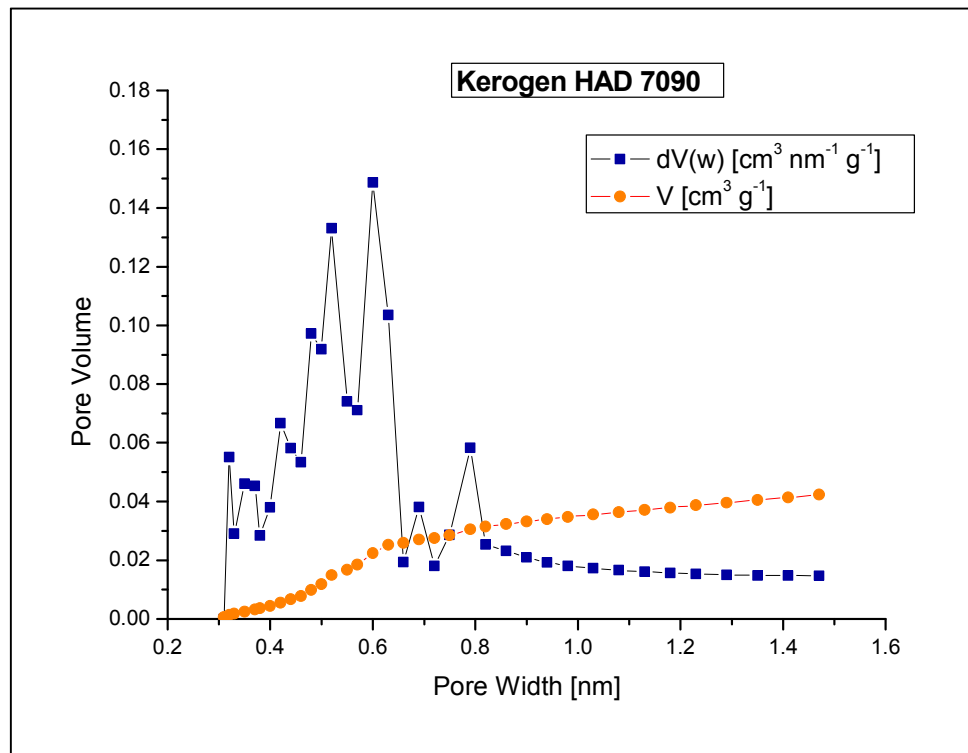
c)



d)



e)



f)

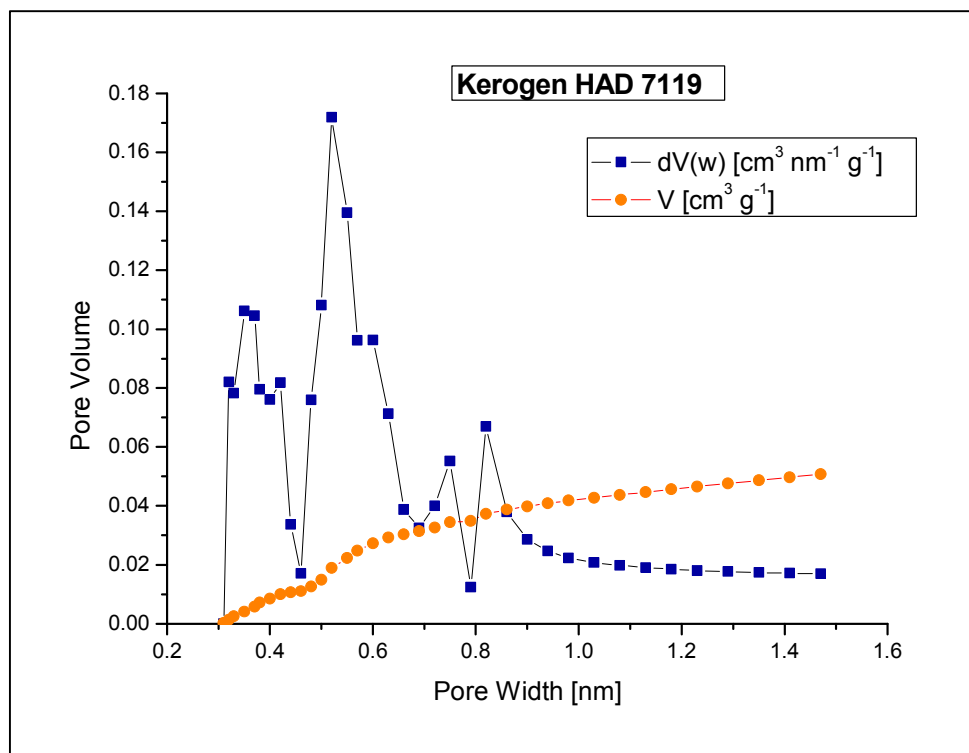
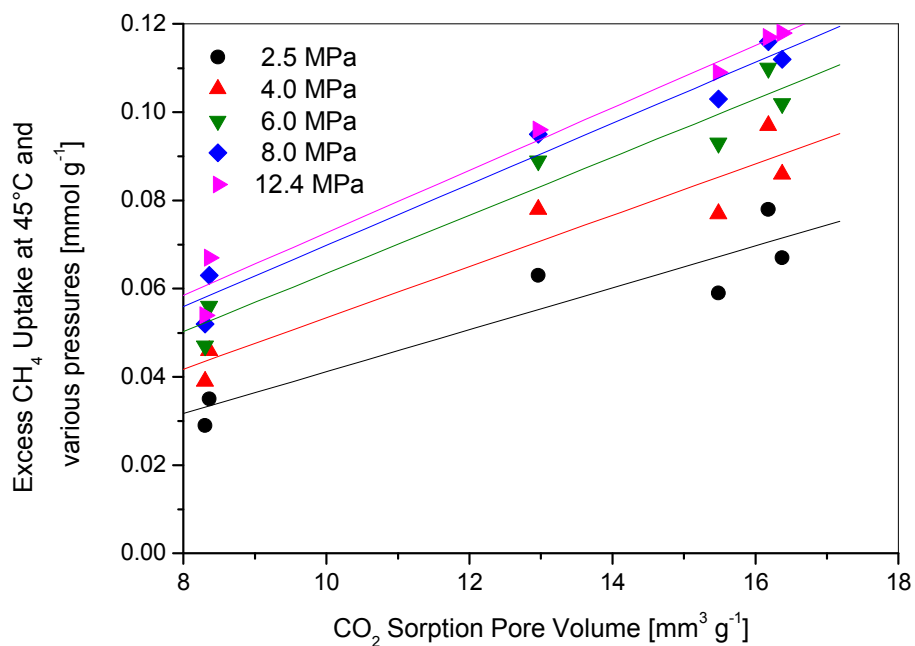


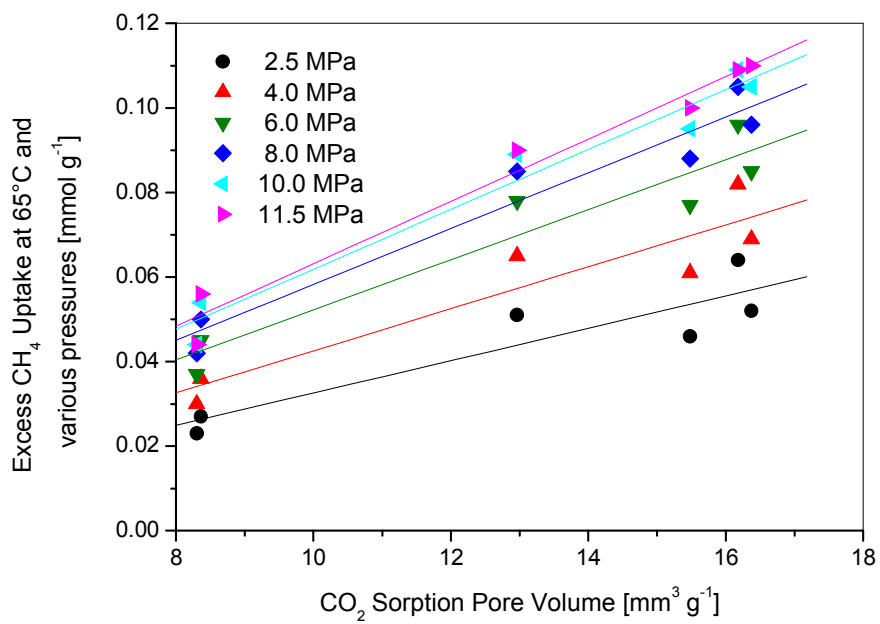
Figure S C7: Micropore Size Distributions on kerogen calculated from CO_2 adsorption at 273 K by a NDFT equilibrium model with a kernel based on slit-shaped pores in carbon. A) WIC7145; b) WIC7155; c) HAR7038; d) HAR7060; e) HAD7090; f) HAD7119.

E. Comparison of methane surface excess at specific pressures with CO₂ sorption pore volume

a)



b)



c)

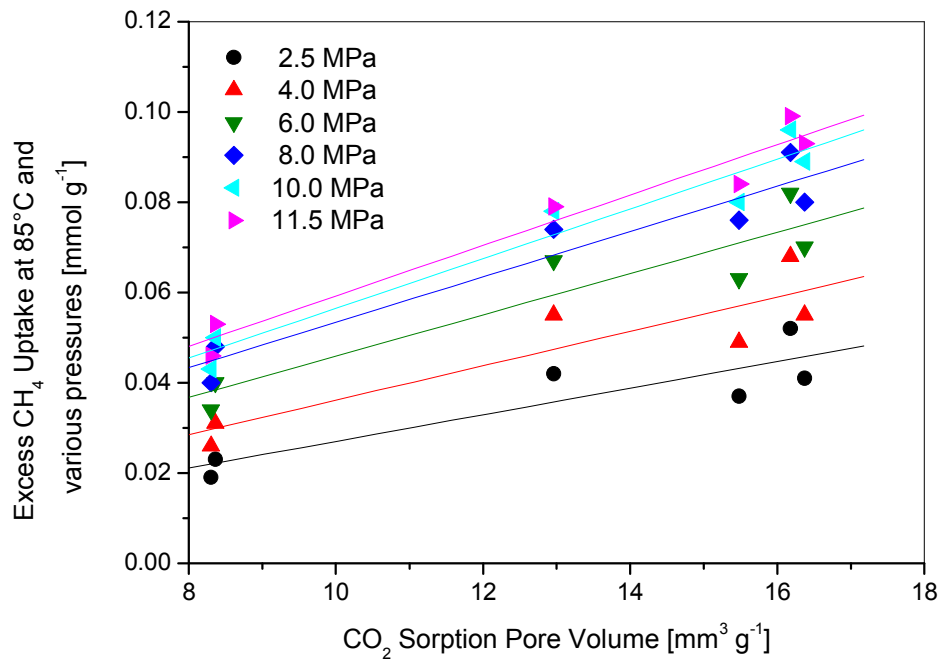
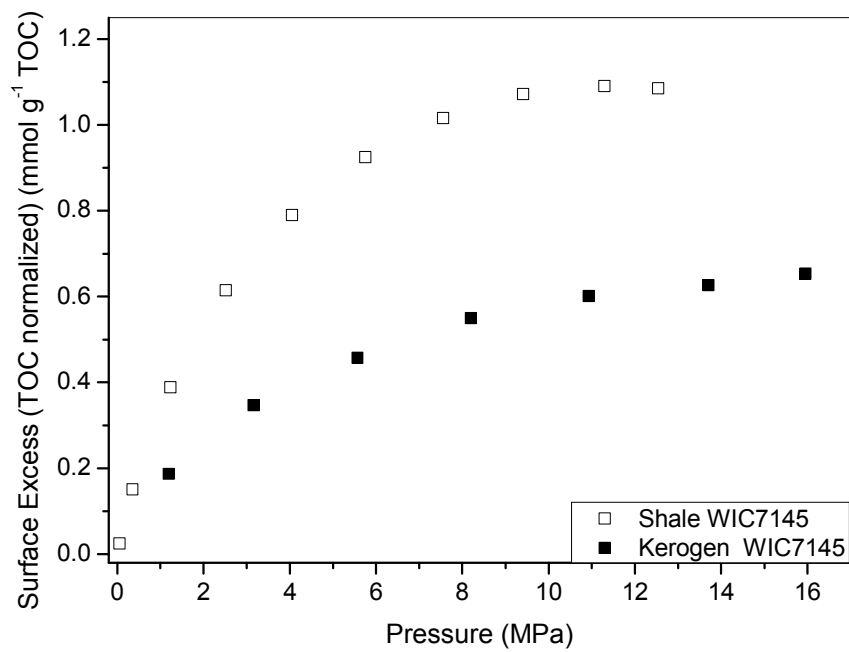


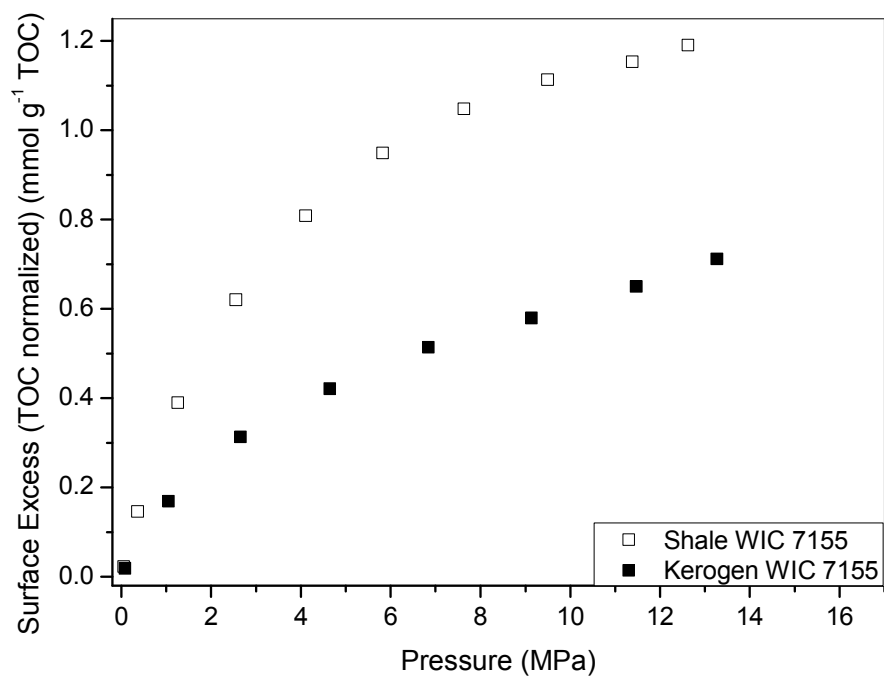
Figure S C8: Comparison of methane surface excess at specific pressures with CO₂ sorption pore volume a) 45°C, b) 65°C, c) 85°C.

F. Comparison of High Pressure Methane Isotherms Normalized to TOC

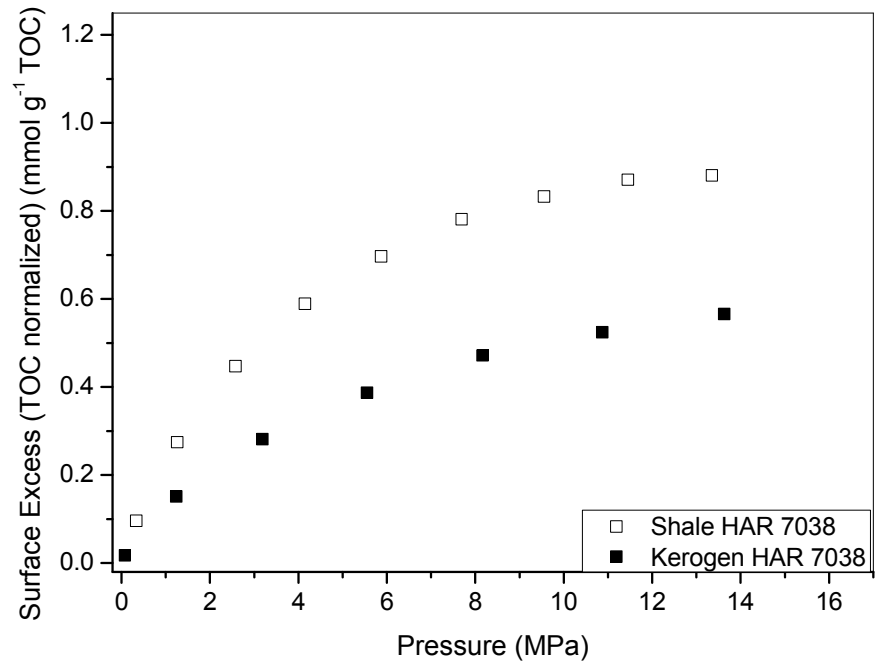
a)



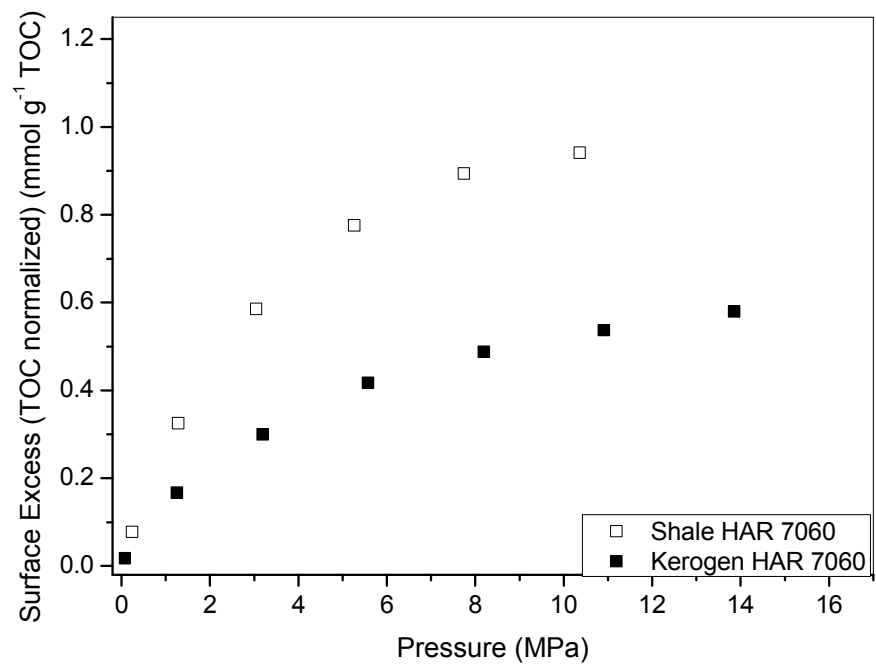
b)



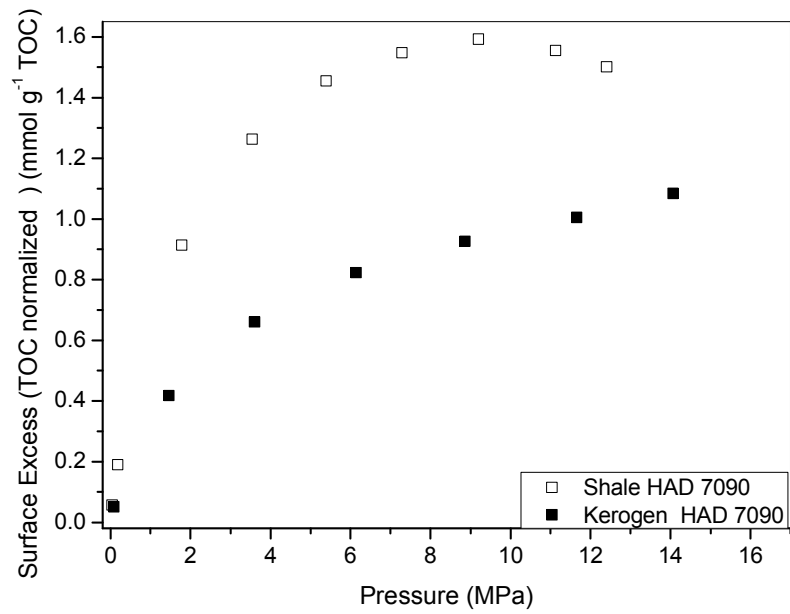
c)



d)



e)



f)

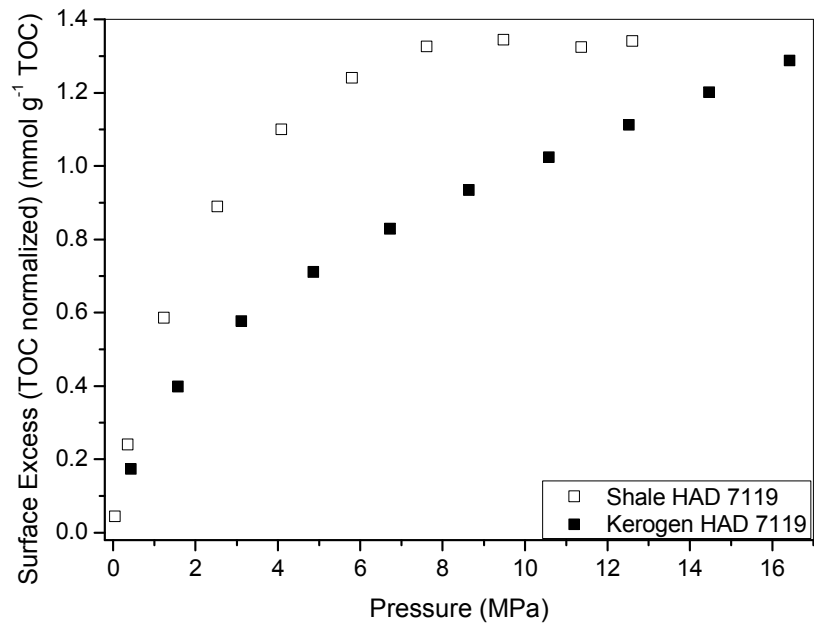
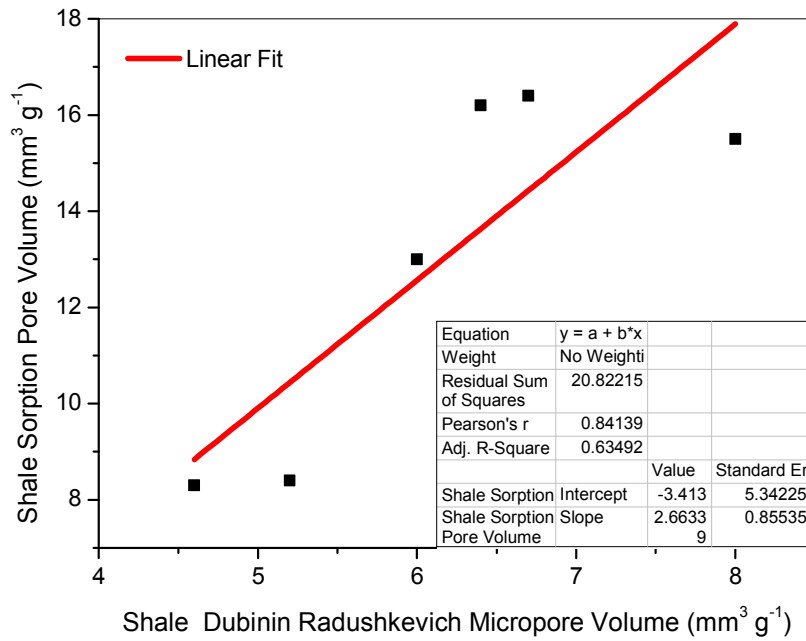


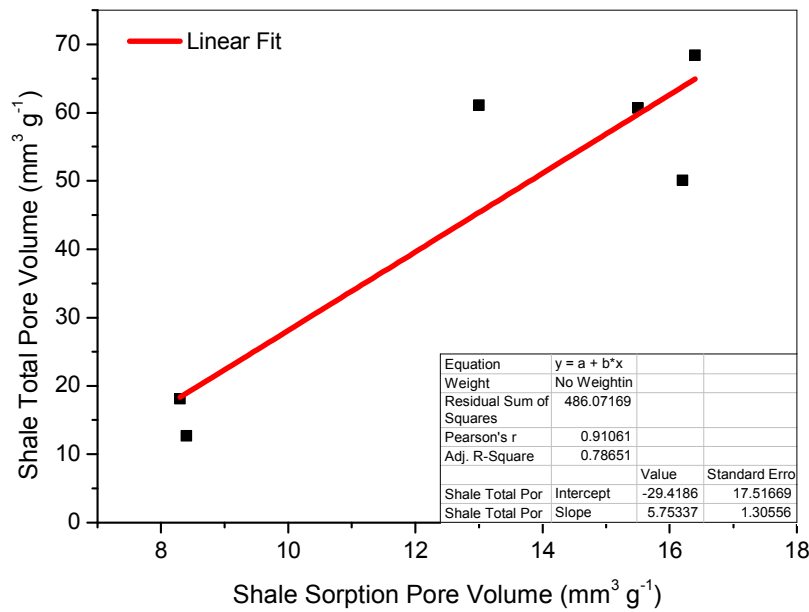
Figure S C9: Comparison of supercritical methane isotherms normalized to TOC for shales and kerogens a) WIC 7145, b) WIC 7155, c) HAR 7038, d) HAR 7060, e) HAD 7090, f) HAD 7119.

G. Comparison of Porosity Characteristics determined from Subcritical Low Pressure/Temperature Adsorption

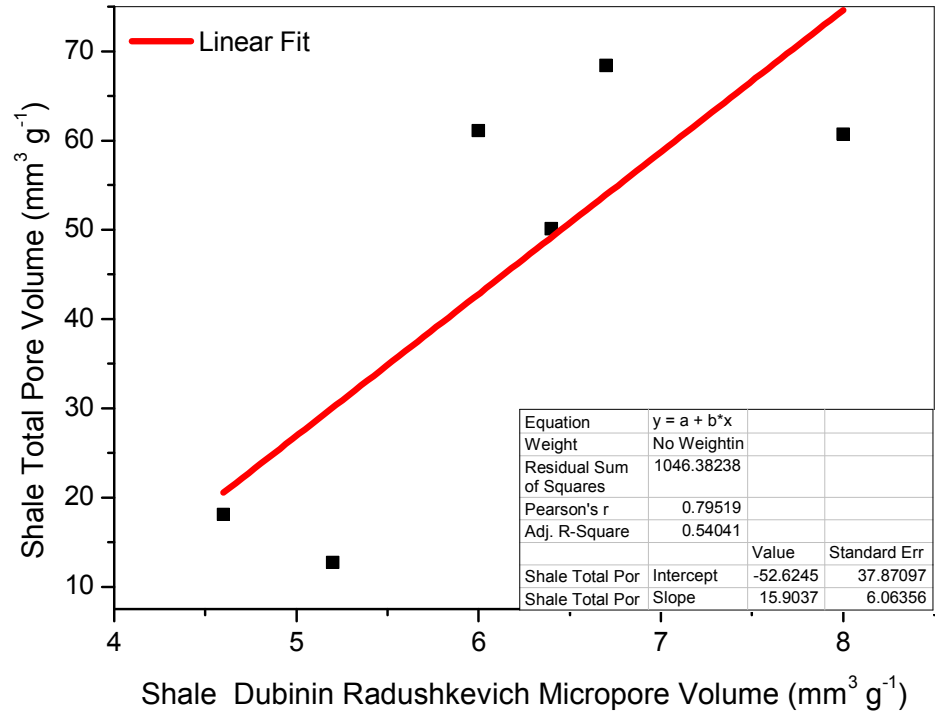
a)



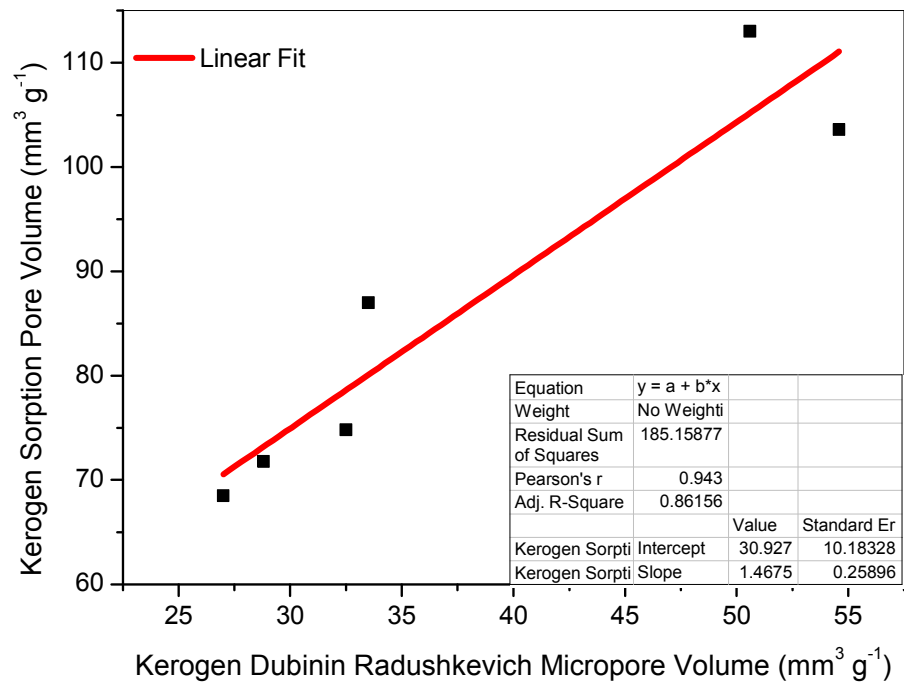
b)



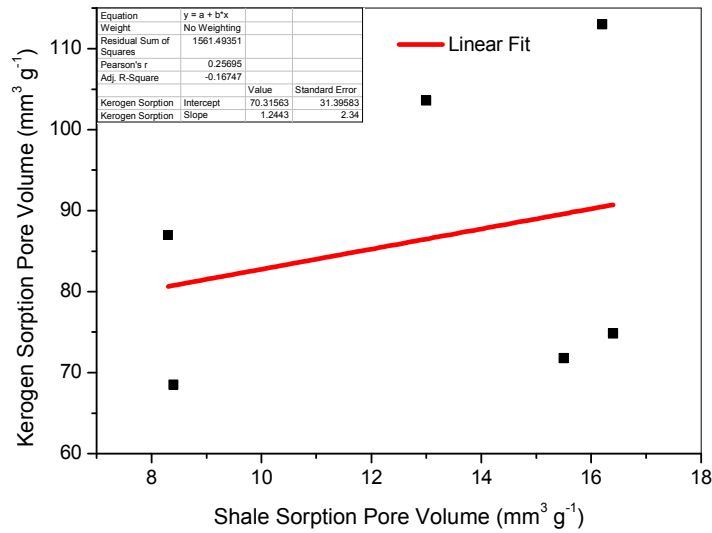
c)



d)



e)



f)

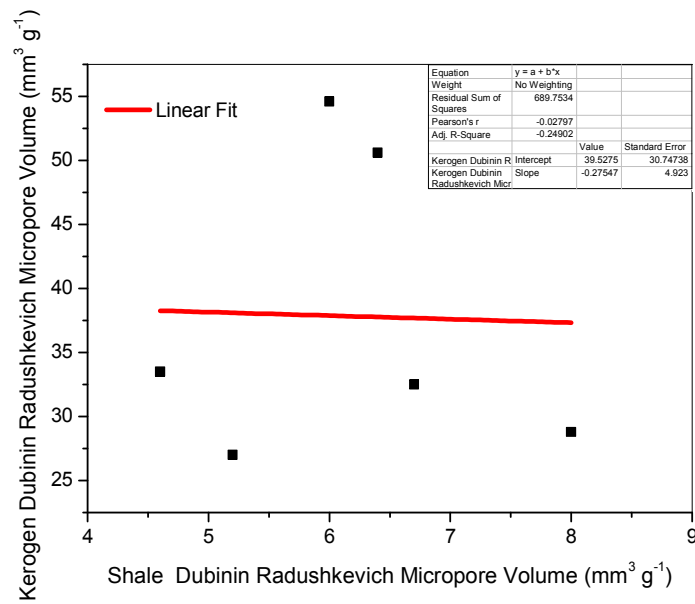


Figure S C10: Comparison of porosity characteristics determined from subcritical low pressure adsorption a) Shale CO₂(-78°C) sorption pore volume versus shale CO₂(0°C) Dubinin-Radushkevich micropore volume, b) shale total pore volume versus Shale CO₂(-78°C) sorption pore volume, c) shale total pore volume versus shale CO₂(0°C) Dubinin-Radushkevich micropore volume, d) kerogen CO₂(-78°C) sorption pore volume versus kerogen CO₂(0°C) Dubinin-Radushkevich micropore volume, e) Shale CO₂(-78°C) sorption pore volume versus kerogen CO₂(-78°C) sorption pore volume f) kerogen CO₂(0°C) Dubinin-Radushkevich micropore volume versus shale CO₂(0°C) Dubinin-Radushkevich micropore volume.

References

- (1) Vandenbroucke, M.; Largeau, C. *Org. Geochem.* **2007**, *38*, 719.
- (2) Durand, B.; Nicaise, G. In *Kerogen - Insoluble organic matter from sedimentary rocks*; Durand, B., Ed.; Editions Technip: Paris, 1980, p 35
- (3) Saxby, J. D. *Chemical Geology* **1970**, *6*, 173.
- (4) Canfield, D. E.; Raiswell, R.; Westrich, J. T.; Reaves, C. M.; Berner, R. A. *Chemical Geology* **1986**, *54*, 149.
- (5) Okiongbo, K. S.; Aplin, A. C.; Larter, S. R. *Energy Fuels* **2005**, *19*, 2495.
- (6) Standard, B. In *Methods for analysis and testing of coal and coke. Proximate analysis. Determination of moisture content of the general analysis test sample. Determination of ash* BSI: 1999, p 12.
- (7) Standard, B. In *Hard coal and coke. Determination of volatile matter* BSI: 2010, p 20.
- (8) Standard, B. In *Solid mineral fuels. Determination of ash*; BSI: 2010, p 16.
- (9) Standard, B. In *Coal. Proximate analysis* 2010, p 14.
- (10) Music, S.; Popovic, S.; Ristic, M. *Journal of Radioanalytical and Nuclear Chemistry-Articles* **1992**, *162*, 217.

Remarks on Unit Conversions

As far as we are aware there is no standard conversion factor for converting mmol g^{-1} to standard cubic foot per ton (scf t^{-1}). The conversion factor depends on the choice of standard conditions (and there are various different definitions in the literature). Furthermore, it depends on whether t denotes metric ton or U.S. “short” ton (907.18474 kg).

We have used the following conversion published in Zhang et al.¹

$$1 \text{ mmol g}^{-1} = 711.42 \text{ scf t}^{-1}$$

with t denoting U.S. “short” ton and 1 scf the amount of an ideal gas at 273.15 K and 102.273 kPa.

(1) Zhang, T. W.; Ellis, G. S.; Ruppel, S. C.; Milliken, K.; Yang, R. S. *Org. Geochem.* **2012**, *47*, 120.